

Development of Quantum Information and Sensing Tools Based on Four-Wave
Mixing in Hot Rubidium Vapor

Ziqi Niu

Shanxi, China

Bachelor of Science, Bucknell University, 2017
Master of Science, The College of William & Mary, 2021

A Dissertation presented to the Graduate Faculty of
The College of William and Mary in Virginia in Candidacy for the Degree of
Doctor of Philosophy

Department of Physics

The College of William and Mary in Virginia
May, 2025

APPROVAL PAGE

This Dissertation is submitted in partial fulfillment of
the requirements for the degree of

Doctor of Philosophy



Ziqi Niu

Approved by the Committee, March 2025



Committee Chair

Irina Novikova, Professor, Physics
College of William & Mary



Eugeny Mikhailov, Professor, Physics
College of William & Mary



Seth Aubin, Associate Professor, Physics
College of William & Mary



Ebubechukwu Ilo-Okeke, Assistant Professor, Physics
College of William & Mary



Jianming Wen, Associate Professor, Electrical and Computer Engineering
Binghamton University

ABSTRACT

Quantum correlated optical fields are crucial in quantum information and sensing applications. Nonlinear optics serves as a primary mechanism for generating these correlated fields. This dissertation focuses on a specific nonlinear interaction known as Four-Wave Mixing (FWM), achieved in a warm atom ensemble and its applications. For this we developed a bi-chromatic continuous variable entangled-photon source, aimed at enhancing long-distance quantum communication, and examined the optimal conditions. Our findings contribute to the advancement of a continuous variable-discrete variable (CV-DV) hybrid quantum computing device. Additionally, we expanded the study of FWM squeezing within the context of non-Hermitian physics, which holds implications for quantum simulation and non-Hermitian sensors. Lastly, we enhanced the conventional homodyne detection method by incorporating spatial resolution, achieving few-photon imaging through quantum noise and pushing the boundary of quantum imaging.

TABLE OF CONTENTS

| | |
|---|------|
| Acknowledgments | v |
| Dedications | vi |
| List of Tables | vii |
| List of Figures | viii |
| Chapter 1. Introduction | 1 |
| 1.1 Historical Review of Nonlinear Optics and FWM | 2 |
| 1.2 Quantum Applications of FWM | 3 |
| 1.2.1 FWM as Photon Pair and Squeezed Light Source | 3 |
| 1.2.2 FWM for Quantum Imaging Applications | 5 |
| 1.2.3 FWM for Simulating Non-Hermitian system | 7 |
| 1.3 Thesis Outline | 8 |
| Chapter 2. Theory Overview | 10 |
| 2.1 Classical Description of Electromagnetic Field | 10 |
| 2.2 Classical Description of FWM | 14 |
| 2.3 Quantum Formalism of FWM | 17 |
| 2.4 Theory for Noise and Squeezing | 19 |
| 2.4.1 Quantum Noise of a Single Optical Field | 19 |
| 2.4.2 Differential Noise & Two-Mode Intensity Squeezing | 22 |
| 2.4.3 Continuous Variable Noise Analysis: Noise Quadratures | 23 |

| | | |
|------------|--|----|
| 2.4.4 | Quadrature of Two-Mode Squeezed State | 25 |
| 2.4.5 | Optical Loss: Beam Splitter Model | 26 |
| 2.4.6 | Optical Loss: Langevin Noise Formalism | 30 |
| Chapter 3. | Fundamentals of Two-Mode Squeezing Generation in Double- Λ and Double-Ladder Atomic Systems | 35 |
| 3.1 | Theoretical Description of Light-Atom Interaction | 36 |
| 3.2 | FWM in Double- Λ Configuration | 38 |
| 3.2.1 | Density Matrix Calculations for a Double- Λ Configuration | 38 |
| 3.2.2 | Experiment Setup | 44 |
| 3.2.3 | Additional Considerations | 48 |
| 3.2.4 | Technical Noises and System Debugging | 52 |
| 3.3 | FWM in Double-Ladder Configuration | 57 |
| 3.3.1 | Density Matrix Calculation and Numerical Simulation | 57 |
| 3.3.2 | Experiment Description | 60 |
| 3.3.3 | Experiment Setup How-to Guide | 62 |
| 3.4 | Comparison between two Configurations | 65 |
| Chapter 4. | Bi-Chromatic Intensity Squeezing using FWM in Hot ^{85}Rb Vapor | 67 |
| 4.1 | Introduction | 67 |
| 4.2 | Numerical Modeling of FWM with Complete Hyperfine Level Structure | 69 |
| 4.3 | FWM Gain Optimization | 74 |
| 4.3.1 | Operational Temperature | 75 |
| 4.3.2 | Laser Detunings | 75 |
| 4.3.3 | Laser Intensities | 81 |
| 4.4 | Results: Bi-chromatic Intensity Squeezing | 83 |
| 4.5 | Gain and Squeezing at High Power: Simulation | 85 |

| | | |
|--|--|-----|
| 4.6 | Possible Improvements in FWM Gain and Squeezing: Preliminary Results | 87 |
| 4.6.1 | Improved Atomic State Preparation via Velocity-Selective Optical Pumping | 87 |
| 4.6.2 | Gain Improvement by Multiwave Dressing with Weak Field | 89 |
| 4.6.3 | FWM Gain Manipulation with the Repeated Seeding | 90 |
| 4.7 | Conclusion | 92 |
| Chapter 5. Weak thermal state imaging | | 93 |
| 5.1 | Quantum Imaging Model | 94 |
| 5.1.1 | Calculation of Normalized Variance | 95 |
| 5.1.2 | Theoretical Signal-to-Noise Ratio (SNR) | 97 |
| 5.2 | Experimental verification | 98 |
| 5.2.1 | General Description | 98 |
| 5.2.2 | Frequently Asked Technical Details | 99 |
| 5.2.3 | Experimental Results | 115 |
| 5.3 | Conclusion | 117 |
| Chapter 6. Anti-Parity-Time Symmetry in Hot Rubidium Vapor | | 120 |
| 6.1 | Introduction | 120 |
| 6.2 | Anti-PT FWM Overview | 122 |
| 6.2.1 | Connecting FWM with Anti-PT Symmetry | 122 |
| 6.2.2 | Numerical Model | 125 |
| 6.2.3 | Comparison between Traditional and Anti-PT Squeezing | 127 |
| 6.3 | Experiment Design | 128 |
| 6.4 | Results and Discussion: Experimental anti-PT squeezing | 129 |
| 6.5 | Conclusion and Outlook | 134 |

| | |
|--|-----|
| Chapter 7. Conclusion and Future Work | 137 |
| Appendix A. Squeezing Calculation Matlab Script with Langevin Correction | 139 |
| A.1 Analytical Calculation for Langevin Terms | 139 |
| A.2 MATLAB Function Script | 142 |
| Appendix B. Double-Ladder Numerical Model Python Script | 150 |
| Appendix C. Circular binning variance Calculation | 158 |
| C.1 Calculation of Normalized Variance | 158 |
| C.2 Circular Binning | 159 |

ACKNOWLEDGMENTS

I would like to thank my advisor Irina Novikova. I own everything I call achievement for the past six years to her. She took me under her wings during the most difficult and unfortunate time of my life, and taught me to be a good scientist and kind person. I held the utmost trust and respect for her and was following her steps since then like a small duck, but it is my time to leave the nest. I searched for all the words to express my gratitude, but I suppose a simple thanks will do. The rest lies in hard work and a helping hand to others. I want to thank my other advisor Eugeniy for all the research and moral supports (and music recommendation too, I still listen to korol i shut from time to time). It's such a delight to be around him, we all begin quoting his words like "what is life without pain" and "finding who's guilty is an existential problem" after working with him for a while. I'm frequently the guilty one though. I want to say thanks for collaborators Pratik Barge and Yue (Joyce) Jiang. It is great to work closely with them, who are very motivated, smart and hard-working. All the arguments and discussions really push me to learn and to improve. I want to thank all my supervisors during the projects: Lior Cohen, Hwang Lee, Jianming Wen, Chuanwei Zhang, and Shengwang Du. They formed the ideas and offered guidance for my work done. I want to say thank you to Professor Wen specifically, who is always kind, responsive and willing to help. I thank my former and current group members: Nik I, Savannah, Nic II, Rob and Charris. Thank you guys for all the moral supports and help in lab. We really work like a team and never hesitate to help each other and it was great time. I want thank Nik and Savannah for all the help I received when I just started working in the lab. They taught me a lot of experiment tricks and details hand by hand. And thanks for Nic, Rob and Charris, for all the emotional supports (Especially for Nic since this unfortunate soul locked with me for all six years and has to hear my ranting). My thanks to all my committee members for their time and effort, especially they willing to attend my defense in Spring break time. Lastly, my thanks to my mother, my uncle and my grandma. They suffered, but they never stop supporting me. Lastly, I want to thank dad, I kept my promise to his death bed. I hope he'll feel proud of me.

To my parents

LIST OF TABLES

| | |
|---|----|
| 3.1 A point by point comparison between the double- Λ and ladder configurations | 66 |
|---|----|

LIST OF FIGURES

- 1.1 Two mode intensity squeezing from photon correlation perspective. Each vertical line denotes photon counts at certain time stamp. The x-axis is the time. (a) The twin fields from FWM. The photons generated in time are always in pairs. In other words, they have a strong temporal correlation. If we measure the differential signal over time, then ideally the differential signal will be 0, leading to reduced temporal variance. (b) Two uncorrelated laser (coherent state) fields. The photons generation in time are independent in this case, and the differential signal variance has no aforementioned cancellation and is therefore noisy. 4
- 1.2 Three main methods for quantum imaging. (a) Interference based quantum imaging, (b) Correlation based quantum imaging, and (c) entanglement based quantum imaging 6
- 2.1 a) Illustration of FWM in a $\chi^{(3)}$ medium. b) geometric phase-matching condition. c) Energy level diagram for FWM. 14
- 2.2 Illustration of quadrature squeezing. a) The coherent state representation. b) Single mode squeezed state representation. c) Quadratures of an individual field from the FWM correlated fields. Each shows super-poissonian statistics. The noise distribution is broader. d) The two-mode squeezed quadrature. In our case, we always measure along direction Z_1 by conducting a differential measurement. 24

- 2.3 (a) Illustration of the continuous beam-splitter model: at each infinitesimal step, the input state is modified by a fictitious beam splitter with a vacuum input. This process is repeated over N steps to obtain the final output. (b) Detailed illustration of the beam-splitter model for an individual step. 27
- 3.1 Energy level diagram used for the FWM model. Here, atomic levels $|1\rangle$ and $|2\rangle$ represent two ground-state hyperfine levels $|5S_{1/2}F = 2, 3\rangle$ of ^{85}Rb , while levels $|3, 4\rangle$ both represent the excited electron state $|5P_{1/2}\rangle$ [109]. In the schematic, the pump field (Ω) applied at both transitions $|1\rangle \rightarrow |3\rangle$ and $|2\rangle \rightarrow |4\rangle$ is shown in red, and the probe (Ω_P) and conjugate (Ω_C) fields are labeled by the blue and black arrows. 38
- 3.2 (a) Double- Λ atomic scheme used for describing the FWM process at the D_1 transition of ^{85}Rb . The strong pump laser is detuned by $\Delta_1 = 0.7$ GHz and $\Delta_2 = 3.7$ GHz from the $|5^2S_{1/2}F = 2\rangle \rightarrow |5^2P_{1/2}\rangle$ and the $|5^2S_{1/2}F = 3\rangle \rightarrow |5^2P_{1/2}\rangle$ optical transitions, respectively. And $\Delta_{HF} = 3035.7$ MHz is the ground-state hyperfine splitting. (b) Geometrical arrangement of the optical fields in the FWM process with the momentum mismatch $\Delta\vec{k} = 2\vec{k} - \vec{k}_P - \vec{k}_C$. 45
- 3.3 Full experimental setup diagram for double- Λ FWM generation 46
- 3.4 Close-up setup diagram for the double- Λ system. 47
- 3.5 Oscilloscope image. The blue trace is the photodiode monitoring of laser frequency using another photodiode. The orange trace is the Etalon transmission spectra, showing the main peak, and the first order modulation peak representing pump, probe, and conjugate. 51

- 3.6 A sample dark calibration for dark noise, with the spectrum analyzer detection range from 0 to 4MHz. The good detection region is shaded. To the left of the shade area the noise is dominated by $1/f$ noise. To the right of the shaded area a noise peak is observed for an unknown reason. 55
- 3.7 SNL calibration setup. This is the same setup used for squeezing measurement to ensure fair comparison, but with two laser inputs of equal power. The overall classical noise is subtracted out. 56
- 3.8 Shot noise data and its functional fit. This fit reveals that the noise power (which represents the optical field variance) scales linearly with the photonvoltage (proportional to the optical power/photon flux). This linear relationship is crucial for calibrating the shot noise level and serves as a diagnostic tool to verify whether a laser field displays super-Poissonian statistics due to extra noise sources contaminating the measurement. The noise power reduced to the measured dark noise line instead of 0. 57
- 3.9 Simplified double-ladder atomic configuration of ^{85}Rb employed in the experiment. The D2 pump ($\Omega_{D2,\text{red}}$) and IR pump ($\Omega_{IR,\text{blue}}$) are linearly polarized in the same direction and intersect inside the vapor cell with an orthogonally-polarized probe beam (Ω_P,black). The conjugate field (Ω_C,purple) is generated with the same polarization as the probe. 58

- 3.10 a) Simplified experimental setup. Non optional input fields are shown as solid lines. Blue: 1367nm pump field. Red:780 nm (D2) pump field. Black: 795 nm (D1) probe field. The generated 1324 nm conjugate field is displayed as purple dotted line. Two optional coupling fields can be coupled into the system to manipulate the atomic populations or activate the higher order wave mixing. The repump field(shown as black dashed line) is counter-propagating with the D1 seed, while the dressing field is coupled. Blue dot: 780 Repump. b) Atomic level diagram 61
- 4.1 (a) Double-ladder atomic configuration of ^{85}Rb employed in the experiment. (b) Experimental setup: The D2 pump (red) and IR pump (blue) are linearly polarized in the same direction and intersect inside the vapor cell with an orthogonally-polarized probe beam (black). The conjugate field (purple) is generated with the same polarization as the probe. (c) Phase-matched FWM geometry of the optical fields within the vapor cell. 69
- 4.2 Detailed level diagram used in the numerical model. Level $|1b\rangle$ does not participate in the interaction but acts as a reservoir, accounting for population changes due to optical pumping, decay, and atomic motion. 70

4.3 Experimentally measured (solid lines) and simulated (dotted and dashed lines) probe and conjugate gains, G_P (a) and G_C (b), are shown as functions of probe detuning Δ_{D1} . Zero detuning corresponds to the maximum resonance absorption, with vertical lines marking the positions of the $|5S_{1/2}, F = 3\rangle \rightarrow |5P_{1/2}, F' = 2, 3\rangle$ optical resonances. For these measurements, the two pump detunings are set at $\Delta_{D2} = -280$ MHz and $\Delta_{IR} = 800$ MHz [152], with their respective powers: $P_{D2} = 260$ mW and $P_{IR} = 33$ mW. The maximum measured FWM gain values are $G_P = 1.73$ and $G_C = 1.05$ at a probe detuning of $\Delta_{D1} \approx 600$ MHz. The calculated spectra account for photodetector quantum efficiencies and probe light's resonant absorption. Simulation data for $\Delta k = 0$ (dashed) and Δk with approximations (dotted, small in the gain region and large elsewhere) are also presented. 72

4.4 Sample data traces used for experimental optimization process. (a) Measured normalized probe transmission G_P with only the D1 laser sweeping while frequencies of both D2 and IR pumps fixed. (b) Recorded normalized probe G_P and conjugate G_C gain spectra, recorded with both D1 and D2 frequencies sweeping while IR frequency locked. For each gain peak, the D1 and D2 detunings can be mapped precisely using the saturation spectroscopy as reference signals. The blue and orange traces represent two data sets with shifted sweeping phase between D1 and D2, causing the gain peak amplitudes and locations to change accordingly. 77

- 4.5 Measurements of the FWM gain for the conjugate field (a) and for the probe field (b) as a function of the two-photon pump detuning $\Delta_{\text{Pump}} = \Delta_{\text{D2}} + \Delta_{\text{IR}}$ in the low-intensity regime. Two ovals indicate the regions of highest conjugate gain G_C . The cell temperature is 100 °C (corresponding Rb density $N = 4.76 \times 10^{12} \text{cm}^{-3}$), pump powers are 26mW and 33mW, respectively, for D2 and IR pump. 78
- 4.6 FWM gain map: Maximum measured values of probe gain G_P (a) and conjugate gain G_C (b) as a function of optimal probe detuning Δ_{D1} (horizontal axis) and two-photon pump detuning $\Delta_{D2} + \Delta_{IR}$ (vertical axis). (c) Unamplified probe transmission (without pump fields). The region where maximum intensity squeezing is achieved is highlighted with a black circle. The same pump laser powers as in Fig.4.3 are used: $P_{D2} = 260 \text{ mW}$ and $P_{IR} = 33 \text{ mW}$. 80
- 4.7 Dependence of the FWM gain $G_{P/C}$ (a, b) and relative intensity squeezing (c, d) on the pump laser powers. The left column shows data for varying D2 pump power with fixed IR pump power at $P_{IR} = 35 \text{ mW}$, while the right column corresponds to varying IR pump power with fixed D2 pump power at $P_{D2} = 290 \text{ mW}$. The solid lines represent theoretical gain predictions from the numerical model, while the dashed lines in the squeezing data provide a visual guide. The small hollow circles denote the experimentally measured values. 82

- 4.8 The variance of the relative photocurrent noise spectrum (red), $\text{Var}(\hat{n}_P - \hat{n}_C)$, for the probe and conjugate fields, along with their individual intensity noise levels, $\text{Var}(\hat{n}_{P/C})$ (black/purple). As reference, the black straight line marks the shot-noise level, $\text{Var}(\hat{n}_P^{(coh)} - \hat{n}_C^{(coh)})$, measured for two coherent laser fields. The relevant detunings are $\Delta_{D1} \approx 800$ MHz, $\Delta_{D2} = -280$ MHz, and $\Delta_{IR} = 800$ MHz, with two pump laser powers of $P_{D2} = 350$ mW and $P_{IR} = 32$ mW, respectively. 83
- 4.9 Theoretically predicted FWM gain values for the probe (a) and conjugate (b) output fields are shown over a wider range of pump laser powers. The calculations assume detunings of $\Delta_{D2} \approx -280$ MHz, $\Delta_{IR} \approx 800$ MHz. To locate the maximum FWM gain peak, we adjust Δ_{D1} from approximately 400 to 800 MHz, accounting for the light shift caused by the vastly different pump powers. (c) Predicted differential intensity squeezing is shown, based on the calculated gain values and the residual resonant absorption of the probe field, using a beam-splitter model. The black squares represent the range of pump powers used in the experiment. 86
- 4.10 Normalized FWM gain for the probe and conjugate optical fields with/without the presence of velocity-selective optical pumping. Experimental settings: input laser powers $P_{D2} \approx 80$ mW, $P_{IR} \approx 37$ mW, $P_{D1} \approx 0.6$ mW, $P_{\text{Repump}} \approx 7$ mW, the cell temperature $T = 96^\circ\text{C}$ (corresponding Rb density $N = 3.6 \times 10^{12} \text{cm}^{-3}$), and $\lambda_{IR} = 1366.8640$ nm 87

4.11 Modification of the FWM gain via the dressing laser field, tuned to $|5S_{1/2} F = 3\rangle \rightarrow |5P_{1/2}\rangle$ transition. (a) Normalized probe transmission under the FWM conditions T_P with and without the dressing field. (b) Similar normalized probe transmission without FWM (no IR pump present) in the presence of the/no dressing field. (c) Saturation spectroscopy D2 laser frequency reference. All trace are recorded with D1 laser tuned to the 83% transmission level. We used f=400 mm lens for D1 seed in this set of data. Experimental settings: input laser powers $P_{D2} \approx 320\text{mW}$, $P_{IR} \approx 35\text{mW}$, $P_{D1} \approx 2\text{mW}$, the cell temperature $T = 100^\circ\text{C}$ (corresponding Rb density $N = 4.76 \times 10^{12}\text{cm}^{-3}$), and $\lambda_{IR} = 1366.8640 \text{ nm}$ 90

4.12 (a) Schematic arrangements for a double-seeded FWM, where the generated conjugate field is fed back into the input. The singly seeded case is shown in Fig.4.1(b). (b) Measured normalized probe transmission G_P for a regular (orange) and double-seeded FWM (blue), where the relative phase of the conjugate field is adjusted to produce maximum FWM gain. The saturation spectroscopy reference D1 laser signal is shown in yellow. Experimental settings: input laser powers $P_{D2} \approx 250\text{mW}$, $P_{IR} \approx 32\text{mW}$, $P_{D1} \approx 2 \text{ mW}$, the cell temperature $T = 92^\circ\text{C}$ (corresponding Rb density $N = 2.78 \times 10^{12}\text{cm}^{-3}$) with 26mW repump field , and $\lambda_{IR} = 1366.8590 \text{ nm}$. 91

5.1 Simplified experimental setup. We show here only the detector side which contains a black-box probe and local oscillator source. 95

| | | |
|-----|--|-----|
| 5.2 | Block diagram of operator actions in QSI scheme: \hat{T}_1 acting on probe state $\hat{\rho}$ in mode 1 represents the object-probe interaction. In mode 2, operator $\hat{D}_2(\alpha)$ displaces vacuum state. Resulting states in both modes are allowed to interfere by the beam splitter operator \hat{B}_{12} . Two output modes of the beam splitter are transformed from the beam basis to the pixel basis by the mode transformation operators, \hat{U}_1 and \hat{U}_2 . | 96 |
| 5.3 | Theoretical plot of single-shot SNR as a function of averaged probe photons. QSI with a thermal probe (orange) is compared with a coherent state differential imaging for dark-count standard deviation (ΔN_d) ranging from 0 to 10 per pixel. For the CCD camera used in our experiments $\Delta N_d = 10$ per pixel. Object is assumed to be completely opaque (i.e. $t = 0$). | 98 |
| 5.4 | Detailed experimental setup using FWM as the thermal field source. | 99 |
| 5.5 | Classical image of an opaque knife edge. The two images have no observable difference even though a slight difference in optical path. | 100 |
| 5.6 | Classical image of the bug wing. In this case we see slight difference in the twin images due to a finer target(10 μm) | 101 |
| 5.7 | Illustration of data acquisition and processing sequence. | 102 |
| 5.8 | Sample interference pattern between the weak probe seed(test beam) and the local oscillator. We observe that instead of displaying a full black(destructive) or bright(constructive) interference pattern, the interference occurs exclusively at the center region. The visibility is generally over 98%. | 104 |

- 5.9 Representative pulsing sequence of the data acquisition illustrating the process. All pulses (green: pump, red: camera trigger, yellow: LO) are triggered from the camera acquisition trigger. Later the pulses are adjusted such that the probe pulse is overlapped with the camera pulse. 106
- 5.10 Illustration of the circular binning procedure. We assign all pixels in a gaussian circle as one. The inset illustrates the case of $R = 2$ circular binning. 108
- 5.11 Variance map (a) of the insect wing is generated with $R = 1$ and 0.03 photons per pixel per $1.7 \mu s$ exposure. Images (b-d) are generated with values of the binning radii $R = 2, 4, \text{ and } 8$, respectively. 109
- 5.12 Experimental setup for a weak thermal state generation. (a) Pseudo-thermal state generated by scattering a coherent beam with rotating polishing film with grain size $\approx 0.1 \mu m$. b) Thermal state source using FWM process: vacuum input is used as seed to generate weak thermal state. Inset: atomic level diagram of FWM process. Δ_{HF} is the hyperfine splitting between $5S_{1/2}F = 2$ and $5S_{1/2}F = 1$ level. Δ is the one-photon detuning and δ is the two-photon detuning. The red line stands for the pump laser. The blue and black lines represent probe and conjugate beams, respectively [174, 175]. 111
- 5.13 Illustration of different thermal vacuum mode generation. Due to the presence of all possible vacuum modes, the output spatial modes show intrinsically multimode behavior, and can occur within a cone region. Here the blue and pink cones show the thermal vacuums for the probe and conjugate fields. 112

- 5.14 Normalized variance (V) as a function of the detection area (a). The best linear fit is $V = a \times (0.01242 \pm 0.0018) + (1.10 \pm 0.11)$, matching the prediction of Eq.(2). Inset: the same plot for a wider range of detection areas, displaying the V saturation by increasing a . 114
- 5.15 (c) Image of an insect wing with dimensions indicated for reference. (d) Inset shows an enlarged image of the region of interest, obtained with a bright beam. (e) Normalized variance map of the wing obtained with $\approx 301,600$ photons and without any processing. The resolution is around $10 \mu m$, limited by the optical setu, and can be further improved. (f) Normalized variance map after binning all the pixel values within one pixel radius (i.e. $R = 1$). The image contrast increases at the expense of spatial resolution. Note that a thermal state with 0.1 photons/pixel/exposure on average is used for generating image (e). 115
- 5.16 SNR for opaque object imaging in QSI scheme as a function of averaged thermal photon number per detection area $\langle \hat{n} \rangle$. The detected photon number was controlled by either changing the total FWM gain (black circles) for detection area size of $a = 113$ pixels, or by changing the detection area size (red triangles) for the highest FWM gain value. Solid blue curve is the theoretical SNR of Eq.(5.13). Experimentally measured SNR values are divided by $\sqrt{600}$ to be compared with the theoretical values. Inset (a): Transmission map of the opaque object by blocking the left half of the thermal probe and calculated with the binning radius 6 ($a = 113$ pixels). A central circular region is selected based on a good overlap between the probe and the LO. Central shaded region is excluded from the analysis. 119

6.1 (a) Anti-PT Hamiltonian eigenvalues $\pm\lambda$ versus atomic density N , calculated using experimental parameters. (b,c) Experimental (markers) and calculated (lines) absolute (c) and normalized (b) gain values for the probe and conjugate optical fields versus N . (d) Relative intensity squeezing parameter S versus N , showing experimental data (markers) and simulated results from the full quantum model with imbalanced (solid line) detector efficiencies ($t_P = 78\%$ and $t_C = 83\%$), from the full quantum model with balanced (dash line) detector efficiencies ($t_P = t_C = 83\%$), and from the model using only imbalanced detector loss ($t_P = 78\%$ and $t_C = 83\%$, 100% transmission in atomic medium) [116](dotted). In all cases the imperfect detector efficiencies are accounted for using a beamsplitter model. In (a)–(c) the dashed vertical lines indicate the predicted EP locations. Experimental parameters: $\theta = 0.39^\circ$, pump Rabi frequency $\Omega = 2\pi \times 0.42$ GHz, cell length $z = 1.9$ cm. Temperature range: 100°C to 108.7°C , corresponding to the atomic density range of $N = 5 \times 10^{12} - 9 \times 10^{12}\text{cm}^{-3}$. Numerical model used $\Delta k = 210$ rad/m extracted from fitting experimental data. 129

6.2 System tuning across anti-PT symmetric and symmetry-breaking regimes via pump laser power modulation. (a) Simulated eigenvalues $\pm\lambda$ of the anti-PT Hamiltonian vs. pump Rabi frequency Ω . Power-dependences of (b) the relative-intensity squeezing parameter S and (c) normalized probe/conjugate gain $G_{P,C}$: experimental measurements (markers) vs numerical simulations (lines). Experimental parameters, also used for the numerical model: $\Delta = 0.7$ GHz, $\delta = -28$ MHz, $N = 7.9 \times 10^{12}\text{cm}^{-3}$ (vapor temperature $\sim 108^\circ\text{C}$), $\Delta k = 210$ rad/m. 135

6.3 Optimized FWM parameters for nearly ideal anti-PT realizations, using higher pump power ($\Omega = 2\pi \times 0.6$ GHz) and larger one-photon detuning ($\Delta_1 = 4$ GHz), in $z = 1.9$ cm and $z = 7.6$ cm vapor cells. Additional parameters: $\delta = -3.5$ MHz, $\Delta k = 210$ rad/m. (a) Real/imaginary components of the eigenvalues as functions of the atomic density N . (b) Normalized probe/conjugate gain vs. N . (c) Relative-intensity squeezing parameter S vs. N . Solid/dashed lines show the predicted squeezing with the Langevin noise $\langle L_N \rangle$ at a $z = 7.6/1.9$ cm vapor cell. No detector losses are considered.

136

Chapter 1

Introduction

The ability of light to travel quickly and non-interactively over long distances renders it a prime choice for communication technologies. This concept dates back to the time of Archimedes. Light has become integral to modern information science and daily life since the invention of lasers in 1960 by Theodore Maiman, as well as the subsequent development of optical fibers. Following the emergence of quantum computing and the potential quantum advantage it could bring, photons as flying qubits become essential for any long-distance quantum network or distributed quantum computing tasks. A clean, decoherence-free quantum systems with photons can reach very high fidelity for quantum information science [1]. However, photons used for quantum information applications require photon correlations or interactions, in many cases at the single photon level [2]. Over the past few decades, quantum optics has undergone rapid development and has been used as a prime source of entangled photon pairs in quantum communication and computing [3–5].

The ability of nonlinear optical effects to generate correlated optical fields also plays a significant role in sensing and imaging. Quantum optics techniques are applied in LIGO gravitational wave detectors [6–8], quantum imaging [9–12], precision measurement [13, 14], and non-Hermitian sensors [15–18].

In this dissertation, we present three projects contributing to quantum communication,

non-hermitian physics, and imaging. At the heart of all three projects is one specific nonlinear optical effect, so-called Four-Wave Mixing (FWM).

1.1 Historical Review of Nonlinear Optics and FWM

Like many other nonlinear optical phenomena, FWM arises from higher-order material susceptibility χ which defines the relationship between the polarization P (the dipole moment sum signifying the medium response) and the involved electric fields. When optical fields are coupled into a medium, the electrons in the medium beat with each field independently, as well as with the sum and difference among the fields. In these latter cases, the polarization responding simultaneously to product of N fields (the dependence is thus nonlinear) is described by $\chi^{(N)}$. This response is where the name nonlinear optics emerges. For instance, second-harmonic generation (SHG) and parametric down-conversion (PDC) depend on the $\chi^{(2)}$ nonlinearity, whereas FWM on $\chi^{(3)}$. Beyond sum- or difference-frequency generation, the field of nonlinear optics encompasses multi-photon absorption [19], stimulated [20], and the Kerr effect [21] (in fact discovered back in the 19th century). Although this dissertation centers on the FWM process, it is valuable to provide an overall review [22–25].

The evolution of nonlinear optics paralleled the rapid progress of laser technology in the 1960s. Foundational contributions from Bloembergen, Boyd, and others established the framework of nonlinear optics [26–29]. In 1961, Franken et al. first demonstrated harmonic generation in quartz [30]. Subsequently, parametric down-conversion and other harmonic processes (relying on the second order susceptibility $\chi^{(2)}$) were shown by various groups using nonlinear crystals, covering frequencies ranging from the infrared to the visible spectral region [31, 32]. These crystals exhibit a large $\chi^{(2)}$ coefficient, enabling effective parametric amplification. It is important to note that higher order interactions such as $\chi^{(3)}$ have also been demonstrated for crystals. Crystal-based nonlinear processes can exhibit broad bandwidth and multiple competing transition channels due to vibrational and

rotational states of the crystal lattice.

An alternative approach utilizes the $\chi^{(3)}$ FWM mechanism in atomic ensembles. Here, $\chi^{(2)}$ vanishes due to lack of symmetry[33]; while the next-order nonlinear susceptibility, $\chi^{(3)}$ becomes exceptionally large for fields especially near resonance, at least comparable to the $\chi^{(2)}$ strength in some crystals. Studies on $\chi^{(3)}$ nonlinearity in atomic vapors flourished in the 1970s, achieving frequency generation across the UV, X-ray, and infrared regions via optical mixing in various atomic species [34–36].

As a primary example of $\chi^{(3)}$ interactions, FWM offers numerous practical applications. Bloembergen and Schawlow were awarded the Nobel Prize in Physics in 1981 for spectroscopy application of FWM [37–40]. As suggested by its name, FWM is a non-linear process involving four electromagnetic(E-M) fields. It encompasses various processes, including coherent anti-Stokes Raman spectroscopy (CARS), stimulated Raman spectroscopy, third harmonics generation, etc. Practically, FWM can involve three beams, with one beam coupled to two transitions, as in the case of CARS. It is widely employed in spectroscopic measurements to probe the energy level of materials [41, 42], UV light generation [43, 44], etc. The focus of this dissertation is on the temporal and photon-number correlations, which can be quantitatively described as $g^{(2)}$ correlation functions (measured by photon joint or coincidence detections through two photodetectors) among two conjugated fields. In this dissertation, however, we do not perform any $g^{(2)}$ joint counts measurement—the term is brought up to help the readers to digest the concept.

1.2 Quantum Applications of FWM

1.2.1 FWM as Photon Pair and Squeezed Light Source

FWM plays a pivotal role in controlled entangled photon-pair generation. The correlated optical fields (i.e, wave nature of light) and photon pairs (i.e, particle nature of light) are both widely studied, and FWM is one way to generate them, both at single-photon and bright field levels [45–47]. However, the Bell-state measurements in quantum pro-

protocols remain probabilistic, limiting the scalability of quantum networks [48]. Hybrid approaches that combine discrete-variable (DV) and continuous-variable (CV) systems, or even multiple-qubit platforms mentioned above, can be extremely advantageous [49, 50].

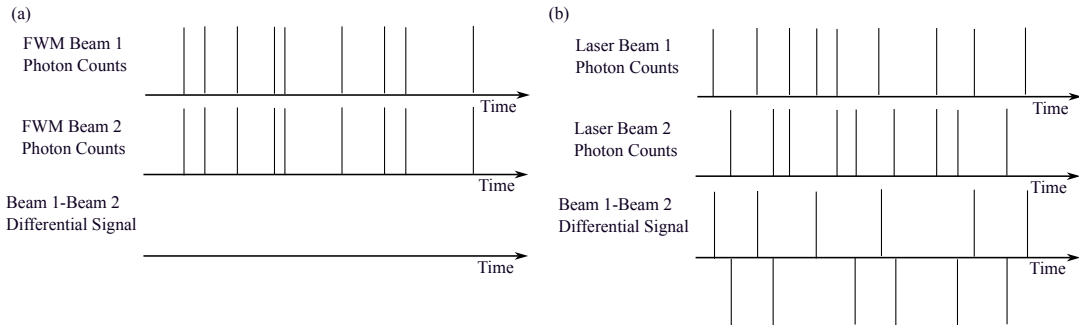


Figure 1.1: Two mode intensity squeezing from photon correlation perspective. Each vertical line denotes photon counts at certain time stamp. The x-axis is the time. (a) The twin fields from FWM. The photons generated in time are always in pairs. In other words, they have a strong temporal correlation. If we measure the differential signal over time, then ideally the differential signal will be 0, leading to reduced temporal variance. (b) Two uncorrelated laser (coherent state) fields. The photons generation in time are independent in this case, and the differential signal variance has no aforementioned cancellation and is therefore noisy.

Here we introduce the concept of two-mode squeezing, which characterizes the temporal correlations of CV entangled fields. In the case of two independent coherent state light sources, the photon counts over time are depicted in Fig.1.1(b). The photon counts in this scenario are independent. Conversely, Fig.1.1(a) illustrates the output of the twin signal fields resulting from FWM. Here, photons are consistently generated in pairs over time, exhibiting strong $g^{(2)}$ correlations. Consequently, the differential measurement of the FWM signal fields demonstrates a smaller variance compared to the two coherent state fields with the same photon flux. Thus, we can interpret two-mode intensity squeezing as a reduction of noise attributable to the temporal correlations of photon pairs in the two optical fields. Yuen, Shapiro and others [37, 51–53] developed a theoretical basis for achieving squeezing through FWM. Shortly thereafter, Slusher et al. [54] provided the first experimental report of -0.3 dB of squeezing. Further enhancements followed, culminating

in -15 dB of intensity squeezing in crystal [55] and up to -9 dB in alkali vapors [56, 57].

In this dissertation, we focus on generating entangled fields where one field lies in the near-infrared (NIR) regime and the other in the telecom range. This arrangement seamlessly integrates into quantum computation protocols and inherently alleviates transmission losses. Although IR-telecom photon pair generation in both cold and warm atomic ensembles is established [45, 58], our emphasis is on CV entangled field generation. This approach provides a promising avenue for scalable quantum computing, robust long-distance communication, and innovative hybrid quantum architectures.

1.2.2 FWM for Quantum Imaging Applications

Another focus of this thesis is quantum imaging. Here, we offer a brief historical overview of imaging and optics in general. Imaging has a long history with a profound impact: early microscopy efforts by Newton, Young, Huygens, Hooke, Fresnel, and others paved the way for modern biological discoveries [59–61]. Innovations such as scanning-tunneling and atomic-force microscopes have expanded the boundaries of chemistry, biology, materials science, and medical research [62, 63]. Substantial efforts have been devoted to breaking the resolution limit, yielding significant benefits for astronomy and biology [64–66]. Fourier optics enables novel image processing and filtering [67, 68]. Beyond intensity-only imaging, holography incorporates phase reconstruction and allows object reconstruction in 3-D. Furthermore, computational approaches—such as compressive sensing [69], single photodiode imaging through mode reconstruction [70], and advanced image-processing algorithms—are continuously propelling advancements in this domain.

Despite these intriguing achievements, photon statistics and correlations have not typically been emphasized. The objective of quantum metrology is to exploit the unique properties of quantum light for more accurate measurements, particularly sub-shot-noise techniques. Certain organic samples, including biological specimens, are extremely photosensitive, and traditional imaging may cause damage or alterations (for instance, retina samples can be triggered by single photons). Additionally, in the few-photon regime, shot

noise becomes a major limitation on measurement sensitivity. Thus, developing sub-shot-noise, few-photon spectroscopy and imaging methods holds significant promise for biology, chemistry, and related biomedical fields. Two broad categories of quantum imaging meth-

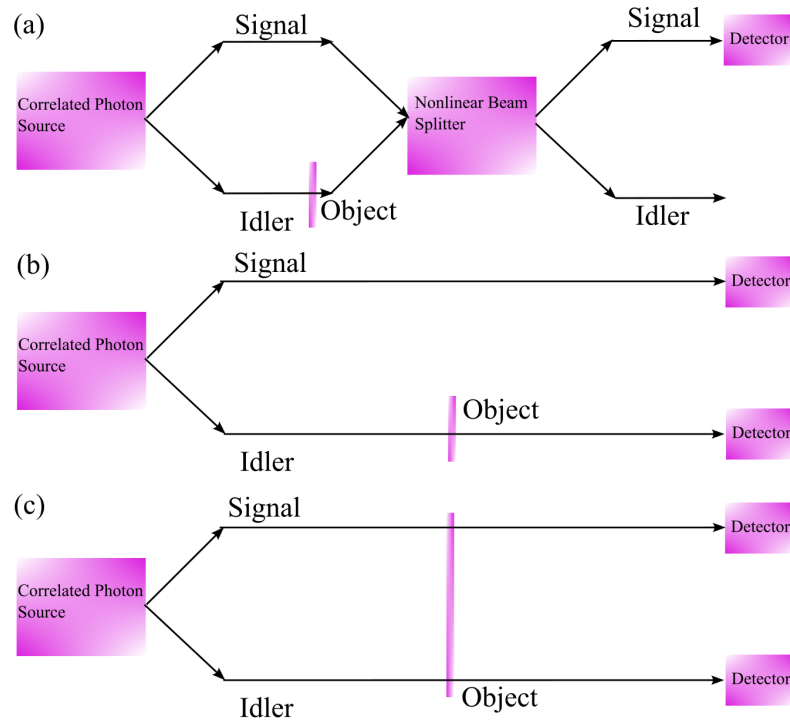


Figure 1.2: Three main methods for quantum imaging. (a) Interference based quantum imaging, (b) Correlation based quantum imaging, and (c) entanglement based quantum imaging

ods can be identified:

Correlation-Based Imaging. This approach employs pairs of entangled photons or optical fields, wherein only one field interacts with the target object while the other serves as a reference. The differential between these fields facilitates sub-shot-noise imaging, requiring a reduced number of photons. A prominent instance of this principle is quantum ghost imaging (QGI), which involves the collection of the signal field by a bucket detector, while the reference field is acquired via a spatially resolving device; the resultant image is reconstructed through correlation [71–73]. Other examples see Ref [74–76]. This dissertation does not cover this method.

Interferometry-Based Imaging As the name suggests, it relies on interference among correlated photons, often involving their indistinguishability and nonlinear interferometers. Both parametric down-conversion (SPDC) and FWM can enable these interferometric techniques. Important example is the imaging of undetected photons demonstrated by Lemos et al [77]. Within this category, schemes vary widely depending on the targeted application. In this thesis, we focus on quadrature-noise-based imaging [78, 79], which forms images from noise statistics by computing the variance map.

1.2.3 FWM for Simulating Non-Hermitian system

Hermiticity is originally considered as a necessary condition for a Hamiltonian to have real energy eigenvalues. However, the concept of imaginary energy eigenvalues appear in interpretation of open quantum systems, such as the studies of alpha decay and neutron scattering interactions [80–83]. In these systems, a singularity point arises, leading to the merging of all eigenmodes [84–86]. In 90s, C.M. Bender and colleagues demonstrated that Hermiticity is a sufficient but not necessary condition for the existence of real eigenvalues [87–89]. A real energy spectrum may arise if the Hamiltonian \hat{H} is symmetric or antisymmetric under joint parity-time transformations. In other words, \hat{H} commutes or anti-commutes with the joint parity-time operator $\hat{P}\hat{T}$. $[\hat{H}, \hat{P}\hat{T}] = 0$ and $\{\hat{H}, \hat{P}\hat{T}\} = 0$ are referred as Parity-Time (PT) symmetry or Anti-Parity-Time (APT) symmetry, respectively [87]. Unlike standard Hermitian Hamiltonians, which consistently exhibit real energy eigenvalues, the PT and APT systems feature exceptional points (EPs) that mark the transition from purely real to imaginary eigenvalues [88].

If we look at Schrodinger’s equation, with form $i\frac{\partial}{\partial t}|\psi\rangle = \hat{H}|\psi\rangle$, and the paraxial light propagation equation (more on Ch. 2), with form $i\frac{\partial}{\partial z}\hat{E}(z) = \hat{H}'\hat{E}(z)$, we notice the mathematical equivalence between the two. The parity and time operator can also be reinterpreted accordingly in each optical system such that they commute or anticommute with \hat{H}' . The optical system thus offers a convenient platform for studying non-Hermitian physics, especially the phase-change behavior near the exceptional point (EP). This phase change

can be extraordinarily pronounced, opening channels for novel high-sensitivity detectors, PT-symmetric lasers, and enabling a variety of quantum simulations [90–97]. However, most PT-system demonstrations in optical system involve spatially interleaved gain/loss channels [82, 98–100], inevitably introducing Langevin noise that undermines sensitivity—a crucial concern for non-Hermitian sensing. In contrast, APT systems possess the potential to circumvent gain/loss configurations [101, 102].

Notably, seeded resonant FWM can be reinterpreted as an APT system, where parity and time symmetry correspond to seeding choices and optical field conjugation, respectively. Experiments in cold Rb vapors demonstrate classical amplification under these conditions [103]. By tuning the nonlinearity strength $\chi^{(3)}$, the system can cross the EP with minimal loss, thanks to on-resonance electromagnetically-induced-transparency (EIT) coexisting for the signal fields. In this context, the phase transition does not manifest as interleaved gain/loss; instead, it is observed as a relative energy exchange. Specifically, within the PT-symmetric region, energy is periodically exchanged between the signal fields, whereas in the anti-PT phase breaking region, both signal fields exhibit exponential power growth or decay. Establishing a connection between FWM processes and anti-PT phase symmetric thus offers a pathway to realizing novel detection schemes within established platforms.

Beyond classical treatments, FWM-based APT systems can be extended to the quantum regime via intensity or quadrature squeezing, offering predicted enhancements in detection sensitivity [104]. APT system study constitutes one of the primary topics of this dissertation.

1.3 Thesis Outline

This dissertation is organized as follows: Ch.2 reviews the fundamental theory of light–atom interactions and FWM. A basic theoretical framework for intensity squeezing is also constructed, with emphasis on its connection to nonlinear gain and loss.

Ch.3 details the analytical calculation and experimental configuration of the double- Λ and double-ladder FWM experiments, which serve as the basis for the experiments described in Ch.4, Ch.5, and Ch.6.

Ch.4 describes the bi-chromatic intensity squeezing experiment, including data optimization and setup procedures. Here, we report the observation of -2.6 dB of squeezing, demonstrating a highly efficient IR-Telecom entangled photon source for continuous variables.

Ch.5 discusses quadrature noise shadow imaging with a thermal field. We perform imaging task in variance space instead of intensity space. This methodology achieves an average photon count of 0.7 per pixel per second for object image retrieval.

Ch.6 introduces the anti-PT squeezing experiment utilizing FWM. This study reinterprets the system as an anti-PT model, extending the analysis into the quantum regime through the implementation of squeezing for the first time. The results from our analytical and computational models exhibit good agreement with the experimental data.

Ch.7 summarizes the dissertation and envisions several directions we can further explore.

Chapter 2

Theory Overview

In this chapter, we develop the theoretical framework necessary for understanding nonlinear light-atom interactions, with a particular focus on the FWM effect and two-mode intensity squeezing.

The chapter is organized as follows. We begin by deriving the wave propagation equation from Maxwell's equations under the rotating-wave approximation. Next, we discuss the induced polarization response of the medium, which leads to FWM and the introduction of a nonlinear gain. Lastly, we discuss noise theory by linking nonlinear gain to intensity squeezing, addressing both optical and detector losses. Optical loss is modeled using two complementary methods: the infinite beamsplitter approximation and the Langevin formalism.

2.1 Classical Description of Electromagnetic Field

Here we formulate the description for nonlinear optics from Maxwell's equations in vacuum, which describe the electromagnetic wave behavior:

$$\nabla \cdot \mathbf{E} = \frac{\rho}{\epsilon_0}, \quad (2.1a)$$

$$\nabla \cdot \mathbf{B} = 0, \quad (2.1b)$$

$$\nabla \times \mathbf{E} = -\frac{\partial \mathbf{B}}{\partial t}, \quad (2.1c)$$

$$\nabla \times \mathbf{B} = \mu_0 \mathbf{J} + \mu_0 \epsilon_0 \frac{\partial \mathbf{E}}{\partial t}. \quad (2.1d)$$

Here \mathbf{E} and \mathbf{B} are the electric and magnetic field respectively. ρ , \mathbf{J} , μ_0 , and ϵ_0 are the charge density, current density, magnetic permeability of vacuum, and electric permittivity of vacuum, respectively, with relation $\mu_0 \epsilon_0 = \frac{1}{c^2}$. We assume a source-free medium with isotropic polarization such that Eq.(2.1a) can be reduced to $\nabla \cdot \mathbf{E} = 0$. To describe propagation in a dielectric medium, Eq.(2.1a-2.1d) can be rewritten using the magnetic intensity $\mathbf{H} = \frac{1}{\mu_0} \mathbf{B} - \mathbf{M}$ and displacement $\mathbf{D} = \epsilon_0 \mathbf{E} + \mathbf{P}$, where \mathbf{M} and \mathbf{P} are magnetization and polarization terms. Applying the relation $\nabla \times (\nabla \times \mathbf{E}) = \nabla(\nabla \cdot \mathbf{E}) - \nabla^2 \mathbf{E}$, we derive the wave equation in a medium,

$$\nabla^2 \mathbf{E} - \frac{1}{c^2} \frac{\partial^2 \mathbf{E}}{\partial t^2} = \mu_0 \frac{\partial^2 \mathbf{P}}{\partial t^2}. \quad (2.2)$$

The left side of the equation corresponds to electric field propagation, the right side describes the medium response, The polarization \mathbf{P} is related to the susceptibility χ and describes the dipole moment of atoms induced by the electric field E , as follows,

$$\mathbf{P} = \epsilon_0 \chi \mathbf{E} = N \langle d \rangle \quad (2.3)$$

where N is the atomic density, and $\langle d \rangle = \langle -e\mathbf{r} \rangle$ represents the average induced dipole moment. Here, we consider electric field propagation along the \hat{z} -axis within Cartesian coordinates, and that the electric field vector \mathbf{E} is along the \hat{x} -axis. We can then write

down the expression for an electric field as [105, 106]:

$$\mathbf{E}(z, t) = \frac{1}{2}E_0(z, t)\hat{x}e^{i(kz-\omega t)} + \text{c.c.}, \quad (2.4)$$

Here *c.c.* stands for complex conjugate. A similar relationship is also applicable to $\mathbf{P}(\mathbf{z}, \mathbf{t}) = P(z, t)e^{i(kz-\omega t)}$ per Eq.(2.3). We observe that $E_0(z, t)$ exhibits a relatively slow variation in comparison to the optical frequency ω . This slowly varying amplitude approximation can be expressed as follows:

$$\frac{\partial E}{\partial z} \ll kE \quad ; \quad \frac{\partial E}{\partial t} \ll \omega E \quad ; \quad \frac{\partial P}{\partial t} \ll \omega P. \quad (2.5)$$

Inserting Eq.(2.4) and Eq.(2.5) into Eq.(2.2) yields the propagation equation for the slowly-varying amplitude.

$$i \left(\frac{\partial}{\partial z} + \frac{1}{c} \frac{\partial}{\partial t} \right) E_0(z, t) = \frac{k}{2\epsilon_0} P(z, t) \quad (2.6)$$

Physically, we adopt a reference frame that oscillates at the optical frequency, effectively removing the rapid oscillations to focus on the slowly varying amplitude. In this dissertation, we generally assume a steady-state solution in which time derivatives are negligible. The propagation equation becomes [105]:

$$i \frac{\partial}{\partial z} E_0(z) = \frac{k}{2\epsilon_0} P(z) \quad (2.7)$$

To get further insight of \mathbf{P} , we can describe the electron displacement \mathbf{x} induced by driving a classical oscillator with an external electric field as follows,

$$\frac{d^2 x}{dt^2} + 2\gamma \frac{dx}{dt} + \omega_0^2 x = \frac{e}{m} E_0 e^{-i\omega t}. \quad (2.8)$$

The driving term arises from the coupling electric field E_0 . ω_0 and ω are the natural frequency of electron oscillation and the coupling field frequency. Furthermore, m and e

denote the mass and charge of an electron. After some algebra, we can find the displacement to be,

$$x(t) = \frac{1}{2i\epsilon_0} \frac{e^2}{m\omega_0} \frac{1}{\gamma + i(\omega_0 - \omega)}. \quad (2.9)$$

It is evident that the displacement reaches its maximum at $\omega_0 = \omega$, reflecting a classical analogy with an on-resonance transition. In an atomic ensemble composed of N atoms, the total induced polarization is equivalent to the summation of all induced dipole moments,

$$\mathbf{P} = N \langle e\hat{x} \rangle = \epsilon_0 \chi \mathbf{E} \quad (2.10)$$

This gives rise to the susceptibility χ as,

$$\chi = \frac{i}{4} \frac{Ne^2 E_0}{m\omega_0} \frac{1}{\gamma + i(\omega_0 - \omega)} \quad (2.11)$$

The real and imaginary parts correspond to the dispersion and linear absorption of an ensemble of N atoms. Here we considered only the simple case with the first-order dependence. Generally we can write the induced polarization \mathbf{P} as a power series expansion,

$$\mathbf{P} = \epsilon_0 \sum_1^n \chi^{(n)} \mathbf{E}^n, \quad (2.12)$$

The $\chi^{(n)}$ terms represent the higher-order nonlinear susceptibility tensor. The terms following $\chi^{(1)}$ decrease progressively, resulting in a convergence to a finite value for the summation. The susceptibility terms are tensors containing 3^n elements which are determined by light direction, frequency and material symmetry [33]. Of particular interest for us, the FWM phenomenon is inherent in the $\chi^{(3)}$ nonlinear susceptibility.

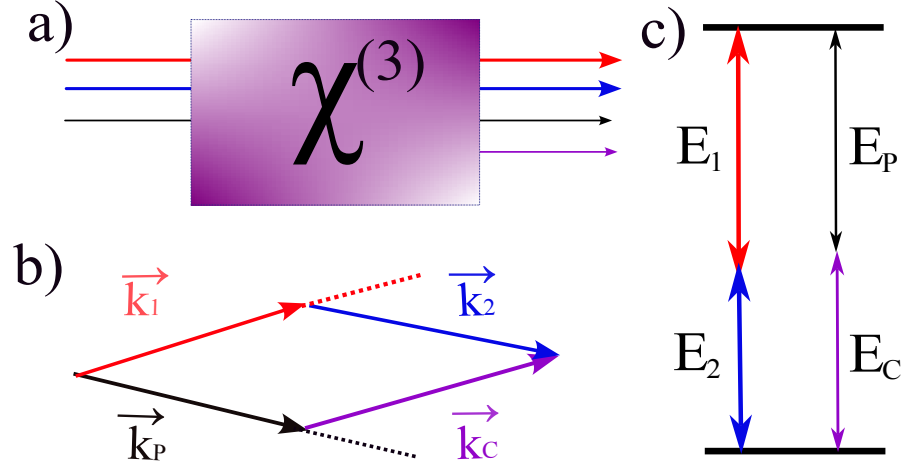


Figure 2.1: a) Illustration of FWM in a $\chi^{(3)}$ medium. b) geometric phase-matching condition. c) Energy level diagram for FWM.

2.2 Classical Description of FWM

We consider a medium characterized by three copropagating input fields E_P , E_1 , and E_2 , as shown in Fig. 2.1(a). Driven simultaneously by these three input fields and their beat signals (which act as new source terms), the polarization of the dielectric medium generates a fourth field E_C . One potential configuration is depicted in Fig. 2.1(c). Mathematically, we can express this as:

$$P^{(3)} = \epsilon_0 \chi^{(3)} (\mathbf{E}_P + \mathbf{E}_1 + \mathbf{E}_2)^3, \quad (2.13)$$

The expansion of Eq.(2.13) contains multiple terms including the higher harmonics generation, sum-/difference frequency generation, etc. However, when accounting for material symmetries and atomic resonance, numerous elements in the $\chi^{(3)}$ tensor become negligibly small. The terms responsible for FWM are given by:

$$\begin{aligned}
P_C^{(3)} &= \epsilon_0 \chi_C^{(3)} E_P^* E_1 E_2 e^{i[(\mathbf{k}_P - \mathbf{k}_1 - \mathbf{k}_2)z - (\omega_P - \omega_1 - \omega_2)t]} \\
&= \epsilon_0 \chi_C^{(3)} E_P^* E_1 E_2 e^{-i[(\mathbf{k}_C + \Delta\mathbf{k})z - (\omega_C - \Delta\omega)t]}. \tag{2.14}
\end{aligned}$$

$$\begin{aligned}
P_P^{(3)} &= \epsilon_0 \chi_P^{(3)} E_C^* E_1 E_2 e^{i[(\mathbf{k}_C - \mathbf{k}_1 - \mathbf{k}_2)z - (\omega_C - \omega_1 - \omega_2)t]} \\
&= \epsilon_0 \chi_P^{(3)} E_C^* E_1 E_2 e^{-i[(\mathbf{k}_P + \Delta\mathbf{k})z - (\omega_P - \Delta\omega)t]}. \tag{2.15}
\end{aligned}$$

The phase-matching terms $\Delta\mathbf{k}$ and $\Delta\omega$ are defined as follows :

$$\Delta\omega = \omega_1 + \omega_2 - \omega_P - \omega_C, \tag{2.16}$$

$$\Delta\mathbf{k} = \mathbf{k}_1 + \mathbf{k}_2 - \mathbf{k}_P - \mathbf{k}_C, \tag{2.17}$$

Because of energy conservation in the FWM process, we generally have $\Delta\omega = 0$. The Δk represents the geometric phase mismatch, which can be non-zero in our case. \mathbf{k} is modified by dispersion such that $|\mathbf{k}| = \frac{n(\omega)\omega}{c}$, where $n(\omega) = \sqrt{1 + Re(\chi)}$ is the refractive index. This dispersion modification permits a nonzero geometric phase matching angle, as illustrated in Fig. 2.1(b). By specifically selecting a rotating frame with symmetric phase accumulation, we denote slowly-varying amplitudes as $E_P = \mathcal{E}_P e^{-i\frac{\Delta k z}{2}}$ and $E_C^* = \mathcal{E}_C^* e^{i\frac{\Delta k z}{2}}$. Next, we also consider E_1 and E_2 as strong inputs, and treat them as constant under the undepleted pump approximation. Then, for the copropagating probe and conjugate fields, we can express the joint propagation equations using Eq.(2.7) as follows [33, 54, 107–110],

$$\left(\frac{\Delta k}{2} - i\frac{\partial}{\partial z}\right)\mathcal{E}_P = \overbrace{\frac{k_P E_1 E_2}{2} \chi_P^{(3)}}^{\kappa_P} \mathcal{E}_C^* \tag{2.18}$$

$$-\left(\frac{\Delta k}{2} - i\frac{\partial}{\partial z}\right)\mathcal{E}_C^* = \overbrace{\frac{k_C E_1 E_2}{2} \chi_C^{(3)}}^{\kappa_C} \mathcal{E}_P. \tag{2.19}$$

We denote the coupling constants using $\kappa_P = \frac{k_P E_1 E_2}{2} \chi_P^{(3)}$ and $\kappa_C = \frac{k_C E_1 E_2}{2} \chi_C^{(3)}$ for

simplicity. The two differential equations can be recast in matrix format,

$$i \frac{\partial}{\partial z} \begin{pmatrix} \mathcal{E}_P \\ \mathcal{E}_C^* \end{pmatrix} = \begin{pmatrix} -\frac{\Delta k}{2} & -\kappa_P \\ \kappa_C & \frac{\Delta k}{2} \end{pmatrix} \begin{pmatrix} \mathcal{E}_P \\ \mathcal{E}_C^* \end{pmatrix} = \mathcal{M} \begin{pmatrix} \mathcal{E}_P \\ \mathcal{E}_C^* \end{pmatrix} \quad (2.20)$$

now we can express the solution to \mathcal{E}_P and \mathcal{E}_C using the eigenvalue $\lambda = \sqrt{\frac{\Delta k^2}{4} - \kappa_C \kappa_P}$. Since Δk is usually small such that the value of λ is imaginary, we define the real value parameter η such that $\pm\lambda = \pm i\eta$. When $\kappa_P = \kappa_C = \kappa$, we can write the symmetric output matrix as follows,

$$\begin{pmatrix} \mathcal{E}_P(L) \\ \mathcal{E}_C^*(L) \end{pmatrix} = e^{-i\mathcal{M}L} \begin{pmatrix} \mathcal{E}_P(0) \\ \mathcal{E}_C^*(0) \end{pmatrix} = \begin{pmatrix} A(\eta) & C(\eta)^* \\ C(\eta) & A(\eta)^* \end{pmatrix} \begin{pmatrix} \mathcal{E}_P(0) \\ \mathcal{E}_C^*(0) \end{pmatrix} \quad (2.21)$$

Using the matrix exponential, we find $A(\eta)$ and $C(\eta)$ as the follows [107, 111, 112],

$$A = \cosh(\eta L) + i \frac{\Delta k}{2\eta} \sinh(\eta L) \quad (2.22)$$

$$C = i \frac{\kappa}{\eta} \sinh(\eta L) \quad (2.23)$$

For more general case with $\kappa_P \neq \kappa_C$, the off-diagonal terms in Eq. (2.21) are replaced with $-i \frac{\kappa_P}{\eta} \sinh(\eta L)$ and $i \frac{\kappa_C}{\eta} \sinh(\eta L)$ respectively. When seeding the probe channel only such that $\mathcal{E}_P(0) \neq 0$ and $\mathcal{E}_C(0) = 0$, the solutions become,

$$\mathcal{E}_P(L) = A \cdot \mathcal{E}_P(0) \text{ and } \mathcal{E}_C^*(L) = C \cdot \mathcal{E}_P(0) \quad (2.24)$$

$$\text{with nonlinear gain } G_P = |A|^2 \text{ and } G_C = |C|^2 \quad (2.25)$$

$G_{P/C}$ are the FWM gain relative to the input field(\mathcal{E}_P). Additionally, it is noted that $G_{P/C}$ depends on Δk , reaching its maximum at $\Delta k = 0$, which corresponds to perfect geometric phase matching. Under this condition, Eq.(2.23) simplifies to $A = \cosh(\eta L)$ and $C = i \sinh(\eta L)$, and we have $G_P - G_C = 1$.

2.3 Quantum Formalism of FWM

In the previous section, we described the optical fields using a classical formalism. Here, we switch to a quantum framework, which enables the accurate analysis of quantum correlations and the optical loss effects of FWM. To this end, we expand the electric field into normal modes summation as follows [105],

$$E_x(z, t) = \sum_i \sqrt{\frac{2\omega_i^2 m_i}{V\epsilon_0}} q_i(t) \sin(k_i z) \quad (2.26)$$

Eq.(2.26) describes the summation of all normal modes for the x-direction linearly polarized electric field in a cavity of length L. The amplitude $q_i(t)$ corresponds to the normal mode amplitude for the i th mode, where $i = 1, 2, 3, \dots$. We have $k_i = i\pi/L$ as the momentum vector, $\omega_i = k_i c$ as the eigenfrequency for the i th mode, and m_i as a constant included to draw an analogy to classical harmonic oscillators. We can set $m_i = 1$. The volume V is defined as $V = L^3$. Similarly, we can write down the magnetic component $H_y (B = \mu_0 H)$ by,

$$H_y(z, t) = \sum_i \sqrt{\frac{2\omega_i^2 m_i}{V\epsilon_0}} \frac{\dot{q}_i(t) \epsilon_0}{k_i} \cos(k_i z) \quad (2.27)$$

Using Eq.(2.26) and (2.27), we can express the energy Hamiltonian as the sum of E_x^2 and H_y^2 . The result simplifies to the follows,

$$\mathcal{H} = \frac{1}{2} \sum_i \left[m_i \omega_i^2 q_i(t)^2 + \dot{q}_i(t)^2 \right] \quad (2.28)$$

As in classical mechanics, we can express \dot{q}_i using the canonical momentum $p_i = m_i \dot{q}_i$. p and q , in classical analogy, carry the meaning of position and momentum [113]. Eq.(2.26) to (2.28) describe essentially the summation of all individual modes of a harmonic oscillator.

To further simplify Eq.(2.28), we define two new operators, the creation and annihilation operators,

$$\hat{a}_i e^{-i\omega_i t} = \frac{1}{\sqrt{2m_i \hbar \omega_i}} (m_i \omega_i q_i + i p_i) \quad (2.29)$$

$$\hat{a}_i^\dagger e^{i\omega_i t} = \frac{1}{\sqrt{2m_i \hbar \omega_i}} (m_i \omega_i q_i - i p_i) \quad (2.30)$$

Now Eq.(2.28) can be rewritten using a and a^\dagger as

$$\mathcal{H} = \hbar \sum_i \omega_i \left(\hat{a}_i^\dagger \hat{a}_i + \frac{1}{2} \right). \quad (2.31)$$

The $\hat{n} = \hat{a}^\dagger a$ is the so-called photon number operator. Physically, this energy Hamiltonian corresponds to the summation of from 1 to the i th mode, each mode with n_i photons with energy $\hbar \omega_i$.

With these, we can re-express the Eq.(2.26) and (2.27) as,

$$E_x(z, t) = \sum_i \left(\frac{\hbar \omega_i}{\epsilon_0 V} \right)^{1/2} \left(\hat{a}_i e^{-i\omega_i t} + \hat{a}_i^\dagger e^{i\omega_i t} \right) \sin k_i z \quad (2.32)$$

$$H_y(z, t) = -i\epsilon_0 c \sum_i \left(\frac{\hbar \omega_i}{\epsilon_0 V} \right)^{1/2} \left(\hat{a}_i e^{-i\omega_i t} - \hat{a}_i^\dagger e^{i\omega_i t} \right) \cos k_i z. \quad (2.33)$$

This solution is for a cavity of length L . In contrast, the free-space electric field solutions correspond to a cavity of length $L \rightarrow \infty$. Note that the plane-wave solution has already been included, which is Eq.(2.4),

$$E_x(z, t) = \left(\frac{\hbar \omega}{\epsilon_0 V} \right)^{1/2} \hat{a} e^{i(kz - \omega t)} + c.c. \quad (2.34)$$

Using Eq.(2.34), an analogy can be drawn to the procedures outlined in Sec.2.1 and 2.2. The probe and conjugate fields described in previous sections correspond to the operators a and a^\dagger respectively, which is described by the two conjugated parts in Eq.(2.34). We can then calculate the quantum version of Eq.(2.20) by substituting $\mathcal{E}_{P/C}(z)$ with operators \hat{a}

and \hat{b}^\dagger [105, 107, 109],

$$i \frac{\partial}{\partial z} \begin{pmatrix} \hat{a}_{out} \\ \hat{b}_{out}^\dagger \end{pmatrix} = \begin{pmatrix} -\frac{\Delta k}{2} & -\kappa \\ \kappa & \frac{\Delta k}{2} \end{pmatrix} \begin{pmatrix} \hat{a} \\ \hat{b}^\dagger \end{pmatrix} \quad (2.35)$$

$$\rightarrow \begin{pmatrix} \hat{a}_{out} \\ \hat{b}_{out}^\dagger \end{pmatrix} = \begin{pmatrix} A & C^* \\ C & A^* \end{pmatrix} \begin{pmatrix} \hat{a} \\ \hat{b}^\dagger \end{pmatrix} \quad (2.36)$$

Note that for the gain calculation, the two methods are equivalent. The quantum treatment is introduced to properly account for the noise and correlations in later sections.

2.4 Theory for Noise and Squeezing

This section develops the fundamental noise theory for optical field calculations, with a particular emphasis on two-mode squeezing using FWM, and provides the theoretical groundwork for subsequent discussions.

2.4.1 Quantum Noise of a Single Optical Field

Noise of Coherent Field and thermal field

Laser light can be approximated as a coherent state. A thermal state is generated from any radiating blackbody. We utilize the thermal field in Ch. 5, while coherent states are involved in all projects.

The physical meaning of the creation and annihilation operators for an EM field can be intuitively understood in the space of number or Fock states, $|n\rangle$. This state is also a convenient basis for describing the coherent state, which takes the form [105],

$$|\alpha\rangle = e^{-|\alpha|^2/2} \sum_{n=0}^{\infty} \frac{\alpha^n}{\sqrt{n!}} |n\rangle. \quad (2.37)$$

In the following, we frequently write this coherent state as a displacement from a vacuum state by using the displacement operator, $|\alpha\rangle = \hat{D}(\alpha)|0\rangle$, where $|0\rangle$ is the vacuum state and $\hat{D}(\alpha)$ assumes [105, 114],

$$\hat{D}(\alpha) = e^{-|\alpha|^2/2} e^{\alpha \hat{a}^\dagger} e^{-\alpha^* \hat{a}}. \quad (2.38)$$

We can easily calculate the photon number variance as,

$$\langle (\Delta \hat{n})^2 \rangle = \langle \hat{n}^2 \rangle - \langle \hat{n} \rangle^2 = \langle n \rangle \quad (2.39)$$

Next, we define the thermal field by considering a cavity in thermal equilibrium at temperature T . The probability that a mode is excited thermally to the i th mode is [114],

$$P_i = \frac{e^{-\frac{E_i}{k_B T}}}{\sum_i e^{-\frac{E_i}{k_B T}}}, \quad (2.40)$$

where $E_i = n_i \hbar \omega_i$ is the energy of i th mode and n_i is the number of photons. Using Eq.(2.40), we can proceed to calculate the expectation value as well as variance. For example, $\langle n \rangle = \sum_i P_i n_i$. The variance can be written as [114, 115],

$$\langle \Delta(n_{th})^2 \rangle = \langle n \rangle^2 + \langle n \rangle \quad (2.41)$$

The photon number $\langle n \rangle$ is directly proportional to the photocurrent or voltage measured in experimental settings. Consequently, a direct correlation is observed in photonvoltage measurements, consistent with Eq.(2.39) and Eq.(2.41) for coherent and thermal fields, respectively.

Noise of FWM Individual Probe and Conjugate Field

We begin our analysis by focusing exclusively on one of the two amplified fields from the FWM. We start with the amplified probe field written with input (seed) fields operators. We note that, from Eq.(2.36), we can write the output operators in terms of the input operators as,

$$\hat{a}_{out} = A\hat{a} + C^*\hat{b}^\dagger \quad (2.42a)$$

$$\hat{b}_{out}^\dagger = C\hat{a} + A^*\hat{b} \quad (2.42b)$$

Then we can write down the variance for a single field output [116],

$$\text{Var}(n_{P,out}) = G_P^2 \langle \hat{a}^\dagger \hat{a} \rangle + G_P G_C \langle \hat{a} \hat{a}^\dagger \hat{b} \hat{b}^\dagger \rangle + G_C^2 \langle \hat{b}^\dagger \hat{b} \rangle \quad (2.43)$$

Here $n_{P,out} = \langle \hat{a}_{out}^\dagger \hat{a}_{out} \rangle$ is the probe output mean photon number. Assuming $\langle \hat{b}^\dagger \hat{b} \rangle = 0$ and $\langle \hat{a}^\dagger \hat{a} \rangle = \langle n_{in} \rangle \gg 0$, since we have vacuum seed for conjugate channel and weak probe seed channel, we can expand the middle term as,

$$\langle \hat{a} \hat{a}^\dagger \hat{b} \hat{b}^\dagger \rangle = \langle (1 + \hat{a}^\dagger \hat{a})(1 + \hat{b}^\dagger \hat{b}) \rangle \simeq \langle \hat{a}^\dagger \hat{a} \rangle \quad (2.44)$$

Then we can express Eq.(2.43) as follows:

$$\text{Var}(\hat{n}_{P,out}) = G_P(G_P + G_C) \langle n_{in} \rangle. \quad (2.45)$$

Similarly we find for the conjugate field,

$$\text{Var}(\hat{n}_{C,out}) = G_C(G_P + G_C) \langle n_{in} \rangle. \quad (2.46)$$

Both fields individually are much noisier than coherent field with same photon counts, given by:

$$\text{Var}(\hat{n}_{SNL,out}) = (G_P + G_C) \langle n_{in} \rangle. \quad (2.47)$$

By comparison of Eq.(2.45) and Eq.(2.47), variance scales quadratically with the gain, while the coherent state variance scales linearly. This reflects the nature of intensity

squeezing: the fluctuations in individually noisy beams canceled out when doing differential measurement.

Another case we want to consider is with dual vacuum seed. In this case, we cannot approximate by using $\langle \hat{a}^\dagger \hat{a} \rangle \gg 0$, and the probe channel becomes,

$$\text{Var}(\hat{n}_{P,out}) = G_C^2 + G_C \text{ where } \langle \hat{n}_{P,out} \rangle = G_C. \quad (2.48)$$

Eq.(2.48) resembles Eq.(2.41) and demonstrates super-poissonian characteristics with thermal field statistics. The field remains sufficiently weak and can thus be regarded as a thermal vacuum, which was employed for the imaging project described in Ch.5.

2.4.2 Differential Noise & Two-Mode Intensity Squeezing

We assume initial condition with vacuum conjugate seeding and weak probe seeding $\langle \hat{a}^\dagger \hat{a} \rangle = n_{in}$ and $\langle \hat{b}^\dagger \hat{b} \rangle = 0$. The differential squeezing then can be easily calculated using above expressions [116],

$$\text{Var}(\hat{a}_{out}^\dagger \hat{a}_{out} - \hat{b}_{out}^\dagger \hat{b}_{out}) = \langle \hat{a}^\dagger \hat{a} \rangle = \langle n_{in} \rangle \quad (2.49)$$

Despite the fact that probe and conjugate fields are individually noisier as stated in Eq.(2.45) and (2.46), the differential noise is actually canceled out, leaving only the noise of the input seed. This suggest strong temporal correlations between the probe and conjugate field. To compare with shot noise, we assume two coherent field input with the same intensity as the amplified probe and conjugate such that $\langle \alpha | \hat{a}^\dagger \hat{a} | \alpha \rangle = G_P \langle n_{in} \rangle$ and $\langle \alpha | \hat{b}^\dagger \hat{b} | \alpha \rangle = G_C \langle n_{in} \rangle$, the differential variance using coherent fields can be shown to be,

$$\text{Var}(\hat{a}_{out}^\dagger \hat{a}_{out} - \hat{b}_{out}^\dagger \hat{b}_{out})_{SNL} = \langle n_{P,out} \rangle + \langle n_{C,out} \rangle \quad (2.50)$$

The intensity squeezing is defined as the variance ratio under logarithm, with the expression,

$$S = 10\log_{10} \left[\frac{\text{Var}(n_{P,out} - n_{C,out})}{\langle n_{P,out} \rangle + \langle n_{C,out} \rangle} \right] \quad (2.51)$$

$$= 10\log_{10} \left[\frac{1}{G_P + G_C} \right] \quad (2.52)$$

2.4.3 Continuous Variable Noise Analysis: Noise Quadratures

Before proceeding to the calculation of optical loss effects, we introduce the quantum noise analysis from another direction by using the concept of optical quadratures for an electromagnetic field. The amplitude and phase quadrature are defined as follows [105, 114, 115],

$$\hat{X}_1 = \frac{1}{2}(\hat{a} + \hat{a}^\dagger), \quad (2.53)$$

$$\hat{X}_2 = \frac{1}{2i}(\hat{a} - \hat{a}^\dagger). \quad (2.54)$$

Physically, the phase and amplitude operators are position and momentum operators scaled by a constant factor [105, 113]. Thus, the Heisenberg uncertainty principle postulate for the quadratures is,

$$\langle (\Delta \hat{X}_1)^2 \rangle \langle (\Delta \hat{X}_2)^2 \rangle \geq \frac{1}{16} \quad (2.55)$$

For a coherent state, $\langle (\Delta \hat{X}_1)^2 \rangle = \langle (\Delta \hat{X}_2)^2 \rangle = \frac{1}{4}$, same as the vacuum state $|0\rangle$. In other words, the coherent state represents a minimum-uncertainties state. We can define the squeezing operator [115],

$$\hat{S}(\zeta) = e^{\frac{1}{2}(\zeta^* \hat{a}^2 + \zeta \hat{a}^{\dagger 2})} \quad (2.56)$$

Such that a squeezed state can be written as $|\alpha, \zeta\rangle = \hat{S}(\zeta)\hat{D}(\alpha)|0\rangle$. For the noiseball depicted in Fig. 2.2(b), the computation of the squeezed quadrature along the direction

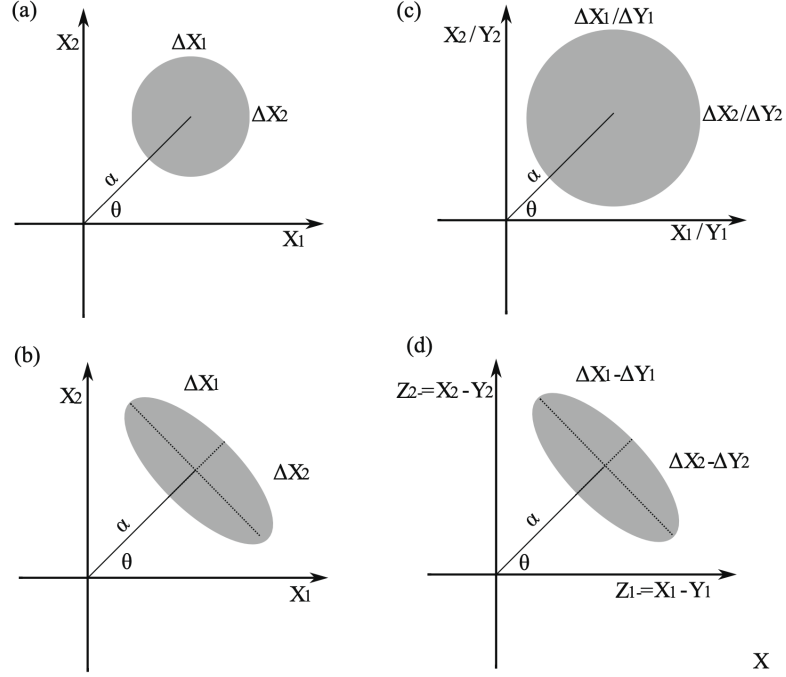


Figure 2.2: Illustration of quadrature squeezing. a) The coherent state representation. b) Single mode squeezed state representation. c) Quadratures of an individual field from the FWM correlated fields. Each shows super-poissonian statistics. The noise distribution is broader. d) The two-mode squeezed quadrature. In our case, we always measure along direction Z_1 by conducting a differential measurement.

of dashed line can be performed as follows:

$$\langle (\Delta \hat{X}_1)^2 \rangle_{sqz} = \frac{1}{4} e^{-2\zeta} \quad (2.57)$$

$$\langle (\Delta \hat{X}_2)^2 \rangle_{anti-sqz} = \frac{1}{4} e^{2\zeta} \quad (2.58)$$

The product remains $\frac{1}{16}$, indicating that we are still at the uncertainty limit. However, we have reduced the variance of one quadrature at the expense of another. The compression of the noise ball, as illustrated in Fig. 2.2, is the origin of the terms "squeezing" and "squeezed state."

Fig. 2.2 gives an example of the so-called "ball-on-stick" representation of a quantum E-M field. The displacement from the origin is α , scales with the expected photon number

$\langle n \rangle$. The noise ball represents the uncertainty. In the coherent state case (Fig. 2.2(a)), the noise ball is the same for all θ , meaning the noise measured is always the same and its radius is $1/4$. For the squeezed states (Fig. 2.2(b)), however, this phase term θ can be used to rotate the noise ball such that we can measure the squeezed (least noise) or anti-squeezed (highest noise) quadratures. Such tuning is usually achieved by using interferometry; in this dissertation, we will not address this aspect, since we measure intensities along the amplitude quadrature direction χ_1 .

2.4.4 Quadrature of Two-Mode Squeezed State

What we have introduced is the single mode quadrature squeezing. Our major interest for this thesis is the two-mode squeezing. Analogous to Eq.(2.56), the two-mode squeezing operator can be expressed as follows:

$$\hat{S}(\zeta)_{2mode} = e^{\frac{1}{2}(\zeta^* \hat{a} \hat{b} + \zeta \hat{a}^\dagger \hat{b}^\dagger)} \quad (2.59)$$

Notice that compared to Eq.(2.56), the two-mode squeezing operator involves both conjugate and probe operators. Physically, this corresponds to the pairwise creation and annihilation of one conjugate photon and one probe photon. In the context of FWM, the \hat{a} and \hat{b} operators represent the probe and conjugate output operators, respectively, as defined by Eq.(2.42). The quadrature of the probe operator \hat{a} is annotated as \hat{X}_1 and \hat{X}_2 , while the quadrature of the conjugate operator \hat{b} is noted as \hat{Y}_1 and \hat{Y}_2 , as shown in Fig. 2.2(c), we can calculate the quadrature variance of single signal field of FWM twin beams as follows [105, 107, 115, 116],

$$\langle (\Delta \hat{X}_1)^2 \rangle \langle (\Delta \hat{X}_2)^2 \rangle = \langle (\Delta \hat{Y}_1)^2 \rangle \langle (\Delta \hat{Y}_2)^2 \rangle = \frac{2G_P - 1}{16} \quad (2.60)$$

$$(2.61)$$

It is observed that for $G_P > 1$, the output fields demonstrate super-Poissonian statistics, validating Eq.(2.45) and (2.46). However, if we define joint quadrature (Fig. 2.2(d)),

$$\hat{Z}_{1\pm} = \hat{X}_1 \pm \hat{Y}_1, \quad (2.62)$$

$$\hat{Z}_{2\pm} = \hat{X}_2 \pm \hat{Y}_2. \quad (2.63)$$

The joint variance can be calculated as,

$$\langle (\Delta \hat{Z}_{1\pm})^2 \rangle = \frac{1}{4} e^{\pm 2\zeta} \quad (2.64)$$

$$\langle (\Delta \hat{Z}_{2\pm})^2 \rangle = \frac{1}{4} e^{\mp 2\zeta} \quad (2.65)$$

We are still at the total minimum variance as $Z_{1\pm} Z_{2\mp} = \frac{1}{16}$. Physically, the measurement of joint quadrature corresponds to conducting a joint measurement of both signal fields. In all experiments discussed in this thesis, the measurements are differential intensity noise, although full joint quadrature analysis has been done in Ref [117].

2.4.5 Optical Loss: Beam Splitter Model

In this section, we review the beamsplitter formalism. An optical field passing through a medium can be considered as passing through a non-polarizing beamsplitter with transmission constant T . Optical loss may be interpreted as ejection from the other beamsplitter input port. If we consider a beamsplitter with bright input \hat{a} and vacuum input \hat{c} for input, the output operator \hat{b} can be expressed as follows:

$$\hat{b} = \sqrt{T} \hat{a} + i\sqrt{1-T} \hat{c} \quad (2.66)$$

The variance can be easily calculated as,

$$Var(\langle \hat{b}^\dagger \hat{b} \rangle) = T^2 \left[Var(\langle \hat{a}^\dagger \hat{a} \rangle) - \langle \hat{a}^\dagger \hat{a} \rangle \right] + T \langle \hat{a}^\dagger \hat{a} \rangle \quad (2.67)$$

We used the commutation relation $\langle \hat{c}\hat{c}^\dagger \rangle = \langle \hat{c}^\dagger\hat{c} \rangle + 1$. Eq.(2.67) involves no explicit dependent on \hat{c} since $\langle \hat{c}^\dagger\hat{c} \rangle = 0$ [116]. The vacuum operator leads to the extra terms in Eq.(2.67). As a sanity check, we consider the case where the input optical field \hat{a} is a coherent state such that its variance equals expected photon counts $\langle n_b \rangle = T\langle n_a \rangle$. The first term in equation Eq.(2.67) vanishes, and we have essentially,

$$Var(\langle \hat{b}^\dagger\hat{b} \rangle) = T\langle \hat{a}^\dagger\hat{a} \rangle = \langle \hat{b}^\dagger\hat{b} \rangle = \langle n_b \rangle \quad (2.68)$$

As expected, for a coherent state, the beamsplitter only reduces its photon counts proportionally. The output field is still a coherent state. Assuming an equal transmission ratio T for the two channels and no optical loss, the FWM differential variance is given by [116],

$$Var(\hat{a}_{out}^\dagger\hat{a}_{out} - \hat{b}_{out}^\dagger\hat{b}_{out}) = [(2G_P - 1)T(1 - 2T) + 2G_P T^2]\langle \hat{a}^\dagger\hat{a} \rangle \quad (2.69)$$

We can check that it reduces to Eq.(2.49) in the limit of zero detector loss($T=1$).

Optical Loss: Infinite Beamsplitter formalism

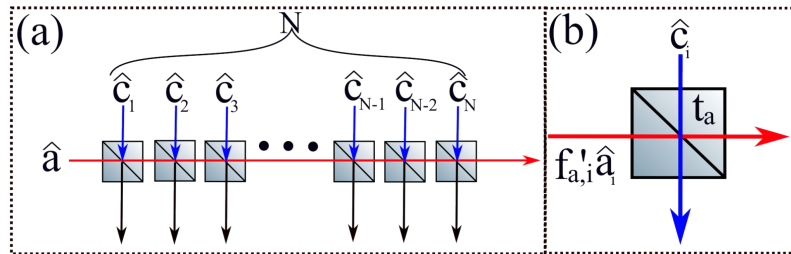


Figure 2.3: (a) Illustration of the continuous beam-splitter model: at each infinitesimal step, the input state is modified by a fictitious beam splitter with a vacuum input. This process is repeated over N steps to obtain the final output. (b) Detailed illustration of the beam-splitter model for an individual step.

When optical loss is changing throughout the medium, a simple beam-splitter model is insufficient. In this case, the loss not only affects the field strength but also impacts both linear and nonlinear processes, which occur continuously throughout the medium.

To account for this, we developed a continuous beam-splitter model [116], as described in Fig. 2.3(a). In this model, we divide the total propagation distance L into N infinitesimally small steps (indexed by i) with a step size δz . For each step (Fig. 2.3(b)), we describe the evolution of the field operators using the following gain equations:

$$\begin{aligned}\hat{a}_{i+1} &= t_a f'_{a,i} \hat{a}_i + \sqrt{1 - t_a^2} \hat{c}_{i+1}, \\ \hat{b}_{i+1} &= t_b f'_{b,i} \hat{b}_i + \sqrt{1 - t_b^2} \hat{d}_{i+1},\end{aligned}\tag{2.70}$$

where the gain factor $f'_{a/b,i}$ represents the nonlinear gain at the i th infinitesimal step, and $t_{a/b} = \sqrt{T_{a/b}}$ is the square root of total transmission for the probe and conjugate fields, respectively. This equation is equivalent to Eq.(2.67). We typically assume $T_b = 1$ for the conjugated field, while T_a is determined experimentally. Since the initial input state is $(\hat{a}_0, 0)$, applying the beam-splitter model iteratively allows us to express the amplification of both the probe and conjugate fields as a product of the initial input operator \hat{a}_0 . After N steps, the output operators can be written as:

$$\begin{aligned}\hat{a}_N &= f_{a,1} \dots f_{a,N} \hat{a}_0 + \sqrt{1 - t_a^2} \hat{c}_N + \dots + f_{a,1} \dots f_{a,N-2} \sqrt{1 - t_a^2} \hat{c}_2 + f_{a,1} \dots f_{a,N-1} \sqrt{1 - t_a^2} \hat{c}_1, \\ \hat{b}_N &= f_{b,1} \dots f_{b,N} \hat{a}_0 + \sqrt{1 - t_b^2} \hat{d}_N + \dots + f_{b,1} \dots f_{b,N-2} \sqrt{1 - t_b^2} \hat{d}_2 + f_{b,1} \dots f_{b,N-1} \sqrt{1 - t_b^2} \hat{d}_1.\end{aligned}\tag{2.71}$$

For conciseness, we define $f_{a/b,i} = t_a f'_{a/b,i}$. Given that the conjugate field is more detuned, and there is minimal population accumulation in the lower state of the transition, we reasonably assume that the conjugate field is lossless ($t_b = 1$). As a result, we retain only the first term in \hat{b}_N . Additionally, we observe that the first two terms are proportional to $\sqrt{G_{P/C}}$. Finally, we rewrite Eq. (2.71) in a more compact form, representing the gain

factors in each term as $\chi_{a,i}$:

$$\begin{aligned}\hat{a}_N &= \sqrt{G_P}\hat{a}_0 + \chi_{a,1}\hat{c}_N + \dots + \chi_{a,N-2}\hat{c}_2 + \chi_{a,N-1}\hat{c}_1, \\ \hat{b}_N &= \sqrt{G_C}\hat{a}_0.\end{aligned}\tag{2.72}$$

We then compute the differential intensity variance $\text{Var}(\hat{a}_N^\dagger\hat{a}_N - \hat{b}_N^\dagger\hat{b}_N)$. Since all c_i operators correspond to vacuum modes, we have $\langle\hat{c}_i^\dagger\hat{c}\rangle = 0$. In addition, the input photon number is $\langle\hat{a}_0^\dagger\hat{a}_0\rangle = n_{in}$. After performing the calculation, we arrive at the following expression:

$$\begin{aligned}S &= 10\log_{10}\left[\frac{\text{Var}(\hat{a}_N^\dagger\hat{a}_N - \hat{b}_N^\dagger\hat{b}_N)}{\langle\hat{n}_P\rangle + \langle\hat{n}_C\rangle}\right] \\ &= 10\log_{10}\left[\frac{(G_P - G_C)n_{in} + \sum_1^N \chi_{a,i} * (n_{in} + 1)}{(G_P + G_C)n_{in}}\right],\end{aligned}\tag{2.73}$$

where S is the squeezing parameter, G_P and G_C stand for the gains for the probe and conjugate fields, and $\chi_{a,i}$ accounts for losses at each step. In the ideal lossless case, $\chi_{a,i} \rightarrow 0$ and $G_P - G_C = 1$, which recovers the standard expression for ideal squeezing. When $t_a = 0$, we essentially are measuring noise of conjugate field only, and we see super-poissonian statistics as expected. To incorporate optical loss into this equation, we use a 2×2 matrix \mathcal{H} (akin to Eq. (3.25)) to relate the input and output fields, as described by

$$\begin{pmatrix}\hat{a}(z) \\ \hat{b}(z)\end{pmatrix} = e^{-i\mathcal{H}z} \begin{pmatrix}\hat{a}(0) \\ \hat{b}(0)\end{pmatrix} = \begin{pmatrix}A(z)\hat{a}(0) \\ B(z)\hat{a}(0)\end{pmatrix}.\tag{2.74}$$

From Eq. (2.74), we can express $\chi_{a,i}$ in terms of the gain factor as

$$\chi_{a,i} = \left(\sqrt{1 - t_a^2}\right)^{N-i+1} [A(\delta z)]^{N-i},\tag{2.75}$$

where δz is the infinitesimal step size, and $A(\delta z)$ is the gain per step. For each experimental data set, we can infer the functions $A(z)$ and $B(z)$ by fitting them based on the

measured values $A(L)$ and $B(L)$, which correspond to the total gain over the entire propagation distance L . Once $A(\delta z)$ is determined, $\chi_{a,i}$ can be computed accordingly, as the transmission T_a is known from experimental measurements. This method is consistent with the procedure used in the work [116].

2.4.6 Optical Loss: Langevin Noise Formalism

In this section, we introduce an alternative method for accounting for the optical loss by using the Langevin formalism. This method quantitatively accounts for the atomic-induced noise due to optical absorptions and emissions that is unavoidable when dealing with hot atoms. The Langevin theory considers the optical field of interest interacting with an external reservoir with closely spaced frequencies and infinite number of different mode, in our case it is an atomic ensemble. The contribution of each atoms is expressed with the so-called noise operator \hat{f} , Physically, \hat{f} is all atom contribution during the interaction time τ and interaction distance z , which takes the form [105],

$$\hat{f} \equiv g_c \sum_i f(\tau, z) \hat{\sigma}^i \quad (2.76)$$

where the g_c is constant, $f(\tau, z)$ represents the addition and later removal of an atom as the atom only affects the field for certain time and range. The σ^i represents the i th atom operator. Conveniently, equivalent FWM Langevin formalism has been developed using the 2×2 propagation matrix [111].

$$\partial_z \begin{pmatrix} \hat{a}_{out} \\ \hat{b}_{out}^\dagger \end{pmatrix} = \overbrace{\begin{pmatrix} -\alpha + i\frac{\Delta k}{2} & i\kappa \\ -i\kappa & -i\frac{\Delta k}{2} \end{pmatrix}}^{\mathcal{M}} \begin{pmatrix} \hat{a} \\ \hat{b}^\dagger \end{pmatrix} + \hat{\mathbb{N}}_R \begin{pmatrix} \hat{f}_a \\ \hat{f}_b^\dagger \end{pmatrix} + \hat{\mathbb{N}}_I \begin{pmatrix} \hat{f}_a^\dagger \\ \hat{f}_b \end{pmatrix}. \quad (2.77)$$

This propagation matrix \mathcal{M} is equivalent to the 2×2 propagation matrix from Eq.(2.36), with the inclusion of linear absorption and dispersion term α and imaginary sign i . In

Eq.(2.77), \hat{f}_a^\dagger and \hat{f}_b are Langevin noise operators that satisfy the following correlations:

$$\langle \hat{f}_m(z) \hat{f}_n(z') \rangle = 0, \langle \hat{f}_m^\dagger(z) \hat{f}_n^\dagger(z') \rangle = 0, \quad (2.78)$$

$$\langle \hat{f}_m^\dagger(z) \hat{f}_n(z') \rangle = 0, \langle \hat{f}_m(z) \hat{f}_n^\dagger(z') \rangle = \delta_{mn} \delta(z - z'). \quad (2.79)$$

Here, the $\hat{\mathbb{N}}_R$ and $\hat{\mathbb{N}}_I$ matrices are determined by the coupling matrix M such that the probe and conjugate field at any given position z satisfy the commutation relations [111], in the forward (probe and conjugate propagate along the same direction) FWM:

$$\hat{\mathbb{N}}_R + i\hat{\mathbb{N}}_I = \sqrt{-(M + M^*)}. \quad (2.80)$$

This equation can be solved at the cell output $z = L$,

$$\begin{pmatrix} \hat{a}_{out} \\ \hat{b}_{out}^\dagger \end{pmatrix} = e^{ML} \begin{pmatrix} \hat{a} \\ \hat{b}^\dagger \end{pmatrix} + \int_0^L e^{M(L-z)} \hat{\mathbb{N}}_R \begin{pmatrix} \hat{f}_a^\dagger(z) \\ \hat{f}_b(z) \end{pmatrix} dz + \int_0^L e^{M(L-z)} \hat{\mathbb{N}}_I \begin{pmatrix} \hat{f}_a^\dagger(z) \\ \hat{f}_b(z) \end{pmatrix} dz. \quad (2.81)$$

Note here that $e^{ML} = \begin{pmatrix} A & B \\ C & D \end{pmatrix}$ is the gain matrix with the same physical meaning as in Eq.(2.36), but written in a more general format. The joint differential variance can be then computed through the standard procedure and is included in the numerical model.

We can calculate the differential variance, $Var(\hat{a}_{out}^\dagger \hat{a}_{out} - \hat{b}_{out}^\dagger \hat{b}_{out})$, based on the above results. Two loss term, η_P and η_C , are applied to both probe and conjugate channels to account for the detector loss arising from the filtering scheme as well as the non-perfect quantum efficiency of the employed photon detector. We annotate use η for total loss to differentiate with medium transmission T . With this modification, the differential intensity variance takes the form:

$$\begin{aligned} Var(\hat{n}_{P,loss} - \hat{n}_{C,loss}) &= \langle (\eta_P \hat{n}_{P,loss} - \eta_C \hat{n}_{C,loss})^2 \rangle - \langle \eta_P \hat{n}_{P,loss} - \eta_C \hat{n}_{C,loss} \rangle^2 \\ &+ \eta_P (1 - \eta_P) |A|^2 \hat{n}_{in} + \eta_C (1 - \eta_C) |A|^2 \hat{n}_{in} \end{aligned} \quad (2.82)$$

The detailed steps and script for Langevin noise calculation is shown in Appendix.A.

Connection between Infinite BS Model and Langevin Formalism

In this section, we discuss the relations, similarity, and difference between two models. Essentially, the infinite beamsplitter model is a convenient numerical approximation, while the Langevin formalism yields a quantitative solution for atomic noise contribution. At each location within the propagation distance, the latter accounts for the noise by considering the light field interacting with an infinite reservoir instead of applying a simple beamsplitter model. We can also examine the form of Eq.(2.81). Physically, the integrand of $\hat{\mathbb{N}}$ accounts for the joint effect of linear loss and nonlinear / linear gain. The overall effect over the propagation z is accounted for by integrating from 0 to L. The physical meaning of Eq.(2.81) is then very similar to the infinite beamsplitter formalism such that at each discrete step with a small distance δz , except that in this case, the noise is no longer modeled merely as a simple beamsplitter at each discrete step. In some cases, however, if the numerical solution is done with a sufficiently large number of steps, both methods yield a close solution. Here, we illustrate this with a simple example.

Consider an atomic medium with nonzero optical depth (OD) through which a coherent optical field (\hat{a}^\dagger) propagates. For each incremental step Δz along the propagation path, a certain transmission $t_{m,dz}$ is incurred. By repeatedly applying Eq.(2.68) over M steps, we derive the expression for the output field \hat{c}^\dagger as follows:

$$Var(\langle \hat{b}^\dagger \hat{b} \rangle) = \left[\prod_{m=1}^M t_{m,dz} \right] \langle \hat{a}^\dagger \hat{a} \rangle = \langle \hat{b}^\dagger \hat{b} \rangle \quad (2.83)$$

In other words, when a coherent field propagates through a lossy medium, such as a crystal or an atomic ensemble, the output state remains coherent.

We now consider the same calculation with the Langevin noise formalism. To illustrate this, consider a coherent input state, $|\alpha\rangle$, propagating through a medium with a loss factor

β . The propagation dynamics can be expressed as follows:

$$\frac{\partial \hat{a}(z)}{\partial z} = \beta \hat{a}(z) + \sqrt{2\beta} \hat{f}(z), \quad (2.84)$$

where z is the propagation distance, ranging from 0 to L , and $\hat{f}(z)$ is the noise operator satisfying $\langle \hat{f}(z) \hat{f}(z') \rangle = \delta(z - z')$. The annihilation operator at the output (distance L) can be thus found to be

$$\hat{a}(L) = \hat{a}(0)e^{-\beta L} + e^{-\beta L} \int_0^L e^{\beta z} \hat{f}(z) dz. \quad (2.85)$$

From this, we can determine the photon number, photon number variance, and quadrature variance after propagation through the medium:

$$\begin{aligned} \langle \hat{n}_{in} \rangle &= e^{-2\beta L} \langle \hat{n}_{out} \rangle, \\ \langle \Delta \hat{n}_{in}^2 \rangle &= e^{-2\beta L} \langle \hat{n}_{out}^2 \rangle, \\ \langle \Delta \hat{X}^2 \rangle &= 1/4. \end{aligned} \quad (2.86)$$

Here, $\langle \hat{n}_{in} \rangle$ and $\langle \Delta \hat{n}_{in}^2 \rangle$ decrease proportionally with the loss factor, while the quadrature variance remains unchanged. For a coherent state propagating through a lossy medium, both the infinite beamsplitter model and the Langevin formalism yield identical results, demonstrating that the coherent state remains coherent. This agreement validates the use of the infinite beamsplitter model as an approximation. It is important to note that the Langevin formalism is exact, while the infinite beamsplitter model is an oversimplified approximation whose accuracy depends on the step size chosen as well as the validity of modeling all losses using the beamsplitter model. Thus, when a precise extraction of the first-order Hamiltonian is possible, or a more systematic noise calculation is required, we employ the proper Langevin treatment; conversely, the infinite beamsplitter model is used as a convenient approximation method. In this dissertation, we utilize both methods for

noise calculation.

Chapter 3

Fundamentals of Two-Mode Squeezing Generation in Double- Λ and Double-Ladder Atomic Systems

In this section, we explore two distinct FWM squeezers in ^{85}Rb vapor: the double- Λ squeezer and the double-Ladder squeezer, both theoretically and experimentally.

The chapter is organized as follows: we first introduce the density matrix formalism to deal with atomic dynamics. We then provide specifications for each FWM configuration: 1) analytically solve the system, 2) detail the experiment, and 3) provide a detailed setup guide as well as answers to frequently encountered questions. Lastly, we compare the two configurations. The experimental setup detailed in this section is utilized fully or partially for Ch.4, Ch.5, and Ch.6. Some of the graphs used in this section are modified from the thesis [107], as we partially shared the setup during our projects, and no conflict of interest is involved.

3.1 Theoretical Description of Light-Atom Interaction

Let's start with the density matrix formalism. This approach enables us to describe a statistical mixture of atomic coherence along with atomic decays and dephasing, thereby yielding more accurate predictions for the ensemble as a whole and allowing for the calculation of induced polarization.

Let's first consider a pure quantum state $|\psi\rangle = \sum_n a_n |n\rangle$. The density matrix operator is then defined as,

$$\hat{\rho} = |\psi\rangle\langle\psi|, \quad (3.1)$$

a matrix with density matrix element expressed as

$$\rho_{ij} = \langle i|\hat{\rho}|j\rangle = \langle i|\psi\rangle\langle\psi|j\rangle = a_i a_j^*, \quad (3.2)$$

Physically, the diagonal elements ρ_{ii} indicate the probability of populating an atom in the state $|i\rangle$ with an overall probability summed to unity. The off-diagonal elements ρ_{ij} , referred to as coherence terms, represent the expectation values of the atomic dipole moments across corresponding transitions. These coherence terms can be directly related to the total induced electric dipole moment:

$$\langle d_{tot} \rangle = \langle \psi | \vec{d}_{ij} | \psi \rangle - \sum_{i,j} \rho_{ij} \langle i | e\mathbf{r} | j \rangle = \sum_{i,j} d_{ij} \rho_{ij}, \quad (3.3)$$

Here $d_{ij} = -\langle \psi | e\mathbf{r} | \psi \rangle$ signifies the dipole matrix moment associated with the transition from $|i\rangle \rightarrow |j\rangle$. This can be related to polarization via Eq.(2.3).

$$\mathbf{P} = \epsilon\chi\mathbf{E} = N \sum_{i,j} d_{ij} \rho_{ij} \quad (3.4)$$

Eq.(3.4) establishes a direct relationship between elements of the density matrix and the polarization of the medium, forming connections with the wave equation Eq.(2.6). By solving for the density matrix elements, one can obtain the system's underlying dynamics.

We next need to introduce the general formulism for finding the exact Hamiltonian of the involved light-atom interaction. Energy of an electron with charge e and mass m interacting with E-M field can be expressed as,

$$\hat{H} = \frac{1}{2m} [\mathbf{p} + e\mathbf{A}]^2 - e\phi + V_c(\mathbf{r}), \quad (3.5)$$

Here \mathbf{A} and ϕ are vector/scalar potential of electromagnetic field, respectively, and $V_c(\mathbf{r})$ is the Coulomb potential. Since we work radiation gauge, in which, $\phi = 0$ and $\nabla \cdot \mathbf{A} = 0$, we can write down the Hamiltonian as [105],

$$\hat{H} = \overbrace{\frac{p^2}{2m} + V_c(\mathbf{r})}^{\hat{H}_0} + \overbrace{\mathbf{A} \cdot \mathbf{p}}^{\hat{H}_I = -\mathbf{d} \cdot \mathbf{E}}, \quad (3.6)$$

The first two terms are the Hamiltonian \hat{H}_0 of the unperturbed atom. The second term is the interaction Hamiltonian \hat{H}_I , which can be rewritten in the form of $\hat{H}_I = -\mathbf{d} \cdot \mathbf{E}$ [105, 115, 118]. This term corresponds physically to the interaction between the electric dipole and the electric field. For quantized atoms with energy levels $\{|i\rangle\}$, the Hamiltonian in the interaction picture can be expressed as the following matrix [105, 106, 115]:

$$\hat{H} = \sum_{i=1}^4 \hbar \Delta_i |i\rangle \langle i| + \frac{1}{2} \hbar \sum_{i \neq j} \Omega_{ij} |i\rangle \langle j| + \text{H.C} \quad (3.7)$$

Here we removed the explicit time dependence by applying an unitary transformation [107, 113]. The Rabi frequency Ω_{ij} is defined by $\Omega_{ij} = \frac{d_{ij}E}{\hbar}$ and quantifies the strength of the light-atom interaction. Finally, we can write down the general form of the master equation as follows [105].

$$\frac{\partial \hat{\rho}(t)}{\partial t} = -\frac{i}{\hbar} [\hat{H}, \hat{\rho}(t)] + \frac{1}{2} \{\Gamma, \hat{\rho}(t)\} \quad (3.8)$$

\hat{H} is the Hamiltonian given by Eq.(3.7). The decay matrix Γ specifies the decay or

dephase channels. Eq.(3.8) allows us to write down a series of differential equations of density matrices describing the system dynamics, which we can use for a comprehensive calculation of FWM in both the double- Λ and double-Ladder configurations.

3.2 FWM in Double- Λ Configuration

3.2.1 Density Matrix Calculations for a Double- Λ Configuration

We first discuss the basic theoretical framework for the double- Λ configuration. A typical double- Λ is shown in Fig.3.1, where we have a strong pump field coupled to both $|1\rangle \rightarrow |3\rangle$ and $|2\rangle \rightarrow |4\rangle$ transition. Its Rabi frequency is annotated as Ω , and it creates the strong ground-excited state coherence. We send in a weak probe field Ω_P (Blue), and the conjugate field Ω_C (Black) is generated.

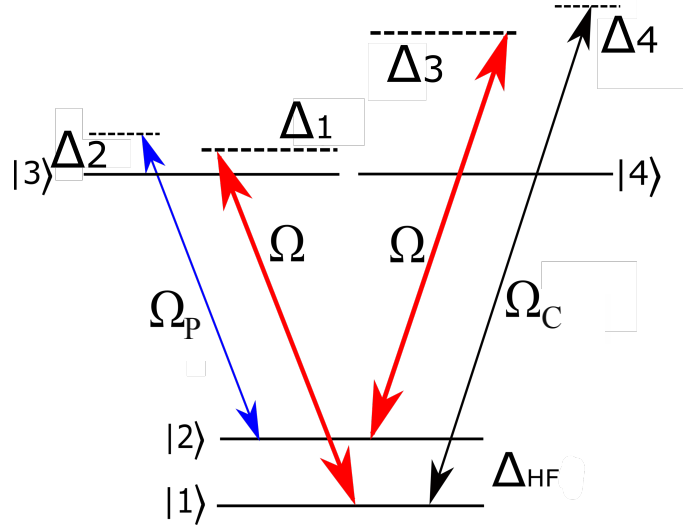


Figure 3.1: Energy level diagram used for the FWM model. Here, atomic levels $|1\rangle$ and $|2\rangle$ represent two ground-state hyperfine levels $|5S_{1/2} F = 2, 3\rangle$ of ^{85}Rb , while levels $|3, 4\rangle$ both represent the excited electron state $|5P_{1/2}\rangle$ [109]. In the schematic, the pump field (Ω) applied at both transitions $|1\rangle \rightarrow |3\rangle$ and $|2\rangle \rightarrow |4\rangle$ is shown in red, and the probe (Ω_P) and conjugate (Ω_C) fields are labeled by the blue and black arrows.

In actual experiment, we construct double- Λ configuration utilizing both $|5S\rangle$ ground states and $|5P_{1/2}\rangle$ excited levels. For analytical calculations, the excited level is treated as

two independent levels for the sake of simplicity, following [9, 108, 109, 119, 120]. Here we combine Eqs. (3.8) and (3.7) to obtain the Maxwell-Bloch equations for the system [109, 121–124]. Assuming a closed system, the general atomic dynamics can be expressed as follows,

$$\begin{aligned}
\dot{\rho}_{11} &= i\frac{\Omega}{2}(\rho_{31} - \rho_{13}) + i\frac{\Omega_C^*}{2}\rho_{41} - i\frac{\Omega_C}{2}\rho_{14} + 2\gamma_{13}\rho_{33} + 2\gamma_{14}\rho_{44}, \\
\dot{\rho}_{22} &= i\frac{\Omega_P^*}{2}\rho_{32} - i\frac{\Omega_P}{2}\rho_{23} + i\frac{\Omega}{2}(\rho_{42} - \rho_{24}) + 2\gamma_{23}\rho_{33} + 2\gamma_{24}\rho_{44}, \\
\dot{\rho}_{33} &= i\frac{\Omega}{2}(\rho_{13} - \rho_{31}) - i\frac{\Omega_P^*}{2}\rho_{32} + i\frac{\Omega_P}{2}\rho_{23} - 2\gamma_3\rho_{33}, \\
\rho_{44} &= 1 - \rho_{11} - \rho_{22} - \rho_{33} \rightarrow \text{Closed System condition} \\
\dot{\rho}_{12} &= i(\Delta_2 - \Delta_1)\rho_{12} + i\frac{\Omega}{2}\rho_{32} - i\frac{\Omega_P}{2}\rho_{13} + i\frac{\Omega_C^*}{2}\rho_{42} - i\frac{\Omega}{2}\rho_{14}, \\
\dot{\rho}_{13} &= -i\Delta_1\rho_{13} + i\frac{\Omega}{2}(\rho_{33} - \rho_{11}) - i\frac{\Omega_P^*}{2}\rho_{12} + i\frac{\Omega_C^*}{2}\rho_{43} - \frac{1}{2}\gamma_3\rho_{13}, \\
\dot{\rho}_{14} &= i(\Delta_2 - \Delta_1 - \Delta_3)\rho_{14} + i\frac{\Omega_C^*}{2}(\rho_{44} - \rho_{11}) - i\frac{\Omega}{2}\rho_{12} + i\frac{\Omega}{2}\rho_{34} - \frac{1}{2}\gamma_4\rho_{14}, \\
\dot{\rho}_{32} &= i\Delta_2\rho_{32} - i\frac{\Omega_P}{2}(\rho_{33} - \rho_{22}) + i\frac{\Omega}{2}\rho_{12} - i\frac{\Omega}{2}\rho_{34} - \frac{1}{2}\gamma_3\rho_{32}, \\
\dot{\rho}_{24} &= -i\Delta_3\rho_{24} + i\frac{\Omega}{2}(\rho_{44} - \rho_{22}) - i\frac{\Omega_C^*}{2}\rho_{21} + i\frac{\Omega_P^*}{2}\rho_{34} - \frac{1}{2}(\gamma_2 + \gamma_4)\rho_{24}, \\
\dot{\rho}_{34} &= -i(\Delta_3 - \Delta_2)\rho_{34} + i\frac{\Omega}{2}\rho_{14} + i\frac{\Omega_P}{2}\rho_{24} - i\frac{\Omega_C^*}{2}\rho_{31} - i\frac{\Omega}{2}\rho_{32} - \frac{1}{2}(\gamma_3 + \gamma_4)\rho_{34}.
\end{aligned} \tag{3.9}$$

Where Ω , Ω_P and Ω_C denotes the pump, probe and conjugate Rabi frequencies, respectively. γ_j is the decay rate of the j^{th} atomic level, $\gamma_{jk} = (\gamma_j + \gamma_k)/2$ is the decoherence rate of atomic coherence ρ_{jk} , and Δ_{jk} is the frequency detunings of the optical fields of the corresponding optical transition, annotated as Δ_i for simplicity (see Fig.3.1). To simplify the discussions, we set ground state decay rate $\gamma_1 = \gamma_2 = 0$ in our case.

Here we can further apply several simplifications. First, by selecting a proper rotating frame, we have real pump Rabi frequency Ω , while Ω_P and Ω_C accumulates a symmetric phase $i\phi/2$ and $-i\phi/2$ respectively. Here, Φ assumes the following format,

$$\Phi = \Delta\omega t - \Delta k z + \phi_0 \quad (3.10)$$

where $\Delta\omega$ and Δk given in Eq.(2.17). ϕ_0 denotes the initial constant phase difference between the input fields. In our analysis, we can set $\phi_0 = 0$ and $\Delta\omega = 0$: The former represents a constant phase term accumulated in the signal Rabi frequencies, which will ultimately diminish as we evaluate photon generation. The latter is derived from the assumption of zero-energy dissipation, implying that energy is solely transferred from the pump field to the signal fields.

Second, time dependences are disregarded by setting $\dot{\rho} = 0$ since we are interested in the steady-state solutions. Third, in a typical double- Λ FWM configuration, we have $\Omega \gg |\Omega_p| \approx |\Omega_c|$, which allows for the neglect of several comparatively small terms in Eq. (3.9). These simplifications effectively decomposes the composite double- Λ system into two independent sets of equations. Combining decay and detuning terms in Eq.(3.9) into complex decay terms ($\Gamma_{14} = \gamma_4/2 + i(\Delta_1 - \Delta_2 + \Delta_3)$, $\Gamma_{12} = \gamma_{12} + i(\Delta_1 - \Delta_2)$, $\Gamma_{32} = \gamma_3/2 - i\Delta_2$ and $\Gamma_{34} = (\gamma_3 + \gamma_4)/2 - i(\Delta_2 + \Delta_3)$), we reach the following set of the steady-state equations [109, 121–124]:

$$\text{Set 1} \begin{cases} 0 = \gamma_{31}\rho_{33} + \gamma_{41}\rho_{44} + \frac{1}{2}i\Omega(\rho_{31} - \rho_{13}), \\ 0 = \gamma_{32}\rho_{33} + \gamma_{42}\rho_{44} + \frac{1}{2}i\Omega(\rho_{42} - \rho_{24}), \\ 0 = -\gamma_3\rho_{33} - \frac{1}{2}i\Omega(\rho_{31} - \rho_{13}), \\ 0 = -\gamma_4\rho_{44} - \frac{1}{2}i\Omega(\rho_{42} - \rho_{24}), \\ 0 = -\left(\frac{\gamma_3}{2} + i\Delta_1\right)\rho_{13} - \frac{1}{2}i\Omega(\rho_{11} - \rho_{33}), \\ 0 = -\left(\frac{\gamma_4}{2} + i\Delta_3\right)\rho_{24} - \frac{1}{2}i\Omega(\rho_{22} - \rho_{44}). \end{cases} \quad (3.11)$$

$$\text{Set 2} \begin{cases} 0 = -\Gamma_{12}\rho_{12} + \frac{1}{2}i\Omega\rho_{32} - \frac{1}{2}i\Omega\rho_{14} - \frac{1}{2}i\Omega_P\rho_{13} + \frac{1}{2}i\Omega_C^*\rho_{42}, \\ 0 = -\Gamma_{14}\rho_{14} + \frac{1}{2}i\Omega\rho_{34} - \frac{1}{2}i\Omega\rho_{12} + \frac{1}{2}i\Omega_C^*(\rho_{44} - \rho_{11}), \\ 0 = -\Gamma_{32}\rho_{32} + \frac{1}{2}i\Omega\rho_{12} - \frac{1}{2}i\Omega\rho_{34} - \frac{1}{2}i\Omega_P(\rho_{33} - \rho_{22}), \\ 0 = -\Gamma_{34}\rho_{34} + \frac{1}{2}i\Omega\rho_{14} - \frac{1}{2}i\Omega\rho_{32} - \frac{1}{2}i\Omega_P\rho_{24} + \frac{1}{2}\Omega_C^*\rho_{31}. \end{cases}$$

The atomic coherence terms of Set 1 can be solved easily as a linear system [122, 123]. We focus on Set 2, the linear system that describes our signal fields. We ignore ρ_{34} as levels $|3\rangle$ and $|4\rangle$ are physically one level, thus atomic coherence ρ_{34} carries no physical meaning. The ground state coherence ρ_{12} does not contribute to the signal fields. We look for the solutions of $\rho_{14}(= -\frac{i\Omega_3}{2\Gamma_{14}}\rho_{12})$ and ρ_{32} , which are related to the two signal fields of our interest. By rewriting Eq.3.11 in Set 2, the optical coherence terms ρ_{41} and ρ_{32} can be obtained by solving the reduced Maxwell-Bloch equations [109, 121–124].

$$\begin{pmatrix} \dot{\rho}_{12} \\ \dot{\rho}_{14} \\ \dot{\rho}_{32} \\ \dot{\rho}_{34} \end{pmatrix} = \begin{pmatrix} -\Gamma_{12} & -\frac{i\Omega}{2} & \frac{i\Omega}{2} & 0 \\ -\frac{i\Omega}{2} & -\Gamma_{14} & 0 & \frac{i\Omega}{2} \\ \frac{i\Omega}{2} & 0 & -\Gamma_{32} & -\frac{i\Omega}{2} \\ 0 & \frac{i\Omega}{2} & -\frac{i\Omega}{2} & -\Gamma_{34} \end{pmatrix} \begin{pmatrix} \rho_{12} \\ \rho_{14} \\ \rho_{32} \\ \rho_{34} \end{pmatrix} + \frac{i}{2} \begin{pmatrix} -\rho_{13}\Omega_P + \rho_{42}\Omega_C^* \\ -\Omega_C^*(\rho_{11} - \rho_{44}) \\ \Omega_P(\rho_{22} - \rho_{33}) \\ \rho_{24}\Omega_P - \rho_{31}\Omega_C^* \end{pmatrix}. \quad (3.12)$$

To obtain analytic expressions for the two field propagation matrix, we make several reasonable assumptions. First, we consider both pairs of optical fields to be in nearly perfect resonances, such that $\Delta_1 \approx \Delta_2$ and $\Delta_4 = \Delta_3 + \Delta_1 - \Delta_2 \approx \Delta_3$. Moreover, we assume that

the first Λ subsystem, formed by the probe and pumps, is not too far detuned from the optical transition, compare to the hyperfine ground state splitting, such that $\Delta_{1,2} \ll \Delta_{HF}$. On the other hand, the second Λ link, formed by the pump and the Stokes fields, is far-detuned so that $\Delta_3 = \Delta_1 + \Delta_{HF} \gg \Delta_{1,2}, \Omega$ and γ_3 . In this case, the atomic population distribution is dominated by the optical pumping on the $|1\rangle - |3\rangle$ transition. In this case, most atoms are in the $|2\rangle$ ground state, while all other optical levels may be considered empty: $\rho_{11}^{(0)} = \rho_{33}^{(0)} = \rho_{44}^{(0)} = \rho_{13}^{(0)} = 0$, and $\rho_{22}^{(0)} = 1$.

With these simplification, we can find the steady state solutions for the optical coherence terms, ρ_{32} and ρ_{14} by solving Eqs. (3.12),

$$\rho_{32} = \frac{2i\Gamma_{12}}{\Omega^2 + 4\Gamma_{12}\Gamma_{32}}\Omega_P + \frac{1}{2\Delta_3} \frac{\Omega^2}{\Omega^2 + 4\Gamma_{12}\Gamma_{32}}\Omega_C^*. \quad (3.13)$$

$$\rho_{14} = \frac{i}{2\Gamma_{14}} \frac{\Omega^2}{\Omega^2 + 4\Gamma_{12}\Gamma_{32}}\Omega_P + \frac{1}{2\Gamma_{14}} \frac{\Omega^2}{2\Delta_3} \frac{2\Gamma_{32}}{\Omega^2 + 4\Gamma_{12}\Gamma_{32}}\Omega_C^* \quad (3.14)$$

Using Eq.(2.19) and (3.4), we formulate the propagation equations for the probe (Ω_P) and conjugate (Ω_C) optical fields under the rotating wave approximation as follows [109, 121–124],

$$-i \frac{\Omega_P}{\partial z} = \frac{g}{c} N \rho_{32}, \quad (3.15)$$

$$i \frac{\Omega_C^*}{\partial z} = \frac{g}{c} N \rho_{14}. \quad (3.16)$$

The coupling constant g is defined as $g = \frac{\omega}{2\epsilon_0 \hbar} d_{eg}^2$. We can write down Eqs.(3.15) and (3.16) in matrix form, and further simplify these expressions by writing $\Gamma_{14} = \gamma_4/2 + i(\Delta_1 - \Delta_2 + \Delta_3) \approx i\Delta_3$ and $\Gamma_{12} = \gamma_{12} + i(\Delta_1 - \Delta_2) \approx 0$ to construct the propagation equations for the probe and conjugate optical fields as follows:

$$i\partial_z \begin{pmatrix} \Omega_P \\ \Omega_C^* \end{pmatrix} = \begin{pmatrix} \frac{gN}{c} \frac{-2i\Gamma_{12}}{\Omega^2 + 4\Gamma_{12}\Gamma_{32}} - \frac{\Delta k}{2} & -\frac{gN}{c} \frac{1}{2\Delta_3} \frac{\Omega^2}{\Omega^2 + 4\Gamma_{12}\Gamma_{32}} \\ \frac{gN}{c} \frac{1}{2\Delta_3} \frac{\Omega^2}{\Omega^2 + 4\Gamma_{12}\Gamma_{32}} & -\frac{gN}{c} \frac{\Omega^2}{4\Delta_3^2} \frac{2i\Gamma_{32}}{\Omega^2 + 4\Gamma_{12}\Gamma_{32}} + \frac{\Delta k}{2} \end{pmatrix} \begin{pmatrix} \Omega_P \\ \Omega_C^* \end{pmatrix}. \quad (3.17)$$

By enforcing the resonance conditions ($\Delta_1 \approx \Delta_2$, $\Delta_3 \approx \Delta_4$) and assuming the pump field to be strong enough to create full EIT transparency window, but still strongly couple only to the near-resonant Λ -link, such that $\Delta_3 \gg \Omega \gg \sqrt{\gamma_{12}\gamma_{13}}$ and $\Omega \ll \Delta_3$, the simplified propagation matrix takes the desired form of the anti-PT Hamiltonian:

$$i\partial_z \begin{pmatrix} \Omega_P \\ \Omega_C^* \end{pmatrix} = \begin{pmatrix} -\frac{\Delta k}{2} & -\frac{gN}{2c\Delta_3} \\ \frac{gN}{2c\Delta_3} & \frac{\Delta k}{2} \end{pmatrix} \begin{pmatrix} \Omega_P \\ \Omega_C^* \end{pmatrix}. \quad (3.18)$$

Notably, all the diagonal atomic contributions vanish, leaving only the wave-vector mismatch Δk to contribute to the evolution of the two optical fields, and constituting the lossless propagation. Indeed, for $\gamma_{12} \ll \Omega$, the residual absorption vanishes. Similarly, the resonant absorption for the conjugate field also vanishes for $\Delta_3 \gg \Omega$.

We can now easily find the two eigen-propagation constants of the effective 2×2 anti-PT Hamiltonian matrix in Eq.(3.18):

$$\lambda_{\pm} = \pm \frac{\Delta k}{2} \sqrt{1 - \left(\frac{gN}{c\Delta_3\Delta k}\right)^2}. \quad (3.19)$$

While in principle, the combination of off-resonant operation and long ground-state coherence lifetime would allow for nearly lossless propagation, it is very hard to achieve such conditions in practice. Indeed, a non-vanishing spin decoherence γ_{12} leads to the appearance of a small imaginary contribution in the first diagonal term of Eq.(3.17), describing the residual absorption coefficient $\alpha \simeq \frac{gN}{c} \frac{2\gamma_{12}}{\Omega^2}$:

$$i\partial_z \begin{pmatrix} \Omega_P \\ \Omega_C^* \end{pmatrix} = \begin{pmatrix} \frac{gN}{c} \frac{2\gamma_{12}}{i\Omega^2} - \frac{\Delta k}{2} & -\frac{gN}{2c\Delta_3} \\ \frac{gN}{2c\Delta_3} & \frac{\Delta k}{2} \end{pmatrix} \begin{pmatrix} \Omega_P \\ \Omega_C^* \end{pmatrix} = \begin{pmatrix} -i\alpha - \frac{\Delta k}{2} & -\frac{gN}{2c\Delta_3} \\ \frac{gN}{2c\Delta_3} & \frac{\Delta k}{2} \end{pmatrix} \begin{pmatrix} \Omega_P \\ \Omega_C^* \end{pmatrix}. \quad (3.20)$$

As this residual absorption term scales with the atomic density N in the same way as the FWM nonlinearity strength, its contribution results in the nonzero real parts of the interaction matrix eigenvalues, which become more pronounced at larger N . At the same time, applying a higher pump laser power may help mitigate this undesirable effect.

The solution to Eq.(3.17) – Eq.(3.20) simply takes exponential form. The overall

solution takes the following form (similar to Eq.(2.21) and Eq.(2.36)) for both λ s,

$$\begin{pmatrix} \Omega(z)_P \\ \Omega(z)_C^* \end{pmatrix} = \begin{pmatrix} A(\lambda) & C(\lambda)^* \\ C(\lambda) & A(\lambda)^* \end{pmatrix} \begin{pmatrix} \Omega(0)_P \\ \Omega(0)_C^* \end{pmatrix}, \quad (3.21)$$

where

$$A(\lambda) = \cos(\lambda L) + i \sin(\lambda L) / \sqrt{1 - \left(\frac{gN}{c\Delta_3\Delta k}\right)^2} \quad (3.22)$$

$$C(\lambda) = -i\beta \sin(\lambda L) / \sqrt{1 - \left(\frac{gN}{c\Delta_3\Delta k}\right)^2}. \quad (3.23)$$

When we seed only the probe channel, the nonlinear gain is defined by $G_P = |A|^2$ and $G_C = |C|^2$ as given by Eq.(2.25). The calculation in this section aligns with our calculations in Sec.2.1 and 2.2. We note that while the presented analysis is highly idealized and involves some rather strong assumptions, it still qualitatively predicts the behavior of the real experimental system, as evident by the reasonable agreement between the analytical predictions of the simplified model, the numerical simulation results, and the experimentally measured parameters presented in Ch.6. The primary value of this analysis lies in its transparency which can be verified for a broader range of parameters using numerical simulations without such approximations.

3.2.2 Experiment Setup

Following previous work (e.g., Refs. [9, 108, 109, 119, 120]), we create the FWM process at the $|5^2S_{1/2}, F=2, 3\rangle \rightarrow |5^2P_{1/2}\rangle$ optical transition of ^{85}Rb using a double- Λ interaction scheme, as shown in Fig.3.2(a). The pump laser (red) with angular frequency ω and Rabi frequency Ω couples the atomic transitions $|1\rangle \rightarrow |3\rangle$ and $|2\rangle \rightarrow |3\rangle$ with respective detuning $\Delta_1 = 0.7$ to 1.5 GHz and $\Delta_2 = \Delta_1 + \Delta_{HF}$, where $\Delta_{HF} = 3035.7$ MHz is the hyperfine splitting of the $|5S_{1/2}\rangle$ ground state. We also define the so-called two-photon detuning $\delta = \Delta_1 - \Delta_2$. The two output modes, conjugate ($\omega_s, \hat{a}_s^\dagger$) and probe (ω_P, \hat{a}_P), are assumed to only couple to the $|3\rangle \rightarrow |2\rangle$ and $|3\rangle \rightarrow |1\rangle$ transitions, respectively. Under the

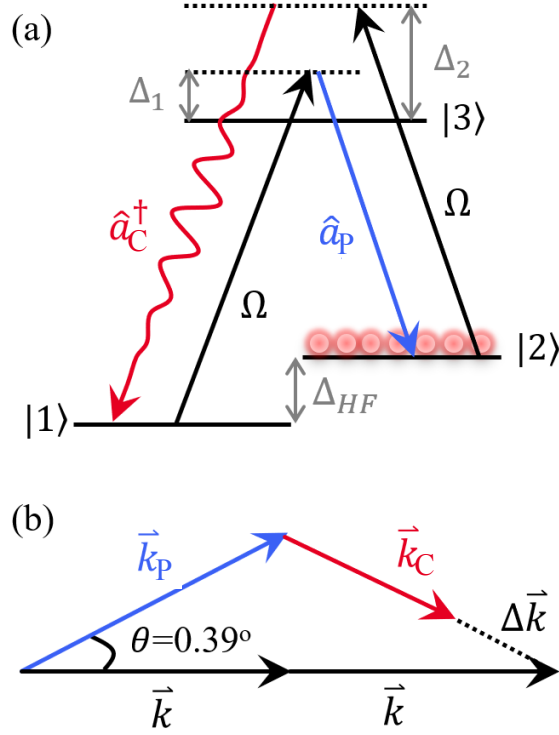


Figure 3.2: (a) Double- Λ atomic scheme used for describing the FWM process at the D₁ transition of ^{85}Rb . The strong pump laser is detuned by $\Delta_1 = 0.7$ GHz and $\Delta_2 = 3.7$ GHz from the $|5^2S_{1/2}F = 2\rangle \rightarrow |5^2P_{1/2}\rangle$ and the $|5^2S_{1/2}F = 3\rangle \rightarrow |5^2P_{1/2}\rangle$ optical transitions, respectively. And $\Delta_{HF} = 3035.7$ MHz is the ground-state hyperfine splitting. (b) Geometrical arrangement of the optical fields in the FWM process with the momentum mismatch $\Delta\vec{k} = 2\vec{k} - \vec{k}_P - \vec{k}_C$.

two-photon resonance condition, they obey the energy conservation $2\omega = \omega_P + \omega_C$. The full schematic is shown in Fig.3.3.

Our pump laser source, depicted as blue region in Fig.3.3, is a TOPTICA TApr system with a built-in laser diode and tapered amplifier. The coarse tuning allows us to probe wavelength range from 775 to 805nm, covering both the D1 and D2 transitions of Rb. This system has two output ports with the main output port factory coupled to a fiberDock coupler. Typically, we achieve a coupling efficiency of over 40%, and the power can reach up to 400 mW after the fiber. We use this channel as our strong pump beam to create coherence. The beam diameter for the pump beam is ≈ 0.5 mm.

The diode pick-off port, with a power of ≤ 0.5 mW, is used for both wavelength mon-

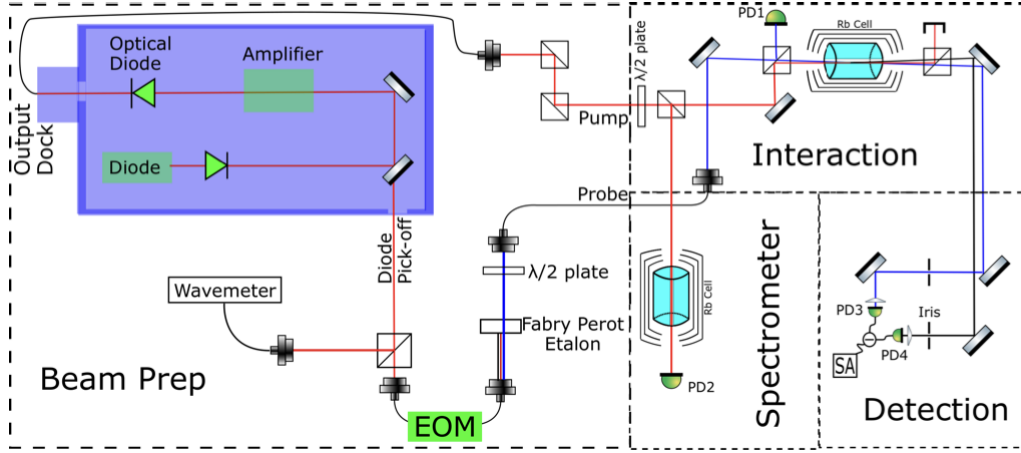


Figure 3.3: Full experimental setup diagram for double- Λ FWM generation

itoring using a wavemeter and weak seed field generation. We send the signal through an electrooptical phase modulator (EOM) powered by a Marconi Instruments 2031 RF source generator. The RF generator is tuned to ≈ 1517.5 MHz with ≈ -1.5 dB modulation power, which is then frequency-doubled to reach 3035 MHz, corresponding to a two-photon detuning $\delta = 0.7$ MHz. The EOM output is directed at a tunable Fabry-Perot etalon to isolate the first order modulation sideband. The beam is then coupled into a single mode fiber to clean the transverse spatial distribution. The output, with power usually ranging from $40 \mu\text{W}$ to $90 \mu\text{W}$ and a beamsize of ≈ 0.3 mm, is used as our seed field. This setup allows us to access both transitions easily with single laser device, enabling the creation of a double- Λ system, as discussed later in Ch.6.

Next, we focus on the nonlinear amplification aspect. In our experiment, we exclusively work with ^{85}Rb . We utilize an AR-coated (with over 98% transmission for D1/D2 lasers) 1.9 cm long pyrex cell. The cell is positioned within a three-layer μ -metal shielding to eliminate any influence from the background magnetic field, with thermal isolation material interposed between the layers. The cell temperature is typically maintained between 105°C and 110°C using a temperature controller; this temperature range is optimized for achieving the best squeezing, which can vary depending on other parameters, particularly laser detuning. A strong pump beam and a weak probe beam, both tuned to have perpen-

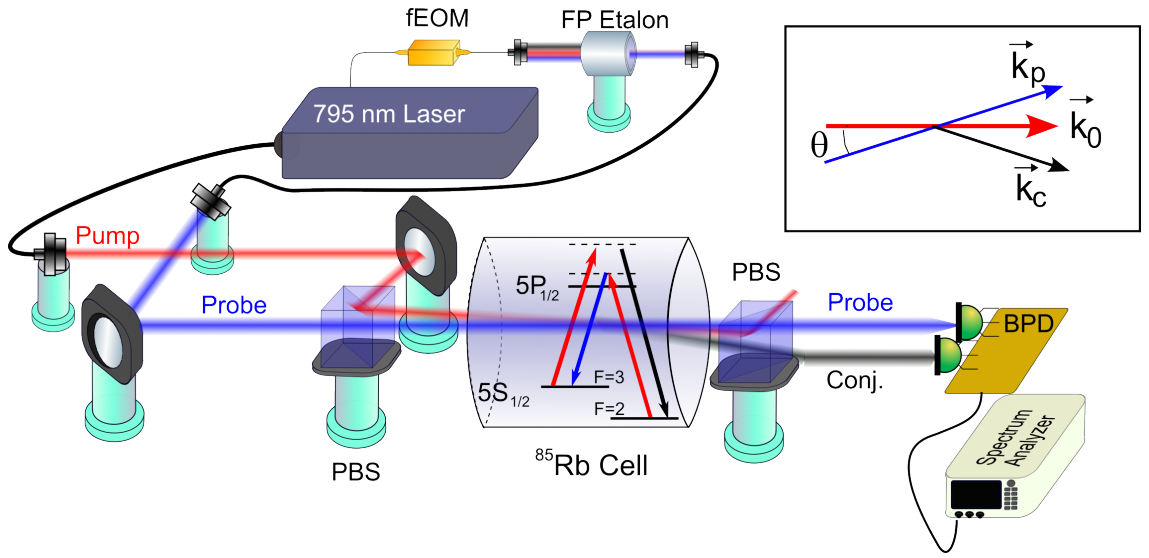


Figure 3.4: Close-up setup diagram for the double- Λ system.

dicular linear polarizations, are overlapped within a small angular range of 0.23° to 0.4° . The nonlinear interaction consequently generates a third beam, commonly referred to as the conjugate or Stokes field in the literature, while the input probe is amplified. The polarization of the conjugate field, which is aligned with the probe field and perpendicular to the pump, is filtered out using a beamsplitter.

The generated conjugate and probe fields are then directed onto a Balanced Photon Detector (BPD). Our BPD design incorporates a pair of Hamamatsu S3883 photodiodes, which have a standard quantum efficiency exceeding 92% at the Rb D1/D2 frequencies. A pair of $f=25.4\text{mm}$ AR-coated lenses is employed to focus the optical fields onto the photodiodes. The resulting photocurrents are electronically subtracted and amplified, with the differential voltage monitored in real-time on an oscilloscope. Additionally, a separate AC channel—with the DC component removed electronically—feeds into a HP8596E spectrum analyzer for intensity noise measurements.

3.2.3 Additional Considerations

In this section, we summarize a series of frequently asked questions and encounter problems during the squeezer setup and adjustment process.

How can you get away without laser lock?

In the double- Λ experiment, we do not use any laser locking. The TOPTICA TA pro laser exhibits a frequency drift of ≤ 100 MHz, which is negligible compared to the one-photon detuning Δ_{1P} and the etalon transmission linewidth. Consequently, the inherent stability of the laser is sufficient for our purposes. Similarly, no phase lock is employed because the pump laser's linewidth (≤ 100 kHz over a 100 μ s period) is much narrower than our gain bandwidth, which spans hundreds of MHz. Eliminating both frequency and phase locks significantly simplifies the system, making long-term stabilization easier.

How does Doppler effect influence the results?

The Doppler effect has a minimal impact on FWM for two primary reasons. First, the one-photon detuning is substantially large (on the order of GHz) compared to the Doppler frequency shift. Consequently, the negative impact of Doppler effect is significantly mitigated. Second, an all-propagation configuration is used with all lasers tuned close to the Rb D1 line. The Doppler shift is similar in magnitude and identical in sign, resulting in significant cancellation. The situation is markedly different in the double-Ladder configuration.

How do we choose the isotope and cell length, and what is the impact of buffer gas?

In all our experiment we use a 1-inch (1.9cm effective length) pure ^{85}Rb cell. However, both ^{87}Rb and ^{85}Rb isotope have been explored in literature with squeezing observed [56, 125], with similar phase matching angles. In case that the coupling field detuning is much larger than the hyperfine splitting (which is exactly the double- Λ case), we can essentially consider all hyperfine levels as one level [126], which from another perspective shows that both isotopes will work similarly.

The selection of cell length is application-dependent, balancing linear and nonlinear optical losses (arising from residual absorption, higher-order Raman absorption, etc.) with gain (from FWM and potential higher-order processes). Notably, the best squeezing results to date have been achieved using a 1.2-cm cell [56]. Generally, when FWM gain is sufficiently high, a shorter cell offers advantages for squeezing generation.

Furthermore, buffer gas is rarely employed in FWM experiments. While buffer gases can enhance spin coherence time and the transverse time of atoms—critical in magnetometer experiments—FWM primarily relies on ground–excited level coherence. The use of buffer gas, therefore, tends to reduce this critical coherence, so most FWM experiments do not incorporate a buffer gas. Additionally, anti-relaxation coated cells, which are often associated with buffer gases, have a lower temperature damage threshold. Since many FWM experiments require heating the cell to between 100°C and 120°C, the use of this cell type is impractical.

How do we choose the right beamsize?

As mathematically demonstrated in Ch.2, the gain is determined by both the pump intensity and the propagation distance. Therefore, the beam size is carefully chosen based on the specific vapor cell so that the probe and pump beams are fully overlapped along the entire cell length. Additionally, to achieve optimal spatial overlap, the beam overlap must occur within the Rayleigh lengths of both the pump and probe beams. Once this condition is met, the smallest practical beam size is used. For the double- Λ case, we deliberately choose different focus for pump and probe such that there is a point after cell the pump is focused and separated spatially from all signal fields, allowing better pump beam filtering. This is a consideration solely for the double- Λ case as the phase matching angle is small (therefore the spatial separation between signal and residual pump). In the case of double-ladder scheme we discuss in next section, pump filtering can be easily done given long enough propagation distance as a result of large angles.

Furthermore, the spatial modes of the probe seed and pump are cleaned by coupling it through an optical fiber, as depicted in Fig.3.3. To minimize additional spatial distortions

and losses, it is advisable to use as few lenses as possible when adjusting the beam size. Ideally, any necessary focusing of the pump or probe should be accomplished with a single, long-focal-length lens that operates within its Rayleigh length.

How Do we setup/tune the Fabry-Parot Etalon?

The quality of the amplified beam—its spatial mode, frequency, and other attributes—is largely determined by the stability of the seed laser. Therefore, it is crucial to maintain its stability by carefully tuning the etalon to prevent both long-term and short-term drifts in frequency and intensity. To achieve this, we use a Fabry-Parot etalon that is temperature-stabilized by a Thorlab TED 200C temperature controller. Thermal conductive paste is applied between the etalon crystal and the temperature sensor/heater, and the crystal is housed within a thermal isolation tube to minimize the effects of external temperature fluctuations. The etalon can be adjusted either by fine-tuning its temperature or by modifying the injection angle of the input beam.

The tuning procedure is following: we first turn on the frequency sweeping of the laser, and we observe the transmission peak as shown in Fig.3.5,

As we adjust the etalon angle, the transmission peak—monitored on an oscilloscope (see Fig.3.5)—shifts in one direction (either left or right) along with changes in transmission intensity and linewidth. The optimal tuning point is reached when the shift reverses direction; for instance, if tuning angle (in one direction) initially moves the transmission peak in Fig.3.5 to the left, eventually the peak will shift direction and move to the right. The shift point signifies the sweet point, exhibiting both the highest transmission and the narrowest linewidth.

Parameter tuning: How to tune the phase matching angle, one/two photon detuning?

Related to the phase matching angle and coupling field frequencies, the Δk term, Δ_1 and δ are the major factors influencing gain and squeezing. The Δk term also affects significantly the beamoverlap and coupling into the BPD detector, as the generated field may be redirected slightly. Therefore, the optimization involves finding the best combination

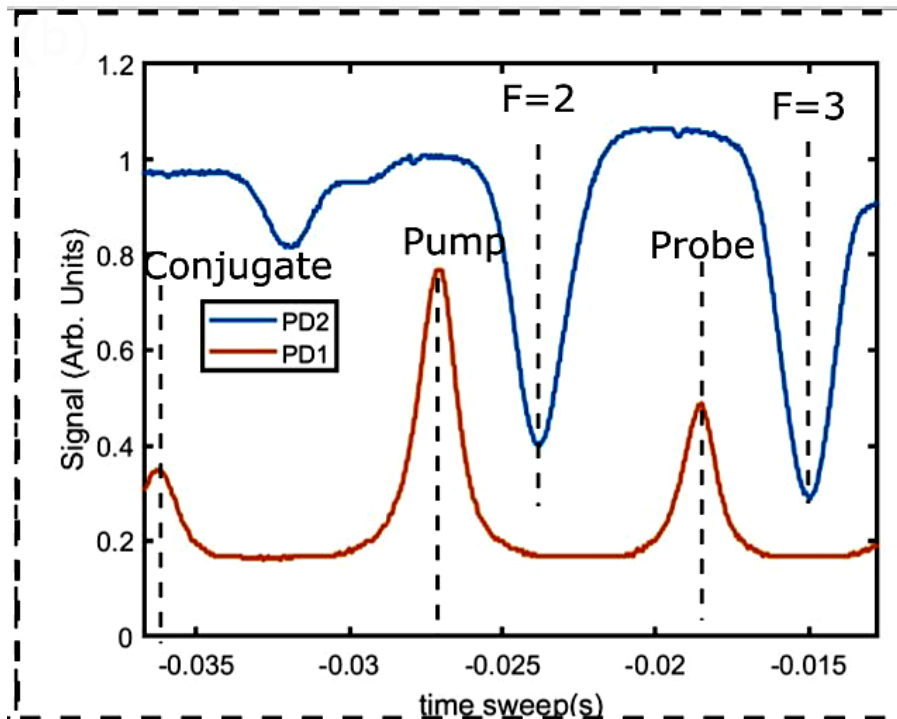


Figure 3.5: Oscilloscope image. The blue trace is the photodiode monitoring of laser frequency using another photodiode. The orange trace is the Etalon transmission spectra, showing the main peak, and the first order modulation peak representing pump, probe, and conjugate.

of several interrelated parameters.

Fortunately, previous literature [13, 127] has identified a favorable parameter space. A good starting point is: $\delta \approx 2$ MHz, $\Delta_1 \approx 1.5$ GHz, and $\theta = 0.3^\circ$ to 0.4° if using the Rb D1 line, with $P_{pump} = 200$ mW to 400 mW. Within this parameter space, achieving a sufficiently high FWM gain is relatively straightforward.

Once sufficient nonlinear gain is achieved, the first objective is to establish two-mode correlation. In practice, this is verified by observing that the differential noise, as measured by a spectrum analyzer, is lower than the noise of either the conjugate or probe beam individually. After confirming this correlation, we implement a step-by-step tuning procedure to optimize the two-mode intensity squeezing.

- Lock the detunings, Δ_1 and δ , by parking the laser and fixing the modulation

frequency.

- Ensure the probe seed field direction is fixed. Since the probe serves as our reference, it must be set up with the highest care.
- Carefully tune the pump laser direction using a pair of mirrors. Avoid using just one mirror for initial adjustments when squeezing is minimal, as this may detrimentally affect beam overlap. Once near the optimal squeezing point, fine adjustments with a single mirror are acceptable.
- Gently adjust the coupling into the photodiode by lightly pressing the coupling mirror in front of the photodiode. It is generally preferable to start with the conjugate channel, given that the probe direction is already established as a reference. This fine tuning should be performed extremely gently and can be bypassed during coarse adjustments.

The procedure described above should be repeated for various combinations of Δ_1 and δ until both optimal gain and squeezing are achieved. Notably, our observations indicate that the settings yielding the highest FWM gain do not necessarily lead to the best squeezing. As a result, a practical tip for squeezing optimization is to first identify the point of maximum gain, and then deliberately adjust the parameters away from that optimum to achieve improved squeezing performance.

3.2.4 Technical Noises and System Debugging

Even after implementing standard tuning procedures, intensity squeezing is sometimes not observed, typically due to excessive noise. In this section, we examine, from an operational perspective, the various noise sources in the experiment and outline the measures we take to mitigate them. Broadly, these noise sources fall into three categories:

- Optical loss

- Extra parasitic photons
- Classical noise and detector dark noise

1. Optical loss

Any optical loss introduces unwanted photons with super-Poissonian statistics that can quickly eliminate the observed squeezing. To minimize optical noise, it is essential to select a sufficiently high Δ_1 and an appropriate δ ; this can be verified by monitoring G_P and G_C immediately after the vapor cell. Assuming conjugate transmission $T_C = 100\%$, the probe transmission is given by

$$T_P = \frac{G_P}{G_C + 1}.$$

In the double- Λ regime, T_P typically reaches 95% or above. If T_P falls below 90%, this may indicate that either Δ_1 is set too low (leading to increased linear loss) or δ is insufficient (potentially triggering a two-photon transition), or there is clipping or scattering within the vapor cell. The latter issues often arise from using a cell with no or a damaged AR coating, or from improper cell positioning. Therefore, for these experiments, it is highly recommended to use a vapor cell with a proper AR coating. It is worth verifying with an IR viewer that no unwanted scattering/clipping occurs, since such scattering, on top of loss, may also introduce parasitic photons—a concern that will be addressed in the following section.

2. Extra parasitic photons

In the double- Λ configuration, parasitic photons arise predominantly from residual pump leakage. Although an after-cell PBS (as shown in Fig.3.4) removes most of it, some unwanted photons may still persist due to a combination of small phase-matching angles and large pump beam sizes (see the beam size selection section). Additionally, scattering within the vapor cell can lead to stray light that further contaminates the signal. To assess pump leakage, we monitor the noise level with the pump field active and the probe seed blocked. If the filtering is effective, the noise should be nearly at the dark noise level. If not, a series of irises positioned along the probe and conjugate beam paths can

be employed to reduce the leakage. These irises must be adjusted carefully to minimize the total differential noise without excessively clipping the signal field, as doing so would compromise the squeezing.

Less common sources of parasitic photons include those generated by higher-order wave mixing processes, such as 6WM or 8WM. While these effects are typically minor when the experimental setup is optimized according to the guidelines, they can still detract from the squeezing level, particularly if scattered light is recoupled into the interaction region. It is also possible, although uncommon, to observe reduced squeezing or excessive noise when multiple competing FWM channels co-exist.

3. Classical Laser noise

Lastly, we address classical laser noise and dark noise in our system. Despite considerable advancements in laser technology, practical lasers are not perfect: fluctuations in temperature and power introduce excess intensity noise beyond that of an ideal coherent state, even when operating well above lasing threshold. In addition, while phase noise is generally less detrimental, it can be converted into intensity noise if η_p is frequency dependent. For this reason, it is important to independently verify the noise level of the probe seed, as any noise present can propagate through the system. In our experiments, the probe seed typically shows noise levels ranging from 0.0 dBm to 0.6 dBm above SNL when it is far detuned.

In the double- Λ configuration, the probe seed is extremely weak (on the order of μW) and is amplified by a high gain, which minimizes the impact of residual classical noise. Furthermore, a sufficiently large Δ_1 helps suppress the conversion of phase noise into intensity noise. In contrast, the noise management strategies for the double-ladder configuration are considerably more challenging.

4. Detector Dark Noise

The dark noise level, determined by the electronics, also the accuracy of squeezing measurements; however, we will not elaborate on the board design in this thesis. Additionally, $1/f$ noise results in elevated noise levels at low frequencies, and other electronic

noise sources can produce extra peaks at specific frequencies, often due to design limitations or malfunctions. Therefore, it is advisable to perform a wide-frequency sweep on a spectrum analyzer to identify regions with minimal noise. For example, Fig.3.6 shows a frequency band where both $1/f$ noise and other dark noise contributions are minimal. Since the electronics' dark noise is independent of and invariant with respect to the other experimental parameters, its measured power is subtracted from the squeezing signal.

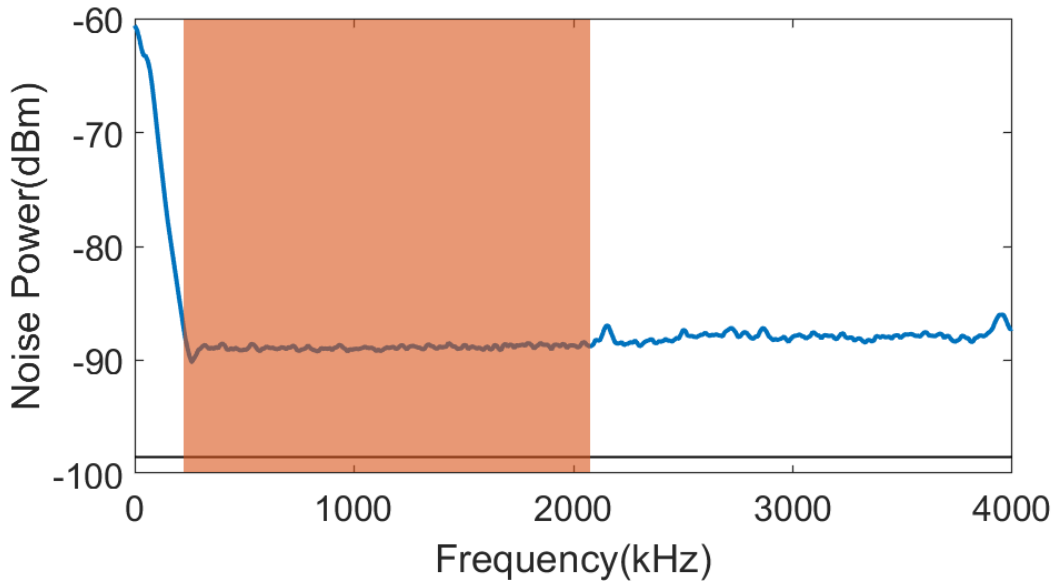


Figure 3.6: A sample dark calibration for dark noise, with the spectrum analyzer detection range from 0 to 4MHz. The good detection region is shaded. To the left of the shade area the noise is dominated by $1/f$ noise. To the right of the shaded area a noise peak is observed for an unknown reason.

How do we calibrate the shot noise and perform dark noise subtraction

All squeezing measurements are referenced to the shot noise level. However, because measuring shot noise repeatedly is both cumbersome and time-consuming, we perform a calibration that allows us to compute the shot noise level for a given power.

Fig.3.7 illustrates the shot noise measurement setup, which essentially replicates the configuration used for squeezing measurements in Fig.3.3. In this setup, the pump (or probe, when sufficient power is available) is split equally into two paths. According to the

derived equations, the differential noise

$$\text{Var}(n_a - n_b) = \langle n_a \rangle + \langle n_b \rangle,$$

scales linearly with the mean photon numbers $\langle n_a \rangle$ and $\langle n_b \rangle$. By ensuring that $\langle n_a \rangle = \langle n_b \rangle = \langle n \rangle$ during calibration, any classical noise contribution is canceled out, thereby allowing for an accurate determination of the shot noise level.

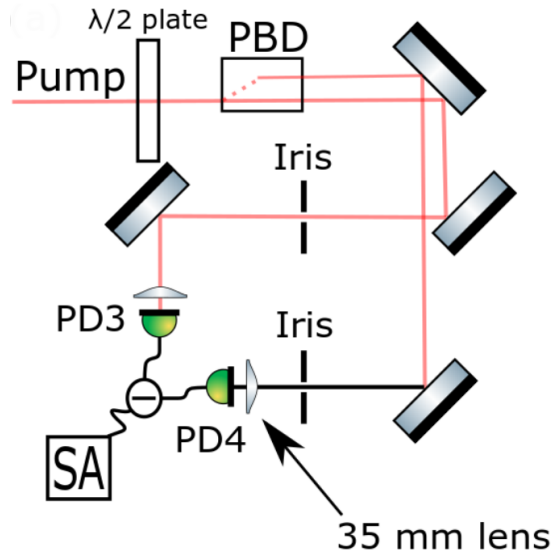


Figure 3.7: SNL calibration setup. This is the same setup used for squeezing measurement to ensure fair comparison, but with two laser inputs of equal power. The overall classical noise is subtracted out.

Fig.3.8 presents a sample shot noise calibration along with its linear fit. In this calibration, the noise power—which reflects the coherent-state variance—and the photovoltage, which is proportional to the photon number, display a clear linear relationship. This linear fit is incorporated into our analysis software to compute the shot noise level corresponding to various photovoltage readings. Importantly, the observed linearity also serves as a critical check on the calibration process and is commonly used to validate the coherence of an optical field. For instance, a quadratic dependence of photovoltage may appear when a near-resonance optical field propagates through an atomic medium due to phase-noise

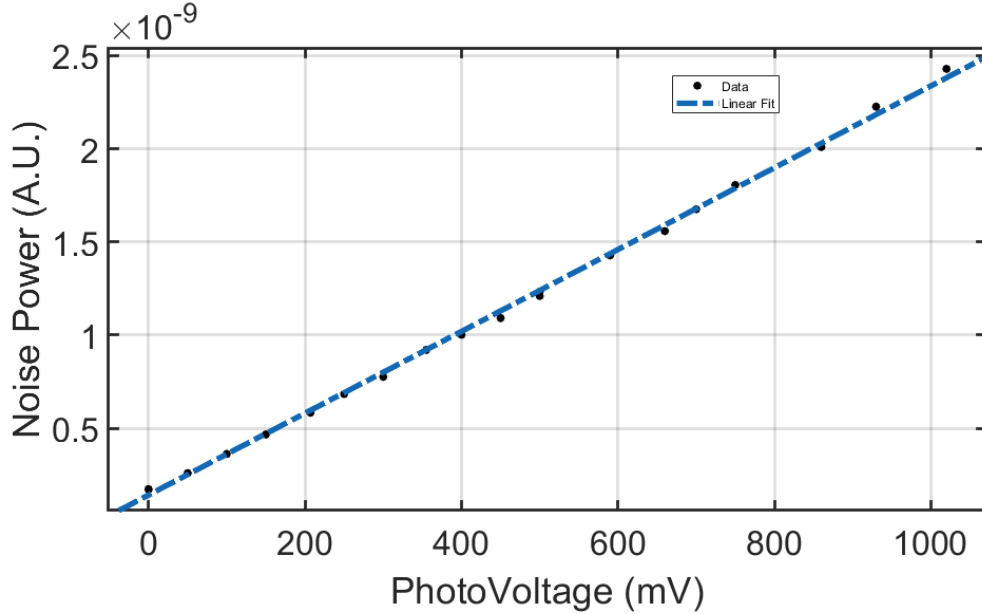


Figure 3.8: Shot noise data and its functional fit. This fit reveals that the noise power (which represents the optical field variance) scales linearly with the photonvoltage (proportional to the optical power/photon flux). This linear relationship is crucial for calibrating the shot noise level and serves as a diagnostic tool to verify whether a laser field displays super-Poissonian statistics due to extra noise sources contaminating the measurement. The noise power reduced to the measured dark noise line instead of 0.

conversion as well as atomic noise near resonance.

3.3 FWM in Double-Ladder Configuration

3.3.1 Density Matrix Calculation and Numerical Simulation

In this section, we analyze another widely used system, the double-ladder, or "Diamond" configuration. A schematic diagram is shown in Fig.3.9. Two strong pump fields, Ω_{IR} and Ω_{D2} , couple $|1\rangle \rightarrow |3\rangle$ and $|3\rangle \rightarrow |4\rangle$ respectively. Meanwhile, a weak probe field is coupled to the transition $|1\rangle \rightarrow |2\rangle$, leading to the generation of the conjugate field Ω_C .

Following the treatment as in Ref [128], we can formulate the Hamiltonian, and use Eq.(3.7) to write down the Bloch equations. By appropriately choosing a rotating reference frame, we simplify the atomic dynamics by treating the Rabi frequencies of the probe, D_2

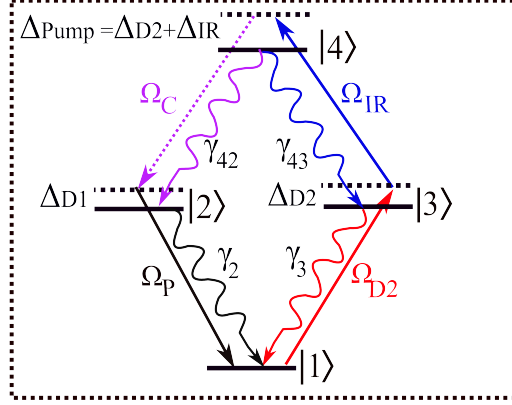


Figure 3.9: Simplified double-ladder atomic configuration of ^{85}Rb employed in the experiment. The D2 pump (Ω_{D2} , red) and IR pump (Ω_{IR} , blue) are linearly polarized in the same direction and intersect inside the vapor cell with an orthogonally-polarized probe beam (Ω_P , black). The conjugate field (Ω_C , purple) is generated with the same polarization as the probe.

pump, and IR pump as real, except for the conjugate Rabi frequency, which carries an accumulated phase $\Phi = \Delta\omega t - \Delta kz + \Delta\phi_{ini}$. The definition is the same as in the previous section, is given by Eq.(2.17).

$$\begin{aligned}
 \text{Set 1} \left\{ \begin{aligned}
 \dot{\rho}_{11} &= i\frac{\Omega_{D2}}{2}(\rho_{13} - \rho_{31}) + \gamma_2\rho_{22} + \gamma_3\rho_{33}, \\
 \dot{\rho}_{22} &= \gamma_{42}\rho_{44} - \gamma_2\rho_{22}, \\
 \dot{\rho}_{33} &= -i\frac{\Omega_{D2}}{2}(\rho_{13} - \rho_{31}) + i\frac{\Omega_{IR}}{2}(e^{i\Phi}\rho_{34} - e^{-i\Phi}\rho_{43}) + \gamma_{43}\rho_{44} - \gamma_3\rho_{33}, \\
 \dot{\rho}_{44} &= 1 - \rho_{11} - \rho_{22} - \rho_{33} - \rho_{44}, \\
 \dot{\rho}_{13} &= \Gamma_{13}\rho_{13} - i\frac{\Omega_{D2}}{2}(\rho_{33} - \rho_{11}) - i\frac{\Omega_{IR}}{2}e^{i\Phi}\rho_{14}, \\
 \dot{\rho}_{34} &= \Gamma_{34}\rho_{34} - i\frac{\Omega_{IR}}{2}e^{-i\Phi}(\rho_{44} - \rho_{33}) - i\frac{\Omega_{D2}}{2}\rho_{14}, \\
 \dot{\rho}_{14} &= \Gamma_{14}\rho_{14} - i\frac{\Omega_{D2}}{2}\rho_{34} + i\frac{\Omega_{IR}}{2}e^{-i\Phi}\rho_{13},
 \end{aligned} \right. \tag{3.24}
 \end{aligned}$$

$$\begin{aligned}
 \text{Set 2} \left\{ \begin{aligned}
 \dot{\rho}_{12} &= \Gamma_{12}\rho_{12} - i\frac{\Omega_P}{2}(\rho_{22} - \rho_{11}) - i\frac{\Omega_{D2}}{2}\rho_{32} - i\frac{\Omega_C^*}{2}\rho_{14}, \\
 \dot{\rho}_{24} &= \Gamma_{24}\rho_{24} - i\frac{\Omega_C}{2}(\rho_{44} - \rho_{22}) - i\frac{\Omega_P}{2}\rho_{14} - i\frac{\Omega_{IR}}{2}e^{-i\Phi}\rho_{23}, \\
 \dot{\rho}_{23} &= \Gamma_{23}\rho_{23} - i\frac{\Omega_P}{2}\rho_{13} - i\frac{\Omega_C}{2}\rho_{43} + i\frac{\Omega_{D2}}{2}\rho_{21} + i\frac{\Omega_{IR}}{2}e^{-i\Phi}\rho_{24}.
 \end{aligned} \right.
 \end{aligned}$$

Here, $\{\gamma_2, \gamma_3, \gamma_4 = \gamma_{43} + \gamma_{42}\}$ are the decay rates of the states $\{|2\rangle, |3\rangle, |4\rangle\}$. $\Gamma_{ij} = i(\Delta_j - \Delta_i) - (\gamma_i + \gamma_j)/2$ is the complex frequency detuning of the $|i\rangle \rightarrow |j\rangle$ transition with $\{\Delta_{1,2,3,4} = 0, \Delta_{D_1}, \Delta_{D_2}, \Delta_{\text{IR}}\}$. An analytical expression for ρ_{12} and ρ_{42} can be obtained, but the exact form is too complex to present in full. In our case, since all frequency detuning and pump field Rabi frequency terms are comparable, further simplification is not justified. Insights into the system's dynamics can be gained by examining the steady-state solutions for ρ_{12} and ρ_{42} , expressed in terms of other atomic coherence terms. In the same manner as we derived Eq. (3.15) and Eq.(3.16), we have,

$$\begin{aligned}
i\partial_z \begin{pmatrix} \Omega_P(z) \\ \Omega_C^*(z) \end{pmatrix} &= \begin{pmatrix} \frac{(i\gamma_2 - 2\Delta_2)\rho_{14}}{4\Delta_2^2 + \gamma_2^2} & \frac{(i\gamma_2 - 2\Delta_2)(\rho_{11} - \rho_{22})}{4\Delta_2^2 + \gamma_2^2} \\ \frac{\rho_{22} - \rho_{44}}{2\Delta_4 - 2\Delta_2 + i\gamma_2 + i\gamma_4} & \frac{-i\rho_{41}}{2\Delta_4 - 2\Delta_2 + i\gamma_2 + i\gamma_4} \end{pmatrix} \begin{pmatrix} \Omega_P(0) \\ \Omega_C^*(0) \end{pmatrix} + \begin{pmatrix} -\frac{(i\gamma_2 - 2\Delta_2)\Omega_{D_2}\rho_{32}}{4\Delta_2^2 + \gamma_2^2} \\ \frac{i\Omega_{\text{IR}}\rho_{32}}{2\Delta_4 - 2\Delta_2 + i\gamma_2 + i\gamma_4} \end{pmatrix} \\
&\equiv \begin{pmatrix} A & B \\ C & D \end{pmatrix} \begin{pmatrix} \Omega_P(0) \\ \Omega_C^*(0) \end{pmatrix}. \tag{3.25}
\end{aligned}$$

The complex matrix elements A , B , C and D are determined by the parameters of the system. In the context of a double- Λ atomic configuration and under the thin-medium approximation, both A and D approach zero, effectively resulting in an anti-parity-time symmetric matrix [103]. In our specific case, however, the condition $A \gg D$ holds, as the linear absorption and dispersion associated with A within the Doppler range are significantly larger than those associated with D . Furthermore, it is evident that the linear absorption terms are governed by population differences, which can vary substantially. The off-diagonal terms responsible for the nonlinear gain explicitly depend on ρ_{14} , the atomic coherence between the ground and excited states. Both absorption and amplification processes are influenced by the density matrix element ρ_{32} , which represents the atomic coherence between the two intermediate states. This term reflects competing processes that either contribute to or undermine the linear gain, particularly over a broader frequency range and at lower amplification efficiency. In contrast, ρ_{14} typically exhibits a narrower width with much higher peak amplification [129]. For the intensity squeezing

studied here, a narrower width with higher gain is generally preferred, highlighting the importance of enhancing ρ_{14} coherence. The steady-state solution for ρ_{14} is expressed as $\rho_{14} = i(\Omega_{D_2}\rho_{34} - \Omega_{IR}e^{-i\Phi}\rho_{13})/\Gamma_{14}$. This coherence is directly tied to Ω_{D_2} and Ω_{IR} , the two pump fields, emphasizing the importance of strong pump intensities. Similarly, ρ_{32} , assuming weak Ω_P and Ω_C , can be expressed in a comparable form, albeit with different decay rates Γ_{ij} . As the IR pump frequency is tuned, a transition is observed from a regime where ρ_{14} dominates at small detuning to one where ρ_{32} dominates at larger detuning.

3.3.2 Experiment Description

In this section we are giving a brief outline of the experimental method and setup. A simplified schematic of our experimental arrangements is shown in Fig. 3.10. For these experiments, we use ^{85}Rb atomic vapor as nonlinear medium. To facilitate the FWM process in a double-ladder interaction system, we use the following energy levels: $|5S_{1/2}\rangle$, $|5D_{1/2}\rangle$, $|5D_{3/2}\rangle$, and $|6S_{1/2}\rangle$ states. Two intense pump fields couple the ground state $5S_{1/2}$ and the highly excited state $6S_{1/2}$: the first laser, (referred in the text as ‘‘D2 pump’’, wavelength: 780nm, $P_{max} = 320$ mW) is tuned near the $|5S_{1/2}F = 3\rangle \rightarrow |5D_{3/2}\rangle$ transition, and the second laser (referred in the text as ‘‘IR pump’’, wavelength: 1367nm, $P_{max} = 35$ mW) is tuned to the $|5D_{3/2}\rangle \rightarrow |6S_{1/2}\rangle$ transition. The D2 pump field is generated by a Vitawave ECDL laser or by a TOPTICA DLCpro system and amplified using the TOPTICA BoosTApro system, which provides the total output up to 370 mW of power. The 1367 nm pump field is generated by a Toptica DLCpro system, providing up to 35mW power at the cell.

In this arrangement of the ladder system, the correlated optical fields are generated at the other lbranch, involving $|5P_{1/2}\rangle$ intermediate stage. In our experiments, we seed the lower transition $|5S_{1/2}F = 3\rangle \rightarrow |5P_{1/2}\rangle$ with a weak probe laser field (wavelength: 795nm, $P_{max} = 2$ mW). This field is generated by either a New Focus Vortex 6000 laser or a TOPTICA DLCpro. The D1 795nm field undergoes amplification at the output, simultaneously producing a conjugate field at 1324 nm. In this experiment all optical

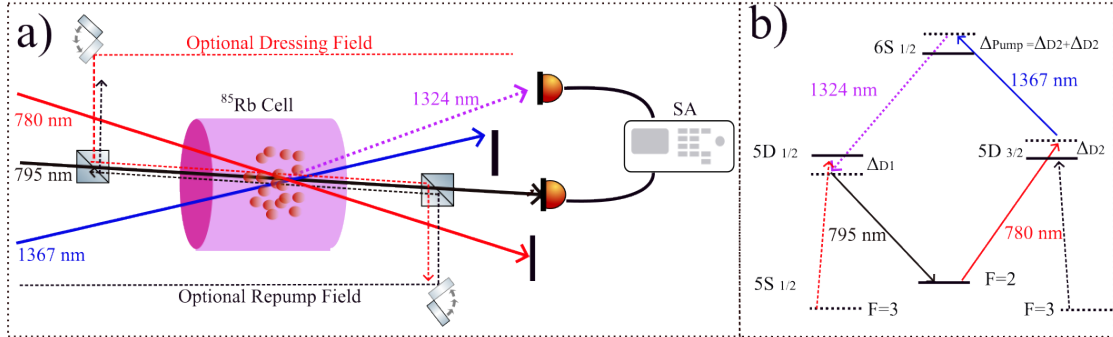


Figure 3.10: a) Simplified experimental setup. Non optional input fields are shown as solid lines. Blue: 1367nm pump field. Red:780 nm (D2) pump field. Black: 795 nm (D1) probe field. The generated 1324 nm conjugate field is displayed as purple dotted line. Two optional coupling fields can be coupled into the system to manipulate the atomic populations or activate the higher order wave mixing. The repump field (shown as black dashed line) is counter-propagating with the D1 seed, while the dressing field is coupled. Blue dot: 780 Repump. b) Atomic level diagram

fields are linearly polarized: the two pumps are vertical polarized, while the probe field, as well as the generated conjugate field are horizontally polarized. The exact frequencies of all lasers are monitored using either a saturation spectroscopy reference cell for the probe and D2 pump lasers, or using a Bristol 621 wavemeter (with precision up to 10^{-4} nm) for the 1367nm pump laser.

The laser beams intersect within the Rb vapor cell at nonzero angles, as shown in Fig.3.10(a). Note that the phase matching angles in this system are larger than those in the double- Λ configuration (0.2 to 0.4°). The required phase-matching angles are even larger if a counter-propagating configuration is chosen, which are default in most ladder-type schemes [130]. Here, we choose to work with all copropagating beams to minimize these angles and increase the beam overlap. Beam focusing also requires careful optimization—tight enough to achieve sufficient intensity, while wide enough to ensure an extended interaction length. The beams shall be adjusted to be nearly collimated over the interaction zone to reduce the spread of k vectors.

We focus the D1 field with a single lens to ensure best beam quality, whereas the D2 field is collimated using a two-lens system ($f = 500\text{mm}/150\text{mm}$ pair, $d \approx 0.6$ mm). The

1367 nm pump is focused with two cylindrical lenses, with $f = 1000$ mm in the horizontal direction ($d_{hor} \approx 0.34$ mm) and $f = 500$ mm in the vertical direction. To maximize the overlap, we maintain relatively large beam sizes for the IR and D2 fields, while the D1 seed beam is comparable or smaller focused (with $f = 400$ mm single lens, $d \approx 0.28$ mm). All beams have a Rayleigh length over 1 inch to guarantee good phase-matching.

After the Rb cell the intensities of the amplified probe and generated conjugate beams are monitored using Hamamatsu S3883 and EXT500 photodiodes, respectively. These photodiodes have quantum efficiency exceeding 95% for Rb D1 line and 85% for 1367 nm, respectively. The responsivity of S3883 is very low in the IR range, and the same for EXT500 at the D1 line. Combined with the large phase-matching angle, this allows for effective pump leakage filtering. We quantify the interaction strength using the generation efficiency (G , or gain), defined as the ratio between the amplified output probe power and input probe seed power: $G_P = P_{795\text{nm, output}}/P_{795\text{nm, seed input}}$. The conjugate gain is defined similarly, $G_C = P_C/P_{795\text{nm, seed input}}$. In an ideal lossless case, we have relation $G_C - G_P = 1$. However, in our experiment, the D1 field suffers strong linear absorption due to near-resonant operation at very high temperature (100 to 115 °C), where the absorption peak is broadened even more. In contrast, the conjugate field is assumed to be loss less, as it corresponds to an upper transition from an intermediate state with small population. We measure the probe transmission (T_P) with either the D2 or IR pump turned off as to estimate probe field optical loss. The actual loss at the gain point could be different due to population difference as well as field intensity difference.

3.3.3 Experiment Setup How-to Guide

In this section we give a comprehensive, step by step guide for setting up the experiment described above. It serves as a tutorial for readers who are interested in reproducing the results presented in this thesis.

A major difficulty in the current experiment is optimizing a large parameter space. The inclusion of three lasers instead of two, as in the double- Λ case, exponentially increases

the complexity of optimization and tuning. We present in this work a set of optimized parameters and should serve as decent starting point.

Tunning the phase matching angle

It is generally easier to start with angular optimization and aligning the beam into photodiode. The geometry, once optimized, is only subject to minor adjustments. By using parameters detailed in previous section, one should be able to achieve some level of FWM signal. After obtaining initial FWM gain, the gain peak is optimized by fixing the probe seed direction along with tunning the other two fields. We usually use the conjugate channel as a metric for gain optimization; however it is advantageous during the tunning stage to monitor both the probe and conjugate channels. Before gain is fully optimized, the probe channel is often subject to strong self-focusing effect, which sometimes affects the beam alignment into the diode. Besides, the gain peak may be significantly attenuated by strong residual absorption, making it difficult to detect during initial alignment. The conjugate field direction usually won't shift too much to impact the photonvoltage, but it is safe to always check the beam alignment into the photodiode after few adjustments.

The general procedure of tunning the two pump fields directions alternatively:

- Adjust 1367 nm pump angle with mirror pair
- Adjust 780 nm pump angle with mirror pair to maximize the gain. It is easier to perform this type of task with both pump field locked while sweeping the probe seed field thus we can not only clearly observe the gain amplitude but also the line shape as well as transmission. From experience, the $G_{P/C}$ peaks can develop significant imbalance for certain frequency, which we wish to avoid for squeezing purpose. We perform usually the angular optimization to get the highest gain before move to the next stage.

Squeezing optimization

In this section, we discuss the process for squeezing optimization. The following procedure is usually followed:

- Parking D1 and IR input while sweeping the D2 pump laser, monitoring the probe channel only. We adjust the D1 seed laser frequency until the gain peak and transmission at the gain peaks are both sufficiently high. The reason we do this is to closely monitor the transmission and gain, as the presence of the intense D2 pump can affect the transmission significantly.
- Look at the probe and conjugate differential signal. Lock the D2 laser to the frequency where the FWM gain peaks are best balanced.
- Fine-tune the IR pump frequency until you have the lowest differential noise.
- Adjust the probe and conjugate transmission using an independent waveplate (WP) and PBS combination until optimal squeezing is achieved.
- Check the squeezing, then adjust the probe seed power accordingly. Repeat previous step and this step until best squeezing is achieved.
- Adjust gently the coupling into photodiode for final optimization.

By following the above procedures, one should be able to achieve a measurable level of squeezing. The squeezing within the Doppler range is a complicated interplay between increased gain, loss, and residual classical noise, all of which are very sensitive to the probe frequency. If one still doesn't achieve squeezing after following the above procedures, we recommend to slightly adjust the IR frequency to improve the transmission (of course, the gain will be lower). It is not uncommon that multiple adjustments need to be done until squeezing is achieved.

Lastly, if one still doesn't observe squeezing, it is also worth to check the classical noise of coupling fields, especially in the probe seed. The phase noise conversion in the double-ladder case is significantly stronger. Since we have lower gain and usually use a stronger probe seed, the situation worsens even more. We recommend to use the quietest laser as seed, and to use a phase-lock to get narrower linewidth and less phase noise conversion (if

this is an option). We also recommend to double-check that the polarization of the probe seed field is well-defined. Extra classical noise can be added due to polarization filtering before the detector.

3.4 Comparison between two Configurations

Double- Λ FWM is widely used for intensity squeezing generation [56, 57]. The two-mode intensity squeezing with different color utilizing the double-Ladder configuration is, on the other hand, demonstrated for the first time in our work. In this section, we compare the traditional double- Λ squeezing with the diamond configuration. The major differences are summarized in Table 3.1.

The most important difference, of course, is the large difference in optical frequency between the signal fields and pump fields. The Doppler factor $k = 2\pi/\lambda$ is vastly different between ground-to-intermediate level transitions and for intermediate-to-excited level transitions. Even using proper geometry won't lead to full cancellation of the Doppler terms, leading to stringent selection of atomic velocity groups. Additionally, we are using a co-propagating geometry for the ladder configuration in which the Doppler term adds up instead of cancel out. Therefore, the double-ladder configuration is more susceptible to Doppler effect.

One additional problem brought by frequency difference is the exaggerated difference in the detector loss. The vapor cell coating gives over 99% transmission for D1/D2, yet only 90% transmission for the O-band frequency (e.g., the 13 μm fields). Similarly, the two photodiodes also have a difference in quantum efficiencies. The total detector efficiency of the 1367 nm channel is 85% of that for the probe channel. Since this difference further degrades the squeezing [116], we need to manually adjust the detector loss of both channels to achieve best squeezing. Given the lower squeezing levels in our case, we usually need to introduce an independent loss rate control for both channels to enhance the squeezing.

Also, for double- Λ configuration we can fully push the gain peak out of the Doppler

range while for the double-ladder configuration, the gain peak still resides in the Doppler range with a significant amount of absorption, leading to more significant optical loss as well as phase noise conversion. Our solution is to use a stronger probe seed far above the saturation, typically in the range of $400\mu\text{W}$ to 2 mW . This is much higher than the probe seed power usually used in the double- Λ case. We note that the FWM generation is most efficient for $\Omega_{Pump} \gg \Omega_{Probe}$. Thus applying a strong probe seed can gradually break this assumption and eventually lead to the reduction in gain. The probe seed power thus needs to be carefully selected.

Another impact of the stronger absorption is the more pronounced phase noise conversion for the double-ladder scheme compared to the double- Λ configuration. With the Vortex 6000 laser as the seed field, for example, we sometimes observe shot noise when the system is far detuned and $+6$ to $+10$ dB of extra noise when transmission drops to 70%. The lower gain in our case means that the residual classical noise can be a dominating source of excess noise, but this is not a problem at all for the double- Λ configuration.

| | | |
|-----------------------------------|-------------------------------------|---------------------------|
| | Double-Ladder | Double- Λ |
| Signal Field λ Difference | Few hundred nm | 10^{-3} nm |
| Gain ($G_{P/C}$) | Low, typically 1-2 | High, easily above 10 |
| Laser phase Noise conversion | Significant | Not Significant |
| Probe Seed Power | $400\ \mu\text{W}$ to 2 mW | $40\text{-}90\mu\text{W}$ |
| Doppler Effect Influence | Heavily Influenced | Lightly Influenced |
| Probe Transmission | 60%-85% | 95% or more |

Table 3.1: A point by point comparison between the double- Λ and ladder configurations

Chapter 4

Bi-Chromatic Intensity Squeezing using FWM in Hot ^{85}Rb Vapor

4.1 Introduction

The results presented in this section are published in [131].

The advancement in quantum information science (QIS) over the past two decades has significantly increased the number of potential applications. These applications encompass various fields, including quantum computing, quantum information processing, quantum cryptography, and quantum sensing. The variety of physical platforms for these applications is steadily increasing. Most quantum information carriers are based on electromagnetic radiation at specified frequencies, making direct interfacing between different platforms challenging or even impossible [132, 133]. This has renewed interest in addressing the problem of interconnects—both local and remote—between various platforms [134, 135]. An efficient frequency converter, capable of shifting the frequency of a quantum state without inducing decoherence, offers an ideal solution. Several such systems have been proposed and realized [48, 136], many of which rely on nonlinear optical materials and often require a waveguide or cavity to achieve sufficient nonlinearity [137, 138].

Nonlinear processes in hot or cold atoms present a promising alternative due to the

strong enhancement of nonlinear interactions near atomic resonances. A double-ladder (or diamond) scheme in Rb or Cs atoms is particularly appealing for frequency conversion [45, 130, 139]. Given that alkali metal atoms have emerged as a versatile platform for quantum information science (QIS), the double-ladder system could facilitate the conversion of their natural optical quantum carriers to the telecom bandwidth, enabling low-loss integration into quantum networks. In this context, several experiments have successfully demonstrated single-photon conversion using both cold and hot Rb ensembles [45, 58, 130, 139–141].

In this work, we focus on generating quantum fields, rather than single photons, to facilitate the implementation of quantum protocols based on continuous variables (CV), or qumodes [142–146], instead of discrete variables (DV) qubits [147–149]. Specifically, we investigate the generation of two optical fields at different frequencies with correlated quantum fluctuations, resulting in two-color, two-mode intensity squeezing. This process is driven by FWM in a double-ladder scheme in ^{85}Rb , as illustrated in Fig.4.1(a). The detunings are referenced to $|5P_{3/2}, F' = 4\rangle$, $|5P_{1/2}, F' = 2$ and $3\rangle$ centroid, and $|6S_{1/2}, F' = 3\rangle$, respectively. In this scheme, two strong pump lasers at 780 nm (D2 Pump) and 1367 nm (IR Pump) excite atomic coherence between the $5S$ ground state and the $6S$ excited state, amplifying the probe field at 795 nm and producing a new conjugate field at 1324 nm. The photon numbers in these two fields are quantum-mechanically correlated. Conceptually, this approach is similar to FWM-based two-mode squeezing and entanglement generation in a double- Λ system, where up to 9 dB of squeezing has been demonstrated [9, 76, 109]. However, FWM in the double-ladder scheme is less efficient [128, 150] due to faster decoherence, weaker available laser power, and larger Doppler mismatch. One potential solution is to operate closer to atomic resonance, but this leads to increase residual resonant absorption of the probe field, which degrades nonclassical correlations [116]. Consequently, the main experimental challenge in this project was optimizing conditions where the FWM gain is sufficiently high and resonance losses are sufficiently low to observe two-mode squeezing. After optimization, we obtain a maximum intensity squeezing of -2.6 dB, corresponding

to the FWM gain of approximately 2.1 (or ≈ 2.45 when accounting for losses). These results are in qualitative agreement with our numerical model and suggest that even better squeezing could be achieved with higher pump laser power.

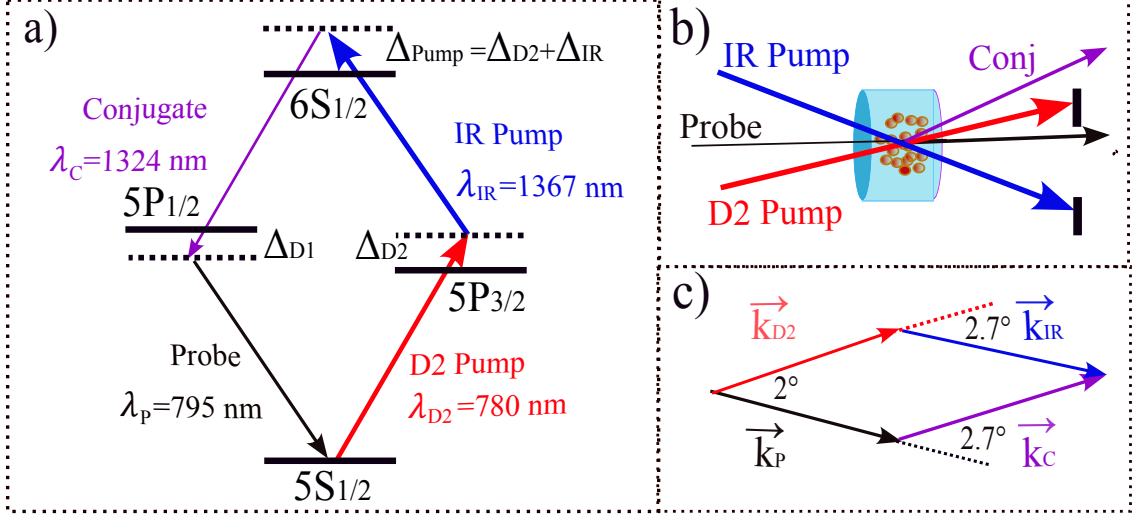


Figure 4.1: (a) Double-ladder atomic configuration of ^{85}Rb employed in the experiment. (b) Experimental setup: The D2 pump (red) and IR pump (blue) are linearly polarized in the same direction and intersect inside the vapor cell with an orthogonally-polarized probe beam (black). The conjugate field (purple) is generated with the same polarization as the probe. (c) Phase-matched FWM geometry of the optical fields within the vapor cell.

4.2 Numerical Modeling of FWM with Complete Hyperfine Level Structure

When comparing experimental results with theoretical predictions, it is essential to account for the atomic hyperfine level structures in our theoretical model. In this regard, we present a fully numerical model based on Rydiqule [151], with the explicit level diagram shown in Fig.4.2. The full Python script of this model is shown in Appendix.B.

This model extends the simplified treatment discussed in the previous section by incorporating all relevant hyperfine levels for a more accurate representation of the system's overall behavior. Specifically, we include the states $|1a\rangle$, $|1b\rangle$, $|3a\rangle$, $|3b\rangle$, $|3c\rangle$, $|4a\rangle$, and $|4b\rangle$, which correspond to these following hyperfine levels: $|5S_{1/2}, F = 2, 3\rangle$; $|5P_{3/2}, F' = 4, 3, 2\rangle$;

$|6S_{1/2}, F = 2, 3\rangle$; and $|5P_{1/2}, F = 2, 3\rangle$. The $|1b'\rangle$ is excluded from coupling as it is far detuned from all atomic resonances and has a negligible effect on the overall interaction.

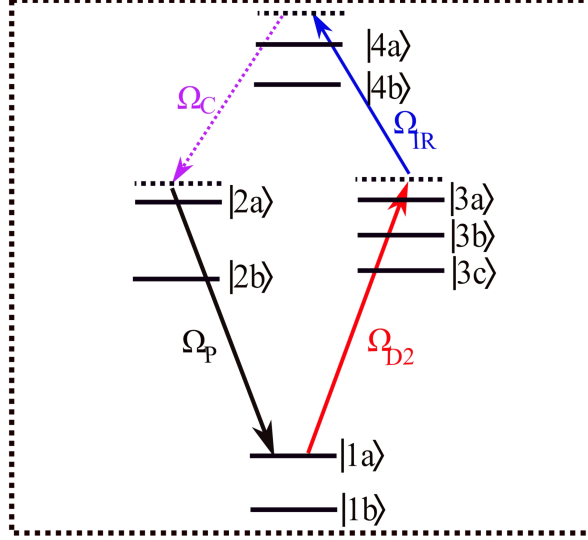


Figure 4.2: Detailed level diagram used in the numerical model. Level $|1b\rangle$ does not participate in the interaction but acts as a reservoir, accounting for population changes due to optical pumping, decay, and atomic motion.

To properly describe the system dynamics, it is essential to accurately account for the Rabi frequency which can be related to intensity through $I = \frac{1}{2}c\epsilon_0 E^2$ [118, 126],

$$\Omega_{ij} = \sqrt{\frac{2I d_{ij}^2}{\hbar^2 \epsilon_0 c}} \quad (4.1)$$

Next we need to determine correct d_{ij} to calculate the correct Ω_{ij} . Because the incident light is linearly polarized, only a single component of the dipole moment (d_{ij} has three components: $d_{ij,x}\hat{x}$, $d_{ij,y}\hat{y}$ and $d_{ij,z}\hat{z}$) contributes to the interaction. A factor of $\frac{1}{3}$ is therefore added to account for it with the assumption that our pump field is isotropic and identical in all three directions. The dipole moment for any ground levels $F \rightarrow F'$ can be expressed as the hyperfine transition strength $S_{FF'}$ such that $\sum_{F'} S_{FF'} = 1$. The effective dipole moment can then be expressed as follows[126],

$$d_{F \rightarrow F'} = \sqrt{\frac{1}{3} S_{FF'} |\langle J | er | J' \rangle|^2}. \quad (4.2)$$

If the input optical field is tuned far away from transition, a significant simplification arises from the condition that the detuning is considerably larger than the hyperfine splitting. Under this approximation, one can effectively sum over all possible transition channels to the excited states. For a linearly polarized field, the overall factor is denoted by [126].

$$\sum_{F'} (2F' + 1)(2J + 1) \left\{ \begin{matrix} J & F' & J' \\ F & 1 & I \end{matrix} \right\}^2 |\langle F m_F | F' m_{F'} \rangle|^2 = \frac{1}{3}. \quad (4.3)$$

Essentially, the far-detuned field interacts with all the hyperfine sublevels together. Since all $S_{FF'}$ s sum to unity, the only factor left is the $\frac{1}{3}$ -factor. It is critical to emphasize that this calculation is valid exclusively within the far-detuned regime. For scenarios with smaller detuning, it is essential to treat each hyperfine level independently to ensure precision. Depending on the specific scenario, it is necessary to correct the dipole moment accordingly to achieve an accurate Rabi frequency. In the diamond scheme simulation, we account for all hyperfine levels individually with $S_{FF'}$.

We assume linearly polarized input for both the pump and probe beams, with the approximation that all m -levels are equally populated and treated collectively. An equal branching ratio is assumed for all decay channels with multiple possible pathways. An effective repump rate of $2\pi \times 0.56$ MHz is coupled from $|1b\rangle$ to $|1a\rangle$ to match the linear absorption level, accounting for repumping due to atomic motion. In other words, $|1b\rangle$ is treated as a reservoir that tracks the atomic population, while all other levels, responsible for the behaviors of interest, are treated as an open system exchanging atoms with $|1b\rangle$. The atom escape rate due to thermal motion is calculated as $\Gamma_{\text{atom}} \approx 1$ MHz, based on an average atomic velocity of 270 m/s and a beam waist of 0.28 mm. All excited states (except $|1a\rangle$) decay into $|1b\rangle$ with an additional decay rate of Γ_{atom} on top of the natural decay rate. The propagation equations for the conjugate field (involving transitions $|2a\rangle \rightarrow |4a\rangle$, $|2b\rangle \rightarrow |4a\rangle$, $|2a\rangle \rightarrow |4b\rangle$, and $|2b\rangle \rightarrow |4b\rangle$) and the probe field (involving transitions $|1a\rangle \rightarrow |2a\rangle$ and $|1a\rangle \rightarrow |2b\rangle$) are solved using two coupled differential equations for $z = 0$

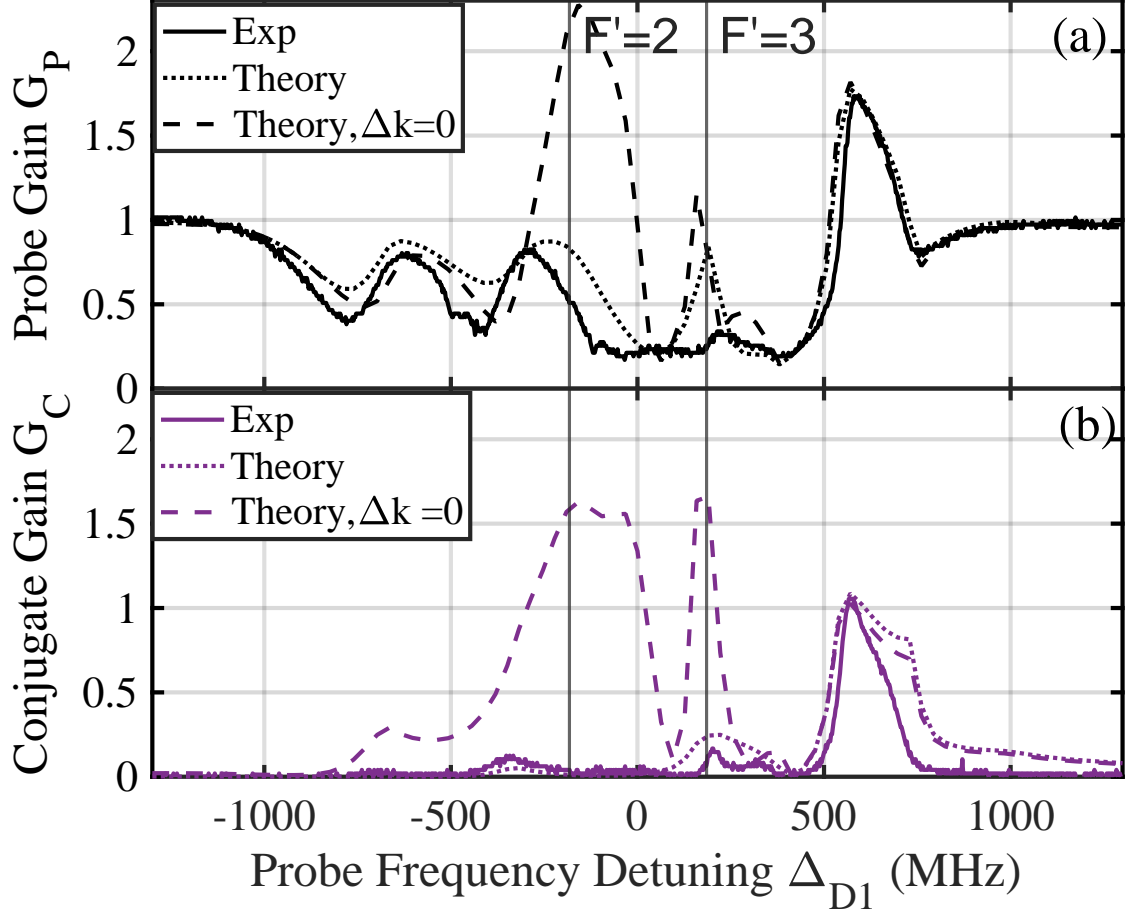


Figure 4.3: Experimentally measured (solid lines) and simulated (dotted and dashed lines) probe and conjugate gains, G_P (a) and G_C (b), are shown as functions of probe detuning Δ_{D1} . Zero detuning corresponds to the maximum resonance absorption, with vertical lines marking the positions of the $|5S_{1/2}, F = 3\rangle \rightarrow |5P_{1/2}, F' = 2, 3\rangle$ optical resonances. For these measurements, the two pump detunings are set at $\Delta_{D2} = -280$ MHz and $\Delta_{IR} = 800$ MHz [152], with their respective powers: $P_{D2} = 260$ mW and $P_{IR} = 33$ mW. The maximum measured FWM gain values are $G_P = 1.73$ and $G_C = 1.05$ at a probe detuning of $\Delta_{D1} \approx 600$ MHz. The calculated spectra account for photodetector quantum efficiencies and probe light's resonant absorption. Simulation data for $\Delta k = 0$ (dashed) and Δk with approximations (dotted, small in the gain region and large elsewhere) are also presented.

to $z = 1.83$ cm. The propagation distance is corrected for overlapping for a 1.9-cm long cell. The contributions from each transition are weighted by their respective hyperfine transition strengths. A rotating frame is chosen such that the accumulated phase factor

($e^{-i\Delta k_{ij}z}$) is applied only to the conjugate wave. The final propagation equations we solve numerically, similar to Eq.(3.25), takes the form:

$$\begin{aligned}\frac{\partial\Omega_P}{\partial z} &= ig\mathbb{N}(S_{1a2a}\rho_{1a2a} + S_{1a2b}\rho_{1a2b}), \\ -\frac{\partial\Omega_C}{\partial z} &= ig\mathbb{N}(S_{2a4a}\rho_{2a4a} + S_{2b4b}\rho_{2b4b} + S_{2a4b}\rho_{2a4b} + S_{2b4a}\rho_{2b4a}),\end{aligned}\quad (4.4)$$

where g represents the effective coupling constant, \mathbb{N} is the atomic number density, and S_{ij} is the hyperfine coupling constant. During the numerical ODE solving process, we recast Eq.(4.4) as

$$-\frac{\partial\Omega_C}{\partial z} = ig\mathbb{N}[S_{2a4a}\rho_{2a4a}e^{i\Delta k_{2a4a}z} + S_{2b4b}\rho_{2b4b}e^{i\Delta k_{2b4b}z} + S_{2a4b}\rho_{2a4b}e^{i\Delta k_{2a4b}z} + S_{2b4a}\rho_{2b4a}e^{i\Delta k_{2b4a}z}],\quad (4.5)$$

with an explicit dependence on the dynamic phase $\Delta k_{ij}z$. To prevent the repetitive accumulation of phase, we remove it at each step of the numerical computation by multiplying by $e^{i\Delta k_{ij}z}$. For simplicity, we assume the momentum mismatch affects the same in the closed loop involving states $|2a\rangle$ and $|2b\rangle$, rather than accounting for each closed loop separately. In other words, we have

$$\begin{aligned}\Delta k_{2a4a} &= \Delta k_{2a4b} = \Delta k_1, \\ \Delta k_{2b4a} &= \Delta k_{2b4b} = \Delta k_2.\end{aligned}\quad (4.6)$$

The value of Δk_j above is frequency-dependent and is related to the real refractive index $n(\omega)$ by the relation $k = k_{\text{vacuum}}/n(\omega)$, where $n = \sqrt{1 + \chi}$. The linear susceptibility χ is calculated using the following equation [126, 151],

$$\chi = \frac{4g\mathbb{N}\rho_{ij}c}{\omega_{ij}\Omega_{ij}}.\quad (4.7)$$

This equation is derived from the polarization per unit volume and expressed in terms of

the coupling constant g . For the simulation shown in Ch.4, we used the experimental values $\Omega_{\text{IR}} = 4800 \text{ MHz}\cdot\text{rad}$, $\Omega_{D_2} = 2200 \text{ MHz}\cdot\text{rad}$, and $\Omega_P = 350 \text{ MHz}\cdot\text{rad}$, which allow us to calculate χ_{IR} , χ_{D_2} , and χ_P , respectively. The calculation of χ_C is more challenging, as Ω_C varies from $z = 0$ to $z = L$. As an approximation, we assume a small testing field with $\Omega_C = 120 \text{ MHz}\cdot\text{rad}$, and we obtain minimal Δk_j in the gain region. Consequently, we utilized the approximated values $\Delta k_1 = 30 \text{ rad}\cdot\text{m}^{-1}$ and $\Delta k_2 = 10 \text{ rad}\cdot\text{m}^{-1}$ for computations in the gain region. For other regions during the D_1 sweeping, we approximated $\Delta k_1 = 3000 \text{ rad}\cdot\text{m}^{-1}$ and $\Delta k_2 = 100 \text{ rad}\cdot\text{m}^{-1}$. In Fig.4.3, we present the numerical results that match the experimental data using $\Delta k_1 = \Delta k_2 = 0$, alongside the aforementioned Δk_j approximations. The overall fit around the FWM gain peak is reasonable in both cases; however, with these adjustments, we achieve a better match for smaller Δ_{D_1} . We discuss this further in Fig.4.3 and the simulation results in next sections.

4.3 FWM Gain Optimization

The experimental details are described in Ch.4, and a simplified schematic is shown in Fig.4.1. To better understand the system and to enhance the FWM strength, we need to carefully deal with a number of experimental parameters including: laser intensities and detunings, beam sizes and overlap, relative beam angles, cell temperature, etc. The effects of varying these parameters are often not independent, and some of them are harder to control or vary than the others. For example, the FWM interaction strength increases with the available pump power, so we need to focus the beam as tightly as possible. At the same time, we must ensure sufficient longitudinal overlap of all laser beams to maximize the interaction length, meaning the Rayleigh length cannot be too short. We also need to make sure that the seed beam size does not exceed the sizes of pump fields so that its amplification is spatially uniform. In the process of optimization, we adjust the laser beam sizes using focusing lenses, and then keep them constant while varying other experimental parameters. We use a similar approach for optimizing the angles between the three laser

beams, which are crucial for satisfying the phase-matching conditions. We begin by roughly tuning all the phase matching angles as in Fig. 4.1, followed by sequential adjustments of the D2/IR beam directions while keeping the D1 field direction fixed in space. This tuning is performed in both the vertical and horizontal directions, ensuring we have the highest possible gain under the given experimental conditions.

4.3.1 Operational Temperature

Since the FWM nonlinearity is proportional to the number of atoms, it is beneficial to work at the highest possible temperature to increase Rb vapor density. However, higher temperatures also increase resonant optical losses for the D1 optical field, which is detrimental to intensity squeezing and entanglement. Because both absorption and residual optical losses increase near to atomic resonance, optimizing the cell temperature and laser detuning must be done together. Previous work on FWM in a double- Λ system has demonstrated the effectiveness of increasing atomic density while tuning the lasers far from atomic resonances. Following the same principle, we heat the Rb cell to a relatively high temperature (from 100 to 115 °C), limited by the physical properties of Pyrex cell windows. The optimal temperature for squeezing is found to be 100.5°C.

4.3.2 Laser Detunings

Since the interaction scheme involves three independent lasers, we have a large parameter space with three intertwined variables. A straightforward measurement procedure would be to sequentially change all three laser in small increments within a reasonable parameter space. However, this approach requires precise frequency control of all three lasers with high accuracy and stability over potentially long data acquisition periods. For example, dividing the target detuning range for all three input fields into 20 divisions (which gives us only moderate precision) would yield 8000 output transmission spectra, requiring more than 20 hours of uninterrupted acquisition given the communication speed with the de-

VICES. Under these conditions, the system stabilization, especially the laser locks, can be a problem.

Instead, we employed an alternative method that involved sweeping of two of the three laser fields (D2 pump and D1 probe), while parked the third laser (IR pump) at a particular frequency that was monitored using a wavemeter. Two sample datasets shown in Fig.4.4 illustrate this method. Fig.4.4(a) shows the simpler case: here we lock both D2 and IR pump fields and sweep only the D1 seeded probe field. The top graph displays the normalized probe gain G_P , showing that a clear gain peak appears as the D1 seed is tuned to $\Delta_{D1} \approx -400$ MHz from the optical resonance. To find the optimal gain for a different D2 laser detuning, we need to repeat the scan with the D2 laser locked at a new frequency. Fig.4.4(b) shows the case when we sweep both the D2 and D1 field simultaneously. For each gain peak, we can read out the precise laser detunings of both D1 and D2 field using corresponding saturation spectroscopy references. As a result, a single spectrum in Fig.4.4(b) contains the detuning information of both sweeping fields.

To scan the parameter space, however, we modify the relative phase between the D1 and D2 sweeps in each consecutive scan, as shown in Fig.4.4(b). The blue and orange traces are two different sets of data. In this particular case we digitally align the sweeps of the D2 laser, while a small phase delay is added between the two D1 sweeps, causing the orange trace in $D1_{\text{Ref}}$ shift to the right compare to the blue trace. The gain peak now appears for slightly different D1 and D2 values. We then change the IR laser frequency by a small amount, and record a trace for each step. Then, we reset the IR laser frequency to its initial value, add another constant phase delay, and repeat the above procedure.

This method gives us several practical advantages. On one hand, it streamlines the data acquisition process: in each data set such as Fig.4.4(b), we find the optimal FWM gain parameters simultaneously for both D1 and D2 detunings. To scan the full parameter space with a relatively good precision, we divide both the phase delay range and IR frequency scan range into 40 segments (λ_{IR} from 1366.8720nm to 1366.8765nm), with total 1600 sets of data that can be accomplished in a reasonable time and involve all information of the

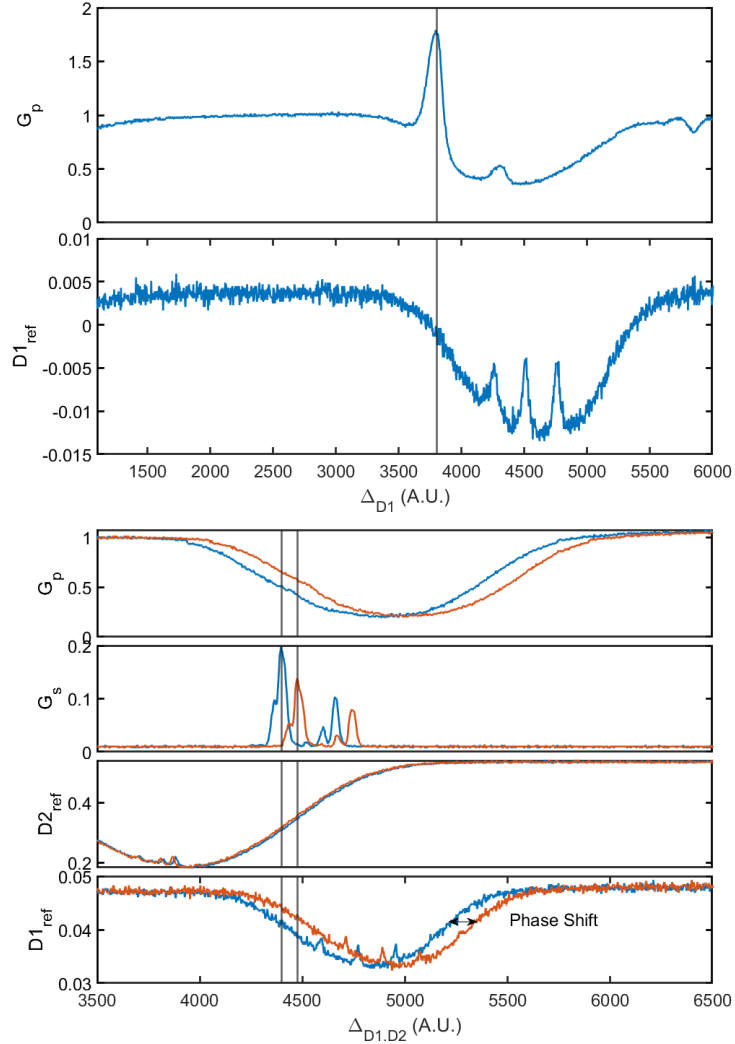


Figure 4.4: Sample data traces used for experimental optimization process. (a) Measured normalized probe transmission G_P with only the D1 laser sweeping while frequencies of both D2 and IR pumps fixed. (b) Recorded normalized probe G_P and conjugate G_C gain spectra, recorded with both D1 and D2 frequencies sweeping while IR frequency locked. For each gain peak, the D1 and D2 detunings can be mapped precisely using the saturation spectroscopy as reference signals. The blue and orange traces represent two data sets with shifted sweeping phase between D1 and D2, causing the gain peak amplitudes and locations to change accordingly.

desired parameter space. On the other hand, we automatically account for any slow drifts of the lasers, thus increasing the operational stability drastically during data collection. Lastly, the laser detunings can be precisely recorded with a straightforward saturation

spectroscopy reference even for off-resonance case. The data presented throughout this thesis is generally in this form, with one or two field sweepings and corresponding gain peaks.

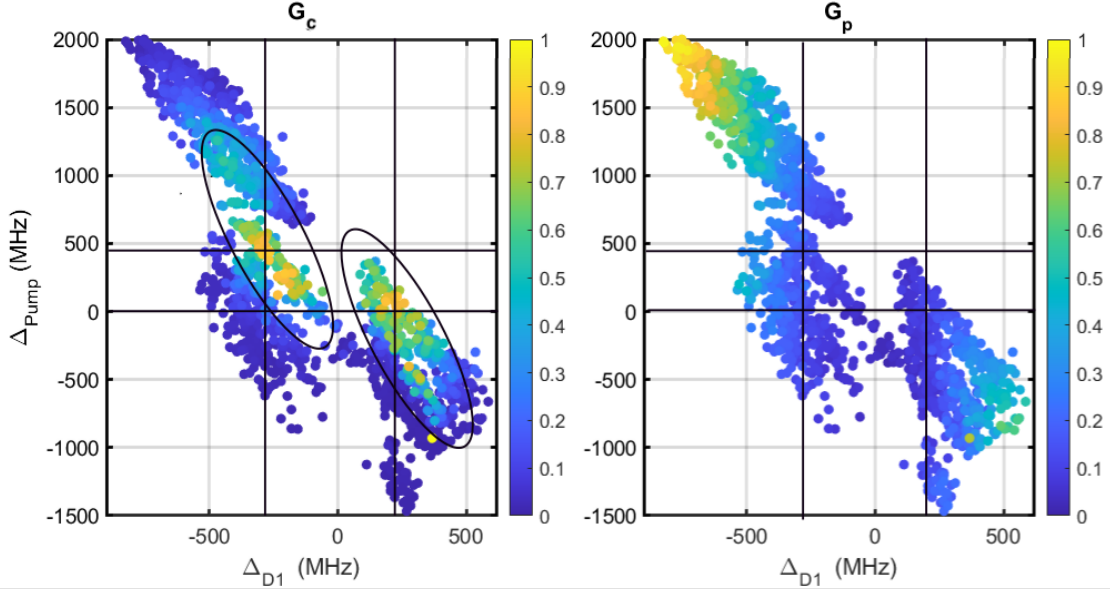


Figure 4.5: Measurements of the FWM gain for the conjugate field (a) and for the probe field (b) as a function of the two-photon pump detuning $\Delta_{\text{Pump}} = \Delta_{D2} + \Delta_{\text{IR}}$ in the low-intensity regime. Two ovals indicate the regions of highest conjugate gain G_C . The cell temperature is 100 °C (corresponding Rb density $N = 4.76 \times 10^{12} \text{cm}^{-3}$), pump powers are 26mW and 33mW, respectively, for D2 and IR pump.

To gain a comprehensive understanding of the laser detuning effects on the system, we track five essential values from a single dataset corresponding to the highest gain peak: the detunings of all three lasers ($\Delta_{D1}, \Delta_{D2}, \Delta_{\text{IR}}$), and the magnitudes of the normalized probe and conjugate field outputs ($G_{P/C}$). Though we often observed multiple gain peaks due to different hyperfine levels, as shown in Fig.4.4(b), only the highest one for each spectrum was included in the analysis. A total of 1600 data points are shown in FIG.4.5 as a 2D-scatter plot, with x-axis showing the frequency detuning of the probe laser Δ_{D1} from centroid frequency of hyperfine splitting, and the y-axis associated with two-photon detuning of the sum pump laser frequencies $\Delta_{\text{Pump}} = \Delta_{D2} + \Delta_{\text{IR}}$ from the $|5S_{1/2} F = 3\rangle \rightarrow |6S_{1/2}\rangle$ transition. In each graph, the values of $G_{P/C}$ are color-coded and within the same range

for a convenient comparison. In Fig.4.5(a), we can see clearly two peaks separated by approximately 400 MHz. It is reasonable to assume that these two peaks correspond to the $|5P_{1/2}\rangle$ hyperfine levels (with 361 MHz separation). The region with maximum gain shows a clear correspondence between Δ_{Pump} and Δ_{D1} , visually represented as two diagonal maximum gain regions centered at $\Delta_{\text{Pump}} = 250 \text{ MHz}$ and $\Delta_{\text{Pump}} = 0 \text{ MHz}$. This separation may result from the hyperfine structure of the intermediate $|5P_{3/2}\rangle$ state, though a more precise explanation requires more detailed modeling. In general, we prefer Δ_{Pump} , or more specifically Δ_{D2} , to be large in order to avoid optical pumping and induced absorption. We note that this laser detuning optimization was done using collimated laser beams with diameters exceeding 1 mm, and relatively low pump power ($P_{D2} = 26 \text{ mW}$, $P_{IR} = 33 \text{ mW}$, $P_{D1} = 2.3 \text{ mW}$). This ensured good beam overlap at the cell and all spatial gradient of wavefront are removed. However, in this arrangement the FWM gain was quite low. So even though it was easy to isolate the FWM peak in the generated conjugate field, if we look at the normalized probe field transmission G_P in Fig.4.5(b), the FWM peak is barely distinguishable, with the spectrum largely dominated by the resonant absorption of the D_1 Rb transition. In later sections, when we used more a intense D_2 pump field, the FWM peak becomes much more prominent, as in Fig.4.4(a). Across all regime, Δ_{D1} remains the lead influencing factor for D_1 field absorption. The comparison between Fig.4.5(a) and (b) indicates a rapid drop in interaction strength as we increase Δ_{D1} . However, the conjugate gain G_C remains significant with sufficiently low absorption, for example at $\Delta_{D1} = \pm 400 \text{ MHz}$.

Figure 4.6 provides further insights into the FWM dependence on the frequencies of the two pump lasers at higher laser intensities. We shrink the pump beam sizes for the transitions: $|1\rangle \rightarrow |3\rangle$ ($\lambda_{D2} = 780 \text{ nm}$, $P_{D2} = 260 \text{ mW}$, $d \approx 0.6 \text{ mm}$) and $|3\rangle \rightarrow |4\rangle$ ($\lambda_{IR} = 1367 \text{ nm}$, $P_{IR} = 35 \text{ mW}$, $d \approx 0.3 \text{ mm}$). Here, we focus on the higher frequency region ($\Delta_P \approx +500 - 800 \text{ MHz}$, whereas in the low-power case, detuning was negative), which corresponds to higher FWM gain and lower resonant absorption. Fig.4.6 also illustrates the necessary trade-off between FWM gain and probe field resonant absorption. For instance,

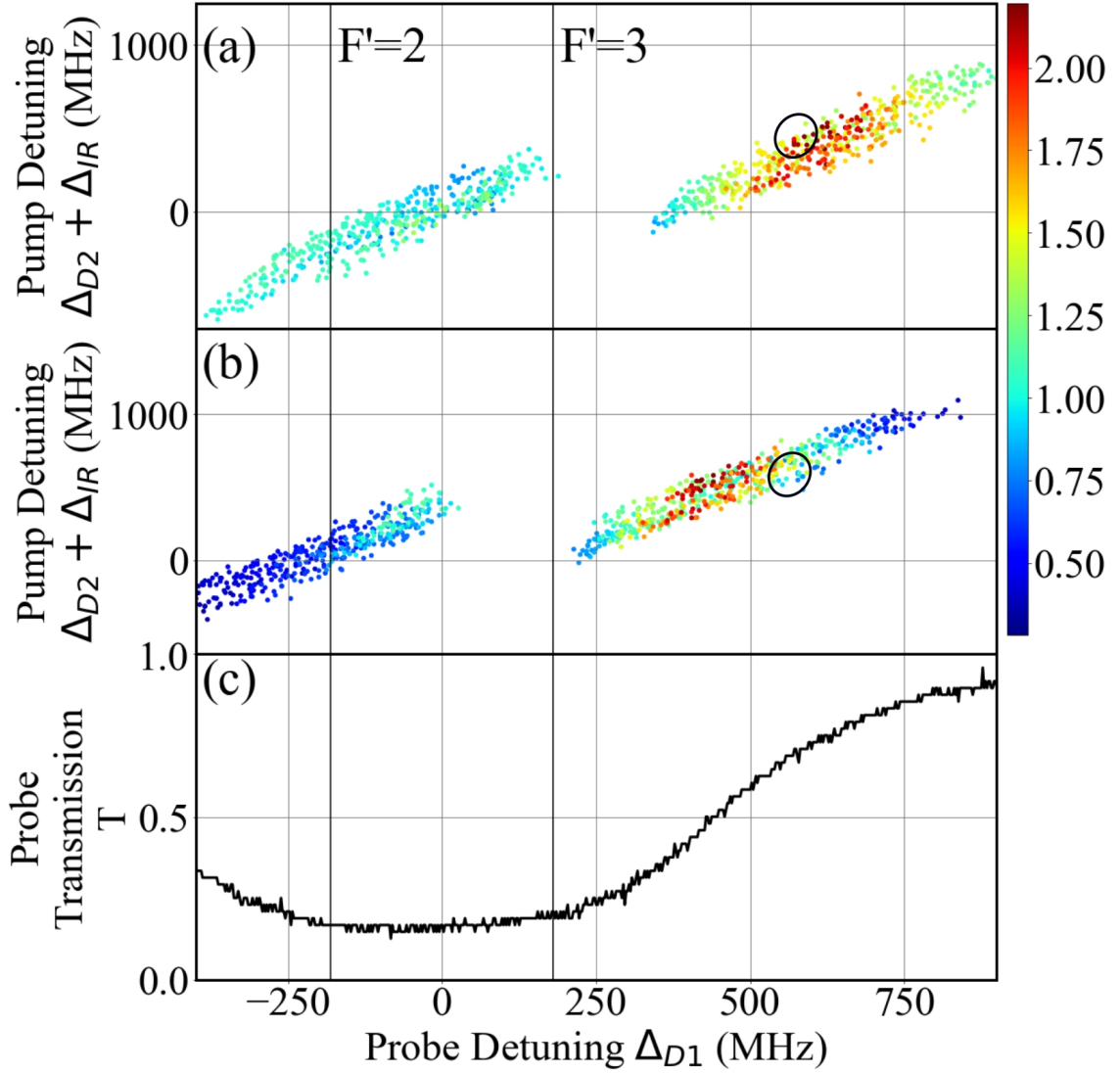


Figure 4.6: FWM gain map: Maximum measured values of probe gain G_P (a) and conjugate gain G_C (b) as a function of optimal probe detuning Δ_{D1} (horizontal axis) and two-photon pump detuning $\Delta_{D2} + \Delta_{IR}$ (vertical axis). (c) Unamplified probe transmission (without pump fields). The region where maximum intensity squeezing is achieved is highlighted with a black circle. The same pump laser powers as in Fig.4.3 are used: $P_{D2} = 260$ mW and $P_{IR} = 33$ mW.

the highest values of G_C occur near the D1 line transition of ^{85}Rb , while maximum G_P shifts toward higher probe detunings. This shift can be explained by the probe field's behavior near the optical resonance (as shown in Fig.4.6(c)), which directly affects its output power. In contrast, the conjugate field experiences negligible atomic absorption, so

its output power is primarily determined by the strength of the FWM process. To observe intensity squeezing, we need to equalize the FWM gains for both optical components, which can be maximally approached within the experimental parameter region marked by circles in Figs. 4.6(a) and (b). We see that in this case, the probe peaks surpass saturation and remains clearly visible, signifying the importance of laser intensity—a topic which we discuss in next section.

4.3.3 Laser Intensities

The analysis of the FWM dependence on the laser detunings indicated the need to operate at higher pump powers to increase the nonlinear gain, allowing us to work farther from the optical transition. We operated a higher D2 pump power (maximum 320 mW), and also employed the lens combination listed in the previous sections to achieve tighter focus for both pump beams (as the available laser power for the 1367 nm IR pump was limited to 35 mW). Under these conditions, much stronger FWM gain was achieved, as shown in Fig.4.3. Two strong gain peaks can be clearly observed, with the highest $G_P \approx 2.1$ at the marked location. We also notice that the highest gain peak occurs at $\Delta_{D1} \approx 0.6\text{MHz}$, which corresponds to the probe absorption without the pumps ($T_P \approx 85\%$).

Nevertheless, unlike in the traditional double- Λ FWM, we were not able to shift the gain the FWM gain peak fully outside the Doppler absorption range, even with the maximum available laser power. In principle, one may compensate for the losses by increasing the D1 seed intensity to increase the saturation of the optical transition. However, increasing the seed power gradually breaks the weak probe assumption, and as a result, G_P becomes smaller. For this experiment, the D1 seed is in general no more than 2 mW before the vapor cell. The optimal squeezing discussed in the next section is obtained with 0.6 mW of power.

Boosting the pump power is another potential method for increasing the gain without increasing the optical loss. This is particularly true for the IR pump laser, whose available power did not exceed 35-40mW, a value significantly lower than the power range (300-

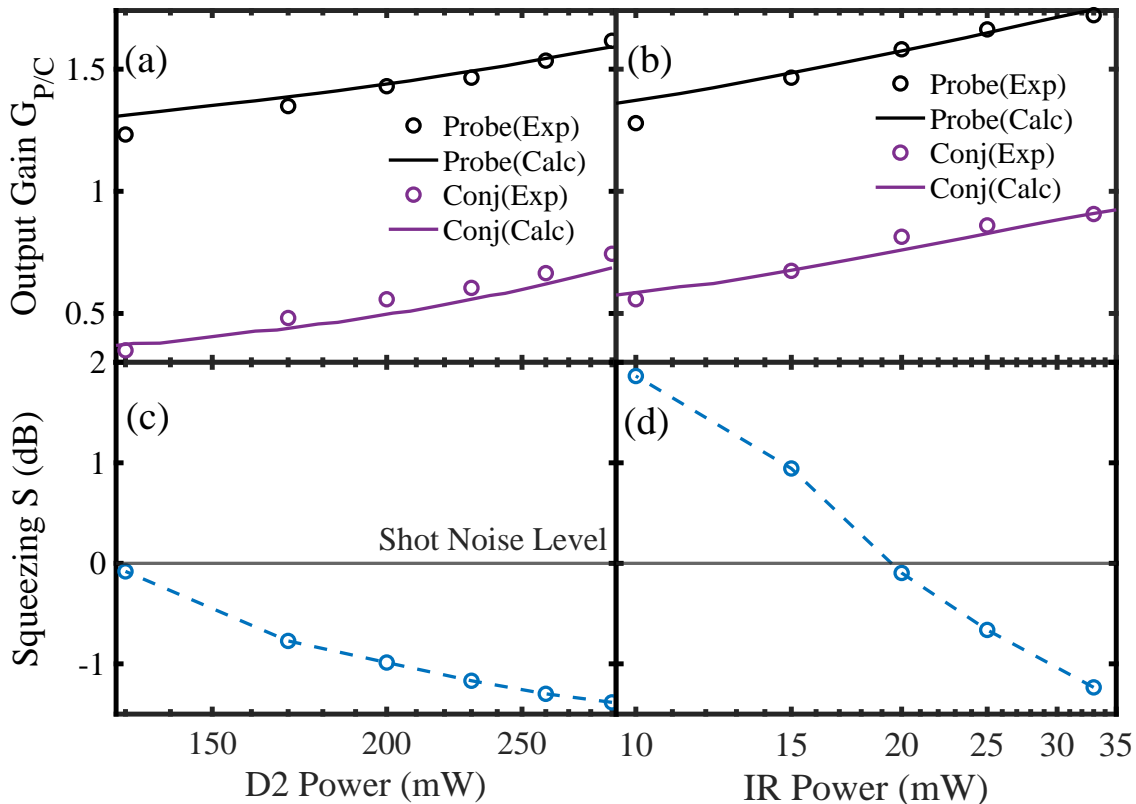


Figure 4.7: Dependence of the FWM gain $G_{P/C}$ (a, b) and relative intensity squeezing (c, d) on the pump laser powers. The left column shows data for varying D2 pump power with fixed IR pump power at $P_{IR} = 35$ mW, while the right column corresponds to varying IR pump power with fixed D2 pump power at $P_{D2} = 290$ mW. The solid lines represent theoretical gain predictions from the numerical model, while the dashed lines in the squeezing data provide a visual guide. The small hollow circles denote the experimentally measured values.

600 mW) typically used in the double- Λ FWM experiment [153]. However, this approach requires substantial hardware upgrade.

The dependence of the FWM gain on the power of both pump lasers is shown in Fig.4.7(a,b). Each spectrum is taken with the other pump power kept at a constant level. For this measurements, we use the conjugate field gain G_C , as this parameter is less affected by the residual resonance losses. We observed that the gain increased almost linearly with the pump power, as expected based on the previous work [45]. However, a high-power laser is not easily accessible for this particular wavelength due to strong water absorption

line, posing difficulty in accessing higher-power laser system. We will show later simulated results with a numerical model for the higher power range.

4.4 Results: Bi-chromatic Intensity Squeezing

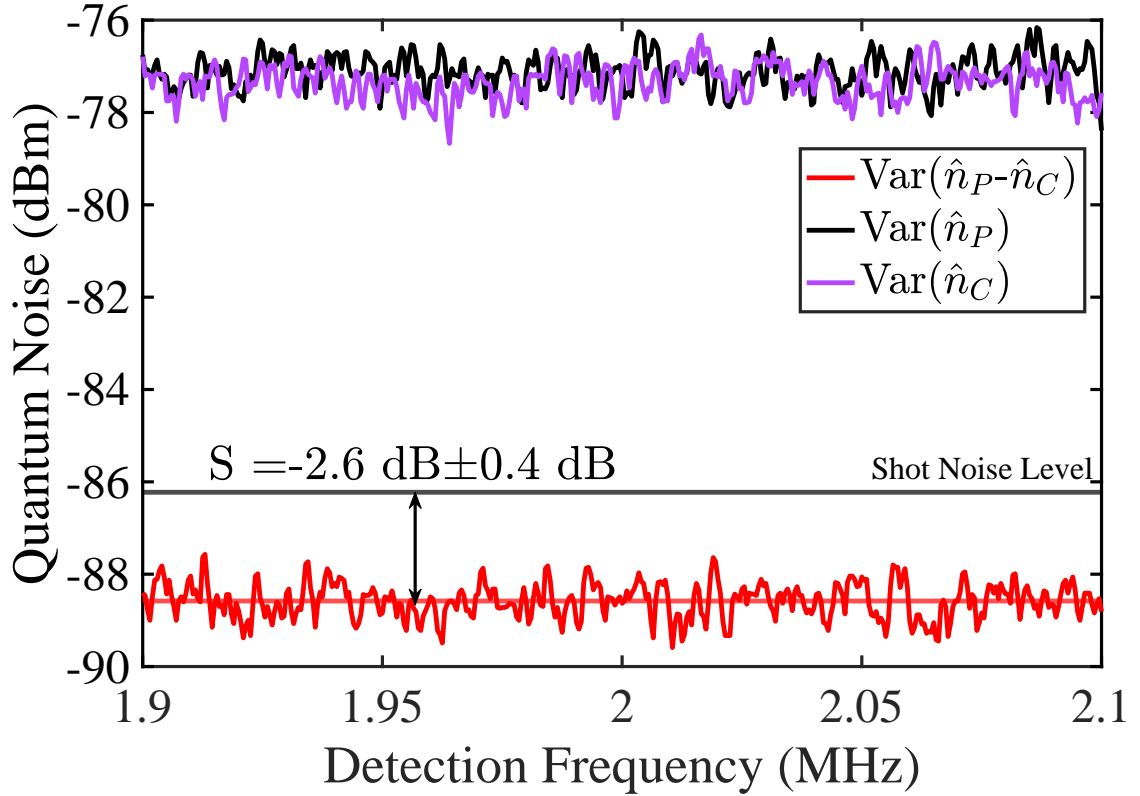


Figure 4.8: The variance of the relative photocurrent noise spectrum (red), $\text{Var}(\hat{n}_P - \hat{n}_C)$, for the probe and conjugate fields, along with their individual intensity noise levels, $\text{Var}(\hat{n}_{P/C})$ (black/purple). As reference, the black straight line marks the shot-noise level, $\text{Var}(\hat{n}_P^{(coh)} - \hat{n}_C^{(coh)})$, measured for two coherent laser fields. The relevant detunings are $\Delta_{D1} \approx 800$ MHz, $\Delta_{D2} = -280$ MHz, and $\Delta_{IR} = 800$ MHz, with two pump laser powers of $P_{D2} = 350$ mW and $P_{IR} = 32$ mW, respectively.

After identifying the optimal experimental configuration to maximize FWM efficiency, the next step involved measuring and analyzing the relative intensity noise of the probe and conjugate fields. To determine the presence of nonclassical photon-number fluctuation correlations between these two fields, we electronically subtracted their photocurrents and

analyzed the resulting noise power spectrum using a spectrum analyzer. We characterized the degree of quantum correlations using Eq.(2.82). In line with quantum optics, both the probe and conjugate fields exhibit super-Poissonian statistics, implying that each field is noisier than a coherent field with the same mean photon number.

Fig.4.8 presents representative measurements of the relative intensity noise for both the probe and conjugate optical fields, along with their respective individual noise levels. The shot-noise level (indicated by the horizontal black line) is computed based on the photodiodes' calibration using coherent state inputs. As anticipated, each of the probe and conjugate fields displays an excess noise of +9 dB above the shot-noise level when measured independently. In contrast, the differential photocurrent noise is reduced by -2.6 dB below the shot-noise level, indicating the emergence of quantum correlations. This degree of squeezing was achieved with a probe field gain of $G_P = 2.08$ and an 85% transmission without the occurrence of FWM (measured with the IR pump laser blocked). The corresponding gain for the conjugate field was $G_C = 1.45$, with no observable resonant absorption.

To compare the measured squeezing values with the theoretically expected performance, it is imperative to account for optical losses during beam propagation. Neglecting the contributions of Langevin forces due to minor resonant absorption, we employ a distributed beam-splitter model. In this approach, the interaction volume is divided into N slices, and the output quantum fields are calculated using the FWM gain and loss in each slice, as described in Ch.2. Under these approximations, we apply Eq.(2.73). For parameters similar to the experimental conditions in Fig.4.8, the predicted two-mode squeezing level is approximately -3 dB. Typically, the model predictions are 1-2 dB below the experimentally measured values.

The primary source of additional noise is the phase noise of the probe laser, which is converted into intensity noise near the atomic resonance. When only the probe field is present in the cell, its intensity noise increases by 1 to 3 dB at this detuning, while it remains at the shot-noise level when the laser is far-detuned. This noise is carried

out through the amplification process, causing each individual beam to exhibit more noise than anticipated. Although this extra technical noise is partially canceled in the differential intensity measurements, the cancellation is incomplete due to the differing gain values for the two fields. Additional technical noise also arises from thermal fluctuations and laser polarization instabilities.

For our system to become practical for QIS applications, its performance must improve to achieve a level of squeezing (and eventually entanglement) suitable for real-world use. For instance, an entanglement threshold of around -9 dB is demanded for implementing hybrid photon conversion protocols [136]. To enhance squeezing, we need to acquire higher gain and reduce losses. However, adjusting laser detunings can only optimize one at the expense of the other. The most promising and straightforward approach is increasing the pump laser intensity. Fig.4.7(a)-(d) shows experimental results alongside numerical simulations of the FWM gains G_P and G_C , as well as the measured squeezing parameter S over a range of pump powers. The results clearly demonstrate that increasing laser power improves not only gain as mentioned in the previous section, but also the quantum squeezing.

4.5 Gain and Squeezing at High Power: Simulation

To explore potential improvements in achievable FWM gain and squeezing levels at higher laser powers, we performed simulations over an extended pump power range (beyond what is currently attainable with the lasers available for this experiment). In these simulations, the laser detunings were fixed near the experimental values: $\Delta_{D1} \approx 400 - 800$ MHz, $\Delta_{D2} = -280$ MHz, and $\Delta_{IR} = 800$ MHz. The results are presented in Fig.4.9. It is evident that increasing the IR pump power consistently leads to higher FWM gain for both the probe and conjugate fields, resulting in greater levels of squeezing. Initially, increasing the D2 pump power also boosts the gain, but it eventually reaches a peak at a value that depends on the available IR pump power. As the IR power increases, the

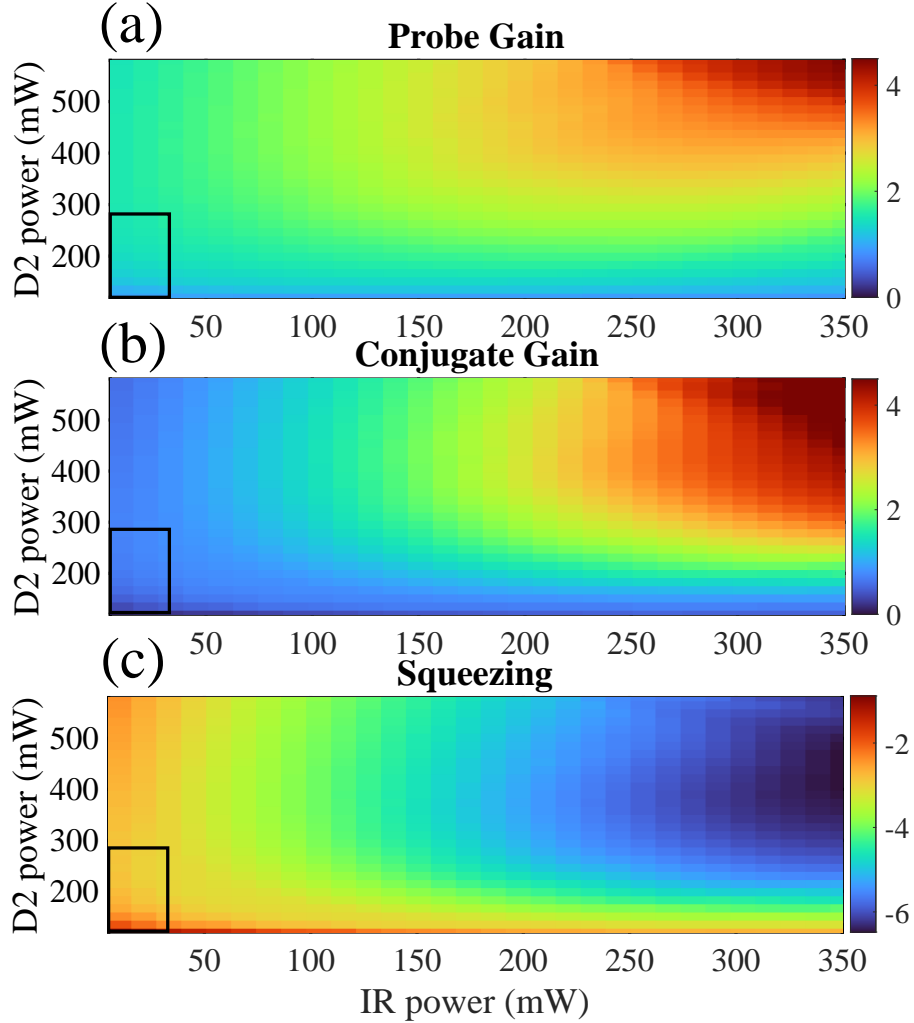


Figure 4.9: Theoretically predicted FWM gain values for the probe (a) and conjugate (b) output fields are shown over a wider range of pump laser powers. The calculations assume detunings of $\Delta_{D2} \approx -280$ MHz, $\Delta_{IR} \approx 800$ MHz. To locate the maximum FWM gain peak, we adjust Δ_{D1} from approximately 400 to 800 MHz, accounting for the light shift caused by the vastly different pump powers. (c) Predicted differential intensity squeezing is shown, based on the calculated gain values and the residual resonant absorption of the probe field, using a beam-splitter model. The black squares represent the range of pump powers used in the experiment.

maximum FWM gain shifts to a higher D2 power range, as shown in Figs. 4.9(a) and (b). The predicted squeezing values in Fig.4.9(c), obtained using Eq.(2.73) and accounting for probe field optical losses calculated for each configuration, indicate that with reasonable laser powers, up to 6.5 dB of two-mode intensity squeezing can be achieved.

4.6 Possible Improvements in FWM Gain and Squeezing: Preliminary Results

In this section we discuss potential modifications that we can employ to further boost $G_{P/C}$ beyond simply increasing the pump laser power. As discussed in previous sections, boosting the pump laser powers is a straightforward approach; nevertheless, it requires significant hardware upgrades. Here we introduce several alternatives that used to circumvent the power limitation. Besides, these methods can be use as potential control methods. For example, the wave-mixing method and the repeated seeding method can strongly change the nonlinear gain, even with relatively weak fields. Therefore, these methods can not only enhance the gain but also be employed as effective control mechanisms for the system.

4.6.1 Improved Atomic State Preparation via Velocity-Selective Optical Pumping

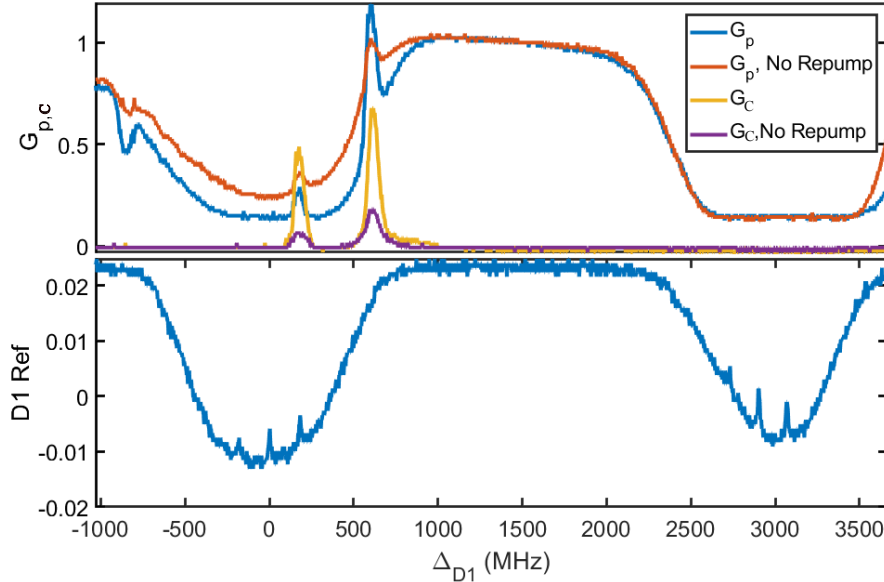


Figure 4.10: Normalized FWM gain for the probe and conjugate optical fields with/without the presence of velocity-selective optical pumping. Experimental settings: input laser powers $P_{D2} \approx 80\text{mW}$, $P_{IR} \approx 37\text{mW}$, $P_{D1} \approx 0.6\text{mW}$, $P_{\text{Repump}} \approx 7\text{ mW}$, the cell temperature $T = 96^\circ\text{C}$ (corresponding Rb density $N = 3.6 \times 10^{12}\text{cm}^{-3}$), and $\lambda_{IR} = 1366.8640\text{ nm}$

One approach is to improve the atomic state preparation by engaging velocity-selective optical pumping. For the double-ladder scheme, the D2 pump laser also efficiently optical pumps atoms from $F=3$ to $F=2$ ground level. Only atoms trapped in the cyclic transition remain in the $F=3$ level, while the rest of the atoms tend to aggregate at the $F=2$ level, effectively excluding them from the FWM process. FWM is also hampered by the thermal motion of the Rb vapor. Due to the relatively large angular separation between the three laser beams, each laser is more likely to address different velocity groups within the Doppler profile so that the atomic population interacting with all three beams simultaneously is only a small fraction of all atoms. In addition the Doppler mismatch between different velocity classes is further enhanced in the co-propagating configuration (required to satisfy the phase-matching conditions), leading to a larger two-photon Doppler broadening.

To partially alleviate these issues, we introduce an additional counter-propagating D2 field coupled from $|5S_{1/2}F=2\rangle \rightarrow |5P_{3/2}\rangle$, as shown in Fig.4.1. Such a repump field can then transfer atoms back to the $F=3$ ground state without the need of increasing the cell temperature. Moreover, the optical pumping process, induced by the counter-propagating repump beam, is velocity-selective. By carefully adjusting the repumping laser parameters we can repopulate the $F=3$ state only for the velocity group contributing to FWM, while leaving other velocity groups unaffected. This can be done by setting the repumping beam at a particular angle or frequency [154]. This method has some advantages, especially when the FWM-amplified field is off-resonance. In such cases, atoms participating in the FWM process “see” the probe field as off-resonant, so their contribution to the resonant losses is small. At the same time, for other atoms the probe field frequency is Doppler-shifted closer to the optical transition, increasing the absorption, but without contributing to the nonlinear amplification. Just increasing the vapor temperature broadens increases the number of atoms for all velocity groups, enhancing both nonlinear interaction strength and optical losses simultaneously. Using the velocity-selective repumping, it is possible to increase the number of atoms in the $F=3$ state only for the “useful” atoms without affecting the rest of the atomic population, boosting the FWM gain without significantly

increasing the optical absorption.

An example of the FWM gain enhancement due to the repump field is shown in Fig.4.10. This dataset is recorded at $T = 96^\circ\text{C}$. We can see that with a moderate amount of repump power, the conjugate gain peak is boosted by ≈ 3.7 times for both peaks. The width of each gain peak remains narrow as compare to the wide gain peak seen in Fig.4.3. This demonstrates the possibility of operating at higher atomic density without risking for higher temperature. However, we did also observe an overall increase in probe field absorption, which deteriorates the entanglement. A comparison between G_P and G_C indicates that the absorption is significant, and achieving intensity correlations may require optimizing the gain peak position further.

4.6.2 Gain Improvement by Multiwave Dressing with Weak Field

An additional coupling field can offer other possible benefits. If we couple a weak copropagating field to $|5S_{1/2}F = 2\rangle \rightarrow |5P_{1/2}\rangle$, it forms a Λ configuration with the probe field. The atomic polarization for $|5S_{1/2}F = 3\rangle \rightarrow |5P_{1/2}\rangle$ transition can be effectively modified to have either higher or lower gain depending on the dressing field detuning. This is the so-called dressing-method [155]. One explanation is the new field serving as a cyclic transition field to activate the 5th-order nonlinearity responsible for the six wave mixing (SWM), which has been experimentally proved to double the gain in the double- Λ system[156].

The preliminary results of such dressing effects are shown in Fig.4.11, with the D1 probe locked for 83% transmission ($P_{D1,Input} = 1.8\text{mW}$) and the D2 frequency swept (yellow line in (b)). The IR pump is parked at $\lambda_{IR} = 1366.8640\text{ nm}$. We use a weak dressing field with $\approx 1.9\text{ mW}$ power, red shifted $\approx 0.4\text{GHz}$ away from the $|5S_{1/2}F = 2\rangle$ resonance. The probe transmission with and without the dressing field is shown in Fig.4.11(a) in blue/orange line, respectively. With this small modification, we observe that the gain peak is significantly boosted. Fig.4.11(b) shows the probe transmission without FWM (with the IR pump blocked) using same color coding. We observed that the presence of the dressing field can potentially increase the probe absorption at certain the two-photon detuning values,

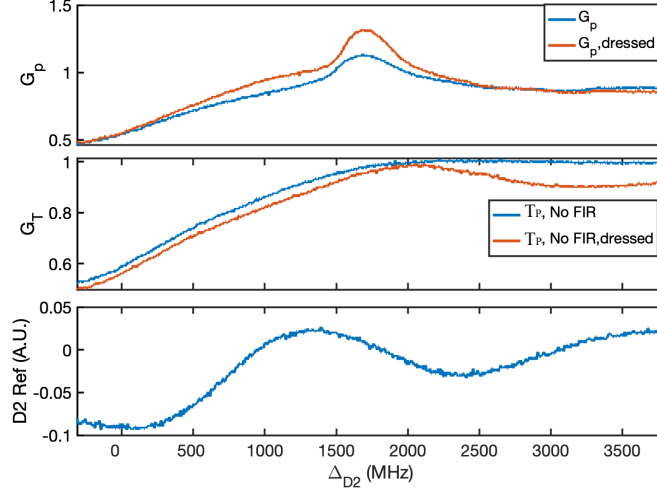


Figure 4.11: Modification of the FWM gain via the dressing laser field, tuned to $|5S_{1/2} F = 3\rangle \rightarrow |5P_{1/2}\rangle$ transition. (a) Normalized probe transmission under the FWM conditions T_P with and without the dressing field. (b) Similar normalized probe transmission without FWM (no IR pump present) in the presence of the/no dressing field. (c) Saturation spectroscopy D2 laser frequency reference. All trace are recorded with D1 laser tuned to the 83% transmission level. We used $f=400$ mm lens for D1 seed in this set of data. Experimental settings: input laser powers $P_{D2} \approx 320\text{mW}$, $P_{IR} \approx 35\text{mW}$, $P_{D1} \approx 2\text{mW}$, the cell temperature $T = 100^\circ\text{C}$ (corresponding Rb density $N = 4.76 \times 10^{12}\text{cm}^{-3}$), and $\lambda_{IR} = 1366.8640$ nm

potentially due to atomic population change or more complex multi-photon effects. On the other hand, the probe transmission near the gain peak is minimally impacted, making this method a seemingly harmless addition to the existing system.

4.6.3 FWM Gain Manipulation with the Repeated Seeding

All the results discussed above assume that only the probe channel is seeded with a weak coherent field. The gain, however, can be greatly enhanced if both channels are seeded with phase-coherent optical fields. The FWM input to output transformation matrix is shown in Eq.2.36.

The output is larger if both $\hat{a}_P^\dagger \hat{a}_P$ and $\hat{a}_C^\dagger \hat{a}_C$ are nonzero, whereas in our case, $\hat{a}_C^\dagger \hat{a}_C = 0$. This illustrates, at a rudimentary level, how seeding both channels can greatly enhance the gain. The full consideration of the phase difference between the two seeding

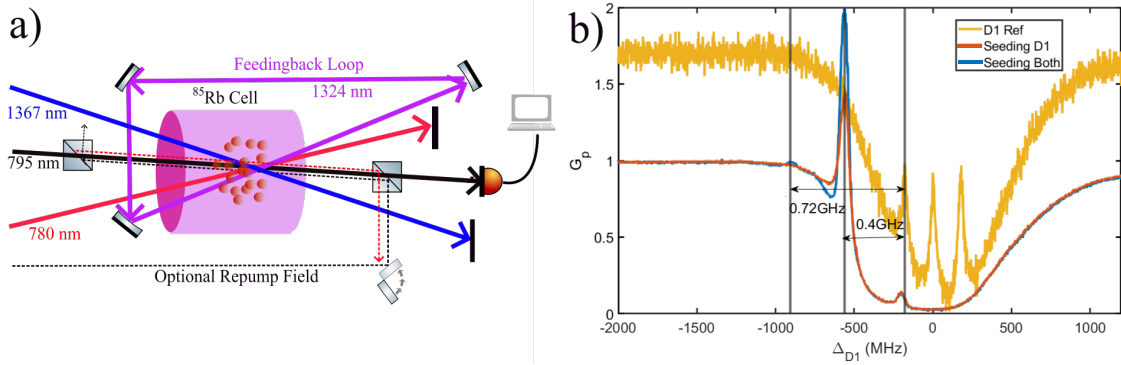


Figure 4.12: (a) Schematic arrangements for a double-seeded FWM, where the generated conjugate field is fed back into the input. The singly seeded case is shown in Fig.4.1(b). (b) Measured normalized probe transmission G_P for a regular (orange) and double-seeded FWM (blue), where the relative phase of the conjugate field is adjusted to produce maximum FWM gain. The saturation spectroscopy reference D1 laser signal is shown in yellow. Experimental settings: input laser powers $P_{D2} \approx 250\text{mW}$, $P_{IR} \approx 32\text{mW}$, $P_{D1} \approx 2\text{ mW}$, the cell temperature $T = 92^\circ\text{C}$ (corresponding Rb density $N = 2.78 \times 10^{12}\text{cm}^{-3}$) with 26mW repump field, and $\lambda_{IR} = 1366.8590\text{ nm}$.

fields, on the other hand, introduces quantum interference effects meaning the gain can actually be boosted, or degraded depending on the relative phase of the optical fields involved [157].

In Fig.4.12 we show the proof of principle demonstration of the double seeding method. In actual applications, we need a two-stage amplification in order to read out both channels. This approach brings additional benefits, as wave mixing is by nature a phase coherent process that stabilize that the two input seed need to be phase-locked to ensure constructive interference. In our case, due to the lack of physical space and apparatus we use a single cell with the generated conjugate field being fed back to the input, essentially forming a cavity, as shown in Fig.4.12 (a). In this case, we can read out only the probe channel. We can see that when we have constructive interference, the double seeding G_P (blue) is almost increased by 33% compare to the single seeding (orange) case. A secondary gain peak, which is not visible in the single seeding case, appears at $\Delta_{D1} = 0.72\text{ GHz}$, with terrific transmission.

Using the conjugate channel as a feedback, of course, presents several problems. Not

only the are generated conjugate photons confined inside the cavity, but the accumulated phase also disturbs the gain in an uncontrollable way. In order to make this method useful, a two-or-more stages cascade method involving more than one vapor cells is required. With more than one vapor cell, the gain can be enhanced at each stage with the benefits of multi-seeding. Moreover, strong squeezing enhancement has been demonstrated using the cascade method[158]. This method brings us another potential option if a higher-power 1367 nm pump is not available.

4.7 Conclusion

In conclusion, we have demonstrated an atom-based narrowband source of two-mode intensity correlations between optical fields at different wavelengths: a 795-nm probe field resonant with the ^{85}Rb atomic transition and a 1324-nm conjugate field, falling within the O-telecom band. This was achieved using FWM in a double-ladder configuration, driven by two pump lasers of moderate power (up to 350 mW for the 780-nm laser and up to 35-mW for the 1367-nm laser). The maximum achieved gain G_P exceeded 2, with up to 85% residual resonant absorption for the probe field. Under optimized conditions, we observed up to -2.6 dB of relative photocurrent noise suppression below the shot-noise level, clearly demonstrating nonclassical correlations between the intensity fluctuations of the two optical fields. Our theoretical model predicts that up to 6 dB relative-intensity squeezing could be reachable with higher laser power and reduced residual noise.

Chapter 5

Weak thermal state imaging

In this chapter, we present a low-photon-count imaging experiment based on a super-Poissonian light state. Please refer to ref [79] for the published work. Here, we primarily discuss the experimental aspects carried out by our group. All figures featured in this chapter were prepared solely or collaboratively by the dissertation author, ensuring no conflict of interest.

Conventional imaging methods normally use order of 10^3 to 10^5 photons per pixel [159]. It would be either impractical or impossible to use such a high number of photons in variety of situations e.g. while imaging fragile samples such as biological specimens, photosensitive chemicals or performing covert military operations. Furthermore, using low-intensity light usually incurs high image-acquisition time. All things considered, low-light imaging is a promising field of inquiry.

Traditionally, imaging is accomplished by comparing the transmitted intensity of a probe beam that examines the sample with the intensity of a reference beam. Classical lower bound on the sensitivity of such method is established by employing probe with Poissonian statistics [160, 161]. Absorption measurement methods [162–164] and quantum imaging methods [159, 165–168] have successfully proven the enhancement in the sensitivity over classical methods using quantum resources such as spatial correlations in twin-beam light produced by spontaneous parametric down conversion (SPDC) process

and high sensitivity CCD array detectors.

Reduction in number of photons used for imaging in low-light regime are limited, among other factors, by intrinsic dark noise of a CCD camera. Origin of dark noise lies in electrons generated in silicon lattice that makes up CCD regardless of absence of any light falling on the detector. In any imaging scheme, dark noise would represent the noise floor above which signal will be detected.

QSI method makes use of the information carried in the noise of the probe state. Image is reconstructed by detecting the changes in quadrature noise profile of the probe beam after its interaction with the object. This technique gets rid of detrimental effects of dark noise of the CCD camera and enables imaging at photon levels as low as 800 photons, utilizing less than one photon per frame on average [169] with significantly short acquisition time using squeezed vacuum probe.

5.1 Quantum Imaging Model

In this section we describe the detailed protocol of the QSI scheme in terms of density matrix. This is a general formalism that allows to analyze the performance of any kind of probe state, both quantum and classical. A low intensity probe field illuminates the object to be imaged. The object transmits some part of it and scatters the rest. Noise statistics of the transmitted field is analysed with a homodyne-like scheme. This is achieved by letting the transmitted field interfere with a strong local oscillator (LO) on a balanced beam splitter and consequent detection by a CCD camera [170]. Intensity maps of two output beams, recorded at multiple time instants by the camera, are subtracted to get a series of "beam difference" maps as shown in Fig.5.7, as shown in Fig.5.1. A temporal variance map of this time series data, normalized by the total intensity, is the signal for this imaging scheme. Since this scheme employs quadrature variance of the probe state, essentially any state with quadrature variance different from coherent state should work as a probe. Thermal state with its super-Poissonian photon statistics and simple, cost-effective

producibility is one such notable candidate. Moreover, availability of thermal probes in wide range of wavelengths makes them promising, particularly for imaging applications.

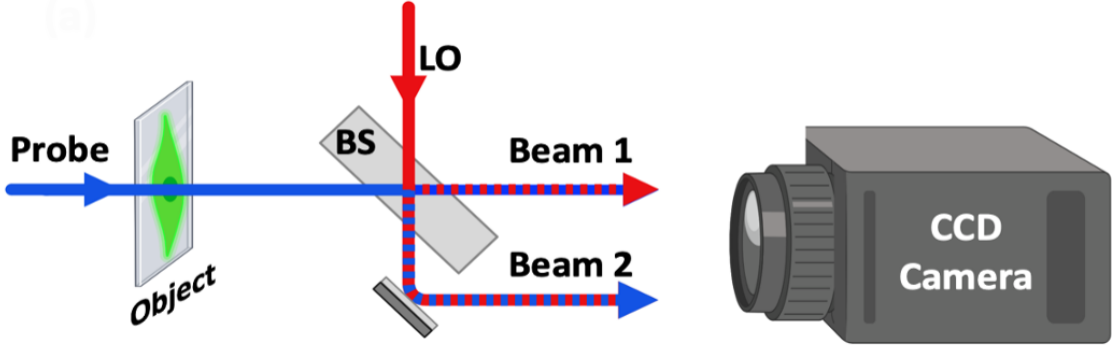


Figure 5.1: Simplified experimental setup. We show here only the detector side which contains a black-box probe and local oscillator source.

5.1.1 Calculation of Normalized Variance

Fig.5.2 represents the theoretical model we use to model the imaging process. A single-mode thermal probe ($\hat{\rho}_1$) with $\langle \hat{n}_{th} \rangle$ of average photons, interacts with an object to be imaged (\hat{T}_1) in mode 1 and mixed with a strong, mode-matched LO ($\hat{D}_2(\alpha)|0\rangle$) in mode 2 on a balanced beam splitter (\hat{B}_{12}). Since we aim to calculate the variance (signal) and the variance of variance (noise) of the photon number difference detected by camera pixels at position $\vec{x} = (x, y)$, operators $\hat{U}_{1,2}(\vec{x})$ facilitate the basis transformation from the probe and LO beam basis to the pixel basis. The eigenfunction of the i^{th} beam mode, $U_i(\vec{x})$, connects the annihilation operators in the beam and pixel basis as $\hat{a}_i^\dagger = \sum_{\vec{x}} U_i(\vec{x}) \hat{a}_{\vec{x}}^\dagger$ [170, 171]. Defining $\hat{N}_{1,2}(\vec{x})$ as the number operator for mode 1 or 2, correspondingly at the output ports, we can write moments of the photon-number difference operator $\hat{\mathcal{N}}(\vec{x}) = \hat{N}_1(\vec{x}) - \hat{N}_2(\vec{x})$ as:

$$\langle \hat{\mathcal{N}}(\vec{x}) \rangle = 0,$$

$$\langle \mathcal{N}^2(\vec{x}) \rangle = Tr \left[\left(\hat{N}_1(\vec{x}) - \hat{N}_2(\vec{x}) \right)^2 \hat{U}_2(\vec{x}) \hat{U}_1(\vec{x}) \hat{B}_{12} \hat{T}_1(\vec{x}) \hat{D}_2(\alpha) |0\rangle \langle 0| \hat{\rho}_1 \hat{D}_2^\dagger(\alpha) \hat{T}_1^\dagger(\vec{x}) \hat{B}_{12}^\dagger \hat{U}_1^\dagger(\vec{x}) \hat{U}_2^\dagger(\vec{x}) \right]. \quad (5.1)$$

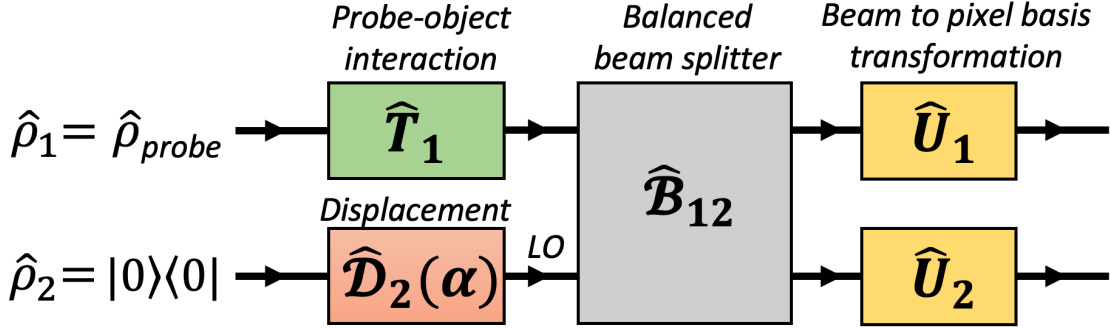


Figure 5.2: Block diagram of operator actions in QSI scheme: \hat{T}_1 acting on probe state $\hat{\rho}$ in mode 1 represents the object-probe interaction. In mode 2, operator $\hat{D}_2(\alpha)$ displaces vacuum state. Resulting states in both modes are allowed to interfere by the beam splitter operator \hat{B}_{12} . Two output modes of the beam splitter are transformed from the beam basis to the pixel basis by the mode transformation operators, \hat{U}_1 and \hat{U}_2 .

Using intensity of the LO for normalization and by neglecting $\mathcal{O}(|\alpha|^{-2})$ terms, it can be shown that normalized variance is:

$$V(\vec{x}) = 1 + 2 \langle \hat{n}_{th} \rangle \left| \tilde{U}_1(\vec{x}) \right|^2 \quad (5.2)$$

with $\tilde{U}_1(\vec{x}) = U_1(\vec{x}) \cdot T_1(\vec{x})$. This is the normalized variance measured by any individual pixel of the camera and represents the smallest unit of the entire noise statistics. Variance of this variance can be directly calculated with the fact that fourth moment of the Gaussian probability distribution is three times the square of the second moment. Measurement sensitivity can be further improved by effectively increasing the detection area by combining the readout of several nearby pixels, in the process we call "binning". Details of the

calculation of binned variance are discussed later in this Ch.C.

5.1.2 Theoretical Signal-to-Noise Ratio (SNR)

In differential imaging scheme, object is illuminated with a probe field and its transmitted intensity is compared with that of a reference beam to infer spatial profile of the object. Denoting the mean value of the probe photons as $\langle \hat{n} \rangle$, theoretical SNR for differential imaging can be defined as

$$SNR = \frac{S_1 - S_0}{\sqrt{\Delta S_1^2 + \Delta S_0^2}} \quad (5.3)$$

with signal, S_0 and S_1 being the detected intensities of the probe and reference beams, respectively. Corresponding noises are quantified by variance terms, ΔS_1^2 and ΔS_0^2 with definition, $\Delta S_i^2 = \langle S_i^2 \rangle - \langle S_i \rangle^2$. To compare our method to a conventional method, we cannot just replace the thermal probe with a laser probe, since this would not produce any image (as the shot-noise variance of a coherent states cannot be distinguished from the shot-noise variance of the vacuum state). The closest alternative is to modify the setup by removing the beam splitter, so that the image is obtained by comparing intensities rather than field amplitudes (in homodyne detection). This is equivalent to the classical differential imaging (CDI) and is often used as a benchmark [165, 172]. For CDI with coherent state probe of $\langle \hat{n}_{coh} \rangle$ average photons, Eq.(5.3) gives

$$SNR_{CDI} = \frac{(1-t) \langle \hat{n}_{coh} \rangle}{\sqrt{\langle \hat{n}_{coh} \rangle (1+t) + 2(\Delta N_d^2)}} \quad (5.4)$$

where t is the object transmittance and ΔN_d^2 is the variance of the dark counts. We expect lower SNR if the input state has more noise than a coherent state, e.g., a thermal state [173]. In the context of QSI, we adapted Eq.(5.3) by defining signal S_0 and S_1 as the variance of the photon number difference in the presence and absence of the object in the setup, respectively. Corresponding ‘noise’ terms, ΔS_1^2 and ΔS_0^2 , are given by the variance of variance terms. For a thermal probe of $\langle \hat{n}_{th} \rangle$ average photons, SNR can be calculated

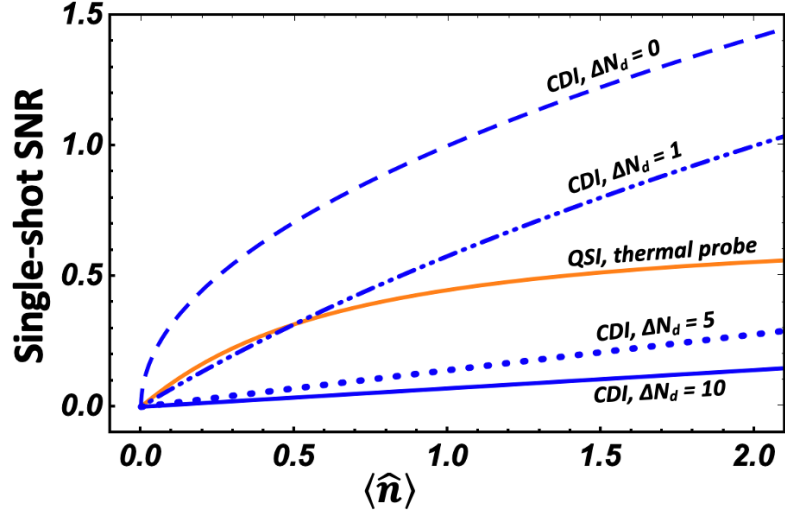


Figure 5.3: Theoretical plot of single-shot SNR as a function of averaged probe photons. QSI with a thermal probe (orange) is compared with a coherent state differential imaging for dark- count standard deviation (ΔN_d) ranging from 0 to 10 per pixel. For the CCD camera used in our experiments $\Delta N_d = 10$ per pixel. Object is assumed to be completely opaque (i.e. $t = 0$).

as:

$$SNR_{QSI} = \frac{2(1-t)\langle \hat{n}_{th} \rangle}{\sqrt{4 + 8\langle \hat{n}_{th} \rangle^2(1+t^2) + 8\langle \hat{n}_{th} \rangle(1+t)}} \quad (5.5)$$

Fig.5.3 shows comparison in terms of theoretical SNR, between QSI (with thermal state probe) and CDI (with coherent state probe). When dark noise is taken into account, QSI method offers higher SNR than the classical method.

5.2 Experimental verification

5.2.1 General Description

In this section, we describe the experimental verification of the theory discussed in the previous section. A close-up layout of the setup is depicted in Fig.5.4. Operationally, the super-Poissonian vacuum probe field passes through an object, then combines with a strong local oscillator at a polarizing beam splitter (PBS). Next, the resulting beams pass through a $\lambda/2$ waveplate(WP) set at 45° , where they interfere before being split again

by a polarizing beam displacer (PBD) and subsequently collected on a Princeton Pixis 1024 camera. This effectively implements a classical homodyne detection scheme using a camera. The FWM setup remains the same as presented in Ch.3. For the actual data acquisition, we replace the bright seed with a vacuum seed.

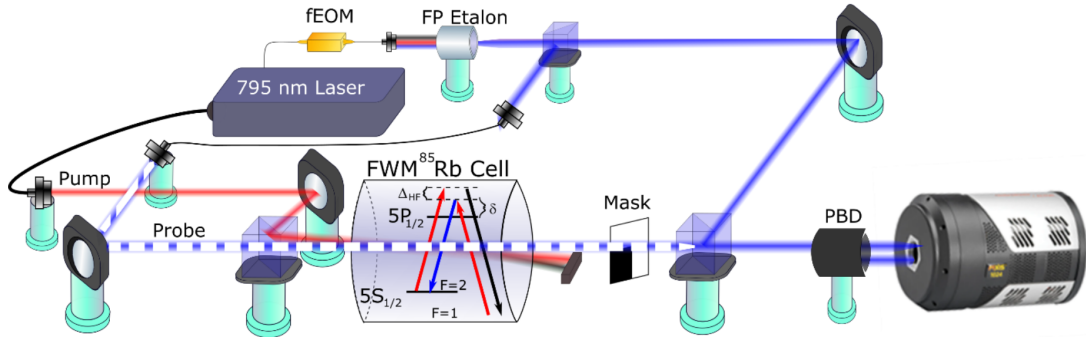


Figure 5.4: Detailed experimental setup using FWM as the thermal field source.

The key distinction between our approach and traditional homodyne detection is the use of a camera rather than a single photodiode, thereby enabling spatially resolved measurements. Essentially, camera-based homodyne detection applies standard homodyne principles to every pixel pair in two pixel arrays, \mathcal{M}_1 and \mathcal{M}_2 . Consequently, each pixel pair $\mathcal{M}_1(a, b)$ and $\mathcal{M}_2(a, b)$ can be viewed as an individual homodyne detector, mirroring the functionality of traditional homodyne setups but scaled to an entire camera's field of view.

5.2.2 Frequently Asked Technical Details

In this section we discuss the essential technical details of the experiment setup. The goal is to provide sufficient information for researchers who wish to reproduce the results of this work.

Imaging System setup

To maximize the resolution of the reconstructed mask or object, we implement a 2F lens system. First, an $f=150$ mm lens is positioned immediately after the polarizing beam

displacer(PBD). By illuminating the setup with a bright probe seed (for calibration), we carefully adjust the lens position to minimize distortion in the recorded image. Another $f=150$ mm lens is placed before the object/mask, ensuring that more thermal photons enter the detection region when the system operates with a vacuum seed. This arrangement helps maintain high-resolution imaging while optimizing photon collection efficiency.

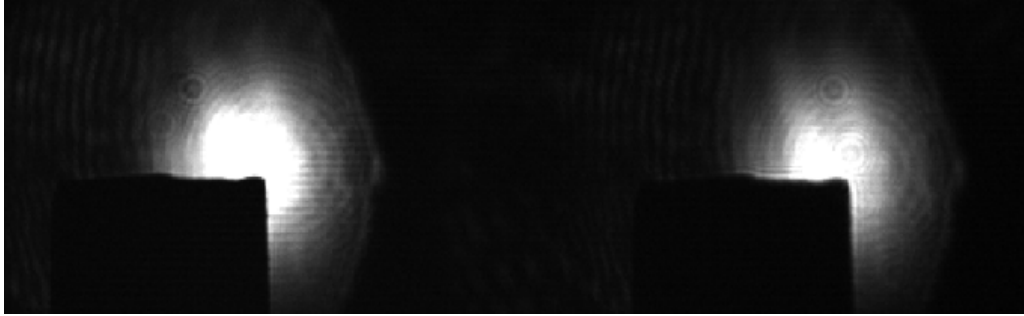


Figure 5.5: Classical image of an opaque knife edge. The two images have no observable difference even though a slight difference in optical path.

We note that our method assumes the twin beams can be recombined with perfect overlap, i.e., no discrepancies in dispersion or focusing before they reach the camera. Mathematically, a focus discrepancy after separation implies that additional transformations after \hat{B}_{12} as in the flow chart in Fig.5.2, introducing additional errors when we calculate everything in the camera’s pixel basis.

In practice, discrepancies in the twin beams do arise. The PBD can also introduce variations in optical path length. Another source of these discrepancies is the use of a single lens with relatively large curvature (short focal length $f = 150$ mm to focus both beams onto the camera, which can cause potential distortion.

We consider these differences negligible for two reasons: first, the optical path and distortion discrepancies remain sufficiently small, and second, because the distance between the lens and camera is only 150 mm, any minor focusing variation has not fully developed. Indeed, as seen in the classical image of an opaque block (Fig.5.5), the twin images remain effectively equivalent.

We note that, when imaging finer targets in the 10–50 μm range, imperfections in the



Figure 5.6: Classical image of the bug wing. In this case we see slight difference in the twin images due to a finer target($10 \mu\text{m}$)

optical system become more significant. As an example, Fig.5.6 shows a classical image of a wasp wing, where the left beam region appears sharp, whereas the right side exhibits slight smudging due to combined effects of optical path differences. This represents a fundamental resolution limitation in our setup. However, we did not pursue finer resolutions in this thesis. For future studies aiming for higher resolution than presented here, correcting discrepancies due to the optical path length difference will be necessary.

Data Acquisition and Analysis Procedure

All imaging data are recorded using the Princeton Pixis 1024 CCD camera, which features low dark noises counts (standard deviation ≈ 10 dark counts per pixel) and high quantum efficiency (95%). To compensate for the camera's relatively low speed, we record a quick sequence of images in clusters, with $1.7 \mu\text{s}$ exposure time for a $544 \mu\text{s}$ duty cycle. Each cluster consists of 6 images, although only the second through fourth images are suitable for the analysis due to leakage contamination. Further steps are shown in Fig.5.7: the recorded images are spatially matched and subtracted pairwise across the beam region (similar to the traditional homodyne detection). We then calculate the normalized temporal variance within one cluster (6 images total, 3 matched pairs) as:

$$V(\vec{x}) = \frac{\langle (N_1(\vec{x}) - N_2(\vec{x}))^2 \rangle}{\langle N_1(\vec{x}) + N_2(\vec{x}) \rangle}. \quad (5.6)$$

Here we assume that the two recorded beams have identical spatial distributions and

are perfectly matched. $N_1(\vec{x})$ and $N_2(\vec{x})$ are photon counts at the point \vec{x} within the corresponding beams. $V(\vec{x})$ is further averaged over all kinetic clusters in a given set to obtain the final variance map. We can construct the transmission map of the object

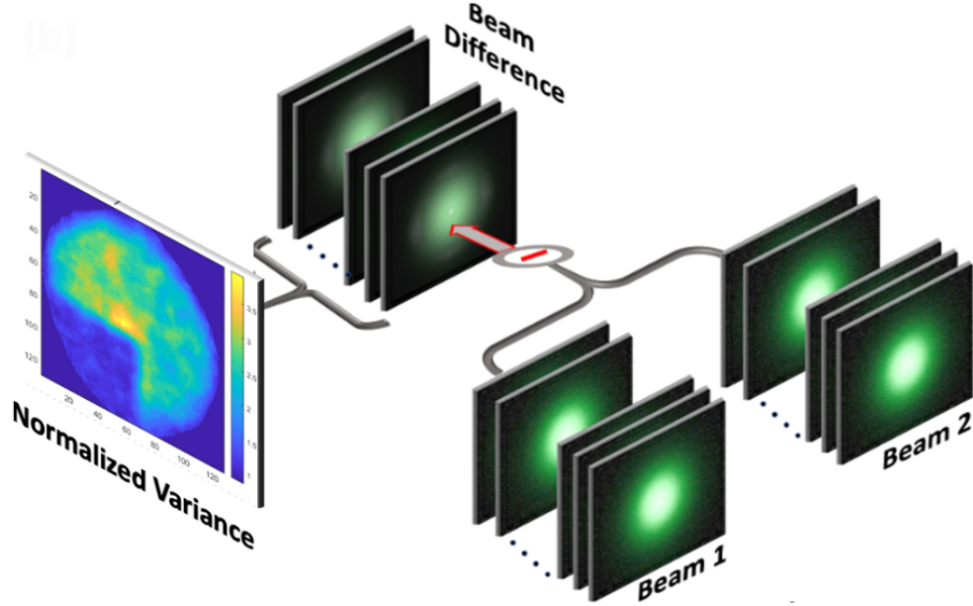


Figure 5.7: Illustration of data acquisition and processing sequence.

from the variance map using Eq.(5.6). Experimentally, the SNR is calculated using the transmission map by selecting two regions of interest (ROI), each within the blocked and unblocked halves (We selected only a small central area with a proper spatial overlap between the probe beam and LO. With this, the experimental SNR is given by,

$$SNR_{single} = \frac{S_{unblocked} - S_{blocked}}{\sqrt{\Delta S_{unblocked}^2 + \Delta S_{blocked}^2} \sqrt{M}} \quad (5.7)$$

with $S_{unblocked}$ and $S_{blocked}$ being the means and $\Delta S_{unblocked}^2$ and $\Delta S_{blocked}^2$ being the spatial variances of the two ROI in the blocked and unblocked halves of the transmission map. M is the total number of datasets.

The spatial mode of the thermal state can be directly explored by seeding the input probe channel, allowing us to optimize the spatial overlap between the LO and the thermal

field. This optimization is achieved by maximizing the visibility of the interference fringes between the seeded, amplified probe field and the LO. Mode matching between thermal and LO modes is quantified by the normalized overlap,

$$\mathcal{O}(\vec{x}) = \frac{\int_A LO_{Th}^* dA}{\sqrt{\int_A LO_{LO}^* dA}} \quad (5.8)$$

The normalized variance detected at any pixel location \vec{x} is affected by the overlap value at that location,

$$V(\vec{x}) = 1 + 2\hat{n}_{th}t(\vec{x}) \cdot \mathcal{O}(\vec{x}). \quad (5.9)$$

In the current work, the overlap was close to unity, thus maximizing the SNR and ensuring good agreement between theory and experiment. However, poor mode matching will reduce the overlap and deteriorate the SNR.

Here we list step by step how we do the image processing. For each duty cycle, we use four intermediate images, each containing two beams separated by the PBD, to calculate the variance. The first step is to perform a pairwise subtraction of the two images to remove the classical noise, analogous to the same subtraction process in homodyne detection.

As we have briefly mentioned above, the two beams need to be properly overlapped before subtraction. The process is done by calculating the center of mass of both beams within the ROI. Such an overlap, however, in many cases are not good enough for our purposes. The reason is the two ROI of beams has a strong spatial correlation, but the pixel size fundamentally limits how good we can shift and overlap.

We thus perform the sub-pixel shift in post-processing. In practice, we artificially divide each physical pixel into several sub-pixels in post-processing process so we can do finer adjustment when doing beamoverlap. In other words, adjustments for smaller than one physical pixels is made possible. Despite a small change, this method in fact greatly improves the overall-variance calculation.

The next step we do is to select a proper ROI. There are two main reasons for consideration.

First, we want to exclude the boundary regions with very low photon counts. In these regions, when we calculate the variance, due to the contribution of dark noise (through relatively small for our purposes) and weak LO (causing potential error in normalization), we frequently observe nonphysically large variance.

Second, we observe an inhomogeneity of visibility. The LO has a distinct spatial mode compared to both the vacuum seed and the bright probe used. Since the interference is done without explicit spatial mode matching, our assumption of unity $\mathcal{O}(\vec{x})$ is not always valid. However, we observe in experiment that the visibility can be vastly different between the beam center and peripheral regions. One example is shown in Fig.5.8

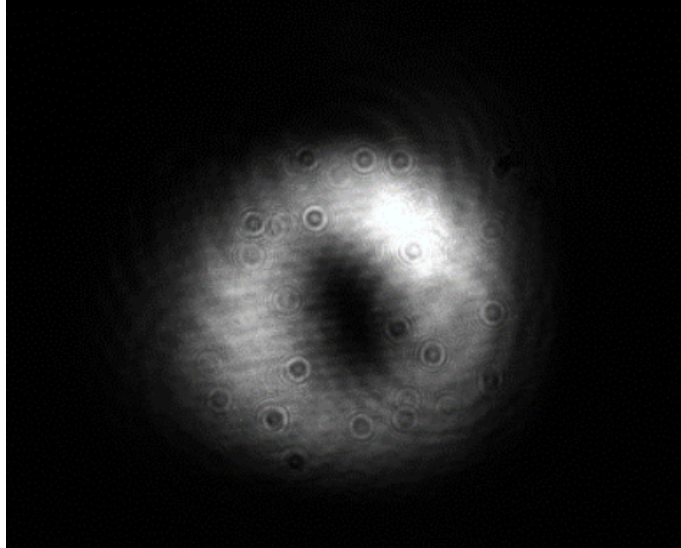


Figure 5.8: Sample interference pattern between the weak probe seed(test beam) and the local oscillator. We observe that instead of displaying a full black(destructive) or bright(constructive) interference pattern, the interference occurs exclusively at the center region. The visibility is generally over 98%.

We see clearly that a destructive interference occurs only at the beam center. We intentionally tune the LO beam path such that the interference pattern is optimized at this location for the probe channel. Since the probe seed, as part of the squeezer(see

Ch.3), shows the strongest FWM gain, we ensure that in the vacuum case, the LO can amplify the thermal vacuum as well. Thus, at the beam center, the visibility is high and our assumption of unity $\mathcal{O}(\vec{x})$ remains valid if we select the ROI around only the center. Besides, due to the interference nature of our method, only the portion of signal field with high $\mathcal{O}(\vec{x})$ will be used.

Based on these two reasons, we usually apply a mask after doing the pairwise subtraction and shift.

This allows us to reconstruct the transmission map of the object using the measured quantum noise map, given by:

$$t = \frac{V_{probe} - 1}{V_{ref} - 1}, \quad (5.10)$$

where V_{ref} is the normalized quadrature variance of the unobstructed thermal beam, and V_{probe} is the normalized quadrature variance measured with the object inserted in its path. This formulation is essentially derived from Eq.(5.6). For a coherent state or vacuum field we have $t = 0$; while for a super-poissonian or sub-poissonian field, we saw positive or negative values, respectively. We therefore can map out the beam shape based on the variance map easily.

Procedure of Laser Pulsing

The major reason we choose this pulsing sequence is to minimize the residual pump leakage. It is true that the leaked pump can still be considered as coherent states. Nevertheless, given that we are working with small photon counts as small as $\langle \bar{n} | \bar{n} \rangle \approx 0.1$ per pixel, the existence of pump leakage can easily wash away any features after normalization as stated in Eq.(5.6). The key to minimize pump leakage is to minimize the pump field on-time by pulsing. We achieve the pulsing by utilizing an acoustic-optical modulator (AOM) in the pump path, with an 80% power conversion efficiency into the 1st-order modulation. Ideally, we prefer to turn on the pump only when the camera is recording the data. However, we notice that there is delay time between the pump field turning on and FWM output stabilizes, a joint effect of atomic coherence, AOM response and camera response

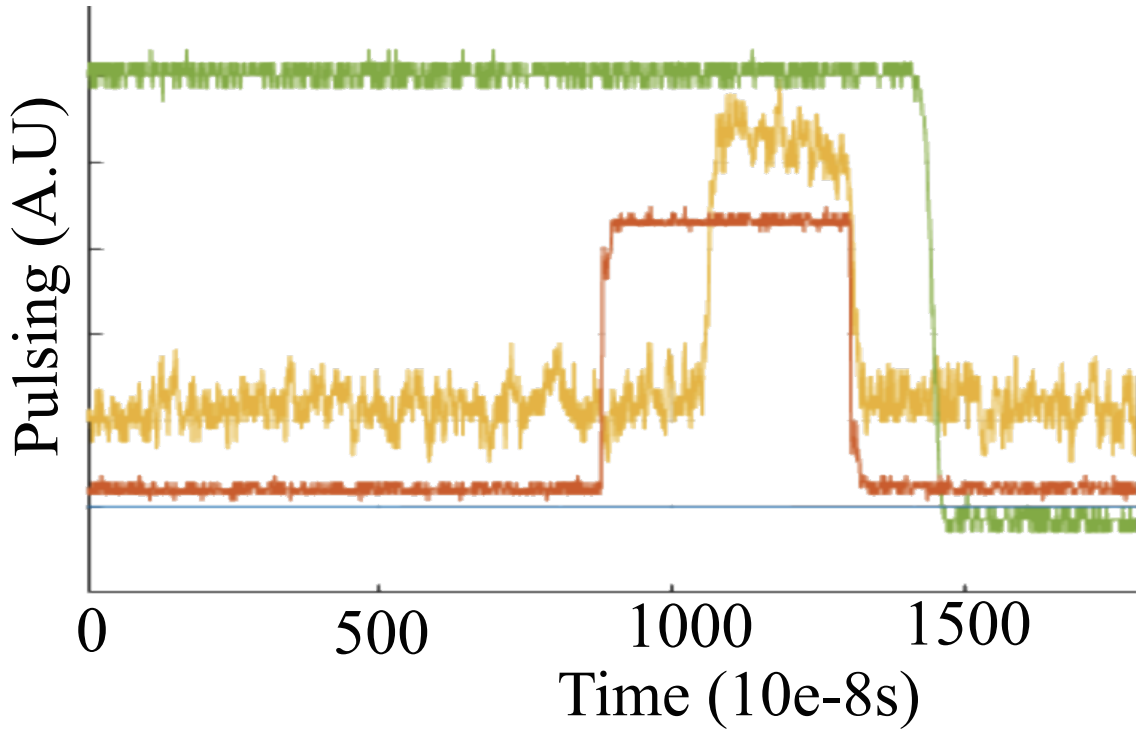


Figure 5.9: Representative pulsing sequence of the data acquisition illustrating the process. All pulses (green: pump, red: camera trigger, yellow: LO) are triggered from the camera acquisition trigger. Later the pulses are adjusted such that the probe pulse is overlapped with the camera pulse.

time. Since the camera data taking time per shot is only $2.7\mu\text{s}$, the system will not reach a steady state if the pump is turned on for each camera shot. The local oscillator is also pulsed using an AOM. However, unlike the pump field pulsing which is limited by the atomic coherence stabilization time, the local oscillator pulsing time can be much shorter. Pulsing also allows us to modulate the signal and stay away from the $1/f$ noise.

We end up turning on the pump before the beginning of a $544\mu\text{s}$ full data acquisition cycle. A sample pulsing sequence for one camera shot (not the full cycle) is shown in Fig. 5.9. The pump (green trace) has a much longer on-time compared to the camera trigger time (orange) and LO pulse time (yellow). We notice a delay between the camera trigger and the probe pulse, which is due to the response time of the probe. We therefore adjust the pulse time such that the probe pulse is slightly shorter and fully overlapped with

the pump pulse. In most cases, the first and last images in a full duty cycle are discarded due to an excessive amount of pump leakage. In the first image, the pump is turned on for a longer duration since it is on before the camera's data-taking sequence. The last image, on the other hand, is usually contaminated due to the pump and camera not turning off on time properly. The remaining four intermediate images are generally clean, and we use them for our variance calculation.

Camera Binning Method

In a CCD camera, each pixel acts as an independent detector, collecting only the light falling on its surface. Since the mode size of thermal field is much larger than the pixel size ($13 \mu m \times 13 \mu m$), the average number of photons per pixel $\langle n \rangle_{pxl}$ is proportionally small, and the variance value is close to one, making it hard to distinguish from the coherent vacuum. To improve the sensitivity of our measurements, we group pixels together to effectively increase their cumulative detection area.

There are two types of pixel binning: square binning, and circular binning. In our data processing process, we used the circular binning to preserve the resolution. Here we first introduce the basics of both binning methods.

Method 1: Square Binning Square binning probably is the most intuitive binning method. Essentially, it groups several pixels in a square shape into a effective larger pixel. For example, if we have a camera detection region of 100×100 pixels, and conduct a 2×2 pixels square binning, we effectively have a camera detection region of 50×50 pixels with each pixel 4 times larger. We note that in this case, each pixel in original basis is grouped into one and only one larger, new pixel with no repetitive counting. This which is one major difference from the circular binning.

Method 2: Circular Binning Circular binning, on the other hand, is a bit harder to digest conceptually. A basic illustration of this procedure is shown in Fig.5.10. In short, it is a running average method that can be effectively view as a spatial low-pass filter.

In this binning protocol, the photon count of each pixel at \vec{x} is replaced by the sum of photon counts from all neighboring pixels within a binning radius, R . Since all pixels are

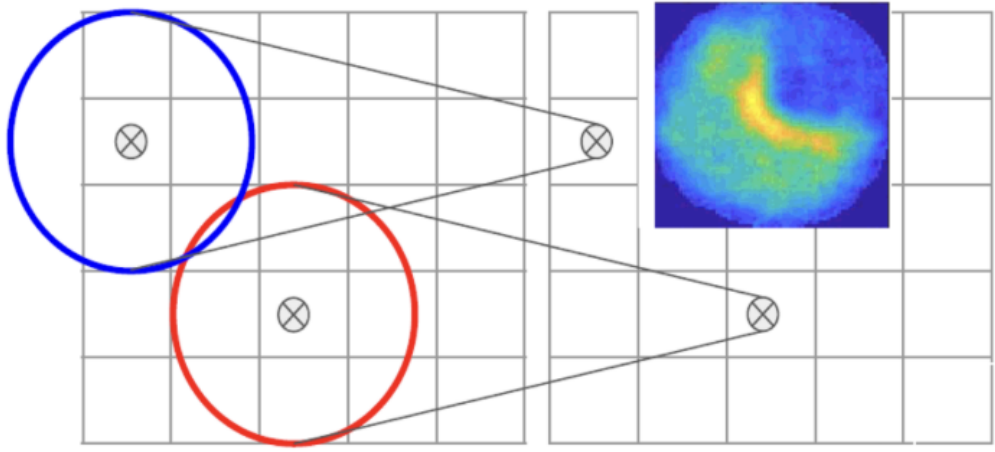


Figure 5.10: Illustration of the circular binning procedure. We assign all pixels in a gaussian circle as one. The inset illustrates the case of $R = 2$ circular binning.

square shape, the number of pixels included is approximated by a Gaussian Circle. This binning method improves the SNR but at the cost of reduced spatial resolution, as we are reassigning value to, not grouping a certain number of, pixels.

Nevertheless, it is often questioned why we can perform circular binning like this, as we are counting pixels repetitively. To see why such circular binning is justified, let us consider the following simple case as illustrated in the inset of Fig.5.10.

We observe that the variance is zero at the knife-edge boundary, while the unblocked region shows nonzero variance. In the ideal case, we should see a sharp cut at the center boundary, resembling a step function. The SNR is related to the contrast between the two regions, as defined in Eq.(5.7). Circular binning can be understood as enhancing the contrast in the non-zero region of the step function, while the resolution (it is still a step function after multiplying the factor) is unchanged. However, for the resolution remain unchanged, we have assumed that the circular binning does not mix the pixels from the blocked and unblocked region. In other words, we are assuming within each binning region, all pixels are from the same region (either blocked or unblocked), thus the recounting doesn't hurt the resolution.

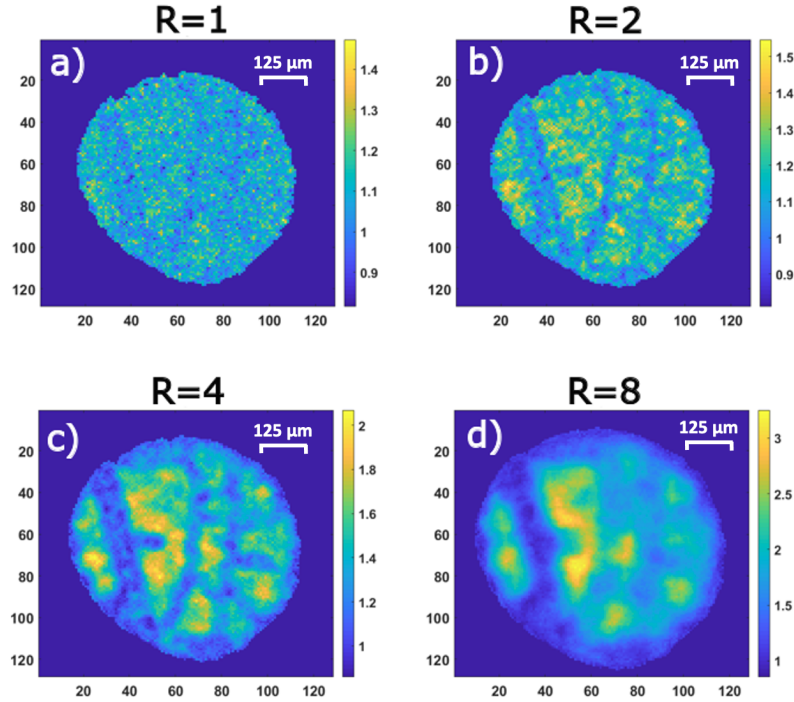


Figure 5.11: Variance map (a) of the insect wing is generated with $R = 1$ and 0.03 photons per pixel per $1.7 \mu s$ exposure. Images (b-d) are generated with values of the binning radii $R = 2, 4,$ and $8,$ respectively.

This assumption, however, is not always true. When pixels from both regions are mixed, the sharp boundary is smudged, and the resolution decreases proportionally to the binning radius R . One clear example of this is shown in Fig.5.11, where different binning sizes are used. We see the contrast increases but the resolution drops, especially in Fig.5.11 (d). We also see that in (d) that the left veins are completely smudged together and not differentiable anymore. This shows the limit of our circular binning method. The binning size is also limited by, and needs to be comparable to, the size of light spatial mode, which we look into the thermal vacuum source and photon calibration sections. See Appendix.C for details of binning variance calculation.

Fig.5.11 shows variance maps of an insect wing at different levels of binning. To construct this variance map, we recorded 0.006 photons/pixel/frame (a total of $\approx 27,000$ thermal photons over 600 frames, generated by the FWM method). Since the binning

process combines photon counts from all neighboring pixels within the binning radius R , the ‘effective’ photon/pixel/frame count to generate as in Fig.5.11(a) is 0.006×5 . Since the variance of the coherent field in the blocked region and the unobstructed weak thermal beam are not very different, smaller bin sizes yield low contrast. Larger binning radii yield better contrast between the two regions, as shown in the last row of Fig.5.11, although their boundary is smoothed by the binning process thus degrading resolution.

Sources of thermal vacuum

In this section, we discuss different methods for generating a thermal vacuum, which is a key component of experiments using low-intensity super-Poissonian optical fields. One approach involves producing a pseudo-thermal state by employing a rotating scatterer. Alternatively, we can utilize one of the twin beams generated by FWM. This beam is a true thermal field, as demonstrated in Ch.2.

Method 1: Pseudo-Thermal Field From Rotating Diffuser

The setup for this method is shown in Fig.5.12(a). To see more details, please refer to citation[176]. Thermal field photons, from the phase coherence perspective, have essentially randomized phase, among each photon. The idea is to send a monochromatic, coherent field through a rotating diffuser. A narrow filter is then applied afterward to select only a small section of the total beam. The transmitted portion, scattered by random spots on the diffuser across the beam profile, acquires random phase while remaining monochromatic.

There are two important things to note. First, the super-poissonian state is only a pseudo-thermal state. The phase, which is highly dependent on the aperture size and the rotation speed of the scatter, is still not fully randomized to approach the extent of a true thermal state.

Let us consider two extreme cases. In the first case that the motor is not turned on, no matter how small the aperture is, the transmitted light is always scattered by the same region on the diffuser, leading to a constant phase delay. In the second case, if no aperture is not applied, all input photons—originally a coherent state—are collected, so there is no change in photon statistics. In this case, only the spatial coherence is destroyed, but the

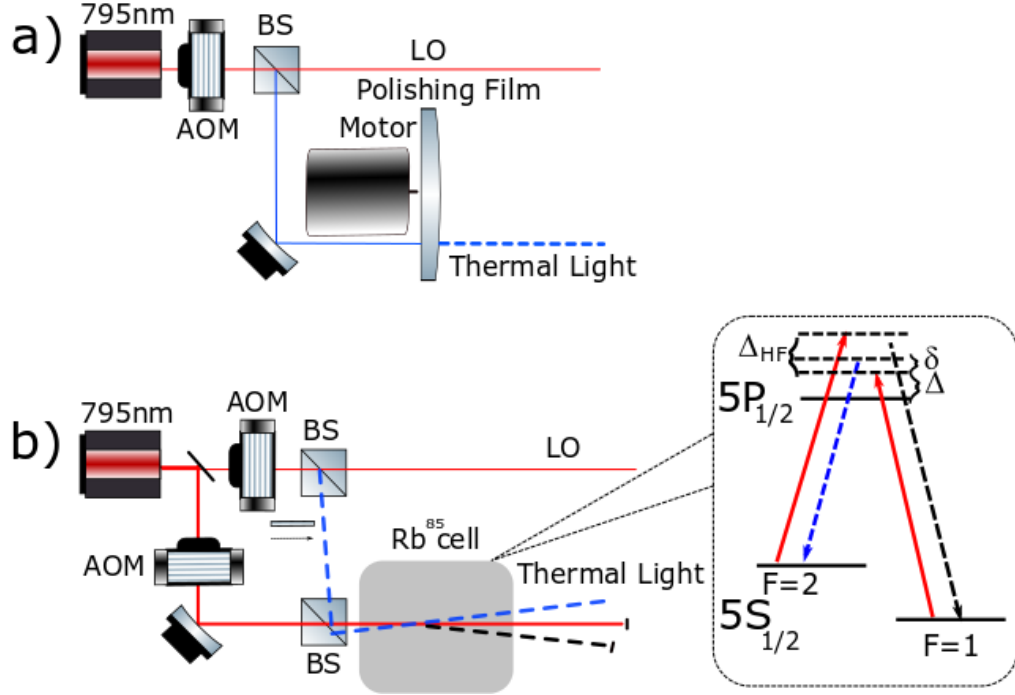


Figure 5.12: Experimental setup for a weak thermal state generation. (a) Pseudo-thermal state generated by scattering a coherent beam with rotating polishing film with grain size $\approx 0.1\mu m$. b) Thermal state source using FWM process: vacuum input is used as seed to generate weak thermal state. Inset: atomic level diagram of FWM process. Δ_{HF} is the hyperfine splitting between $5S_{1/2}F = 2$ and $5S_{1/2}F = 1$ level. Δ is the one-photon detuning and δ is the two-photon detuning. The red line stands for the pump laser. The blue and black lines represent probe and conjugate beams, respectively [174, 175].

temporal coherence remains intact. In conclusion, we need both a sufficiently high rotation rate and the smallest aperture to approach a true thermal state. Nevertheless, since both parameters have limitations, we can never reach, but can only get infinitely close to, a real thermal state. Thus, we refer the output of this method as a Pseudo-Thermal state. In the actual experiment, we sent a coherent input field ($\lambda \approx 795$ nm) through a rotating diamond polishing film with a grain-size of $0.1 \mu m$.

Method 2: True thermal state using FWM

Another method for generating a super-poissonian state is by utilizing the FWM process. In the case of a vacuum input seed, the output fields are entangled, but each probe and conjugate field individually displays thermal statistics with normalized photon count

variation $\Delta n^2 / \langle \hat{n} \rangle = 1 + \langle \hat{n} \rangle$. The squeezer setup is the same as discussed in Ch.3, and is shown in Fig.5.12(b). The pump field ($\lambda = 794.7930$ nm) is collimated (beam diameter 0.55 mm) and directed to a 2.5 cm-long ^{85}Rb vapor cell, maintained at 104.5°C . A fraction of the same laser output is used to produce both, the LO at probe field frequency and the input probe field, when necessary. For this, the split beam is phase-modulated at 3035 MHz (corresponding to the ^{85}Rb $5S_{1/2}$ hyperfine splitting) using a fiber electro-optical modulator (fEOM), and the lower modulation sideband is filtered using a Fabry-Perot (FP) etalon. Under these conditions, the FWM gain is sufficiently strong $G \geq 7$ for ≈ 80 mW pump power, with no significant atomic absorption at the probe field frequency. After the vapor cell, the pump field is filtered using the polarization and spatial filtering, and only the output probe field is directed first to the imaged object and then to the detection unit. Both the pump and the probe fields are pulsed using AOMs, synchronized with the camera's image-taking sequence.

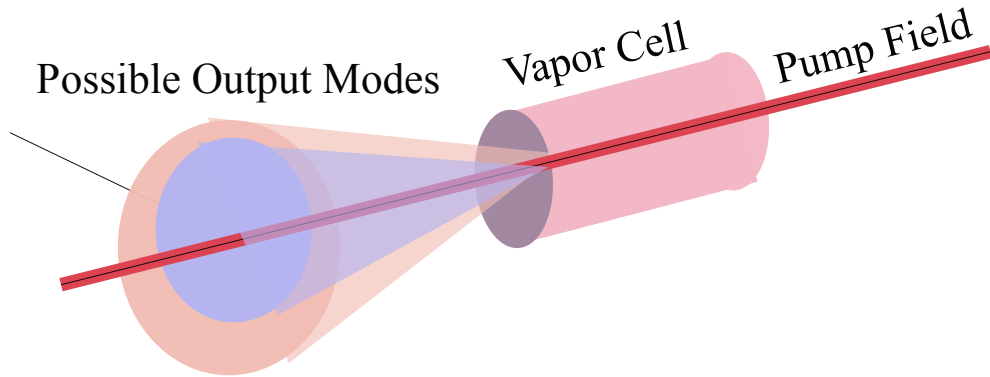


Figure 5.13: Illustration of different thermal vacuum mode generation. Due to the presence of all possible vacuum modes, the output spatial modes show intrinsically multimode behavior, and can occur within a cone region. Here the blue and pink cones show the thermal vacuums for the probe and conjugate fields.

It is convenient to use this source for precise comparison between theory and experiment, since it provides a reliable and repeatable way to control the average photon number in a specific spatial mode through the FWM gain by adjusting the pump beam strength or laser detuning.

It is worth discussing the difference between vacuum-seeded FWM and the seeded FWM described in previous sections. The strong atomic coherence and dispersion created by the pump field allow for a nonzero Δk . Physically, this means that the thermal vacuum is generated over a wide range of angular spreads, as shown in Fig.5.13. Mathematically, the output state for different spatial modes $|0\rangle_i$ can be expressed as

$$|0\rangle_1 \otimes |0\rangle_2 \otimes |0\rangle_3 \dots |0\rangle_i \quad (5.11)$$

In contrast, in the seeded case, one bright spatial mode is fixed by the probe seed field [177], so that the output field can be represented as

$$|n\rangle_1 \otimes |0\rangle_2 \otimes |0\rangle_3 \dots |0\rangle_i \quad (5.12)$$

Here, the other vacuum fields are much weaker. In our experiment, we must consider infinitely many different thermal states. This intrinsic spatial multimode behavior directly affects our variance calculations and photon number calibration. For example, if the circular binning size is chosen to be too large, it begins to mix different thermal modes. Further details are provided in the next section.

Photon Number Calibration

To compare the experimental SNR values with Eq.(5), we need to accurately estimate the average photon number in the thermal probe field. This requires taking into account the bin size and the number of physical pixels integrated during the binning process. If $\langle n \rangle_{pxl}$ is the average number of photons in the unobstructed thermal beam per physical pixel, then the number of photons in each binned pixel scales as $\langle \hat{n} \rangle = a \langle \hat{n} \rangle_{pxl} = \frac{a}{A} \langle \hat{n}_{tot} \rangle$. Conveniently, this allows us to vary the average photon number by varying the binning radius. Since our measurement procedure involves subtraction of the two outputs before the camera, the measured normalized variance of the photon counts as a function of transmission coefficient is given by Eq.(2), where it maps to $\left| \tilde{U}_1(\vec{x}) \right|^2$. Fig.5.14 shows the measured

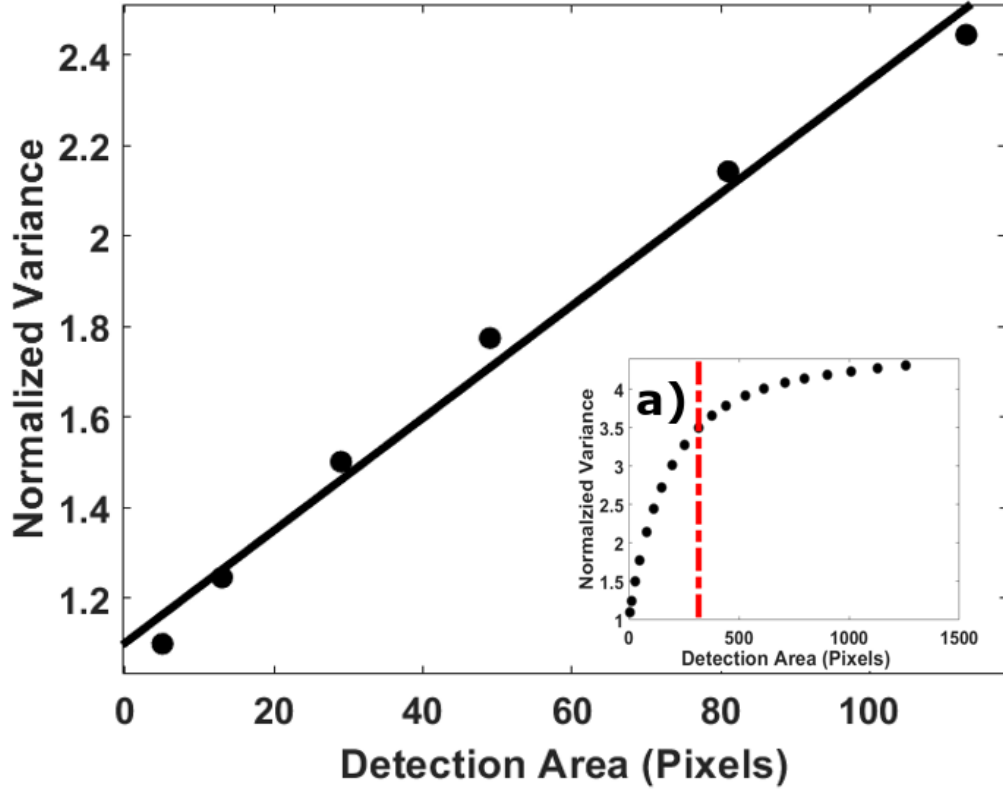


Figure 5.14: Normalized variance (V) as a function of the detection area (a). The best linear fit is $V = a \times (0.01242 \pm 0.0018) + (1.10 \pm 0.11)$, matching the prediction of Eq.(2). Inset: the same plot for a wider range of detection areas, displaying the V saturation by increasing a .

normalized variance as a function of photon number (black dots) for a set of experimental data obtained with the FWM method. As expected, the variance depends linearly on the bin area for small binning radii. The slope of this curve allowed us to extract information about $\langle n \rangle_{pxl} = 6.2 \times 10^{-3}$ for a pump power ≈ 80 mw. However, for large binning ($R > 10$), the variance starts to deviate from the linear behavior and exhibits signs of saturation (Fig.5.14 inset). This behavior can be explained by noting that the outputs of the FWM process are expected to contain multiple spatial modes [178, 179]. Assuming j such thermal modes are to be equally populated, theoretical normalized variance saturates as $V = 1 + \frac{2 \langle \hat{n}_{th} \rangle}{j}$ [180]. Thus, for larger binning radii, the measured variance must contain contributions from multiple thermal modes, deviating from the predictions of a

single-mode theory.

5.2.3 Experimental Results

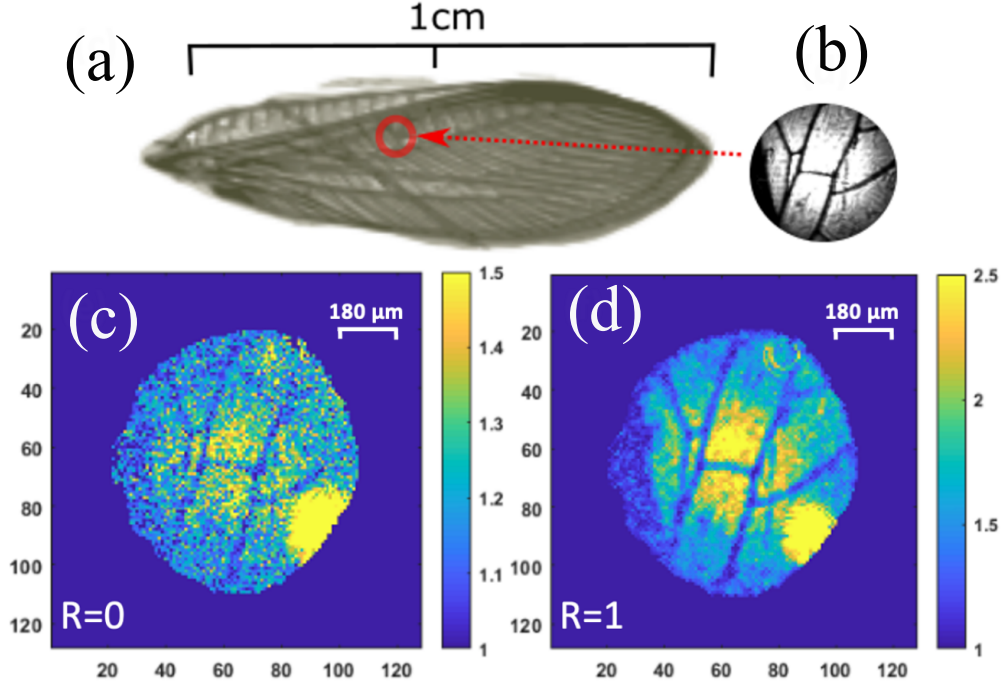


Figure 5.15: (c) Image of an insect wing with dimensions indicated for reference. (d) Inset shows an enlarged image of the region of interest, obtained with a bright beam. (e) Normalized variance map of the wing obtained with $\approx 301,600$ photons and without any processing. The resolution is around $10 \mu m$, limited by the optical setu, and can be further improved. (f) Normalized variance map after binning all the pixel values within one pixel radius (i.e. $R = 1$). The image contrast increases at the expense of spatial resolution. Note that a thermal state with 0.1 photons/pixel/exposure on average is used for generating image (e).

In this section, we present main results of this project. We experimentally demonstrate QSI with a weak thermal state, produced using two different sources. Fig.5.15 shows an image of a semi-transparent insect wing, obtained using a pseudo-thermal light, generated by passing a coherent laser field through a rotating diffuser. The corresponding normalized variance map is constructed using 200 image clusters (3 images/cluster, with an time of $1.7 \mu s$ per image) and an average photon number per pixel per frame $\langle n \rangle_{pxl} \approx 0.1$, which

is well below the dark noise level of 10 photons per pixel. Thus, this image required total of a 60 photons per pixel. The finer details of the wing structure (width $\approx 17\mu\text{m}$) can be clearly resolved without further processing, as shown in Fig.5.15 . However, we can boost the image contrast by increasing the effective number of photons per detected area following the binning process. The same image, post-processed with the smallest binning radius $R = 1$ is shown in Fig.5.15, demonstrating a significant improvement in quality, without much deterioration in the spatial resolution. Considering the simplicity of producing such pseudo-thermal light across a wide range of optical frequencies, this imaging technique can be easily adopted for various low-light imaging applications where resources like squeezed state are unavailable.

The variance is calculated based on Eq.(5.10). If a portion of the beam is blocked by a completely opaque object, we expect to have, on average, $t \approx 0$ for the blocked region and $t \approx 1$ for the unblocked region. The inset of Fig.5.16 is an example of the transmission map of a half-blocked thermal beam. Since we use $M = 600$ image clusters to calculate the SNR, it is divided by a factor of \sqrt{M} to compare it to the single-shot theoretical case and ensure fair a comparison with theory. We compare these experimental SNR measurements with theory by setting $t = 0$ in Eq.(5.5) for a completely opaque object:

$$SNR_{QSI} = \frac{2\langle\hat{n}\rangle}{\sqrt{2 + 2[1 + 2\langle\hat{n}\rangle]^2}}. \quad (5.13)$$

In such a case, the SNR is determined only by the average number of the detected photons $\langle\hat{n}\rangle$. We employ two different strategies to verify this experimentally. One approach is to vary the effective detection area by binning multiple pixels together. The number of photons in detection area can be expressed as $\langle\hat{n}\rangle = \left(\frac{a}{A}\right)\langle\hat{n}_{tot}\rangle$, where a is the detection area, A is the whole beam size, and $\langle\hat{n}_{tot}\rangle$ is the total average incoming photon counts. While a is determined by binning radius, $\langle\hat{n}_{tot}\rangle$ is controlled by the FWM gain. For these measurements, we carefully select the ‘dark’ and ‘bright’ areas in a partially blocked thermal beam, as shown in the inset of Fig.5.16, and verify that for a detection area with

less than a 10-pixel radius, the recorded optical field is strictly single-mode, and $\langle \hat{n} \rangle_{pxl}$ is calibrated independently. In second approach, we fixed a and varied $\langle \hat{n}_{tot} \rangle$ by changing the FWM gain with different pump powers. Fig.5.16 shows the experimental SNR as a function of $\langle \hat{n} \rangle$ for both methods. Black circles are recorded with a fixed detection area and varying FWM gain. Red triangles are recorded by changing the detection area while the FWM gain is held fixed at its maximum value. Remarkably, both approaches yield experimental data matching very well with each other, proving their equivalence. They are in reasonably good agreement with the theoretical SNR values from Eq.(5.5).

In the context of QSI, the contrast (C) of the images can be calculated as:

$$C = \frac{(V_{bright} - 1) - (V_{dark} - 1)}{V_{(bright - 1)} + (V_{dark} - 1)}, \quad (5.14)$$

with V_{bright} and V_{dark} being spatial averages of the normalized variances recorded by pixels in the bright and dark regions, respectively. We measured $C = 0.88 \pm 0.02$ for the image inset in Fig.5.16.

5.3 Conclusion

To summarize, we theoretically developed an approach to a low-exposure imaging using classical or quantum states that differ from a coherent one, and experimentally demonstrated its realization using thermal and pseudo-thermal light. We showcased this ability by imaging a biological sample, detecting as low as 0.03 photons/pixel/exposure on average, with just 27,000 photons making up the entire image. We also showed that in the low photon number regime, QSI with thermal light outperforms the classical differential imaging method when dark counts are taken into account.

The ability of image reconstruction using very low photon flux is desirable for numerous scientific, commercial, and defense imaging applications. The proposed method offers several attractive features. First and foremost, the wide availability of thermal light sources

broadens the scope of applications, potentially extending it in the visible and UV frequencies. Second, since thermal light does not have a fixed phase, our method does not require the LO phase stabilization, substantially increasing in reliability. Finally, since a portion of the thermal field still displays the thermal statistics with lower photon numbers, the spatial resolution can be optimized depending on the required SNR, as given by Eq.(5.5).

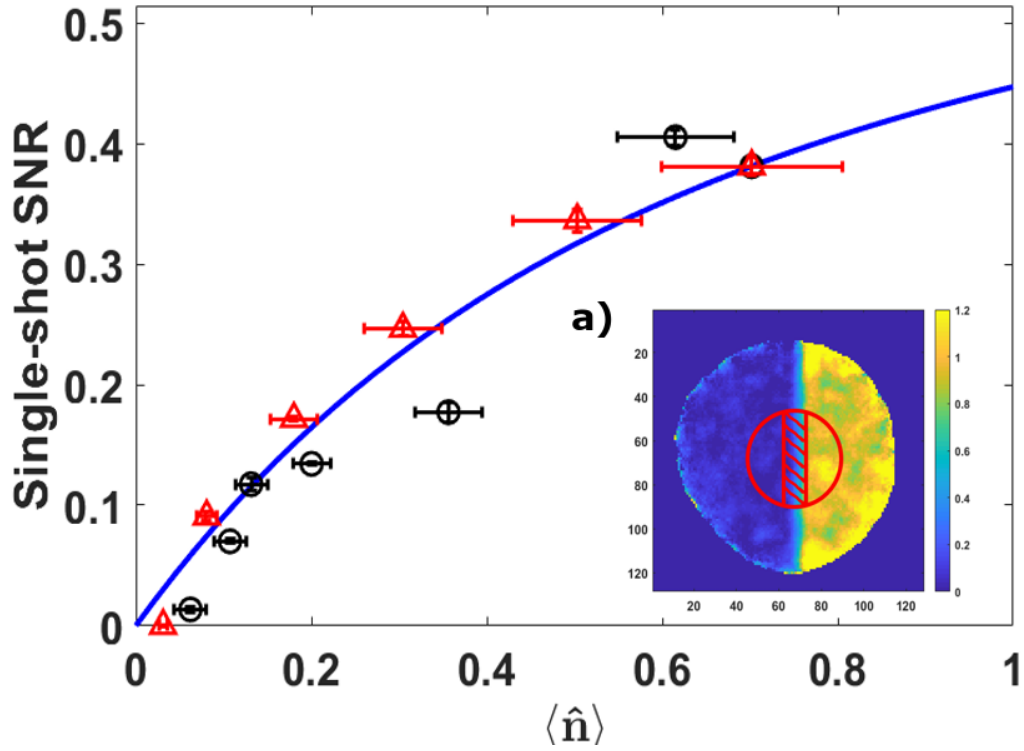


Figure 5.16: SNR for opaque object imaging in QSI scheme as a function of averaged thermal photon number per detection area $\langle \hat{n} \rangle$. The detected photon number was controlled by either changing the total FWM gain (black circles) for detection area size of $a = 113$ pixels, or by changing the detection area size (red triangles) for the highest FWM gain value. Solid blue curve is the theoretical SNR of Eq.(5.13). Experimentally measured SNR values are divided by $\sqrt{600}$ to be compared with the theoretical values. Inset (a): Transmission map of the opaque object by blocking the left half of the thermal probe and calculated with the binning radius 6 ($a = 113$ pixels). A central circular region is selected based on a good overlap between the probe and the LO. Central shaded region is excluded from the analysis.

Chapter 6

Anti-Parity-Time Symmetry in Hot Rubidium Vapor

6.1 Introduction

This chapter presents our investigation into Anti-Parity-Time(APT) Symmetry in hot Rubidium vapor. For the published work, please refer to Ref [127].

While all Hermitian operators possess real eigenvalues, being Hermitian is not a requisite condition for this property. Recent findings indicate that any Hamiltonian \hat{H} , whether symmetric [82, 87, 89] or anti-symmetric [181, 182] under joint parity-time ($\hat{P}\hat{T}$) transformations, can yield a real energy spectrum, corresponding to either $[\hat{H}, \hat{P}\hat{T}] = 0$ or $\{\hat{H}, \hat{P}\hat{T}\} = 0$. Both classifications of systems experience a phase transition at which the Hamiltonian's real eigenvalues become imaginary at a singular point in parameter space, referred as an exceptional point (EP). Notably, even minor perturbations of the interaction parameters near the EP can result in significant alterations in system observable behavior, thereby facilitating the enhancement of various sensors [15–18] and many other applications [183]. The mathematical equivalence between the Schrödinger equation and paraxial wave propagation equation in materials characterized by complex refractive indices has facilitated the experimental realization of PT and anti-PT symmetric optical

and photonic structures through manipulation of their spatially varying optical properties. PT-symmetric structures often utilize spatially interleaved gain and loss channels [82, 98–100], showing exciting opportunities for practical applications such as EP-enhanced sensing and PT-symmetric lasers [92, 184–188]. However, unavoidable optical gain and loss pose challenges to many sensing schemes that hold great theoretical promise, since the associated Langevin noises disrupt PT symmetry in the quantum regime [101, 102]. In contrast, anti-PT symmetric systems provide a promising alternative to address this challenge, as they can potentially be implemented without loss or gain by exclusively manipulating the spatial variation of the real part of the refractive indices [181, 189, 190].

Recently, a fascinating alternative realization of anti-PT symmetry, without the need for spatially alternating regions with different refractive indices, has been demonstrated in cold Rb atoms [103]. In this system, the coupling between two optical fields (referred to as probe and conjugate) is established via resonant FWM with the help of two intense pump laser fields, and a nearly lossless propagation of a resonant field and tunable nonlinearity is achieved thanks to strong coupling of light and long-lived ground-state atomic coherence under the conditions of electromagnetically induced transparency (EIT). By varying the nonlinearity strength, the system exhibited an anti-PT phase transition with the eigenvalues transforming from imaginary to real at the EP. However, implementing such a lossless FWM scheme in inhomogeneously broadened optical systems is challenging due to unavoidable residual absorption, even under the EIT resonances. Here, we recreated similar conditions for anti-PT symmetry breaking by operating away from exact optical transition, thus mitigating the adverse effects of inhomogeneous broadening. This allows us to use a Rb vapor cell and a single strong pump laser field, rather than a cold atomic ensemble, which greatly reduces the complexity of the experiment and can operate in continuous regime. This system also enables experimental studies of the quantum properties of anti-PT phase breaking by measuring intensity squeezing and entanglement of the two output optical fields [153, 191–194]. Theory predicts distinct behaviors in their quantum fluctuations near the EP, offering promising avenues for precision quantum sens-

ing [195, 196]. This knowledge can be used to gain additional insights into the operation of a wide range of quantum sensors based on this FWM system [153, 197–200]. In this work, we first characterize the anti-PT features classically by tracking the FWM gain for both probe and conjugate optical fields, and then present theoretical and experimental analysis of nonclassical correlations in their relative-intensity noise. We consider a more realistic scenario, accounting for residual optical loss and associated Langevin noise, which inevitably reshape the emergence of the anti-PT phase transition and modify squeezing attributes. Finally, we identify the parameter space where the distinct anti-PT breaking features around the EP can be observed more clearly.

6.2 Anti-PT FWM Overview

6.2.1 Connecting FWM with Anti-PT Symmetry

To explore the analogy between the time-dependent Schrödinger equation for a two-level system and the propagation equations for two coupled optical fields in the FWM case, we need to find the interaction matrix \hat{H} that governs the propagation of the probe and conjugate optical fields with Rabi frequencies Ω_p and Ω_c :

$$i\partial_z \begin{pmatrix} \Omega_P \\ \Omega_C^* \end{pmatrix} = \hat{H} \begin{pmatrix} \Omega_P \\ \Omega_C^* \end{pmatrix} \quad (6.1)$$

To obey anti-PT symmetry, its accompanied Hamiltonian operator \hat{H} should anti-commute with the parity-time product operator. For the two-mode case, the action of the parity operator is equivalent to a “spatial flip”: $\hat{P} = \begin{pmatrix} 0 & 1 \\ 1 & 0 \end{pmatrix}$, while the time reversal operator conjugates the two output fields, such that $\hat{T}\hat{H}\hat{T} = \hat{H}^*$.

From previous calculations in Ch.2 and Ch.3, the nonlinear FWM interaction between the probe and conjugate field operators, \hat{a}_P and \hat{a}_C , is described by the following coupled

equations [103, 111],

$$i\frac{\partial}{\partial z} \begin{pmatrix} \hat{a}_P \\ \hat{a}_C^\dagger \end{pmatrix} = \begin{pmatrix} -\frac{\Delta k}{2} & -\kappa \\ \kappa & \frac{\Delta k}{2} \end{pmatrix} \begin{pmatrix} \hat{a}_P \\ \hat{a}_C^\dagger \end{pmatrix}, \quad (6.2)$$

where Δk is the phase mismatch. Note that, unlike most previous FWM studies, we operate at non-zero Δk s. This is required for achieving APT symmetric interaction and the existence of the EP. In simulation, we extract Δk by fitting the classical gain data, as its value can be effectively modified by the medium. At the two-photon resonance, $\kappa = gN/2c\Delta_2$ is a real and tunable parametric interaction amplitude with the optical transition coupling strength g , atomic density N , and speed of light in vacuum c .

Eq.(6.2) clearly resembles the Schrödinger-like equation with an effective Hamiltonian:

$$\mathbb{H}_{\text{APT}} = \begin{pmatrix} -\frac{\Delta k}{2} & -\kappa \\ \kappa & \frac{\Delta k}{2} \end{pmatrix}, \quad (6.3)$$

that anti-commutes with the joint parity-time operator [103], $\{\mathbb{H}_{\text{APT}}, \hat{P}\hat{T}\} = 0$. Since Eq.(6.3) does not contain any gain or loss, the commutation relations remain intact, and the Langevin noise is unnecessary in Eq.(6.2).

The Hamiltonian (6.3) has two eigenvalues,

$$\pm\lambda = \pm\frac{\Delta k}{2}\sqrt{1-\beta^2}, \quad (6.4)$$

where $\beta = |2\kappa/\Delta k|$ characterizes standard anti-PT features in parameter space: $\beta = 1$ indicates the EP of the regular anti-PT phase transition, marked by both eigenvalue and eigenstate coalescence.

We begin with this idealized APT model to gain some insights. We alter the atomic density N to tune β and so the eigenvalue λ . In this experiment, all the detunings are achieved by changing the atomic density, or at the operational level changing the cell temperature. This is because the experimental complications, which we will specify in later sessions.

For $\beta < 1$, $\pm\lambda$ are real, placing the system in the anti-PT phase-broken regime; $\beta > 1$

yields imaginary $\pm\lambda$, preserving anti-PT symmetry. In addition to the aforementioned anti-PT phase transition with $\pm\beta$, we also expect clear variations of quantum properties of the probe and conjugate fields after interaction with the atomic medium. These variations depend on a transfer matrix connecting output fields at $z = L$ to their corresponding inputs at $z = 0$,

$$\begin{pmatrix} \hat{a}_P(L) \\ \hat{a}_C^\dagger(L) \end{pmatrix} = e^{-i\mathbb{H}_{\text{APT}}L} \begin{pmatrix} \hat{a}_P(0) \\ \hat{a}_C^\dagger(0) \end{pmatrix} = \begin{pmatrix} A & C^* \\ C & A^* \end{pmatrix} \begin{pmatrix} \hat{a}_P(0) \\ \hat{a}_C^\dagger(0) \end{pmatrix}, \quad (6.5)$$

where $A = \cos(\lambda L) + i \sin(\lambda L)/\sqrt{1 - \beta^2}$ and $C = -i\beta \sin(\lambda L)/\sqrt{1 - \beta^2}$, equivalent to Eq.(2.36). To evaluate anti-PT breaking, we focus on two experimentally-achievable parameters: the gain coefficients and relative-intensity fluctuations of the strongly correlated probe and conjugate fields for different β values, and compare their behaviors with ideal double- Λ system considered earlier.

We first examine the classical traits of anti-PT behavior using probe and conjugate field gain values. The gain $G_{P/C}$ is defined in Eq.(2.25). As a reminder, physically it is the ratio of the measured output power to the input power of the seeded input field. In this way, we define the normalized gains G_P^N and G_C^N as:

$$\begin{aligned} G_P^N &= \frac{G_P}{G_P + G_C} = \frac{|A|^2}{|A|^2 + |C|^2}, \\ G_C^N &= \frac{G_C}{G_P + G_C} = \frac{|C|^2}{|A|^2 + |C|^2}. \end{aligned} \quad (6.6)$$

For $\beta > 1$, both output fields grow exponentially due to the presence of imaginary components in the eigenvalues. Since $|A|^2 \approx |C|^2$ for a larger β , the two powers increase at a similar rate, and both G_P^N and G_C^N tend to converge to 0.5. Below the EP ($\beta < 1$), coherent power oscillations emerge in both fields. Moreover, as β varies, the normalized gain for one field increases while for the other decreases. When $\beta \rightarrow 0$, a weak FWM strength results in $|A|^2 \rightarrow 1$ and $|C|^2 \rightarrow 0$.

Given the capability of this experimental system for generating strong quantum cor-

relations and entanglement between probe and conjugate fields [109, 191, 192], it is an ideal platform for investigating the quantum aspects of an anti-PT-symmetric system by monitoring the reduction of the relative-intensity fluctuations between the two fields below the shot noise level. This reduction is described by the squeezing parameter S which is defined in Eq.(2.52).

In this ideal case, it is easy to predict the quantum noise behavior. When $\beta < 1$, S follows sinusoidal oscillations of the classical relative gains, occasionally dropping below the shot noise level (when the output powers of the probe and conjugate fields become equal), indicating the emergence of moderate quantum squeezing. However, when $\beta > 1$, S monotonically decreases, implying growing quantum correlations in relative photon-number fluctuations. A larger κ corresponds to better intensity squeezing. Near the EP, S can undergo rapid variations as $\beta \rightarrow 1$, offering intriguing opportunities for quantum sensing [195].

6.2.2 Numerical Model

In practice, however, optical loss and imperfect detection efficiency limit the achievable squeezing level, and any further growth in κ only leads to deterioration of squeezing and eventually excess noise. For example, the simplified model predicts maximum FWM gain at zero two-photon detuning, yet the actual detunings have to be corrected for light shifts of the atomic energy level. Thus, to meet experimental requirements, we develop a model that incorporates the effects of these imperfections.

In the numerical modeling, we reduce the amount of absorptions to match with the real experimental data. However, we still assume that $\Omega_{P/C} \ll \Omega_{Pump}$, since the pump is 4 orders of magnitude larger than the probe seed. This assumption is fully justified and we show later we have a reasonable fit with data. The model constructed under this assumption allows us to extract the anti-PT Hamiltonian for all analysis as well as simplifies the calculation significantly. The ability to extract the 2×2 matrix also allows us to quantitatively compute the Langevin noise contribution following the formalism given

in Ref[111], as discussed in Ch.2.

Note that in this work, most experimental parameters—such as the pump laser frequency and Rabi frequency, and two-photon detuning $\delta = \omega - \omega_P - \Delta_{HF} = \omega_C - \omega - \Delta_{HF}$ have been optimized to maximize the relative-intensity squeezing for different atomic densities. Parameters used for the numerical simulations are derived from independent experimental characterizations. Since in our model we do not take into account the detailed hyperfine structure of ^{85}Rb D₁ line, the theoretically predicted values for the two optimal two-photon detunings ($\delta \approx -28$ MHz for maximum squeezing and -17 MHz for highest gain) differ from the corresponding experimentally measured ones (1 MHz and 12 MHz). However, that in both cases these values are 11 MHz apart from each other.

Another factor to consider is the Doppler effect. Unlike the case of cold or ultracold atoms, hot atomic dynamics can be significantly influenced by the Doppler broadening, with the Doppler range reaching up to several hundred megahertz. The Doppler effect is given by $\Delta_{\text{atom}} = \Delta_{\text{atom},v=0} + k \cdot v$. In our case, we selected all beams to be copropagating. Since the involved fields are near D1 transitions, the relative Doppler shift cancels out, thereby reducing the Doppler broadening effect. Furthermore, the large detuning Δ we used also mitigates the influence of the Doppler effect. Nevertheless, we include the Doppler effect for completeness and accuracy in the model.

Next, we solve Eq.(3.11) numerically without further simplification for all propagation matrix elements. The calculated anti-PT matrix usually takes the form,

$$\mathcal{M} = \begin{pmatrix} -\alpha + i\frac{\Delta k}{2} & i\kappa N \\ -i\kappa N & -i\frac{\Delta k}{2} \end{pmatrix} \quad (6.7)$$

where α/N , Δk , and κ represents, respectively, the optical absorption, momentum vector mismatch, and nonlinear coupling coefficient. Eigenvalues $G_{P/C}$ and squeezing S are computed accordingly for comparison with experiment. We annotate the numerically computed Hamiltonian with \mathcal{M} to distinct from the H_{APT} . Notice that for Eq.(6.7), we also included the imaginary term i for the propagation matrix. The gain and Langevin noise

can be calculated from Eq.(6.7), as outlined in Ch.2.

6.2.3 Comparison between Traditional and Anti-PT Squeezing

Our prior discussion has focused exclusively on classical nonlinear amplification. The present objective is to extend the study of anti-PT symmetry into the full quantum regime by incorporating two-mode squeezing.

As described in Ch.2, squeezing is directly related to gain. Therefore, it is expected that oscillations in squeezing will emerge as a function of the parameter λ . However, a key difference exists between conventional and anti-PT squeezing. Traditional squeezing is typically optimized for $\Delta k = 0$ (or very small Δk) with $G_{P/C}$ near maximum gain—although squeezing often deteriorates at the absolute maximum gain and is optimal when tuned slightly away from it. In contrast, for the FWM system to exhibit anti-PT characteristics, a variable Δk is required, allowing λ to shift from real to imaginary within the parameter space.

This necessity for a larger Δk highlights the difference between traditional squeezing and squeezing under anti-PT conditions. The anti-PT system represents a new regime that extends beyond the typical two-photon correlation picture found in conventional squeezing. For instance, in traditional squeezing, detection sensitivity is enhanced by maximizing gain and minimizing noise. In the proposed anti-PT system, however, enhanced sensitivity is achieved via an oscillatory squeezing response in the anti-PT-symmetric region near the exceptional point. Specifically, it has been shown that when $\lambda z = n\pi$ (with n an integer), enhanced sensitivity occurs due to the strength of the squeezing response rather than the squeezing value alone [104]. This approach also permits the observation of strong squeezing under non-optimal conditions—namely, with a large Δk in both the anti-PT-symmetric and anti-PT-broken regimes—which is generally not possible with traditional methods. In summary, anti-PT intensity squeezing offers a unique interpretation that differs significantly from conventional squeezing.

6.3 Experiment Design

Further experimental details of the squeezer are described in Ch.3, so we will not repeat the technical details of the setup here. Instead, this section focuses on the specific modifications made to transform our system into a pseudo anti-PT system and how we tune the system between its anti-PT symmetric and broken regions.

The primary modification is that we intentionally tune the phase-matching angle slightly larger than the one corresponding to maximum gain, thereby optimizing the squeezing under this condition. This deliberate detuning introduces a non-zero Δk into our system. Ideally, to achieve a larger λz —which is desirable for observing a sharp phase change—we would prefer Δk to be as large as possible, as λ is proportional to Δk (see Eq.(3.19)). In practice, however, increasing Δk is not always feasible because altering the phase-matching angle also changes the beam overlap and interaction length. For a fixed beam size, an increase in Δk (and consequently λ) is typically accompanied by a reduction in the propagation length and beam overlap, thereby limiting the extent to which Δk can be increased in our setup. For the same reason, tuning Δk by changing the phase-matching angle is not realistic. Tuning the beam direction can potentially also introduce additional detector loss or residual pump leakage, adding uncertainties to the experiment.

To overcome these issues, we tune the system by adjusting the atomic density—or, equivalently, the vapor cell temperature—which allows us to vary the system around the exceptional point. Because the atomic density is independent of other experimental parameters, it provides a means of probing the anti-PT Hamiltonian with minimal disturbance. It should be noted that a systematic error exists between the measured temperature and the actual temperature; the measured value is corrected by adding $+3.7^\circ C$.

Another parameter available for tuning is the pump power (or Rabi frequency). Since the pump field establishes atomic coherence between the ground and excited states, varying the pump power affects the nonlinear strength, represented by the off-diagonal term κ in the pseudo anti-PT Hamiltonian. Besides, the pump Rabi frequency directly affects the

Autler–Townes splitting, thereby influencing all detunings when altered. As a result, it is less decoupled from other system parameters than the atomic density, making it a less favorable parameter for tuning the anti-PT system, even though adjusting the laser power is more convenient and rapid.

6.4 Results and Discussion: Experimental anti-PT squeezing

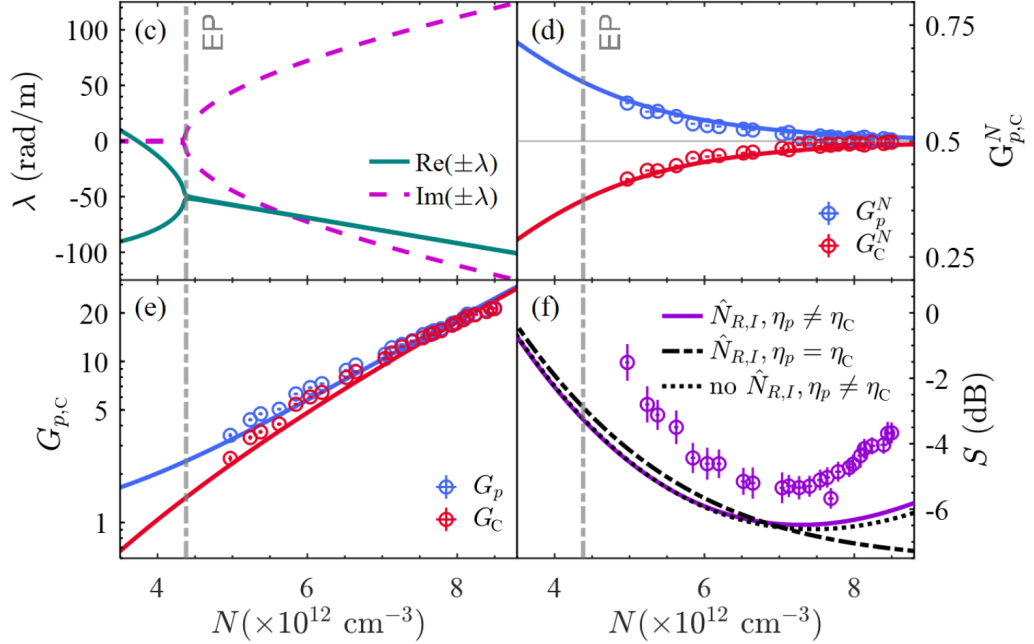


Figure 6.1: (a) Anti-PT Hamiltonian eigenvalues $\pm\lambda$ versus atomic density N , calculated using experimental parameters. (b,c) Experimental (markers) and calculated (lines) absolute (c) and normalized (b) gain values for the probe and conjugate optical fields versus N . (d) Relative intensity squeezing parameter S versus N , showing experimental data (markers) and simulated results from the full quantum model with imbalanced (solid line) detector efficiencies ($t_P = 78\%$ and $t_C = 83\%$), from the full quantum model with balanced (dash line) detector efficiencies ($t_P = t_C = 83\%$), and from the model using only imbalanced detector loss ($t_P = 78\%$ and $t_C = 83\%$, 100% transmission in atomic medium) [116] (dotted). In all cases the imperfect detector efficiencies are accounted for using a beamsplitter model. In (a)–(c) the dashed vertical lines indicate the predicted EP locations. Experimental parameters: $\theta = 0.39^\circ$, pump Rabi frequency $\Omega = 2\pi \times 0.42$ GHz, cell length $z = 1.9$ cm. Temperature range: 100°C to 108.7°C , corresponding to the atomic density range of $N = 5 \times 10^{12} - 9 \times 10^{12} \text{ cm}^{-3}$. Numerical model used $\Delta k = 210$ rad/m extracted from fitting experimental data.

Fig.6.1(a)-(d) present the variation of the classical and quantum characteristics of the probe and conjugate fields during the anti-PT phase transition as functions of N . Fig.6.1(a) show the calculated real (green) and imaginary (purple) components of $\pm\lambda$. Under the given experimental conditions, the real part of λ_{\pm} above EP does not completely disappear, as expected in the ideal anti-PT scenario. This non-vanishing deviation is caused by additional contribution of α to the diagonal term of the matrix(see Eq.(6.7) above), introduced to account for residual optical losses for the probe field. Nonetheless, its presence does not fundamentally disrupt the optical field dynamics, and, under certain conditions, does not significantly deteriorate the expected application performance. Fig.6.1(b) and (c) depict the net gains, $G_P = |A|^2$ and $G_C = |C|^2$, along with the normalized gains, $G_{P,C}^N$, for the probe and conjugate fields, respectively. Both numerical simulations and experimental data exhibit close agreement. Notably, we do not observe any oscillations in the probe and conjugate fields power below EP; instead, the output power of the seeded probe field gradually decreases while the generated conjugate field slowly grows. In principle, right after the EP, their normalized gains rapidly converge to 0.5 as the two optical fields tend to equate and grow together, signifying the system's transition into the unbroken domain of the anti-PT phase. Before EP, oscillatory conversion between probe and conjugate is anticipated in the low-atomic-density region for small κ , stemming from spontaneous symmetry breaking. However, observing these periodic oscillations as well as rapid convergence require longer optical path L (as discussed later) or a significantly larger phase mismatch Δk . Under these conditions the FWM gain below the EP is very low, posing experimental challenges. While understanding of this FWM gain dependence on Rb density does not require analysis of its internal symmetries, casting it in the light of anti-PT symmetry breaking provides valuable insights into the principle characteristics of the two distinct regimes. For instance, it provides a clear distinction between energy-conserving probe-conjugate propagation in the anti-PT symmetric regime and the common-mode amplification once the anti-PT symmetry is broken. Also, this allows for straightforward prediction of the experimental conditions corresponding to the EP, where the system can

exhibit maximum sensitivity to its parameter variations. The anti-PT symmetry analysis also connects the experimental observation to the broader field of non-Hermitian physics.

Fig.6.1(d) presents the experimentally measured relative intensity squeezing parameter S as well as its numerical simulations for various scenarios. The solid line shows the predictions of the full theoretical model that assumes the experimentally measured imbalance between probe and conjugate detection efficiencies. For completeness, we also plot the model predictions for the case of the identical detector efficiency, shown as a dashed line. The dotted line gives the predictions of a simplified calculation [116] that neglects the atomic Langevin noise correction terms ($\hat{N}_{R,I}$). As previously mentioned, in an ideal case, quantum correlations between the probe and conjugate intensify with increasing N . However, as shown here, in reality the squeezing parameter S reaches its optimal value of ≈ 5 dB at a certain N , above which quantum correlations continuously deteriorate. This shift primarily originates from residual optical loss (particularly for the probe field) that increases quantum noise of each individual optical field and detector losses that hamper fully capturing the generated relative intensity squeezing.

From Eq.(2.82), We can then solve the propagation equations for quantum operators and obtain the differential photon-number variance in terms of the gain coefficients $|A|$ and $|C|$:

$$\text{Var}(\hat{n}_P - \hat{n}_C) = (|A|^2 - |C|^2)^2 \langle \hat{n}_P(0) \rangle + \langle L_N \rangle, \quad (6.8)$$

where $\langle \hat{n}_P(0) \rangle$ and $\langle L_N \rangle$, respectively, denote the mean photon number of the seeding probe field and the grouped Langevin noise contributions.

In the ideal lossless case ($|A|^2 - |C|^2 = 1$) without additional noise terms, Eq.(6.8) matches Eq.(2.52) as $\langle \hat{n}_P \rangle + \langle \hat{n}_C \rangle = (|A|^2 + |C|^2) \langle \hat{n}_P(0) \rangle$. However, higher N enhances probe-field optical loss, leading to increased excess noise (with super-Poisson statistics) in both probe and conjugate fields, and hence prevents further squeezing improvements. Moreover, small imbalanced detector losses for the probe and conjugate channels ($t_P = 78\%$ and $t_C = 83\%$, respectively) further shift the conditions for optimal detectable squeezing

further towards lower temperature (atomic density). Eventually, relative intensity noise exceeds the shot-noise level, as depicted by the dotted and solid curves in Fig.6.1(d). In the case of perfectly balanced detection better squeezing level can be achieved at higher atomic density. As a side note, one can notice that for low FWM gain slightly higher detection losses for the probe field compensate for unity gain difference between probe and conjugate fields, and allows for minuscule improvement in the detected squeezing. Overall, we observe reasonable agreement between the experimental and theoretically predicted squeezing density dependence. The overall ≈ 2 dB difference between the measured and calculated noise level is observed. We can attribute it to experimental imperfections, including laser drifts, beam self-focusing, and residual pump field leakage. Additionally, other parasitic nonlinear effects, such as self-focusing or alternative wave-mixing channels, can emerge at higher atomic densities. Nevertheless, the model achieves a reasonably accurate prediction for the overall squeezing trend. This preliminary study is focused within the anti-PT symmetric region, since accurate measurements of quantum noise deviations from the shot noise in the low-gain regime was not possible due to technical noises, such as detector dark noise.

The pump laser power is another experimental parameter that we can use to control the FWM strength. For sufficiently powerful pump field, the FWM gain is independent of the pump laser intensity, but for weaker pump this approach holds potential advantages for much faster tuning across the anti-PT EP, compared to the temperature tuning of the atomic density. Unfortunately, the reduction in pump power generally results in higher optical losses. Fig.6.2 compares the simulation and experimental results of the pump power dependence. While the experimental normalized gain and measured squeezing align well with the simulations, it is clear that, at lower laser powers, the calculated eigenvalues deviate more substantially from the ideal expectations ($\text{Re}(\pm\lambda) = 0$ above the EP, and $\text{Im}(\pm\lambda) = 0$ below the EP).

To demonstrate the capability of our proposed system in simulating near-perfect anti-PT Hamiltonian, we employ the developed numerical model to identify the required ex-

perimental conditions, as shown in Fig.6.3. We find that operating at sufficiently large one-photon detuning $\Delta_1 \leq 4$ GHz provides necessary reduction in residual loss. However, to achieve necessary FWM gain, one will have to operate at higher cell temperature ($\geq 120^\circ\text{C}$) and greater pump laser power than what was available in the current experiments. Under these conditions, the calculated eigenvalues become symmetric and switch from almost entirely real to predominantly imaginary at the EP. For a longer vapor cell ($z = 7.6$ cm), $\pm\lambda z$ attains sufficient magnitude to enable relative oscillation in the normalized gain plot within the anti-PT symmetry breaking region. The negligible optical losses make it possible to observe corresponding variations in relative-intensity noise below the EP [103], under certain conditions even dipping below the shot-noise level. Realization of this regime will allow us to explore the alternative mechanisms for quantum enhancement related to extreme sensitivity of the system near the EP in addition to a more traditional benefits of high two-mode intensity squeezing above EP. Previous theoretical analysis predicts that operating near the EP enables optimal quantum sensing, even when low FWM gain produces negligible amount of intensity squeezing. Ref. [195] proves that by comparing the inverse variance (akin to the Cramer-Rao bound) with the corresponding quantum Fisher information and showing that they converge in the ideal case. However, under the same parametric gain, traditional squeezing-based sensing deviates significantly from the quantum Fisher information, indicating suboptimal performance, and it requires significantly higher parametric gain to also saturate the quantum Fisher information [201].

It is important to note that complete elimination of the Langevin noise contributions proves to be challenging. Although in an ideal lossless scenario, squeezing continually improves with N , our model predicts that even under more favorable conditions the inescapable optical losses will cause rapid squeezing degradation above certain atomic density as shown in Fig.6.3(c). Operating at larger laser detuning only pushes this optimal squeezing point to higher atomic densities, (compare, e.g., the horizontal scales in Figs.6.1 and 6.3). Nevertheless, in the vicinity of the EP, the ability to reproduce rapidly changing quantum squeezing behavior, as identified in Ref. [195], remains feasible. Thus, the exten-

sion of the original quantum Fisher information analysis accounting for optical loss and Langevin noise remains an open question for future theoretical and experimental work.

6.5 Conclusion and Outlook

In conclusion, our preliminary work establishes the practicality of modeling the anti-PT-symmetric Hamiltonian by utilizing two correlated optical fields generated through the near-resonant forward FWM process in hot Rb atoms, particularly for studying its quantum properties. We demonstrated that it is possible to tune the interaction parameters across the anti-PT phase transition, verifying that both classical and quantum behavior of the probe and conjugate fields exhibit the expected characteristics below and above the exceptional point. Namely, we observe two-mode relative-intensity squeezing at the anti-PT symmetric regime, when both output fields experience matched exponential FWM gain. We also analyze the influence of excess noise resulting from residual optical absorption, which imposes constraints on the attainable level of squeezing in distinct domains. Finally, we identified reasonable experimental parameters for the observation of the nearly lossless oscillatory behavior, that can be used for advanced quantum sensor applications.

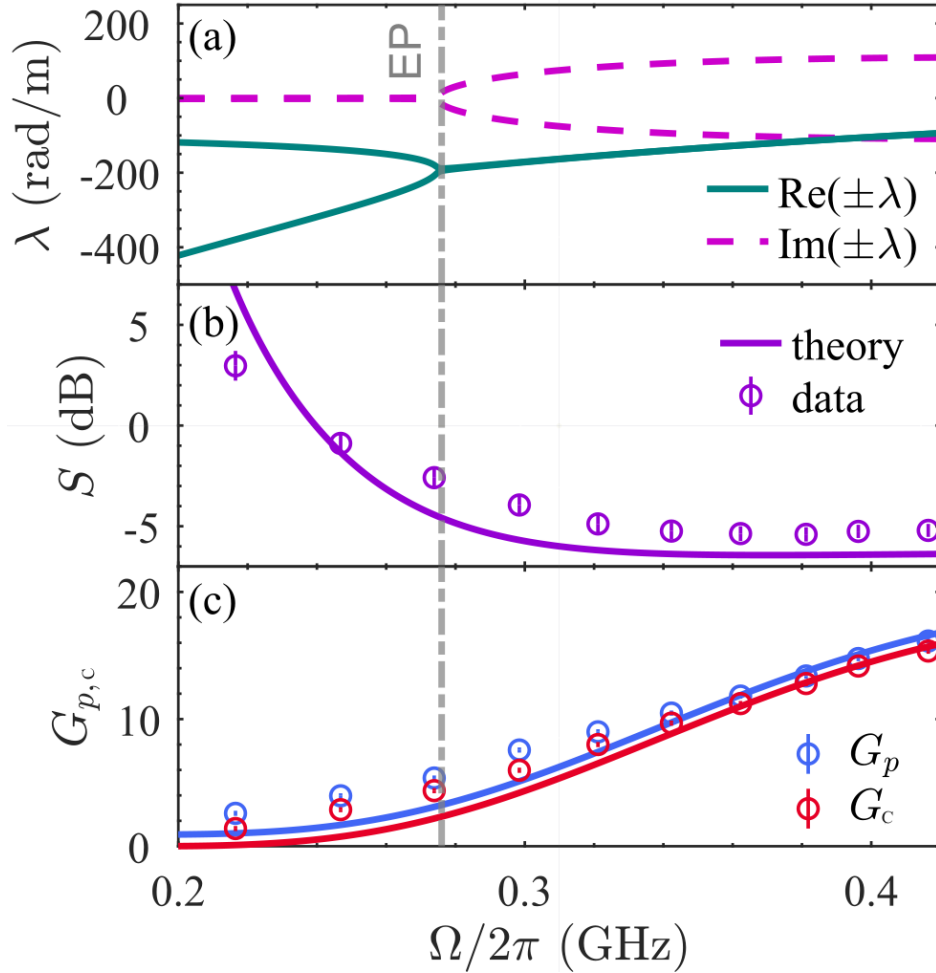


Figure 6.2: System tuning across anti-PT symmetric and symmetry-breaking regimes via pump laser power modulation. (a) Simulated eigenvalues $\pm\lambda$ of the anti-PT Hamiltonian vs. pump Rabi frequency Ω . Power-dependences of (b) the relative-intensity squeezing parameter S and (c) normalized probe/conjugate gain $G_{P,C}$: experimental measurements (markers) vs numerical simulations (lines). Experimental parameters, also used for the numerical model: $\Delta = 0.7$ GHz, $\delta = -28$ MHz, $N = 7.9 \times 10^{12} \text{cm}^{-3}$ (vapor temperature $\sim 108^\circ\text{C}$), $\Delta k = 210$ rad/m.

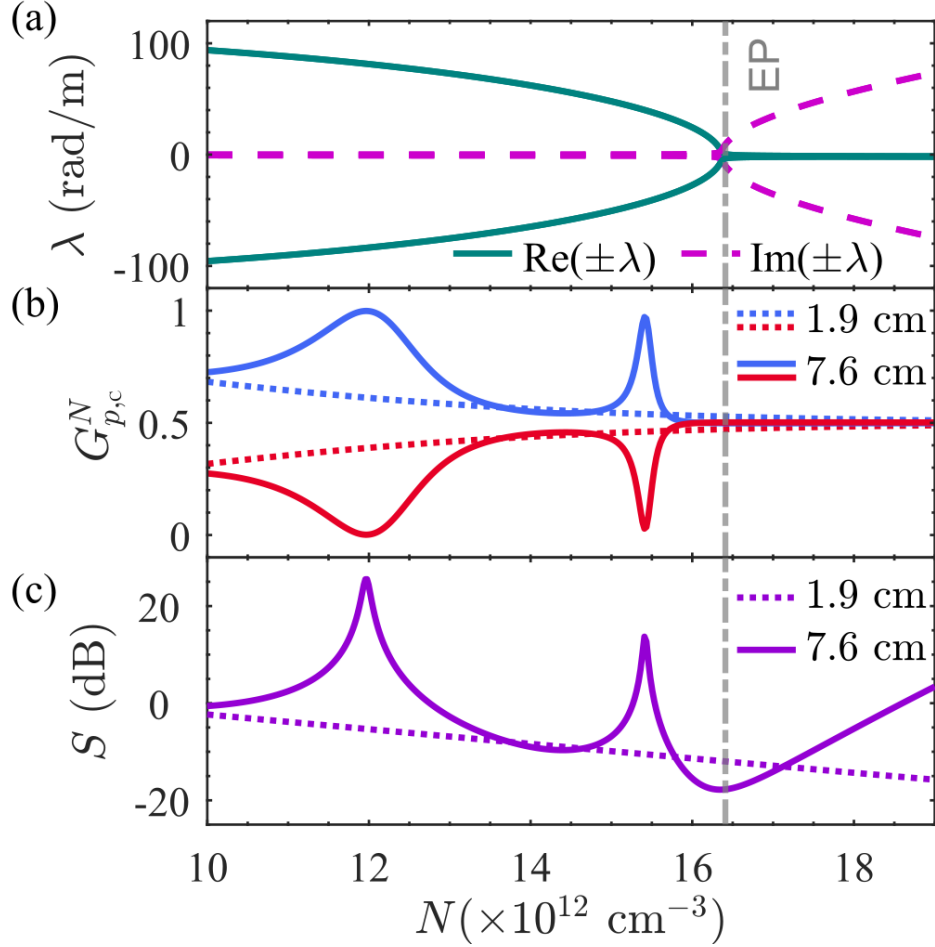


Figure 6.3: Optimized FWM parameters for nearly ideal anti-PT realizations, using higher pump power ($\Omega = 2\pi \times 0.6$ GHz) and larger one-photon detuning ($\Delta_1 = 4$ GHz), in $z = 1.9$ cm and $z = 7.6$ cm vapor cells. Additional parameters: $\delta = -3.5$ MHz, $\Delta k = 210$ rad/m. (a) Real/imaginary components of the eigenvalues as functions of the atomic density N . (b) Normalized probe/conjugate gain vs. N . (c) Relative-intensity squeezing parameter S vs. N . Solid/dashed lines show the predicted squeezing with the Langevin noise $\langle L_N \rangle$ at a $z = 7.6/1.9$ cm vapor cell. No detector losses are considered.

Chapter 7

Conclusion and Future Work

In this dissertation, we discussed the development of quantum information and sensing tools utilizing FWM in ensembles of warm atoms. We formulated a theoretical framework for FWM and associated two-mode squeezing, emphasizing the impact of optical loss. With these, we extended the applications of squeezing to quantum communication and non-Hermitian systems by developing a bi-chromatic two-mode squeezer.

The bichromatic squeezer contributes to the long-distance quantum communication applications and has significant implications for hybrid constructions. We experimentally achieved strong quantum correlations up to -2.6dB for two distinct wavelengths. We also show theoretically that more than 6dB of squeezing can be achievable, which is promising for real-world quantum communication applications.

We also explored the realization of APT Hamiltonian using an FWM system. The APT squeezer opens the door for the investigation near exceptional points in non-Hermitian systems. We theoretically calculated and experimentally verified the practicality of using FWM as an ant-PT system, and outlined the practical limitations. Most importantly, we extend the study into the quantum regime by looking at the squeezing response near EP.

Finally, we developed a few-photon imaging method utilizing quantum noise by extending the homodyne detection method to account for spatial distributions. We successfully imaged a wasp wing sample, with $50\mu\text{m}$ resolution and on average 0.006 photons per pixel.

Moving forward, there are several interesting directions to be explored, as many practical applications can be developed based on the materials presented in this thesis. For example, the efficient bichromatic squeezer can be modified as an IR-Telecom wavelength conversion device, which is another important aspect of quantum communications. Both the bichromatic squeezer and the wavelength converter can be easily integrated into existing quantum information experiments. Further investigations into quantum transduction can include microwave-IR-Telecom conversion. We can also advance the FWM-based APT studies by developing sensors with enhanced sensitivity near EP. What's more, we can study the FWM system at the single-photon level instead of in the bright-mode squeezing regime. In this case, The EP crossing behavior could be used as a control mechanism for biphoton waveform shaping.

Appendix A

Squeezing Calculation Matlab Script with Langevin Correction

A.1 Analytical Calculation for Langevin Terms

From Eq. (2.77), the noise matrix $\hat{\mathbb{N}}_R$ and $\hat{\mathbb{N}}_I$ are determined by the coupling matrix:

$$\hat{\mathbb{N}}_R + i\hat{\mathbb{N}}_I = \sqrt{-} \left(\begin{pmatrix} -\alpha + i\frac{\Delta k}{2} & i\kappa \\ -i\kappa & -i\frac{\Delta k}{2} \end{pmatrix} - \begin{pmatrix} -\alpha^* - i\frac{\Delta k}{2} & -i\kappa^* \\ i\kappa^* & i\frac{\Delta k}{2} \end{pmatrix} \right) = \begin{pmatrix} \alpha_r & \kappa_i \\ -\kappa_i & 0 \end{pmatrix} \quad (\text{A.1})$$

Where α_r represents the loss, the real part of α , and κ_i is the imaginary part of the nonlinear coupling coefficient κ . Noise operators, defined by considering atoms as reservoirs[115], have the following relationship,

$$\langle \hat{f}_m(\omega, z) \hat{f}_n(\omega', z') \rangle = \langle \hat{f}_m^\dagger(\omega, z) \hat{f}_n^\dagger(\omega', z') \rangle = \langle \hat{f}_m(\omega, z) \hat{f}_n^\dagger(\omega', z') \rangle = 0 \quad (\text{A.2})$$

$$\langle \hat{f}_m^\dagger(\omega, z) \hat{f}_n(\omega', z') \rangle = \delta_{mn} \delta(\omega - \omega') \delta(z - z') \quad (\text{A.3})$$

We can write the Eq.(2.77) with matrices as,

$$\frac{\partial}{\partial z} \begin{pmatrix} \hat{a}_P \\ \hat{a}_C^\dagger \end{pmatrix} = \overbrace{\begin{pmatrix} -\alpha + i\frac{\Delta k}{2} & i\kappa \\ -i\kappa & -i\frac{\Delta k}{2} \end{pmatrix}}^{\mathcal{M}} \begin{pmatrix} \hat{a}_P \\ \hat{a}_C^\dagger \end{pmatrix} + \begin{pmatrix} \hat{\mathbb{N}}_{R11} & \hat{\mathbb{N}}_{R12} \\ \hat{\mathbb{N}}_{R21} & \hat{\mathbb{N}}_{R22} \end{pmatrix} \begin{pmatrix} \hat{f}_P \\ \hat{f}_C^\dagger \end{pmatrix} + \begin{pmatrix} \hat{\mathbb{N}}_{I11} & \hat{\mathbb{N}}_{I12} \\ \hat{\mathbb{N}}_{I21} & \hat{\mathbb{N}}_{I22} \end{pmatrix} \begin{pmatrix} \hat{f}_P^\dagger \\ \hat{f}_C \end{pmatrix} \quad (\text{A.4})$$

The solution to Eq.(A.4) is,

$$\begin{pmatrix} \hat{a}_P(L) \\ \hat{a}_C^\dagger(L) \end{pmatrix} = e^{ML} \begin{pmatrix} \hat{a}_P(0) \\ \hat{a}_C^\dagger(0) \end{pmatrix} + \int_0^L e^{M(L-z)} \begin{pmatrix} \hat{\mathbb{N}}_{R11} & \hat{\mathbb{N}}_{R12} \\ \hat{\mathbb{N}}_{R21} & \hat{\mathbb{N}}_{R22} \end{pmatrix} \begin{pmatrix} \hat{f}_P \\ \hat{f}_C^\dagger \end{pmatrix} dz \\ + \int_0^L e^{M(L-z)} \begin{pmatrix} \hat{\mathbb{N}}_{I11} & \hat{\mathbb{N}}_{I12} \\ \hat{\mathbb{N}}_{I21} & \hat{\mathbb{N}}_{I22} \end{pmatrix} \begin{pmatrix} \hat{f}_P^\dagger \\ \hat{f}_C \end{pmatrix} dz \quad (\text{A.5})$$

If we define matrices,

$$e^{ML} \equiv \begin{pmatrix} A & B \\ C & D \end{pmatrix}, \quad e^{M(L-z)} \equiv \begin{pmatrix} A_1(z) & B_1(z) \\ C_1(z) & D_1(z) \end{pmatrix} \quad (\text{A.6})$$

We can solve the output matrix as following,

$$\begin{pmatrix} \hat{a}_P(L) \\ \hat{a}_C^\dagger(L) \end{pmatrix} = \begin{pmatrix} A(L) & B(L) \\ C(L) & D(L) \end{pmatrix} \begin{pmatrix} \hat{a}_P(0) \\ \hat{a}_C^\dagger(0) \end{pmatrix} \\ + \int_0^L \begin{pmatrix} A_1(z) & B_1(z) \\ C_1(z) & D_1(z) \end{pmatrix} \begin{pmatrix} \hat{\mathbb{N}}_{1r} & \hat{\mathbb{N}}_{2r} \\ \hat{\mathbb{N}}_{3r} & \hat{\mathbb{N}}_{4r} \end{pmatrix} \begin{pmatrix} \hat{f}_P(z) \\ \hat{f}_C^\dagger(z) \end{pmatrix} dz \\ + \int_0^L \begin{pmatrix} A_1(z) & B_1(z) \\ C_1(z) & D_1(z) \end{pmatrix} \begin{pmatrix} \hat{\mathbb{N}}_{1i} & \hat{\mathbb{N}}_{2i} \\ \hat{\mathbb{N}}_{3i} & \hat{\mathbb{N}}_{4i} \end{pmatrix} \begin{pmatrix} \hat{f}_P^\dagger(z) \\ \hat{f}_C(z) \end{pmatrix} dz \quad (\text{A.7})$$

The noise terms are defined as follows:

$$\begin{aligned} \hat{\mathbb{N}}_{1r} &= A_1 \hat{\mathbb{N}}_{R11} + B_1 \hat{\mathbb{N}}_{R21}, & \hat{\mathbb{N}}_{2r} &= A_1 \hat{\mathbb{N}}_{R12} + B_1 \hat{\mathbb{N}}_{R22}, \\ \hat{\mathbb{N}}_{3r} &= C_1 \hat{\mathbb{N}}_{R11} + D_1 \hat{\mathbb{N}}_{R21}, & \hat{\mathbb{N}}_{4r} &= C_1 \hat{\mathbb{N}}_{R12} + D_1 \hat{\mathbb{N}}_{R22}, \\ \hat{\mathbb{N}}_{1i} &= A_1 \hat{\mathbb{N}}_{I11} + B_1 \hat{\mathbb{N}}_{I21}, & \hat{\mathbb{N}}_{2i} &= A_1 \hat{\mathbb{N}}_{I12} + B_1 \hat{\mathbb{N}}_{I22}, \\ \hat{\mathbb{N}}_{3i} &= C_1 \hat{\mathbb{N}}_{I11} + D_1 \hat{\mathbb{N}}_{I21}, & \hat{\mathbb{N}}_{4i} &= C_1 \hat{\mathbb{N}}_{I12} + D_1 \hat{\mathbb{N}}_{I22} \end{aligned} \quad (\text{A.8})$$

Finally, we can write down our $\hat{a}_P(L)$ and $\hat{a}_C(L)$ as,

$$\hat{a}_P(L) = A(L)\hat{a}_P(0) + B(L)\hat{a}_C^\dagger(0) \quad (\text{A.9})$$

$$\begin{aligned} &+ \int_0^L dz \hat{\mathbb{N}}_{1r}(z) \hat{f}_P(z) + \int_0^L dz \hat{\mathbb{N}}_{2r}(z) \hat{f}_C^\dagger(z) \\ &+ \int_0^L dz \hat{\mathbb{N}}_{1i}(z) \hat{f}_P^\dagger(z) + \int_0^L dz \hat{\mathbb{N}}_{2i}(z) \hat{f}_C(z) \end{aligned}$$

$$\hat{a}_P^\dagger(L) = A^*(L)\hat{a}_P^\dagger(0) + B^*(L)\hat{a}_C(0) \quad (\text{A.10})$$

$$\begin{aligned} &+ \int_0^L dz \hat{\mathbb{N}}_{1r}^*(z) \hat{f}_P^\dagger(z) + \int_0^L dz \hat{\mathbb{N}}_{2r}^*(z) \hat{f}_C(z) \\ &+ \int_0^L dz \hat{\mathbb{N}}_{1i}^*(z) \hat{f}_P(z) + \int_0^L dz \hat{\mathbb{N}}_{2i}^*(z) \hat{f}_C^\dagger(z) \end{aligned}$$

$$\hat{a}_C(L) = C(L)\hat{a}_P(0) + D(L)\hat{a}_C^\dagger(0) \quad (\text{A.11})$$

$$\begin{aligned} &+ \int_0^L dz \hat{\mathbb{N}}_{3r}(z) \hat{f}_P(z) + \int_0^L dz \hat{\mathbb{N}}_{4r}(z) \hat{f}_C^\dagger(z) \\ &+ \int_0^L dz \hat{\mathbb{N}}_{3i}(z) \hat{f}_P^\dagger(z) + \int_0^L dz \hat{\mathbb{N}}_{4i}(z) \hat{f}_C(z) \end{aligned}$$

$$\hat{a}_C^\dagger(L) = C^*(L)\hat{a}_P^\dagger(0) + D^*(L)\hat{a}_C(0) \quad (\text{A.12})$$

$$\begin{aligned} &+ \int_0^L dz \hat{\mathbb{N}}_{3r}^*(z) \hat{f}_P^\dagger(z) + \int_0^L dz \hat{\mathbb{N}}_{4r}^*(z) \hat{f}_C(z) \\ &+ \int_0^L dz \hat{\mathbb{N}}_{3i}^*(z) \hat{f}_P(z) + \int_0^L dz \hat{\mathbb{N}}_{4i}^*(z) \hat{f}_C^\dagger(z) \end{aligned}$$

Using the aforementioned solutions, we can compute any desired quantities, such as gain and squeezing by following the same procedure as in Ch.2. Calculating the $(\langle \hat{a}_P(L)\hat{a}_P(L) - \langle \hat{a}_P(L)\hat{a}_P(L) \rangle)^2$ and $\langle [\hat{a}_P(L)\hat{a}_P(L) - \langle \hat{a}_P(L)\hat{a}_P(L) \rangle]^2 \rangle$ terms involves many high-order correlation terms; thus, we will not detail these calculations, even in the Appendix. In next section, we will provide the complete code in which all Langevin noise components are explicitly defined. We will compute the value of each component and sum them to derive the total noise contribution.

A.2 MATLAB Function Script

The subsequent Matlab code was used to compute the Langevin noise. The function takes four variables, with the corresponding script parameters shown in parentheses: the propagation matrix \mathcal{M} (Propagation_mat), propagation distance L (L), input photon number n_P during collection time (np), and probe and conjugate detector efficiency (Dloss_p and Dloss_s). The output is the probe and conjugate gain $G_{P/C}$ (G_p and G_c) and the squeezing S (Sqz) with all loss term accounted. Note that we do not include any additional noise terms such as converted laser phase noise; this code deals with only the atomic and detector loss.

```
1 function [G_p,G_c,Sqz]= Langevin_Correcton_Intensity_Squeezing(  
    Propagation_mat,L,np,Dloss_p,Dloss_s)  
2 %Prepare the Langevin terms for corrected-noise calculation  
3 %G_p: Probe Gain  
4 %G_c:conjugate gain  
5 %Sqz:two_mode squeezing  
6 %Propagation_mat: 2 by 2 propagation matrix  
7 %L: propagation distance  
8 %np: input photon number  
9 %D_loss_p: probe channel detector efficiency  
10 %D_loss_s:conjugate channel detector efficiency  
11 %It takes the propagation matrix as an input.  
12 %This propagation matrix should be of float/double/integer numbers, no any  
13 %sort of symbolic expression invovled.  
14 %IMPORTANT: This version includes the imbalanced detection method we have  
15 %not included in previous version.  
16 %%  
17 %Here we prepare all the general matrix and noise terms that we can use for  
18 %later time  
19 tic;  
20 syms z %create the propagation distance z we can integrate over  
21 syms x %Create a variable for purely computational reason, this prevents
```

```

    error at integrand = 0 case
22 assume([x z], 'real');
23 %=====
24 Gain_Mat_out = expm(Propagation_mat*L); %gain at the output, added 07272023
    for eliminating imaginary parts test
25 Gain_Mat_in = vpa(expm(Propagation_mat*(L-z)));%gain at a certain point
26 A = Gain_Mat_out(1,1);B = Gain_Mat_out(1,2);C = Gain_Mat_out(2,1);D =
    Gain_Mat_out(2,2);%Define the matrix elements of amplification matrix
27 A1 = Gain_Mat_in(1,1);B1 = Gain_Mat_in(1,2);C1 = Gain_Mat_in(2,1);D1 =
    Gain_Mat_in(2,2);%Define the matrix elements of intermidiate amp matrix
28 EMat = vpa(sqrtm(-Propagation_mat-conj(Propagation_mat)));%Caculated the
    overall error matrix
29 NFR = real(EMat);NR11 = NFR(1,1); NR21 = NFR(2,1); NR12 = NFR(1,2); NR22 =
    NFR(2,2);
30 NFI = imag(EMat);NI11 = NFI(1,1); NI21 = NFI(2,1); NI12 = NFI(1,2); NI22 =
    NFI(2,2);%Define error matrix as in (A.1) to (A.7)
31 N1r = A1*NR11+B1*NR21;N2r = A1*NR12+B1*NR22;N3r = C1*NR11+D1*NR21;N4r = C1*
    NR12+D1*NR22;
32 N1i = A1*NI11+B1*NI21;N2i = A1*NI12+B1*NI22;N3i = C1*NI11+D1*NI21;N4i = C1*
    NI12+D1*NI22;%Define terms in (A.8)
33 %%
34 apc = 1*sqrt(np); %define <\alpha|a^\dagger value
35 ap = 1*sqrt(np);%define a|\alpha> value
36 %%
37 %Define function form.
38 N1rN1i = matlabFunction(vpa(N1r*N1i+x*z));
39 N2iN2r = matlabFunction(vpa(N2i*N2r+x*z));
40 N1icN1rc = matlabFunction(vpa(conj(N1i)*conj(N1r)+x*z));
41 N2rcN2ic = matlabFunction(vpa(conj(N2r)*conj(N2i)+x*z));
42 N3icN3rc = matlabFunction(vpa(conj(N3i)*conj(N3r)+x*z));
43 N4rcN4ic = matlabFunction(vpa(conj(N4r)*conj(N4i)+x*z));
44 N3rN3i = matlabFunction(vpa(N3r*N3i+x*z));
45 N4iN4r = matlabFunction(vpa(N4i*N4r+x*z));
46 N1rsqr = matlabFunction(vpa(abs(N1r)^2+x*z));

```

```

47 N2isqr = matlabFunction(vpa(abs(N2i)^2+x*z));
48 N1iN3rc = matlabFunction(vpa(N1i*conj(N3r)+x*z));
49 N2iN4ic = matlabFunction(vpa(N2i*conj(N4i)+x*z));
50 N1rN3i = matlabFunction(vpa(N1r*N3i+x*z));
51 N2iN4r = matlabFunction(vpa(N2i*N4r+x*z));
52 N1icN3rc = matlabFunction(vpa(conj(N1i)*conj(N3r)+x*z));
53 N2rcN4ic = matlabFunction(vpa(conj(N2r)*conj(N4i)+x*z));
54 N3isqr = matlabFunction(vpa(abs(N3i)^2+x*z));
55 N4rsqr = matlabFunction(vpa(abs(N4r)^2+x*z));
56 N1icN3i = matlabFunction(vpa(conj(N1i)*N3i+x*z));
57 N2rcN4r = matlabFunction(vpa(conj(N2r)*N4r+x*z));
58 N1isqr = matlabFunction(vpa(abs(N1i)^2+x*z));
59 N2rsqr = matlabFunction(vpa(abs(N2r)^2+x*z));
60 N3icN1i = matlabFunction(vpa(conj(N3i)*N1i+x*z));
61 N4rcN2r = matlabFunction(vpa(conj(N4r)*N2r+x*z));
62 N3icN1rc = matlabFunction(vpa(conj(N3i)*conj(N1r)+x*z));
63 N4rcN2ic = matlabFunction(vpa(conj(N4r)*conj(N2i)+x*z));
64 N3rN1i = matlabFunction(vpa(N3r*N1i+x*z));
65 N4iN2r = matlabFunction(vpa(N4i*N2r+x*z));
66 N3rN1rc = matlabFunction(vpa(N3r*conj(N1r)+x*z));
67 N4iN2ic = matlabFunction(vpa(N4i*conj(N2i)+x*z));
68 N3rsqr = matlabFunction(vpa(abs(N3r)^2+x*z));
69 N4isqr = matlabFunction(vpa(abs(N4i)^2+x*z));
70 N1icN1i = matlabFunction(vpa(conj(N1i)*N1i+x*z));
71 N1rN1rc = matlabFunction(vpa(N1r*conj(N1r)+x*z));
72 N2rcN2r = matlabFunction(vpa(conj(N2r)*N2r+x*z));
73 N2iN2ic = matlabFunction(vpa(N2i*conj(N2i)+x*z));
74 N3rN3rc = matlabFunction(vpa(N3r*conj(N3r)+x*z));
75 N3icN3i = matlabFunction(vpa(conj(N3i)*N3i+x*z));
76 N4iN4ic = matlabFunction(vpa(N4i*conj(N4i)+x*z));
77 N4rcN4r = matlabFunction(vpa(conj(N4r)*N4r+x*z));
78 N1rN3rc = matlabFunction(vpa(N1r*conj(N3r)+x*z));
79 %%
80 %calculate the integrand

```

```

81 N1rN1i = integral(@(z) N1rN1i(0,z),0,L);
82 N2iN2r = integral(@(z) N2iN2r(0,z),0,L);
83 N1icN1rc = integral(@(z) N1icN1rc(0,z),0,L);
84 N2rcN2ic = integral(@(z) N2rcN2ic(0,z),0,L);
85 N3icN3rc = integral(@(z) N3icN3rc(0,z),0,L);
86 N4rcN4ic = integral(@(z) N4rcN4ic(0,z),0,L);
87 N3rN3i = integral(@(z) N3rN3i(0,z),0,L);
88 N4iN4r = integral(@(z) N4iN4r(0,z),0,L);
89 N1rsqr = integral(@(z) N1rsqr(0,z),0,L);
90 N2isqr = integral(@(z) N2isqr(0,z),0,L);
91 N2iN4ic = integral(@(z) N2iN4ic(0,z),0,L);
92 N1rN3i = integral(@(z) N1rN3i(0,z),0,L);
93 N2iN4r = integral(@(z) N2iN4r(0,z),0,L);
94 N1icN3rc = integral(@(z) N1icN3rc(0,z),0,L);
95 N2rcN4ic = integral(@(z) N2rcN4ic(0,z),0,L);
96 N3isqr = integral(@(z) N3isqr(0,z),0,L);
97 N4rsqr = integral(@(z) N4rsqr(0,z),0,L);
98 N1icN3i = integral(@(z) N1icN3i(0,z),0,L);
99 N2rcN4r = integral(@(z) N2rcN4r(0,z),0,L);
100 N1isqr = integral(@(z) N1isqr(0,z),0,L);
101 N2rsqr = integral(@(z) N2rsqr(0,z),0,L);
102 N3icN1i = integral(@(z) N3icN1i(0,z),0,L);
103 N4rcN2r = integral(@(z) N4rcN2r(0,z),0,L);
104 N3icN1rc = integral(@(z) N3icN1rc(0,z),0,L);
105 N4rcN2ic = integral(@(z) N4rcN2ic(0,z),0,L);
106 N3rN1i = integral(@(z) N3rN1i(0,z),0,L);
107 N4iN2r = integral(@(z) N4iN2r(0,z),0,L);
108 N3rN1rc = integral(@(z) N3rN1rc(0,z),0,L);
109 N4iN2ic = integral(@(z) N4iN2ic(0,z),0,L);
110 N3rsqr = integral(@(z) N3rsqr(0,z),0,L);
111 N4isqr = integral(@(z) N4isqr(0,z),0,L);
112 N1icN1i = integral(@(z) N1icN1i(0,z),0,L);
113 N1rN1rc = integral(@(z) N1rN1rc(0,z),0,L);
114 N2rcN2r = integral(@(z) N2rcN2r(0,z),0,L);

```

```

115 N2iN2ic = integral(@(z) N2iN2ic(0,z),0,L);
116 N3rN3rc = integral(@(z) N3rN3rc(0,z),0,L);
117 N3icN3i = integral(@(z) N3icN3i(0,z),0,L);
118 N4iN4ic = integral(@(z) N4iN4ic(0,z),0,L);
119 N4rcN4r = integral(@(z) N4rcN4r(0,z),0,L);
120 N1rN3rc = integral(@(z) N1rN3rc(0,z),0,L);
121 %%
122 %2nd order square terms
123 %Now included the detection efficiency value
124
125 S1 = (Dloss_p*abs(A)^2-Dloss_s*abs(C)^2)^2*np^2+...
126     (Dloss_p^2*abs(A)^4+Dloss_s^2*3*abs(C)^4+Dloss_p^2*3*abs(A)^2*abs(B)^2-
127     Dloss_p*Dloss_s*4*abs(A)^2*abs(C)^2-Dloss_p*Dloss_s*2*abs(B)^2*abs(
128     C)^2+Dloss_s^2*abs(C)^2*abs(D)^2 ...
129     -Dloss_p*Dloss_s*A*conj(B)*conj(C)*D-Dloss_p*Dloss_s*conj(A)*B*C*conj(D
130     ))*np+...
131     Dloss_p^2*abs(B)^4+Dloss_s^2*abs(C)^4-Dloss_p*Dloss_s*2*abs(B)^2*abs(C)
132     ^2+Dloss_p^2*abs(A)^2*abs(B)^2+Dloss_s^2*abs(C)^2*abs(D)^2- ...
133     Dloss_p*Dloss_s*A*conj(B)*conj(C)*D-Dloss_p*Dloss_s*conj(A)*B*C*conj(D)
134     ;
135 %%
136 %2nd order correlation/field operator required terms
137 T1 = conj(A)^2*apc*apc*(N1rN1i+N2iN2r)*Dloss_p^2;%checked.
138 T2 = A^2*ap*ap*(N1icN1rc+N2rcN2ic)*Dloss_p^2;%checked
139 T3 = C^2*ap*ap*(N3icN3rc+N4rcN4ic)*Dloss_s^2;%checked
140 T4 = conj(C)^2*apc*apc*(N3rN3i+N4iN4r)*Dloss_s^2;%checked
141 T5 = (abs(A)^2*np+abs(B)^2)*(N1rsqr+N2isqr)*Dloss_p^2;%checked
142 T6 = -(conj(A)*C*np+conj(B)*D)*(N1rN3rc+N2iN4ic)*Dloss_p*Dloss_s;%checked
143 T7 = -conj(A)*conj(C)*apc*apc*(N1rN3i+N2iN4r)*Dloss_p*Dloss_s;%checked
144 T8 = -A*C*ap*ap*(N1icN3rc+N2rcN4ic)*Dloss_p*Dloss_s;%checked
145 T9 = abs(C)^2*(np+1)*(N3isqr+N4rsqr)*Dloss_s^2;%checked
146 T10 = -A*conj(C)*(np+1)*(N1icN3i+N2rcN4r)*Dloss_p*Dloss_s;%checked
147 T11 = abs(A)^2*(np+1)*(N1isqr+N2rsqr)*Dloss_p^2;%checked
148 T12 = -(conj(A)*C*(np+1))*(N3icN1i+N4rcN2r)*Dloss_p*Dloss_s;%checked

```

```

144 T13 = -A*C*ap*ap*(N3icN1rc+N4rcN2ic)*Dloss_p*Dloss_s;%checked
145 T14 = -conj(A)*conj(C)*apc*apc*(N3rN1i+N4iN2r)*Dloss_p*Dloss_s;%checked
146 T15 = -(A*conj(C)*np+B*conj(D))*(N3rN1rc+N4iN2ic)*Dloss_p*Dloss_s;%checked
147 T16 = (abs(C)^2*np+abs(D)^2)*(N3rsqr+N4isqr)*Dloss_s^2;%checked
148 T17 = (abs(A)^2*np+abs(B)^2)*(N1isqr+N2rsqr)*Dloss_p^2;%checked
149 T18 = -(abs(A)^2*np+abs(B)^2)*(N3rsqr+N4isqr)*Dloss_p^2;%checked
150 T19 = -abs(C)^2*(np+1)*(N1isqr+N2rsqr)*Dloss_s^2;%checked
151 T20 = abs(C)^2*(np+1)*(N3rsqr+N4isqr)*Dloss_s^2;%checked
152 %%
153 %4th order terms
154 F1 = (N1icN1rc*N1rN1i+N1icN1i*N1rN1rc)*Dloss_p^2;%checked
155 F2 = (N2rcN2ic*N2iN2r+N2rcN2r*N2iN2ic)*Dloss_p^2;%checked
156 F3 = N1icN1i*N2iN2ic*Dloss_p^2;%checked
157 F4 = N2rcN2r*N1rN1rc*Dloss_p^2;%checked
158 F5 = N1icN1rc*N2iN2r*Dloss_p^2;%checked
159 F6 = N2rcN2ic*N1rN1i*Dloss_p^2;%checked
160 F7 = N1icN1i*N2rcN2r*Dloss_p^2;%checked
161 F8 = N2rcN2r*N1icN1i*Dloss_p^2;%checked
162 F9 = (N3rN3i*N3icN3rc+N3rN3rc*N3icN3i)*Dloss_s^2;%checked
163 F10 = (N4iN4r*N4rcN4ic+N4iN4ic*N4rcN4r)*Dloss_s^2;%checked
164 F11 = N3rN3rc*N4rcN4r*Dloss_s^2;%checked
165 F12 = N4iN4ic*N3icN3i*Dloss_s^2;%checked
166 F13 = N3rN3i*N4rcN4ic*Dloss_s^2;%checked
167 F14 = N4iN4r*N3icN3rc*Dloss_s^2;%checked
168 F15 = N3rN3rc*N4iN4ic*Dloss_s^2;%checked
169 F16 = N4iN4ic*N3rN3rc*Dloss_s^2;%checked
170 F17 = (-N1icN3i*N1rN3rc-N1icN3rc*N1rN3i)*Dloss_p*Dloss_s;%checked
171 F18 = (-N2rcN4r*N2iN4ic-N2rcN4ic*N2iN4r)*Dloss_p*Dloss_s;%checked
172 F19 = -N1icN3rc*N2iN4r*Dloss_p*Dloss_s;%checked
173 F20 = -N2rcN4ic*N1rN3i*Dloss_p*Dloss_s;%checked
174 F21 = -N1icN3i*N2iN4ic*Dloss_p*Dloss_s;%checked
175 F22 = -N2rcN4r*N1rN3rc*Dloss_p*Dloss_s;%checked
176 F23 = -N1icN1i*N4iN4ic*Dloss_p*Dloss_s;%checked
177 F24 = -N2rcN2r*N3rN3rc*Dloss_p*Dloss_s;%checked

```

```

178 F25 = (-N3rN1rc*N3icN1i-N3rN1i*N3icN1rc)*Dloss_p*Dloss_s;%checked
179 F26 = (-N4iN2ic*N4rcN2r-N4iN2r*N4rcN2ic)*Dloss_p*Dloss_s;%checked
180 F27 = -N3rN1i*N4rcN2ic*Dloss_p*Dloss_s;%checked
181 F28 = -N4iN2r*N3icN1rc*Dloss_p*Dloss_s;%checked
182 F29 = -N3rN1rc*N4rcN2r*Dloss_p*Dloss_s;%checked
183 F30 = -N4iN2ic*N3icN1i*Dloss_p*Dloss_s;%checked
184 F31 = -N3rN3rc*N2rcN2r*Dloss_p*Dloss_s;%checked
185 F32 = -N4iN4ic*N1icN1i*Dloss_p*Dloss_s;%checked
186 %%
187 %Summing over all the terms we have to the the expectation value
188 expNpNcsqr = S1 + ...
189     (T1+T2+T3+T4+T5+T6+T7+T8+T9+T10+T11+T12+T13+T14+T15+T16+T17+T18+T19+T20
190     )+...
191     (F1+F2+F3+F4+F5+F6+F7+F8+F9+F10+F11+F12+F13+F14+F15+F16+F17+F18+F19+F20
192     +F21+F22+F23+F24+F25+F26+F27+F28+F29+F30+F31+F32);%<a_p^*a_p-a_c^*
193     a_c)^2> term
194 %%
195 %calculate the non-square terms
196 expNpNc = Dloss_p*abs(A)^2*np-Dloss_s*abs(C)^2*(np+1)+Dloss_p*abs(B)^2+
197     Dloss_p*N2rsqr+Dloss_p*N1isqr-Dloss_s*N3rsqr-Dloss_s*N4isqr;%<a_p^*a_p-
198     a_c^*a_c> term
199 %%
200 %The actual gain of the two field can be mapped as
201 G_p = (abs(A)^2*np+abs(B)^2+N1isqr+N2rsqr)/np;%
202 G_c = (abs(C)^2*(np+1)+N3rsqr+N4isqr)/np;
203 %%
204 %The squeezing variance
205 %Beaware that the actual squeezing is calculated by using the
206 VarNpNc = expNpNcsqr-expNpNc^2+Dloss_p*(1-Dloss_p)*abs(A)^2*np+Dloss_s*(1-
207     Dloss_s)*abs(C)^2*np;%variance of squeezed lights efined using Eq.
208     (2.82), this calculation has included the detector loss
209 SN2 = 2*G_cc*np*Dloss_s;%Shot Noise reference level using SNL = 2<n_c>.
210     Accurate approximation for large Gain. for small gain one should
211     account by properly using SNL = <n_p>+<n_c>

```

```
203 Sqz = 10*log10(VarNpNc/SN2);%squeezing level
204 toc
205 end
```

Appendix B

Double-Ladder Numerical Model

Python Script

We provide the full python script used in Ch.4. This code is based on Rydiqule [151] and computes G_P and G_C . It accounts for all hyperfine levels of $|5S\rangle, |5P\rangle$, and $|6S\rangle$, thus producing reasonably accurate predictions for both linear and nonlinear behavior such as FWM and EIT. The code can be modified easily for the interest of future researchers. By default, executing this code generates the simulated gain spectra illustrated in Fig.4.3.

```
1 #!/usr/bin/env python3
2 # -*- coding: utf-8 -*-
3 """
4 Created on Wed Feb 14 13:29:53 2024
5
6 @author: Ziqi Niu
7 The purpose of this program is to build a model for diamond 4-level system,
8     with all hyperfine levels included. All delta_k
9     is added to the stokes field by default. Running this program generates the
10     gain spectra with D1 probe field frequency varying.
11     User can easily adjust this program to model system of interest.
12 """
13 #%%
14 'Importing the packages'
```

```

13 import numpy as np
14 import matplotlib.pyplot as plt
15 from scipy.spatial.transform import Rotation as R
16 import rydiqule as rq
17 from rydiqule.sensor_utils import get_rho_ij
18 from rydiqule.sensor_solution import Solution
19 import time
20 import scipy as sp
21 #from rydiqule.sensor_utils import get_transmission_coef
22 'Define Running Range'
23 size =83;#number of datapoints run
24 detunings = np.linspace(-1300,1300,size)#plot range, in MHz
25 'Define Doppler Terms'
26 Probe_Input = 350;#default Probe input frequency
27 kp = 2*np.pi/795e-3*np.array([1,0,0])
28 kd = 2*np.pi/780e-3*np.array([1,0,0])
29 kc = 2*np.pi/1367e-3*np.array([1,0,0])
30 ks = 2*np.pi/1324e-3*np.array([1,0,0])#define the k vectors for all
    involved optical fields, Mrad/m
31 #[1,0,0] is the dimension term, we in our case consider only 1-D doppler
    broadening.
32 vP = np.sqrt(2*1.38e-23*(100.5+273.15)/1.44e-25) # thermal speed, m/s
33 "Define Constans"
34 hbar = 1.0546e-34;#hbar number
35 e0 = 8.8542e-12;#permeability;
36 c = 299792458;#speed of light;
37 w_D1 = 377106120801483.6875;#D1 Transition
38 w_5S6S = c/((1/20132.5158)*1e-2);#5S F=3 to 6S F=3, centeriud wavelength.
39 w_6S = w_5S6S -w_D1;#6S
40 Dmoment_D1 = 2.5377e-29;#D1 transition dipole moment, C.m
41 Dmoment_IR = 2.4694e-29;#IR dipole moment
42
43
44 d_PUMP = 280*1#D2 detuning, from F'=4

```

```

45 IR_Pump = 800*1#IR detuning, from F'=3
46 IRPUMPON = 0.7*1#turning on/off/modify IR pump. By default this is 1 to
    match experimental conditions
47 D2PUMPON = 1.0*1#turning on/off/modify D2 pump. By default this is 0.7 to
    match experimental conditions
48 couple = {'states':(2,6), 'rabi_frequency':3200*np.sqrt(1/1)*IRPUMPON, 'kvec'
    ':vP*kc, 'detuning': (IR_Pump)*2*np.pi*1}
49 couple1 = {'states':(3,5), 'rabi_frequency':3200*np.sqrt(5/9)*IRPUMPON, '
    kvec':vP*kc, 'detuning': (IR_Pump+717-120)*2*np.pi*1}
50 couple2 = {'states':(4,5), 'rabi_frequency':3200*np.sqrt(2/9)*IRPUMPON, '
    kvec':vP*kc, 'detuning': (IR_Pump+717-180)*2*np.pi*1}
51 couple3 = {'states':(3,6), 'rabi_frequency':3200*np.sqrt(4/9)*IRPUMPON, '
    kvec':vP*kc, 'detuning': (IR_Pump-120)*2*np.pi*1}
52 couple4 = {'states':(4,6), 'rabi_frequency':3200*np.sqrt(7/9)*IRPUMPON, '
    kvec':vP*kc, 'detuning': (IR_Pump-180)*2*np.pi*1}#IR Pump coupling(5P3
    /2->6S)
53 #
54 dress1 = {'states':(1,2), 'rabi_frequency':4800*1.0*np.sqrt(9/14)*D2PUMPON
    , 'kvec':vP*kd, 'detuning':-d_PUMP*2*np.pi*1}
55 dress2 = {'states':(1,3), 'rabi_frequency':4800*1.0*np.sqrt(5/18)*D2PUMPON
    , 'kvec':vP*kd, 'detuning':-(d_PUMP-120)*2*np.pi*1}
56 dress3 = {'states':(1,4), 'rabi_frequency':4800*1.0*np.sqrt(5/63)*D2PUMPON
    , 'kvec':vP*kd, 'detuning':-(d_PUMP-180)*2*np.pi*1}#D2 pump coupling(5S
    ->5P3/2)
57 ##
58 #ladder 3
59 probe1 = {'states':(1,7), 'rabi_frequency':Probe_Input*np.sqrt(5/9), 'kvec'
    ':vP*kp, 'detuning': 0, 'phase':0}#D1,F=3 ->F'=2
60 probe2 = {'states':(1,8), 'rabi_frequency':Probe_Input*np.sqrt(4/9), 'kvec':
    vP*kp, 'detuning': 0, 'phase':0}#D1,F=3 ->F'=3
61 stokes1 = {'states':(7,5), 'rabi_frequency':1*2/9, 'kvec':vP*ks, 'detuning':
    0, 'phase':0}
62 stokes2 = {'states':(8,5), 'rabi_frequency':1*5/9, 'kvec':vP*ks, 'detuning':
    0, 'phase':0}

```

```

63 stokes11 = {'states':(7,6), 'rabi_frequency':1*7/9,'kvec':vP*ks, 'detuning'
      : 0,'phase':0}
64 stokes22 = {'states':(8,6), 'rabi_frequency':1*4/9,'kvec':vP*ks, 'detuning'
      : 0,'phase':0}
65 #ground ladder
66 ground = {'states':(0,1), 'rabi_frequency':0,'kvec':vP*kd, 'detuning': 0,'
      phase':0}#F=2 state ground state
67
68 #Define levels
69 n = 9
70 sensor = rq.Sensor(n)
71 #Define decoherence terms, assuming equal branching ratio
72 #Double-Ladder Origin
73 sensor.add_decoherence((2,1), 2*np.pi*(6+1/2*0))
74 sensor.add_decoherence((2,0), 2*np.pi*(0+1/2/np.pi))
75 sensor.add_decoherence((3,1), 2*np.pi*(6*1/2+1/2*0))
76 sensor.add_decoherence((3,0), 2*np.pi*(6*1/2+1/2/np.pi))
77 sensor.add_decoherence((4,1), 2*np.pi*(6*1/2+1/2*0))
78 sensor.add_decoherence((4,0), 2*np.pi*(6*1/2+1/2/np.pi))
79 ##hyperfine D1
80 sensor.add_decoherence((7,1), 2*np.pi*(5.75*1/2+1/2*0))
81 sensor.add_decoherence((7,0), 2*np.pi*(5.75*1/2+1/2/np.pi))
82 sensor.add_decoherence((8,1), 2*np.pi*(5.75*1/2+1/2*0))
83 sensor.add_decoherence((8,0), 2*np.pi*(5.75*1/2+1/2/np.pi))
84 ##ground population state exchange
85 sensor.add_decoherence((0,1), 2*np.pi*0.56)
86 sensor.add_decoherence((1,0), 2*np.pi*0)
87 ##6s decay down
88 sensor.add_decoherence((5,3), 2*np.pi*3.5/4)
89 sensor.add_decoherence((5,4), 2*np.pi*3.5/4)
90 sensor.add_decoherence((5,7), 2*np.pi*3.5/4)
91 sensor.add_decoherence((5,8), 2*np.pi*3.5/4)
92
93 sensor.add_decoherence((6,2), 2*np.pi*3.5/5*1)

```

```

94 sensor.add_decoherence((6,3), 2*np.pi*3.5/5*1)
95 sensor.add_decoherence((6,4), 2*np.pi*3.5/5*1)
96 sensor.add_decoherence((6,7), 2*np.pi*3.5/5*1)
97 sensor.add_decoherence((6,8), 2*np.pi*3.5/5*1)
98 ##
99 sensor.add_decoherence((5,0), 2*np.pi*(1/2)/np.pi)
100 sensor.add_decoherence((5,1), 2*np.pi*1/2*0)
101 sensor.add_decoherence((6,0), 2*np.pi*1/2/np.pi)
102 sensor.add_decoherence((6,1), 2*np.pi*1/2*0)#Here we have only decaying
    rate due to atomic movement
103 #transit broadening
104 sensor.add_couplings(couple, couple1, couple2, couple3, couple4, dress1, dress2,
    dress3, probe1, probe2, ground, stokes1, stokes2, stokes11, stokes22)
105 rq.draw_diagram(sensor)#create the sensor object and draw level diagram
106
107
108 #%%
109 N = 5e18*1.0#atomic density, in m^-3
110
111 fc = rq.atom_utils.calc_kappa(2*np.pi*377e12, 2.5377e-29/np.sqrt(3), N)#
    input are transition frequency(Hz), Dipole Moment (C.m), Atomic density
    (should be in m^-3)
112 fs = rq.atom_utils.calc_kappa(2*np.pi*226e12, 2.4694e-29/np.sqrt(3), N);#
113 #%%
114 k1324 = 2*np.pi/1324e-9
115 k795 = 2*np.pi/795e-9
116 def PropagationEq_2(t, y, t_prev0, nD1_prev0, nIR_prev0, t_prev=[None], nD1_prev
    =[None], nIR_prev = [None]):
117     '''
118     This is the main propagation function. The calculation solves the
        signal fields
119     In terms of Rabi frequency with delta_k explicitly removed.
120     '''
121     probe1['rabi_frequency'] = y[0]*np.sqrt(5/9);#17, F=3-->F=2

```

```

122 probe2['rabi_frequency'] = y[0]*np.sqrt(4/9); #18,F=3-->F=3
123 stokes1['rabi_frequency'] = y[1]*np.sqrt(2/9)*np.exp(-1j*dk1*t);#57, F
    =3-->F=2
124 stokes2['rabi_frequency'] = y[1]*np.sqrt(5/9)*np.exp(-1j*dk2*t);#58, F
    =2-->F=2
125 stokes11['rabi_frequency'] = y[1]*np.sqrt(7/9)*np.exp(-1j*dk1*t)*1;#67,
    F=3-->F=3
126 stokes22['rabi_frequency'] = y[1]*np.sqrt(4/9)*np.exp(-1j*dk2*t)*1;#68,
    F=2-->F=3
127 sensor.add_couplings(probe1,probe2,stokes1,stokes2,stokes11,stokes22);
128 s1 = rq.solve_steady_state(sensor,doppler=True)
129 rho17 = get_rho_ij(s1.rho,1,7);
130 rho18 = get_rho_ij(s1.rho,1,8);
131 rho57 = get_rho_ij(s1.rho,5,7)*np.exp(1j*dk1*t);
132 rho58 = get_rho_ij(s1.rho,5,8)*np.exp(1j*dk2*t);
133 rho67 = get_rho_ij(s1.rho,6,7)*np.exp(1j*dk1*t);
134 rho68 = get_rho_ij(s1.rho,6,8)*np.exp(1j*dk2*t);#adding the phase terms
    , before add_coupling
135 rho_IR = (1*2/9*rho57+1*5/9*rho58+1*7/9*rho67+1*4/9*rho68*1);
136 rho_D1 = (1*5/9*rho17+1*4/9*rho18);
137 if t==0.0183:
138     print('population00',get_rho_ij(s1.rho,0,0))
139     return [-1j*1e-6*fc*rho_D1, 1j*1e-6*fs*rho_IR]#joint propagation
    equation
140 #%%
141 intial_Condition = [Probe_Input+0j,0+0j]#initial condition, we seed only
    probe channel here.
142 #%%
143 '''
144 Numerical ODE solving. Here by default we used z0= 0.0183
145 '''
146 ct = 1#set initial counter
147 z0 = 0.0183#effective cell length/propagation length, in m
148 repetition = np.linspace(0,size-1,size)

```

```

149 Ssolution = np.zeros([2,size])#create set for probe
150 for k in repetition:
151     time_start= time.time()
152     if detunings[int(k)]<400:
153         print(detunings[int(k)])
154         dk1 = 3000*1
155         dk2 = 30*1#far-detuned dk approximation
156     else:
157         dk1 = 40*1
158         dk2 = 30*1#near resonance dk approximation
159     probe1['detuning'] = detunings[int(k)]*2*np.pi+180.791*2*np.pi;#17,F
160         =3-->F=2
161     probe2['detuning'] = detunings[int(k)]*2*np.pi-180.791*2*np.pi;#18,F
162         =3-->F=3
163     sensor.add_couplings(probe1,probe2);
164     DiffSol = sp.integrate.solve_ivp(PropagationEq_2,[0,z0],
165         intial_Condition,args = (int(0),int(0),int(0)),method = 'RK45')
166     Ysol = DiffSol.y;#full solution during propgation length
167     zz = DiffSol.t;
168     Solution_current = abs(Ysol[:,-1]);#the final solution at distance z
169     Ssolution[:,int(k)]= Solution_current;
170     time_elapsed = (time.time() - time_start)
171     print(time_elapsed,'s',ct,'round')
172     ct+=1
173
174 #%%
175 '''Calculate the conversion ratio'''
176 def omega_to_n(omega,dipole_moment,Trans_freq,V=1):
177     'Using Scully Quantum Optics book definition'
178     E_amp = omega*hbar/dipole_moment
179     n = e0*E_amp**2*V/2/hbar/Trans_freq
180     return n
181
182 n_in = omega_to_n(abs(intial_Condition[0]),Dmoment_D1,w_D1)
183 n_out_probe = omega_to_n(abs(SSolution[0,:]),Dmoment_D1,w_D1)
184 n_out_stokes = omega_to_n(abs(SSolution[1,:]),Dmoment_IR,w_6S)

```

```

180 G_probe = n_out_probe/n_in
181 G_stokes =n_out_stokes/n_in#the nonlinear gain in terms of G_P/C
182 #%%
183 '''
184 Plot the gain spectra
185 '''
186 loss_ratio= 0.85#correction for the detector quantum efficiency/loss rate
      on opics
187
188 fig, ax = plt.subplots(figsize=(8,6))
189 ax.plot(detunings, G_probe, label="G_P")
190 ax.set_xlim([-1250,1250])
191 ax.plot(detunings, G_stokes*loss_ratio, label="G_C")
192 ax.set_xlabel("Coupling Laser Detuning (MHz)")
193 ax.set_ylabel("G_{P/C}")
194 ax.legend()

```

Appendix C

Circular binning variance Calculation

C.1 Calculation of Normalized Variance

In Eq. (5.1), order of intra-mode and intermode interferences can be exchanged (i.e. $\hat{U}_2\hat{U}_1\hat{B}_{12} = \hat{B}_{12}\hat{U}_2\hat{U}_1$). Using this, along with cyclic property of trace, Eq. (1) can be written as:

$$\mathcal{V}(\vec{x}) = \text{Tr} \left[\hat{B}_{12}^\dagger \left(\hat{N}_1(\vec{x}) - \hat{N}_2(\vec{x}) \right)^2 \hat{B}_{12} \hat{U}_2(\vec{x}) \hat{U}_1(\vec{x}) \right. \\ \left. \hat{D}_2(\alpha) |0\rangle\langle 0| \hat{\rho}_1 \hat{D}_2^\dagger(\alpha) \hat{U}_1^\dagger(\vec{x}) \hat{U}_2^\dagger(\vec{x}) \right] \quad (\text{C.1})$$

where $\hat{U}_1(\vec{x}) = \hat{U}_1(\vec{x}) \cdot \hat{T}_1(\vec{x})$. For any unitary operators \hat{P} and \hat{Q} ,

$$\hat{P}^\dagger \hat{Q} \hat{P} \rightarrow P^{-1} \hat{Q} \\ \hat{P}^\dagger \hat{Q}^\dagger \hat{P} \rightarrow (P^{-1})^* \hat{Q}^\dagger, \quad (\text{C.2})$$

with P^{-1} being the inverse of the matrix representation of \hat{P} . This leads to,

$$\hat{B}_{12}^\dagger \left(\hat{N}_1(\vec{x}) - \hat{N}_2(\vec{x}) \right)^2 \hat{B}_{12} = \hat{a}_1^\dagger \hat{a}_1 + \hat{a}_2^\dagger \hat{a}_2 + 2\hat{a}_1^\dagger \hat{a}_1 \hat{a}_2^\dagger \hat{a}_2 - \hat{a}_1^2 \hat{a}_2^{\dagger 2} - \hat{a}_2^2 \hat{a}_1^{\dagger 2} \quad (\text{C.3})$$

And Eq. (C.1) yields:

$$\mathcal{V}(\vec{x}) = |U_2(\vec{x})|^2 |\alpha|^2 + \langle \hat{n}_{th} \rangle \left| \tilde{U}_1(\vec{x}) \right|^2 + \quad (C.4)$$

$$+ 2 \langle \hat{n}_{th} \rangle |\alpha|^2 |U_2(\vec{x})|^2 \left| \tilde{U}_1(\vec{x}) \right|^2. \quad (C.5)$$

Using intensity of the local oscillator for normalization and by neglecting $\mathcal{O}(|\alpha|^{-2})$ terms, normalized variance is:

$$V(\vec{x}) = 1 + 2 \langle \hat{n}_{th} \rangle \left| \tilde{U}_1(\vec{x}) \right|^2. \quad (C.6)$$

C.2 Circular Binning

In a CCD camera, each pixel acts as an independent detector, collecting only the light falling on its surface. Since the mode size of thermal field is much larger than the pixel size ($13 \mu m \times 13 \mu m$), the average number of photons per pixel $\langle n \rangle_{pxl}$ is proportionally small, and the variance value is close to one, making it hard to distinguish from the coherent vacuum. To improve the sensitivity of our measurements, we group pixels together to effectively increase their cumulative detection area. In our binning protocol, individual photon count of each pixel at \vec{x} is replaced by the sum of photon counts of all the neighbouring pixels within a binning radius, R . Binning improves the SNR but at the cost of reduced spatial resolution.

$$\mathcal{V}_R(\vec{x}) = Tr \left[\hat{U}_1^\dagger(\vec{x}) \hat{D}_2^\dagger(\alpha) \hat{U}_2^\dagger(\vec{x}) \hat{B}_{12}^\dagger \sum_{\vec{x}'} \left(\hat{N}_1(\vec{x}') - \hat{N}_2(\vec{x}') \right)^2 \right. \quad (C.7)$$

$$\left. \hat{B}_{12} \hat{U}_2(\vec{x}') \hat{D}_2(\alpha) \hat{U}_1(\vec{x}') |0\rangle \langle 0| \hat{\rho}_1 \right].$$

Central sum of the previous equation can be written as a product of two terms,

$$\begin{aligned} \left\langle \left(\sum_{\vec{x}'} \hat{N}_1(\vec{x}') - \hat{N}_2(\vec{x}') \right)^2 \right\rangle &= \sum_{\vec{x}'} \left\langle \left(\hat{N}_1(\vec{x}') - \hat{N}_2(\vec{x}') \right)^2 \right\rangle \\ &+ \sum_{\vec{x}'} \sum_{\vec{x}'' \neq \vec{x}'} \left\langle \left(\hat{N}_1(\vec{x}') - \hat{N}_2(\vec{x}') \right) \left(\hat{N}_2(\vec{x}'') - \hat{N}_1(\vec{x}'') \right) \right\rangle, \end{aligned} \quad (\text{C.8})$$

in which the first term is already evaluated in Eq. (C.5) and the second term can be evaluated using Eq. (C.2), to get the binned variance:

$$\begin{aligned} \mathcal{V}_R(\vec{x}) &= |\alpha|^2 \sum_{\vec{x}'} \left| U_2(\vec{x}') \right|^2 \left(1 + 2 \langle \hat{n}_{th} \rangle \left| \tilde{U}_1(\vec{x}') \right|^2 \right) \\ &+ 2 \langle \hat{n}_{th} \rangle |\alpha|^2 \left(\left| \sum_{\vec{x}'} U_2^*(\vec{x}') \tilde{U}_1(\vec{x}') \right|^2 - \sum_{\vec{x}'} \left| U_2^*(\vec{x}') \tilde{U}_1(\vec{x}') \right|^2 \right). \end{aligned} \quad (\text{C.9})$$

T_1 matrix is written as a diagonal matrix with entries being 0's (1's) representing the presence (absence) of the opaque part of the object. Mode matching between probe and LO allows us to write $\tilde{U}_1(\vec{x}) = T_1(\vec{x}) \cdot U_2(\vec{x})$. With this, expression for binned normalized variance simplifies to

$$V_R(\vec{x}) = 1 + 2 \langle \hat{n}_{th} \rangle \frac{\left(\sum_{\vec{x}'} T_1(\vec{x}') \left| U_2(\vec{x}') \right|^2 \right)^2}{\sum_{\vec{x}'} \left| U_2(\vec{x}') \right|^2}. \quad (\text{C.10})$$

References

- [1] S. Slussarenko and G. J. Pryde, Photonic quantum information processing: A concise review, *Applied Physics Reviews* **6** (2019).
- [2] D. E. Chang, V. Vuletić, and M. D. Lukin, Quantum nonlinear optics—photon by photon, *Nature Photonics* **8**, 685 (2014).
- [3] C. Xiong, C. Monat, A. S. Clark, C. Grillet, G. D. Marshall, M. Steel, J. Li, L. O’Faolain, T. F. Krauss, J. G. Rarity, *et al.*, Slow-light enhanced correlated photon pair generation in a silicon photonic crystal waveguide, *Optics letters* **36**, 3413 (2011).
- [4] B. S. Elkus, K. Abdelsalam, S. Fathpour, P. Kumar, and G. S. Kanter, Quantum-correlated photon-pair generation via cascaded nonlinearity in an ultra-compact lithium-niobate nano-waveguide, *Optics Express* **28**, 39963 (2020).
- [5] H. Takesue and K. Inoue, 1.5- μm band quantum-correlated photon pair generation in dispersion-shifted fiber: suppression of noise photons by cooling fiber, *Optics express* **13**, 7832 (2005).
- [6] J. Aasi, J. Abadie, B. Abbott, R. Abbott, T. Abbott, M. Abernathy, C. Adams, T. Adams, P. Addesso, R. Adhikari, *et al.*, Enhanced sensitivity of the ligo gravitational wave detector by using squeezed states of light, *Nature Photonics* **7**, 613 (2013).

- [7] S. Chua, B. Slagmolen, D. Shaddock, and D. McClelland, Quantum squeezed light in gravitational-wave detectors, *Classical and Quantum Gravity* **31**, 183001 (2014).
- [8] B. J. Lawrie, P. D. Lett, A. M. Marino, and R. C. Pooser, Quantum sensing with squeezed light, *Acs Photonics* **6**, 1307 (2019).
- [9] C. McCormick, A. M. Marino, V. Boyer, and P. D. Lett, Strong low-frequency quantum correlations from a four-wave-mixing amplifier, *Physical Review A* **78**, 043816 (2008).
- [10] A. M. Marino, V. Boyer, R. C. Pooser, P. D. Lett, K. Lemons, and K. Jones, Delocalized correlations in twin light beams with orbital angular momentum, *Physical review letters* **101**, 093602 (2008).
- [11] M. W. Holtfrerich and A. M. Marino, Control of the size of the coherence area in entangled twin beams, [Phys. Rev. A **93**, 063821 \(2016\)](#).
- [12] A. Kumar, H. Nunley, and A. M. Marino, Observation of spatial quantum correlations in the macroscopic regime, [Phys. Rev. A **95**, 053849 \(2017\)](#).
- [13] N. Prajapati, Z. Niu, and I. Novikova, Quantum-enhanced two-photon spectroscopy using two-mode squeezed light, *Optics Letters* **46**, 1800 (2021).
- [14] T. Li, V. Cheburkanov, V. V. Yakovlev, G. S. Agarwal, and M. O. Scully, Harnessing quantum light for microscopic biomechanical imaging of cells and tissues, *Proceedings of the National Academy of Sciences* **121**, e2413938121 (2024).
- [15] W. Chen, Şahin Kaya Özdemir, G. Zhao, J. Wiersig, and L. Yang, Exceptional points enhance sensing in an optical microcavity, *Nature* **548**, 192 (2017).
- [16] J. Wiersig, Review of exceptional point-based sensors, [Photon. Res. **8**, 1457 \(2020\)](#).

- [17] J. M. Nair, D. Mukhopadhyay, and G. Agarwal, Enhanced sensing of weak anharmonicities through coherences in dissipatively coupled anti-pt symmetric systems, *Physical Review Letters* **126**, 180401 (2021).
- [18] M. De Carlo, Exceptional points of parity-time and anti-parity-time-symmetric devices for refractive index and absorption-based sensing, *Results in Optics* **2**, 100052 (2021).
- [19] T. Wang, N. Venkatram, J. Gosciniaik, Y. Cui, G. Qian, W. Ji, and D. T. Tan, Multi-photon absorption and third-order nonlinearity in silicon at mid-infrared wavelengths, *Optics express* **21**, 32192 (2013).
- [20] J. Ralston and R. Chang, Spontaneous-raman-scattering efficiency and stimulated scattering in silicon, *Physical Review B* **2**, 1858 (1970).
- [21] R. Stolen and A. Ashkin, Optical kerr effect in glass waveguide, *Applied Physics Letters* **22**, 294 (1973).
- [22] U. L. Andersen, T. Gehring, C. Marquardt, and G. Leuchs, 30 years of squeezed light generation, *Physica Scripta* **91**, 053001 (2016).
- [23] Y. Shen, Recent advances in nonlinear optics, *Reviews of Modern Physics* **48**, 1 (1976).
- [24] S. Suresh, A. Ramanand, D. Jayaraman, and P. Mani, Review on theoretical aspect of nonlinear optics, *Rev. Adv. Mater. Sci* **30**, 175 (2012).
- [25] C. Thiel, Four-wave mixing and its applications, Faculty of Washington, Washington DC (2008).
- [26] N. Bloembergen, The stimulated raman effect, *American Journal of Physics* **35**, 989 (1967).

- [27] M. Levenson and N. Bloembergen, Dispersion of the nonlinear optical susceptibility tensor in centrosymmetric media, *Physical Review B* **10**, 4447 (1974).
- [28] G. Boyd and D. Kleinman, Parametric interaction of focused gaussian light beams, *Journal of Applied Physics* **39**, 3597 (1968).
- [29] N. Bloembergen, R. K. Chang, S. Jha, and C. Lee, Optical second-harmonic generation in reflection from media with inversion symmetry, *Physical Review* **174**, 813 (1968).
- [30] P. Franken, A. E. Hill, C. e. Peters, and G. Weinreich, Generation of optical harmonics, *Physical review letters* **7**, 118 (1961).
- [31] J. Bergman Jr and S. Kurtz, Nonlinear optical materials, *Materials Science and Engineering* **5**, 235 (1970).
- [32] A. Ashkin, G. Boyd, J. i. Dziedzic, R. Smith, A. Ballman, J. Levinstein, and K. Nassau, Optically-induced refractive index inhomogeneities in linbo3 and litao3, *Applied Physics Letters* **9**, 72 (1966).
- [33] R. W. Boyd, A. L. Gaeta, and E. Giese, Nonlinear optics, in *Springer Handbook of Atomic, Molecular, and Optical Physics* (Springer, 2008) pp. 1097–1110.
- [34] S. Harris and R. Miles, Proposed third-harmonic generation in phase-matched metal vapors, *Applied Physics Letters* **19**, 385 (1971).
- [35] S. E. Harris, Generation of vacuum-ultraviolet and soft—x-ray radiation using high-order nonlinear optical polarizabilities, [Phys. Rev. Lett.](#) **31**, 341 (1973).
- [36] A. Kung, J. F. Young, G. Bjorklund, and S. Harris, Generation of vacuum ultraviolet radiation in phase-matched cd vapor, *Physical Review Letters* **29**, 985 (1972).
- [37] H. P. Yuen and J. H. Shapiro, Generation and detection of two-photon coherent states in degenerate four-wave mixing, *Optics letters* **4**, 334 (1979).

- [38] L. Rothberg and N. Bloembergen, High-resolution four-wave light-mixing studies of collision-induced coherence in Na vapor, *Physical Review A* **30**, 820 (1984).
- [39] M. Ćurčić, T. Khalifa, B. Zlatković, I. Radojčić, A. Krmpot, D. Arsenović, B. Jenković, and M. Gharavipour, Four-wave mixing in potassium vapor with an off-resonant double- λ system, *Physical Review A* **97**, 063851 (2018).
- [40] V. F. Lukinykh, S. A. Myslivets, A. K. Popov, and V. V. Slabko, Four-wave frequency mixing in dye vapor, *Soviet Journal of Quantum Electronics* **16**, 927 (1986).
- [41] J. Sung and R. J. Silbey, Four wave mixing spectroscopy for a multilevel system, *The Journal of Chemical Physics* **115**, 9266 (2001).
- [42] Y. Wang, C.-Y. Lin, A. Nikolaenko, V. Raghunathan, and E. O. Potma, Four-wave mixing microscopy of nanostructures, *Advances in optics and photonics* **3**, 1 (2010).
- [43] S. Hu, B. Gai, J. Li, Y. Chen, X. Cai, P. Wang, J. Liu, and J. Guo, Competition of collimated ultraviolet lights generated by four-wave mixing process in Cs vapor, *Optics Communications* **527**, 128960 (2023).
- [44] F. Bencivenga, R. Cucini, F. Capotondi, A. Battistoni, R. Mincigrucci, E. Giangrisostomi, A. Gessini, M. Manfredda, I. Nikolov, E. Pedersoli, *et al.*, Four-wave mixing experiments with extreme ultraviolet transient gratings, *Nature* **520**, 205 (2015).
- [45] R. Willis, F. Becerra, L. Orozco, and S. Rolston, Four-wave mixing in the diamond configuration in an atomic vapor, *Physical Review A* **79**, 033814 (2009).
- [46] X. Pan, S. Yu, Y. Zhou, K. Zhang, K. Zhang, S. Lv, S. Li, W. Wang, and J. Jing, Orbital-angular-momentum multiplexed continuous-variable entanglement from four-wave mixing in hot atomic vapor, *Physical Review Letters* **123**, 070506 (2019).

- [47] Y. Yu, J. Sheng, and M. Xiao, Generation of bright quadricolor continuous-variable entanglement by four-wave-mixing process, *Physical Review A—Atomic, Molecular, and Optical Physics* **83**, 012321 (2011).
- [48] S. Takeda, T. Mizuta, M. Fuwa, P. Van Loock, and A. Furusawa, Deterministic quantum teleportation of photonic quantum bits by a hybrid technique, *Nature* **500**, 315 (2013).
- [49] U. L. Andersen, J. S. Neergaard-Nielsen, P. Van Loock, and A. Furusawa, Hybrid discrete-and continuous-variable quantum information, *Nature Physics* **11**, 713 (2015).
- [50] M. S. Podoshvedov and S. A. Podoshvedov, Universal dv-cv interaction mechanism for deterministic generation of entangled hybridity, *JOSA B* **37**, 963 (2020).
- [51] R. S. Bondurant, P. Kumar, J. H. Shapiro, and M. Maeda, Degenerate four-wave mixing as a possible source of squeezed-state light, *Physical Review A* **30**, 343 (1984).
- [52] P. Kumar and M. I. Kolobov, Degenerate four-wave mixing as a source for spatially-broadband squeezed light, *Optics communications* **104**, 374 (1994).
- [53] M. Reid and D. Walls, Quantum statistics of degenerate four wave mixing, *Optics communications* **50**, 406 (1984).
- [54] R. Slusher, L. Hollberg, B. Yurke, J. Mertz, and J. Valley, Observation of squeezed states generated by four-wave mixing in an optical cavity, *Physical review letters* **55**, 2409 (1985).
- [55] H. Vahlbruch, M. Mehmet, K. Danzmann, and R. Schnabel, Detection of 15 db squeezed states of light and their application for the absolute calibration of photoelectric quantum efficiency, *Physical review letters* **117**, 110801 (2016).
- [56] M. Dowran, A. Kumar, B. J. Lawrie, R. C. Pooser, and A. M. Marino, Quantum-enhanced plasmonic sensing, *Optica* **5**, 628 (2018).

- [57] Q. Glorieux, L. Guidoni, S. Guibal, J.-P. Likforman, and T. Coudreau, Strong quantum correlations in four wave mixing in 85rb vapor, in *Quantum Optics*, Vol. 7727 (SPIE, 2010) pp. 9–16.
- [58] A. Radnaev, Y. Dudin, R. Zhao, H. Jen, S. Jenkins, A. Kuzmich, and T. Kennedy, A quantum memory with telecom-wavelength conversion, *Nature Physics* **6**, 894 (2010).
- [59] I. Newton, *Opticks, or, a treatise of the reflections, refractions, inflections & colours of light* (Courier Corporation, 1952).
- [60] T. Young, *A course of lectures on natural philosophy and the mechanical arts*, Vol. 1 (Taylor and Walton, 1845).
- [61] L. Zuppiroli and M.-N. Bussac, *Traité de la lumière* (EPFL Press, 2009).
- [62] G. Binnig and H. Rohrer, Scanning tunneling microscopy—from birth to adolescence, *Rev. Mod. Phys.* **59**, 615 (1987).
- [63] F. Ohnesorge and G. Binnig, True atomic resolution by atomic force microscopy through repulsive and attractive forces, *Science* **260**, 1451 (1993), <https://www.science.org/doi/pdf/10.1126/science.260.5113.1451> .
- [64] J. H. Rice, Beyond the diffraction limit: far-field fluorescence imaging with ultrahigh resolution, *Molecular BioSystems* **3**, 781 (2007).
- [65] R. Heintzmann and G. Ficz, Breaking the resolution limit in light microscopy, *Briefings in Functional Genomics* **5**, 289 (2006).
- [66] J. Valli, A. Garcia-Burgos, L. M. Rooney, B. V. d. M. e Oliveira, R. R. Duncan, and C. Rickman, Seeing beyond the limit: A guide to choosing the right super-resolution microscopy technique, *Journal of Biological Chemistry* **297** (2021).
- [67] J. W. Goodman, *Introduction to Fourier optics* (Roberts and Company publishers, 2005).

- [68] O. K. Ersoy, *Diffraction, fourier optics and imaging* (John Wiley & Sons, 2006).
- [69] M. Fornasier and H. Rauhut, Compressive sensing., *Handbook of mathematical methods in imaging* **1**, 187 (2015).
- [70] S. L. Cuozzo, C. Gabaldon, P. J. Barge, Z. Niu, H. Lee, L. Cohen, I. Novikova, and E. E. Mikhailov, Wave-front reconstruction via single-pixel homodyne imaging, *Optics Express* **30**, 37938 (2022).
- [71] T. B. Pittman, Y. Shih, D. Strekalov, and A. V. Sergienko, Optical imaging by means of two-photon quantum entanglement, *Physical Review A* **52**, R3429 (1995).
- [72] J. H. Shapiro and R. W. Boyd, The physics of ghost imaging, *Quantum Information Processing* **11**, 949 (2012).
- [73] M. J. Padgett and R. W. Boyd, An introduction to ghost imaging: quantum and classical, *Philosophical Transactions of the Royal Society A: Mathematical, Physical and Engineering Sciences* **375**, 20160233 (2017).
- [74] H. Defienne, M. Reichert, J. W. Fleischer, and D. Faccio, Quantum image distillation, *Science advances* **5**, eaax0307 (2019).
- [75] T. Gregory, P.-A. Moreau, E. Toninelli, and M. J. Padgett, Imaging through noise with quantum illumination, *Science advances* **6**, eaay2652 (2020).
- [76] V. Boyer, A. M. Marino, R. C. Pooser, and P. D. Lett, Entangled images from four-wave mixing, *Science* **321**, 544 (2008).
- [77] G. B. Lemos, V. Borish, G. D. Cole, S. Ramelow, R. Lapkiewicz, and A. Zeilinger, Quantum imaging with undetected photons, *Nature* **512**, 409 (2014).
- [78] S. L. Cuozzo, P. J. Barge, N. Prajapati, N. Bhusal, H. Lee, L. Cohen, I. Novikova, and E. E. Mikhailov, Low-light shadow imaging using quadrature-noise detection with a camera, *Advanced Quantum Technologies* **5**, 2100147 (2022).

- [79] P. J. Barge, Z. Niu, S. L. Cuozzo, E. E. Mikhailov, I. Novikova, H. Lee, and L. Cohen, Weak thermal state quadrature-noise shadow imaging, *Optics Express* **30**, 29401 (2022).
- [80] G. Gamow, Zur quantentheorie des atomkernes, *Zeitschrift für Physik* **51**, 204 (1928).
- [81] H. Feshbach, C. Porter, and V. Weisskopf, Model for nuclear reactions with neutrons, *Physical review* **96**, 448 (1954).
- [82] R. El-Ganainy, K. G. Makris, M. Khajavikhan, Z. H. Musslimani, S. Rotter, and D. N. Christodoulides, Non-hermitian physics and pt symmetry, *Nature Physics* **14**, 11 (2018).
- [83] G. Lindblad, On the generators of quantum dynamical semigroups, *Communications in mathematical physics* **48**, 119 (1976).
- [84] N. Moiseyev, *Non-Hermitian quantum mechanics* (Cambridge University Press, 2011).
- [85] W. Heiss, Exceptional points of non-hermitian operators, *Journal of Physics A: Mathematical and General* **37**, 2455 (2004).
- [86] M. V. Berry, Physics of nonhermitian degeneracies, *Czechoslovak journal of physics* **54**, 1039 (2004).
- [87] C. M. Bender, Making sense of non-hermitian hamiltonians, *Reports on Progress in Physics* **70**, 947 (2007).
- [88] C. Bender, S. ddboettcher and pn meisinger, *J. Math. Phys* **40**, 2201 (1999).
- [89] C. M. Bender and S. Boettcher, Real spectra in non-hermitian hamiltonians having p t symmetry, *Phys. Rev. Lett* **80**, 5243 (1998).

- [90] Z. Xiao, H. Li, T. Kottos, and A. Alù, Enhanced sensing and nondegraded thermal noise performance based on pt-symmetric electronic circuits with a sixth-order exceptional point, *Physical Review Letters* **123**, 213901 (2019).
- [91] J. Li, R. Yu, C. Ding, and Y. Wu, Pt-symmetry-induced evolution of sharp asymmetric line shapes and high-sensitivity refractive index sensors in a three-cavity array, *Physical Review A* **93**, 023814 (2016).
- [92] S. Yu, Y. Meng, J.-S. Tang, X.-Y. Xu, Y.-T. Wang, P. Yin, Z.-J. Ke, W. Liu, Z.-P. Li, Y.-Z. Yang, *et al.*, Experimental investigation of quantum pt-enhanced sensor, *Physical Review Letters* **125**, 240506 (2020).
- [93] M. Farhat, M. Yang, Z. Ye, and P.-Y. Chen, Pt-symmetric absorber-laser enables electromagnetic sensors with unprecedented sensitivity, *ACS Photonics* **7**, 2080 (2020).
- [94] J. Wen, C. Zheng, X. Kong, S. Wei, T. Xin, and G. Long, Experimental demonstration of a digital quantum simulation of a general pt-symmetric system, *Physical Review A* **99**, 062122 (2019).
- [95] N. Maraviglia, P. Yard, R. Wakefield, J. Carolan, C. Sparrow, L. Chakhmakhchyan, C. Harrold, T. Hashimoto, N. Matsuda, A. K. Harter, *et al.*, Photonic quantum simulations of coupled pt-symmetric hamiltonians, *Physical Review Research* **4**, 013051 (2022).
- [96] H. Jing, S. Özdemir, X.-Y. Lü, J. Zhang, L. Yang, and F. Nori, Pt-symmetric phonon laser, *Physical review letters* **113**, 053604 (2014).
- [97] S. Longhi, Pt-symmetric laser absorber, *Physical Review A—Atomic, Molecular, and Optical Physics* **82**, 031801 (2010).
- [98] D. Christodoulides, J. Yang, *et al.*, *Parity-time symmetry and its applications*, Vol. 280 (Springer, 2018).

- [99] Ş. K. Özdemir, S. Rotter, F. Nori, and L. Yang, Parity–time symmetry and exceptional points in photonics, *Nature materials* **18**, 783 (2019).
- [100] P. Peng, W. Cao, C. Shen, W. Qu, J. Wen, L. Jiang, and Y. Xiao, Anti-parity–time symmetry with flying atoms, *Nature Physics* **12**, 1139 (2016).
- [101] M. Zhang, W. Sweeney, C. W. Hsu, L. Yang, A. Stone, and L. Jiang, Quantum noise theory of exceptional point amplifying sensors, *Phys. Rev. Lett* **123**, 180501 (2019).
- [102] M. Naghiloo, M. Abbasi, Y. N. Joglekar, and K. Murch, Quantum state tomography across the exceptional point in a single dissipative qubit, *Nature Physics* **15**, 1232 (2019).
- [103] Y. Jiang, Y. Mei, Y. Zuo, Y. Zhai, J. Li, J. Wen, and S. Du, Anti-parity-time symmetric optical four-wave mixing in cold atoms, *Phys. Rev. Lett.* **123**, 193604 (2019).
- [104] X.-W. Luo, C. Zhang, and S. Du, Quantum squeezing and sensing with pseudo-anti-parity-time symmetry, *Physical Review Letters* **128**, 173602 (2022).
- [105] P. Meystre and M. O. Scully, *Quantum optics* (Springer, 2021).
- [106] C. Gerry and P. Knight, Nonclassical light, in *Introductory Quantum Optics* (Cambridge University Press, 2004) p. 150–194.
- [107] N. Prajapati, *Development of Quantum Information Tools Based on Multi-Photon Raman Processes in Rb Vapor* (The College of William and Mary, 2020).
- [108] M. Turnbull, P. Petrov, C. Embrey, A. Marino, and V. Boyer, Role of the phase-matching condition in nondegenerate four-wave mixing in hot vapors for the generation of squeezed states of light, *Phys.Rev.A* **88**, 033845 (2013).

- [109] Q. Glorieux, R. Dubessy, S. Guibal, L. Guidoni, J.-P. Likforman, T. Coudreau, and E. Arimondo, Double- λ microscopic model for entangled light generation by four-wave mixing, *Phys. Rev. A* **82**, 033819 (2010).
- [110] A. Yariv and D. M. Pepper, Amplified reflection, phase conjugation, and oscillation in degenerate four-wave mixing, *Optics letters* **1**, 16 (1977).
- [111] Y. Jiang, Y. Mei, and S. Du, Quantum langevin theory for two coupled phase-conjugated electromagnetic waves, [Phys. Rev. A **107**, 053703 \(2023\)](#).
- [112] M. Turnbull, *Multi-spatial-mode quadrature squeezing from four-wave mixing in a hot atomic vapour*, Ph.D. thesis, University of Birmingham (2014).
- [113] J. J. Sakurai and J. Napolitano, *Modern quantum mechanics* (Cambridge University Press, 2020).
- [114] C. C. Gerry and P. L. Knight, *Introductory quantum optics* (Cambridge university press, 2023).
- [115] M. O. Scully and M. S. Zubairy, *Quantum optics* (Cambridge university press, 1997).
- [116] M. Jasperse, *Relative Intensity Squeezing by Four-Wave Mixing in Rubidium* (2010).
- [117] K. Peng, Q. Pan, H. Wang, Y. Zhang, H. Su, and C. Xie, Generation of two-mode quadrature-phase squeezing and intensity-difference squeezing from a cw-nopo, *Applied Physics B* **66**, 755 (1998).
- [118] N. B. Phillips, *Slow and stored light under conditions of electromagnetically induced transparency and four wave mixing in an atomic vapor* (The College of William and Mary, 2011).
- [119] A. V. Gorshkov, T. Calarco, M. D. Lukin, and A. S. Sørensen, Photon storage in Λ -type optically dense atomic media. iv. optimal control using gradient ascent, [Phys. Rev. A **77**, 043806 \(2008\)](#).

- [120] M. Lukin, P. Hemmer, and M. O. Scully, Resonant nonlinear optics in phase-coherent media, *Advances in Atomic, Molecular, and Optical Physics* **42**, 347 (2000).
- [121] M. Mahmoudi and J. Evers, Light propagation through closed-loop atomic media beyond the multiphoton resonance condition, *Phys. Rev. A* **74**, 063827 (2006).
- [122] N. B. Phillips, I. Novikova, E. E. Mikhailov, D. Budker, and S. Rochester, Controllable steep dispersion with gain in a four-level n-scheme with four-wave mixing, *Journal of Modern Optics* **60**, 64 (2013).
- [123] N. B. Phillips, A. V. Gorshkov, and I. Novikova, Light storage in an optically thick atomic ensemble under conditions of electromagnetically induced transparency and four-wave mixing, *Phys. Rev. A* **83**, 063823 (2011).
- [124] N. B. Phillips, A. V. Gorshkov, and I. Novikova, Slow light propagation and amplification via electromagnetically induced transparency and four-wave mixing in an optically dense atomic vapor, *Journal of Modern Optics* **56**, 1916 (2009).
- [125] S. Kim and A. M. Marino, Generation of 87 rb resonant bright two-mode squeezed light with four-wave mixing, *Optics Express* **26**, 33366 (2018).
- [126] D. A. Steck, Rubidium 85 d line data, <https://steck.us/alkalidata/rubidium85numbers.pdf>, (2001).
- [127] Z. Niu, Y. Jiang, J. Wen, C. Zhang, S. Du, and I. Novikova, Four-wave mixing with anti-parity-time symmetry in hot 85rb vapor, *Applied Physics Letters* **124** (2024).
- [128] G. Morigi, S. Franke-Arnold, and G.-L. Oppo, Phase-dependent interaction in a four-level atomic configuration, *Physical Review A* **66**, 053409 (2002).
- [129] Y.-S. Lee and H. S. Moon, Atomic coherence effects in four-wave mixing process of a ladder-type atomic system, *Optics Express* **24**, 10723 (2016).

- [130] R. T. Willis, *Photon pair production from a hot atomic ensemble in the diamond configuration* (University of Maryland, College Park, 2009).
- [131] Z. Niu, J. Wen, C. Zhang, S. Du, and I. Novikova, Bi-chromatic intensity squeezing using four-wave mixing in 85rb vapor, *Optica Quantum* **3**, 72 (2025).
- [132] L.-M. Duan, M. D. Lukin, J. I. Cirac, and P. Zoller, Long-distance quantum communication with atomic ensembles and linear optics, *Nature* **414**, 413 (2001).
- [133] K. Azuma, S. E. Economou, D. Elkouss, P. Hilaire, L. Jiang, H.-K. Lo, and I. Tzitrin, Quantum repeaters: From quantum networks to the quantum internet, *Reviews of Modern Physics* **95**, 045006 (2023).
- [134] H. J. Kimble, The quantum internet, *Nature* **453**, 1023 (2008).
- [135] S. Wehner, D. Elkouss, and R. Hanson, Quantum internet: A vision for the road ahead, *Science* **362**, eaam9288 (2018).
- [136] X.-W. Luo, C. Zhang, I. Novikova, C. Qian, and S. Du, Wavelength conversion for single-photon polarization qubits through continuous-variable quantum teleportation, *Physical Review A* **105**, 052444 (2022).
- [137] M. Allgaier, V. Ansari, L. Sansoni, C. Eigner, V. Quiring, R. Ricken, G. Harder, B. Brecht, and C. Silberhorn, Highly efficient frequency conversion with bandwidth compression of quantum light, *Nature communications* **8**, 14288 (2017).
- [138] X. Wang, X. Jiao, B. Wang, Y. Liu, X.-P. Xie, M.-Y. Zheng, Q. Zhang, and J.-W. Pan, Quantum frequency conversion and single-photon detection with lithium niobate nanophotonic chips, *npj Quantum Information* **9**, 38 (2023).
- [139] A. N. Craddock, Y. Wang, F. Giraldo, R. Sekelsky, M. Flament, and M. Namazi, High-rate subgigahertz-linewidth bichromatic entanglement source for quantum networking, *Physical Review Applied* **21**, 034012 (2024).

- [140] F. Becerra, R. Willis, S. Rolston, and L. Orozco, Nondegenerate four-wave mixing in rubidium vapor: The diamond configuration, *Physical review A* **78**, 013834 (2008).
- [141] C.-Y. Hsu, Y.-S. Wang, J.-M. Chen, F.-C. Huang, Y.-T. Ke, E. K. Huang, W. Hung, K.-L. Chao, S.-S. Hsiao, Y.-H. Chen, *et al.*, Generation of sub-mhz and spectrally-bright biphotons from hot atomic vapors with a phase mismatch-free scheme, *Optics Express* **29**, 4632 (2021).
- [142] S. L. Braunstein and P. van Loock, Quantum information with continuous variables, *Rev. Mod. Phys.* **77**, 513 (2005).
- [143] C. Weedbrook, S. Pirandola, R. García-Patrón, N. J. Cerf, T. C. Ralph, J. H. Shapiro, and S. Lloyd, Gaussian quantum information, *Rev. Mod. Phys.* **84**, 621 (2012).
- [144] P. Wang, M. Chen, N. C. Menicucci, and O. Pfister, Weaving quantum optical frequency combs into continuous-variable hypercubic cluster states, *Physical Review A* **90**, 032325 (2014).
- [145] P. C. Humphreys, W. S. Kolthammer, J. Nunn, M. Barbieri, A. Datta, and I. A. Walmsley, Continuous-variable quantum computing in optical time-frequency modes using quantum memories, *Physical review letters* **113**, 130502 (2014).
- [146] N. Liu, J. Thompson, C. Weedbrook, S. Lloyd, V. Vedral, M. Gu, and K. Modi, Power of one qumode for quantum computation, *Physical Review A* **93**, 052304 (2016).
- [147] G. Adesso, S. Ragy, and A. R. Lee, Continuous variable quantum information: Gaussian states and beyond, *Open Systems & Information Dynamics* **21**, 1440001 (2014).
- [148] N. Killoran, T. R. Bromley, J. M. Arrazola, M. Schuld, N. Quesada, and S. Lloyd, Continuous-variable quantum neural networks, *Physical Review Research* **1**, 033063 (2019).
- [149] U. Andersen, G. Leuchs, and C. Silberhorn, Continuous-variable quantum information processing, *Laser & Photonics Reviews* **4**, 337 (2010).

- [150] H.-R. Noh and H. S. Moon, Four-wave mixing in a ladder configuration of warm 87 rb atoms: a theoretical study, *Optics Express* **29**, 6495 (2021).
- [151] B. N. Miller, D. H. Meyer, T. Virtanen, C. M. O'Brien, and K. C. Cox, Rydiqule: A graph-based paradigm for modeling rydberg and atomic sensors, *Computer Physics Communications* **294**, 108952 (2024).
- [152] Due to the limited accuracy of the wavemeter used for pump frequency calibration, the exact pump detuning values are determined by comparing the numerical model with the measured data.
- [153] B. J. Lawrie, P. D. Lett, A. M. Marino, and R. C. Pooser, Quantum sensing with squeezed light, *ACS Photonics* **6**, 1307 (2019).
- [154] A. Akulshin, A. Orel, and R. McLean, Collimated blue light enhancement in velocity-selective pumped rb vapour, *Journal of Physics B: Atomic, Molecular and Optical Physics* **45**, 015401 (2011).
- [155] Z. Wang, Y. Zhang, H. Zheng, C. Li, F. Wen, and H. Chen, Switching enhancement and suppression of four-wave mixing via a dressing field, *Journal of Modern Optics* **58**, 802 (2011).
- [156] D. Zhang, C. Li, Z. Zhang, Y. Zhang, Y. Zhang, and M. Xiao, Enhanced intensity-difference squeezing via energy-level modulations in hot atomic media, *Physical Review A* **96**, 043847 (2017).
- [157] Y. Fang and J. Jing, Quantum squeezing and entanglement from a two-mode phase-sensitive amplifier via four-wave mixing in rubidium vapor, *New Journal of Physics* **17**, 023027 (2015).
- [158] Z. Qin, L. Cao, H. Wang, A. M. Marino, W. Zhang, and J. Jing, Experimental generation of multiple quantum correlated beams from hot rubidium vapor, [Phys. Rev. Lett.](#) **113**, 023602 (2014).

- [159] P. A. Morris, R. S. Aspden, J. E. Bell, R. W. Boyd, and M. J. Padgett, Imaging with a small number of photons, *Nature Communications* **6**, 1 (2015).
- [160] A. Meda, E. Losero, N. Samantaray, F. Scafirimuto, S. Pradyumna, A. Avella, I. Ruo-Berchera, and M. Genovese, Photon-number correlation for quantum enhanced imaging and sensing, *Journal of Optics* **19**, 094002 (2017).
- [161] I. R. Berchera and I. P. Degiovanni, Quantum imaging with sub-Poissonian light: challenges and perspectives in optical metrology, *Metrologia* **56**, 024001 (2019).
- [162] P.-A. Moreau, J. Sabines-Chesterking, R. Whittaker, S. K. Joshi, P. M. Birchall, A. McMillan, J. G. Rarity, and J. C. Matthews, Demonstrating an absolute quantum advantage in direct absorption measurement, *Scientific Reports* **7**, 1 (2017).
- [163] R. Whittaker, C. Erven, A. Neville, M. Berry, J. O'Brien, H. Cable, and J. Matthews, Absorption spectroscopy at the ultimate quantum limit from single-photon states, *New Journal of Physics* **19**, 023013 (2017).
- [164] E. Losero, I. Ruo-Berchera, A. Meda, A. Avella, and M. Genovese, Unbiased estimation of an optical loss at the ultimate quantum limit with twin-beams, *Scientific Reports* **8**, 1 (2018).
- [165] G. Brida, M. Genovese, and I. R. Berchera, Experimental realization of sub-shot-noise quantum imaging, *Nature Photonics* **4**, 227 (2010).
- [166] F. Ferri, D. Magatti, L. Lugiato, and A. Gatti, Differential ghost imaging, *Phys. Rev. Lett.* **104**, 253603 (2010).
- [167] N. Samantaray, I. Ruo-Berchera, A. Meda, and M. Genovese, Realization of the first sub-shot-noise wide field microscope, *Light: Science & Applications* **6**, e17005 (2017).
- [168] M. A. Taylor and W. P. Bowen, Quantum metrology and its application in biology, *Physics Reports* **615**, 1 (2016).

- [169] S. L. Cuozzo, P. J. Barge, N. Prajapati, N. Bhusal, H. Lee, L. Cohen, I. Novikova, and E. E. Mikhailov, Low-light shadow imaging using quantum-noise detection with a camera, arXiv preprint arXiv:2106.00785 (2021).
- [170] E. S. Matekole, S. L. Cuozzo, N. Prajapati, N. Bhusal, H. Lee, I. Novikova, E. E. Mikhailov, J. P. Dowling, and L. Cohen, Quantum-limited squeezed light detection with a camera, *Phys. Rev. Lett.* **125**, 113602 (2020).
- [171] Z. Xiao, R. N. Lanning, M. Zhang, I. Novikova, E. E. Mikhailov, and J. P. Dowling, Why a hole is like a beam splitter: A general diffraction theory for multimode quantum states of light, *Physical Review A* **96**, 023829 (2017).
- [172] E. Brambilla, L. Caspani, O. Jedrkiewicz, L. Lugiato, and A. Gatti, High-sensitivity imaging with multi-mode twin beams, *Physical Review A* **77**, 053807 (2008).
- [173] T. S. Woodworth, K. W. C. Chan, C. Hermann-Avigliano, and A. M. Marino, Transmission estimation at the cramer-rao bound for squeezed states of light in the presence of loss and imperfect detection, *Physical Review A* **102**, 052603 (2020).
- [174] N. Prajapati and I. Novikova, Polarization-based truncated SU(1,1) interferometer based on four-wave mixing in Rb vapor, *Optics Letters* **44**, 5921 (2019).
- [175] N. Prajapati, N. Super, N. R. Lanning, J. P. Dowling, and I. Novikova, Optical angular momentum manipulations in a four-wave mixing process, *Optics Letters* **44**, 739 (2019).
- [176] W. Martienssen and E. Spiller, Coherence and fluctuations in light beams, *American Journal of Physics* **32**, 919 (1964).
- [177] V. Boyer, A. Marino, and P. Lett, Generation of spatially broadband twin beams for quantum imaging, *Physical review letters* **100**, 143601 (2008).

- [178] A. Kumar and A. Marino, Spatial squeezing in bright twin beams generated with four-wave mixing: Constraints on characterization with an electron-multiplying charge-coupled-device camera, *Physical Review A* **100**, 063828 (2019).
- [179] M. Holtfrerich and A. Marino, Control of the size of the coherence area in entangled twin beams, *Physical Review A* **93**, 063821 (2016).
- [180] L. Mandel and E. Wolf, *Optical coherence and quantum optics* (Cambridge university press, 1995).
- [181] L. Ge and H. E. Türeci, Antisymmetric pt-photonic structures with balanced positive-and negative-index materials, *Phys. Rev. A* **88**, 053810 (2013).
- [182] H. Fan, J. Chen, Z. Zhao, J. Wen, and Y.-P. Huang, Antiparity-time symmetry in passive nanophotonics, *ACS Photonics* **7**, 3035 (2020).
- [183] C. Wang, Z. Fu, W. Mao, J. Qie, A. D. Stone, and L. Yang, Non-hermitian optics and photonics: from classical to quantum, [Adv. Opt. Photon.](#) **15**, 442 (2023).
- [184] L. Feng, Z. J. Wong, R.-M. Ma, Y. Wang, and X. Zhang, Single-mode laser by parity-time symmetry breaking, *Science* **346**, 972 (2014).
- [185] S. Longhi, Bloch oscillations in complex crystals with p t symmetry, *Phys. Rev. Lett* **103**, 123601 (2009).
- [186] L. Ge, Y. Chong, S. Rotter, H. E. Türeci, and A. Stone, Unconventional modes in lasers with spatially varying gain and loss, *Phys. Rev. A* **84**, 023820 (2011).
- [187] M. H. Teimourpour, L. Ge, D. N. Christodoulides, and R. El-Ganainy, Non-hermitian engineering of single mode two dimensional laser arrays, *Scientific reports* **6**, 1 (2016).
- [188] M. P. Hokmabadi, N. S. Nye, R. El-Ganainy, D. N. Christodoulides, and M. Khajavikhan, Supersymmetric laser arrays, *Science* **363**, 623 (2019).

- [189] Y. Li, Y.-G. Peng, L. Han, M.-A. Miri, W. Li, M. Xiao, X.-F. Zhu, J. Zhao, A. Alù, S. Fan, *et al.*, Anti-parity-time symmetry in diffusive systems, *Science* **364**, 170 (2019).
- [190] A. Bergman, R. Duggan, K. Sharma, M. Tur, A. Zadok, and A. Alù, Observation of anti-parity-time-symmetry, phase transitions and exceptional points in an optical fibre, *Nature communications* **12**, 1 (2021).
- [191] C. F. McCormick, A. M. Marino, V. Boyer, and P. D. Lett, Strong low-frequency quantum correlations from a four-wave-mixing amplifier, *Phys. Rev. A* **78**, 043816 (2008).
- [192] V. Boyer, A. M. Marino, R. C. Pooser, and P. D. Lett, Entangled images from four-wave mixing, *Science* **321**, 544 (2008).
- [193] M.-C. Wu, B. L. Schmittberger, N. R. Brewer, R. W. Speirs, K. M. Jones, and P. D. Lett, Twin-beam intensity-difference squeezing below 10 Hz, *Opt. Express* **27**, 4769 (2019).
- [194] N. Prajapati and I. Novikova, Polarization-based truncated $su(1,1)$ interferometer based on four-wave mixing in Rb vapor, *Opt. Lett.* **44**, 5921 (2019).
- [195] X.-W. Luo, C. Zhang, and S. Du, Quantum squeezing and sensing with pseudo-anti-parity-time symmetry, *Phys. Rev. Lett.* **128**, 173602 (2022).
- [196] H.-K. Lau and A. A. Clerk, Fundamental limits and non-reciprocal approaches in non-hermitian quantum sensing, *Nature communications* **9**, 4320 (2018).
- [197] B. E. Anderson, B. L. Schmittberger, P. Gupta, K. M. Jones, and P. D. Lett, Optimal phase measurements with bright- and vacuum-seeded $su(1,1)$ interferometers, *Phys. Rev. A* **95**, 063843 (2017).
- [198] N. Prajapati, Z. Niu, and I. Novikova, Quantum-enhanced two-photon spectroscopy using two-mode squeezed light, *Optics Letters* **46**, 1800 (2021).

- [199] R. C. Pooser, N. Savino, E. Batson, J. L. Beckey, J. Garcia, and B. J. Lawrie, Truncated nonlinear interferometry for quantum-enhanced atomic force microscopy, [Phys. Rev. Lett. **124**, 230504 \(2020\)](#).
- [200] X. Liang, Z. Yu, C.-H. Yuan, W. Zhang, and L. Chen, Phase sensitivity improvement in correlation-enhanced nonlinear interferometers, [Symmetry **14**, 10.3390/sym14122684 \(2022\)](#).
- [201] T. S. Woodworth, C. Hermann-Avigliano, K. W. C. Chan, and A. M. Marino, Transmission estimation at the quantum cramer-rao bound with macroscopic quantum light, [EPJ Quantum Technology **9**, 38 \(2022\)](#).